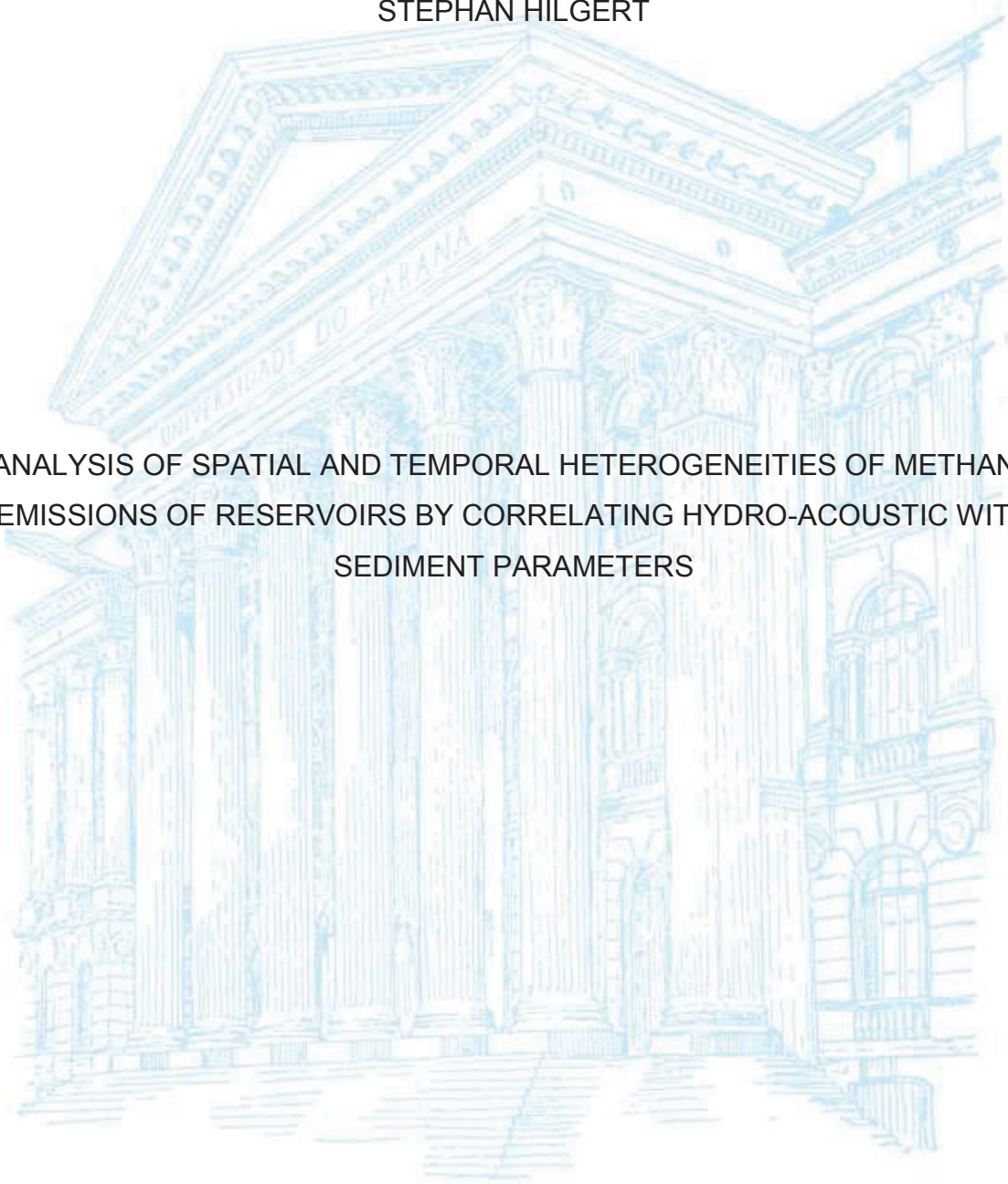


UNIVERSIDADE FEDERAL DO PARANÁ

STEPHAN HILGERT

ANALYSIS OF SPATIAL AND TEMPORAL HETEROGENEITIES OF METHANE
EMISSIONS OF RESERVOIRS BY CORRELATING HYDRO-ACOUSTIC WITH
SEDIMENT PARAMETERS



CURITIBA

2014

ANALYSIS OF SPATIAL AND TEMPORAL HETEROGENEITIES OF METHANE
EMISSIONS OF RESERVOIRS BY CORRELATING HYDRO-ACOUSTIC WITH
SEDIMENT PARAMETERS

Submitted in Partial Fulfillment
of the Requirements for the Degree of
DOCTOR OF ENGINEERING

by the Department of
Civil Engineering, Geo and Environmental Sciences

of the Karlsruhe Institute of Technology (KIT)
approved
DISSERTATION

by
Dipl. Geoecol. Stephan Hilgert

born in Bergisch Gladbach

Supervisor: Prof. Dr. Stefan Hinz
Co-supervisor: Prof. Dr. Cristóvão Vicente
Scapulatempo Fernandes

Karlsruhe 2014

STEPHAN HILGERT

ANALYSIS OF SPATIAL AND TEMPORAL HETEROGENEITIES OF METHANE
EMISSIONS OF RESERVOIRS BY CORRELATING HYDRO-ACOUSTIC WITH
SEDIMENT PARAMETERS

Tese apresentada como requisito parcial à obtenção do grau de Doutor em Engenharia de Recursos Hídricos e Ambiental, no Curso de Pós-Graduação em Engenharia de Recursos Hídricos e Ambiental, Setor de Tecnologia da Universidade Federal do Paraná, em regime de Cotutela firmado entre a UFPR e o Karlsruhe Institute of Technology (KIT, Karlsruhe, Alemanha).

Orientador: Prof. Dr. Stefan Hinz (KIT)
Co-orientador: Prof. Dr. Cristóvão Vicente Scapulatempo Fernandes (UFPR)

KARLSRUHE (ALEMANHA) E CURITIBA

2014

Catálogo na Fonte: Sistema de Bibliotecas, UFPR
Biblioteca de Ciência e Tecnologia

H643a

Hilgert, Stephan

Analysis of spatial and temporal heterogeneities of methane emissions of reservoirs by correlating hydro-acoustic with sediment parameters/ Stephan Hilgert. – Curitiba ; Karlsruhe, 2015.

Tese - Universidade Federal do Paraná, Setor de Tecnologia, Programa de Pós-graduação em Engenharia de Recursos Hídricos e Ambiental; Karlsruhe Institute of Technology, Department of Civil Engineering, Geo and Environmental Sciences, 2015.

Orientador: Stefan Hinz – Co-orientador: Cristóvão Vicente Scapulatempo Fernandes

1. Gases estufa. 2. Metano. 3. Sedimentologia. 4. Acústica subaquática. I. Universidade Federal do Paraná. II. Hinz, Stefan. III. Fernandes, Cristóvão Vicente Scapulatempo. IV. Karlsruhe Institute of Technology. V. Título.

CDD: 363.73874

Bibliotecário: Elias Barbosa da Silva CRB-9/1894

DECLARATION OF CONSENT

Note:

A rapid return of this consent form to the Office of the Dean will accelerate the completion of the doctoral certificate.

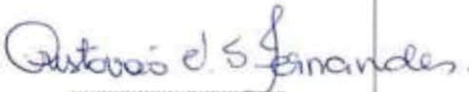
We agree to the title listed below and the textual version of the dissertation of
Mr. Dipl.-Geodol. Stephan **Hilgert**.

Title: Analysis of Spatial and Temporal Heterogeneities of Methane Emissions of Reservoirs by
Correlating Hydro-acoustic with Sediment Parameters


Prof. Dr.-Ing. habil. Stefan Hinz


(main referee)

Prof. Cristóvão Vicente S. Fernandes, Ph.D


(co-referee)

Acknowledged by


(doctoral candidate)

Das Karlsruher Institut für Technologie (KIT)

verleiht

durch die KIT-Fakultät für Bauingenieur-, Geo und Umweltwissenschaften

Dipl.-Geoökol. Stephan Hilgert

geboren am 27. Juli 1982 in Bergisch Gladbach

Titel und Würde eines

Doktors der Ingenieurwissenschaften (Dr.-Ing.)

nachdem er in ordnungsgemäßem gemeinsam von dem Karlsruher Institut für Technologie (KIT) und der Universidade Federal do Paraná, Brasil, betreuten Promotionsverfahren durch seine Dissertation

Analysis of Spatial and Temporal Heterogeneities of Methane Emissions by Correlating Hydro-acoustic with Sediment Parameters

sowie durch die mündliche Prüfung seine wissenschaftliche Befähigung erwiesen hat.

Stephan Hilgert hat das Recht, den Doktorgrad entweder in der deutschen oder brasilianischen Form zu führen. In Klammern können die Namen der beiden Universitäten, die das Promotionsverfahren betreut haben, hinzugefügt werden. Dieser Doktorgrad bedarf zur Führung in der Bundesrepublik Deutschland keiner weiteren staatlichen Genehmigung.

Diese Urkunde gilt nur in Verbindung mit der Promotionsurkunde der Universidade Federal do Paraná, Brasil.

Karlsruhe, 30. April 2015



Präsident des Karlsruher Instituts
für Technologie (KIT)



Dekan der KIT-Fakultät
für Bauingenieur-, Geo- und
Umweltwissenschaften

Acknowledgements:

I would like to extend thanks to my supervisors Prof. Stefan Hinz from the Karlsruhe Institute of Technology and Prof. Cristóvão Vicente Scapulatempo Fernandes from the Universidade Federal do Paraná, for taking over the supervision of this work.

Many thanks go to Stephan Fuchs for giving me the chance to work on this topic and for a lot of faith in my work.

I thank Anthony P. Lyons and Tonya del Sontro for scientific support and Helge Balk for the license of Sonar5 pro.

Um Obrigado grande goes to the DHS-team at the UFPR for hosting me during the measurement campaigns, for technical support and for awesome times with the best Churrasco sessions.

I thank my colleagues for a great time at the institute, for ping-pong sessions and support. Sincere thanks to Tobias Morck for introducing me to the world of centrifuged espresso and leaving me with an adequate sound system for long working nights. A big time thank you, to Frieder Gauger for letting me use the rendered designs of ELKE and highly inventionional creatism. To Adrian and Marc for incredible particle separation work. To Isabel and Lisa for the domestication of data heaps and finally to Sebastian for membrane-bagging the reservoir.

Marcella, Melanie and Adrian deserve a lot of thanks for diligent corrections and criticism during the writing process.

I thank my parents for sparking my interests and for giving me what it takes to come that far.

- Et hätt noch ever jot jejange -

Finally and most importantly, thanks go to the One, who gave me perpetual and invaluable support and for putting up with me during a long time, to Tina Becker.

Resumo

A interrupção dos sistemas fluviais, pela construção das barragens, representa um fenômeno mundial que causa mudanças graves nos ciclos biogeoquímicos.

Represas atuam como depósitos para todos os materiais transportados, convertendo rios em lagos. Cada represa representa um sistema individual e um reator complexo.

Todos os corpos de água congestionados têm em comum que uma parte do carbono orgânico é transformada em gases do efeito estufa, e particularmente em metano.

Através do aumento intensivo das áreas inundadas antropogênicas nas últimas décadas, a quantificação dos gases relevantes ao clima se transformou em um foco da pesquisa. No entanto, a avaliação das emissões reais do metano fica imprecisa. Apesar da existência de métodos funcionais, a heterogeneidade temporal e espacial das emissões permanece um problema. Por isso, apresenta o balanço global das emissões dos gases do efeito estufa altas incorreções.

Este trabalho tem como objetivo o melhoramento dos métodos relevantes, assim como a ampliação da compreensão do sistema no contexto dos padrões heterogêneos das emissões.

A identificação de “hot spots” da produção de metano em reservatórios é o objetivo principal do trabalho. Esse objetivo é realizado pelo desenvolvimento de estratégias inovadoras de medições que são capazes de diminuir erros sistemáticos do balanço das emissões.

Seguindo o pressuposto que reservatórios trópicos emitem quantidades maiores de gases do efeito estufa e incluindo a alta relevância da geração de energia hidroelétrica no Brasil, dois reservatórios brasileiros foram selecionados para as medições, as quais foram realizadas em campo no período de 2010 a 2013.

Três conceitos diferentes foram utilizados no contexto da formação do metano para compreender a heterogeneidade temporal e espacial. Adicionalmente, os processos biogeoquímicos eram investigados no sedimento em escala local.

Dados batimétricos e morfométricos eram levantados durante os estudos hidroacústicos com um eco sonda 38/200 kHz Single Beam. Além disso, uma classificação hidroacústica do sedimento foi realizada junto com amostras de perfuração. Isso tudo vai possibilitar a interpolação espacial com base nos dados hidroacústicos e do sedimento.

As amostras de perfuração tem a vantagem que o sedimento se forma lentamente e por isso eles contém informações de períodos anteriores. Adicionalmente, investigações da água capilar no sedimento eram realizadas, destinadas a medir a concentração do metano e outros componentes relacionados com o potencial de redução e oxidação.

Consequentemente, era possível combinar a distribuição do sedimento no reservatório com os parâmetros biogeoquímicos e correlacionar os resultados com as condições de formação do metano. Pela espessura medida do sedimento junto com o conteúdo do carbono orgânico, era calculada a distribuição e a massa do carbono orgânico no sedimento. Para o reservatório Capivari foi calculado uma massa de 205.129 Mg (\pm 60.8 Mg).

Com base nestes resultados, foi possível atribuir potenciais de emissões de metano, altas ou baixas, nas zonas do reservatório.

Por conseguinte, é possível prever as margens das emissões com o erro estatístico, que pode ser reduzido.

Palavras-chave: Gases de Efeito Estufa, Reservatórios, Detecção do sedimento, Estudos hidroacústicos, Metano

Abstract

The worldwide phenomenon of disrupting riverine ecosystems by dams leads to severe changes of biogeochemical cycles. Impoundments act as a sink for all transported materials as they turn a river into a lake. Each particular impoundment represents an individual and complex reactor.

All dams have in common that they turn parts of the retained organic material into greenhouse gases and particularly into methane. Since the number and area of artificially created lake ecosystems significantly increased in the last decades, the amount of climate-relevant emissions became a focus of research.

However, the quantification of methane emissions from reservoirs is still imprecise. Although there are efficient measurement techniques, the spatial and temporal heterogeneity causes problems. Hence, the calculations of global methane budgets are affected by high inaccuracies.

This study aims on the improvement of methods as well as the enhancement of the understanding of the most relevant processes influencing the addressed heterogeneities. The overall objective is the identification of methane production hot spots in reservoirs, leading to innovative sampling strategies which are capable of minimizing the statistical error of overall emission budgets.

Following the assumption that tropical reservoirs are prone to produce significant shares of methane and considering the importance of hydroelectricity in Brazil, two Brazilian reservoirs were selected for the field investigations. Measurements were conducted during four field campaigns between 2010 and 2013.

The combination of three different approaches related to methane formation made it possible to address temporal and spatial heterogeneities, while still including process understanding on a local scale.

By conducting hydro-acoustic surveys using a 38/200 kHz single beam echo sounder, basic morphometric information was obtained. Additionally, seabed classification was conducted, including extensive ground truthing, which allowed the spatial interpolation of the found results.

Sediment core information features the advantage of a time-integrating momentum, since the formation of sediment volumes is a long term process.

Moreover, the pore water of the sediment at the corresponding sampling sites was examined for methane production and relevant redox-indicating compounds.

Consequently, it was possible to link the sediment distribution in the reservoir to quality parameters and correlate those to characteristics determining methane production. Derived sediment thickness information and organic carbon contents was used to calculate the carbon stock and its distribution. The entire Capivari reservoir holds a mass of 205,129 Mg (± 60.8 Mg) of organic carbon.

Based on the carbon distribution parts of the reservoir could be assigned to specific methane-formation behavior. Therefore, it is possible to predict the results from methane emission measurements which gives the chance to systematically reduce the statistical error of those.

Key words: GHG emissions, Reservoirs, Sediment detection, Echo sounding, Methane

Zusammenfassung

Das weltweite Phänomen der Unterbrechung von Flusssystemen durch den Bau von Dämmen führt zu gravierenden Veränderungen der biogeochemischen Kreisläufe.

Stauhaltungen wirken als Speicher für alle transportierten Stoffe, indem sie Flüsse in Seen umwandeln. Jede Stauhaltung stellt einen individuellen komplexen Reaktor dar.

Alle aufgestauten Wasserkörper haben gemeinsam, dass sie Teile des eingetragenen organischen Kohlenstoffs in Treibhausgase und insbesondere in Methan umsetzen. Durch die flächenmäßige Vergrößerung der anthropogen geschaffenen Wasserkörper in den letzten Jahrzehnten, wurde die Quantifizierung der dort ausgestoßenen klima-relevanten Gase zu einem Forschungsfokus.

Jedoch ist die Abschätzung der realen Methanemissionen noch immer ungenau. Obwohl es funktionierende Messmethoden gibt, bleibt die räumliche und zeitliche Heterogenität der Emissionen ein Problem, auf Grund dessen die Berechnung der globalen Treibhausgasbudgets große Ungenauigkeiten aufweist.

Diese Forschungsarbeit zielt auf die Verbesserung der relevanten Methoden, sowie auf die Erweiterung des nötigen Systemverständnisses, im Kontext der heterogenen Emissionsmuster. Das übergeordnete Ziel der Arbeit ist die Identifikation von Methan-Entstehung „Hot-Spots“ in den Stauseen, durch die Entwicklung innovativer Messstrategien, welche in der Lage sind die systematischen Fehler der Emissionsbudgets zu minimieren.

Der Annahme folgend, dass tropische Reservoirs höhere Mengen an Treibhausgasen emittieren und unter Einbeziehung der hohen Relevanz der Wasserkraft in Brasilien, wurden zwei brasilianische Stauseen für die Messkampagnen ausgewählt. Die Messungen wurden im Zeitraum 2010 bis 2013 durchgeführt.

Es wurden drei unterschiedliche Messansätze im Kontext der Methanentstehung kombiniert, um die temporale und räumliche Heterogenität zu erfassen. Zusätzlich wurden lokale geochemische Prozesse untersucht.

Während hydroakustischer Messungen mit einem 38/200 kHz Single Beam Echolot wurden morphometrische Daten der Stauseen erhoben. Des Weiteren wurde eine Klassifizierung des Seebodens, gemeinsam mit Sedimentbohrkernen durchgeführt. Dies erlaubt im Folgenden eine räumliche Interpolation auf Basis der Verschneidung der Echolot- mit den Sedimentinformationen.

Die Sedimentbohrkerne haben den Vorteil, dass sie integrierend, langfristige Prozesse wieder geben, da die Ablagerungsprozesse relativ langsam ablaufen. Darüber hinaus wurden an den Probenahmestellen Porenwasseruntersuchungen durchgeführt, mit dem Ziel die Methangehalte aber auch redox-Potential anzeigende Verbindungen zu bestimmen.

Somit war es möglich die Sedimentverteilung im Reservoir mit geochemischen Qualitätsparametern zu verbinden und die gewonnen Ergebnisse mit Methanentstehungsbedingungen zu korrelieren. Mittels der gemessenen Sedimentmächtigkeit und dem organischen Kohlenstoffgehalt im Sediment wurde die Verteilung und die Speichermenge des organischen Kohlenstoffs berechnet. Für das gesamte Reservoir Capivari wurde eine Menge von 205.129 Mg (\pm 60.8 Mg) errechnet.

Gestützt auf diese Ergebnisse, konnten Bereiche des Reservoirs hohen oder niedrigen Methan-Entstehungspotentialen zugewiesen werden. In Folge dessen ist eine Vorhersage der Emissionsmessungen möglich, womit der statistische Fehler der Messungen reduziert werden kann.

Schlüsselworte: Treibhausgasemissionen, Stauseen, Sedimentdetektion, Echolotsondierung, Methan

List of Figures

Figure 1-1:	Overview scheme of the conducted research of this work.....	7
Figure 2-1:	Exemplary reservoir configuration and depth distribution in comparison to a natural lake , the reservoirs show riverine behavior in the proximal and lacustrine characteristics in the profundal after Morris & Fan (1998).....	11
Figure 2-2:	Basic sedimentation patterns after Morris & Fan (1998), 10.3.....	14
Figure 2-3:	Zonation of sediment erosion, transportation and accumulation in a reservoir	15
Figure 2-4:	general longitudinal patterns of production and sedimentation of organic matter in a reservoir, after Morris & Fan (1998, 4.21).....	18
Figure 2-5:	Carbon cycle in a surface water body; after Wetzel, R., G. (2001).....	19
Figure 2-6:	Model of the sediment related pathways of organic compounds; based on Jorgensen, 2000	21
Figure 2-7:	Dependence of the bio-chemical sediment conditions on the sedimentation rate	23
Figure 2-8:	Simplified concept of methane emission pathways within the reservoir, the plant mediated pathway is excluded.....	25
Figure 2-9:	Basic design of a gas trap funnel.....	26
Figure 2-10:	Different types of bubble formations in the sediment are shown; the sediment is displaced with increasing bubble size; modified after Anderson et al. (1998).....	28
Figure 2-11:	Modeled response of bubble release on pressure changes from a sediment with conduits, after Scandella et al., 2011.....	29
Figure 2-12:	Spherical spreading, after Lurton, 2010, 20–22	33
Figure 2-13:	Principle of Time-Varying Gain (TVG), after (Lurton, 2010).....	34
Figure 2-14:	Set up of the EA400 echo sounding system.....	35
Figure 2-15:	Echo sounding sequence, showing the transmitted pulse and the following echo.....	36
Figure 2-16:	Example of an echogram; Sonar5 pro, colors represent the echo strength in dB referring to an adaptable scale, the black line depicts the identified bottom	37
Figure 2-17:	Differences between high and low frequency.....	38
Figure 2-18:	Refraction, reflection and scattering due to the interaction of sound with the sediment.....	40
Figure 2-19:	Interaction of a ping with the lakebed - The three phases of bottom ensonification depending on the position of the sound pulse inside the sediment (lateral view) with the resulting shapes of the ensonified areas reflecting from the bottom (top view).	43
Figure 2-20:	Exemplary acoustic wave showing the integrated areas of the wave signature for the “First / second bottom ratio method”; the	

	first part is the attack phase, the second the decay phase and last part of the echo is called the release phase	44
Figure 2-21:	Exemplary acoustic wave showing the integrated areas of the wave signature for the “First echo division method”	44
Figure 2-22:	Simulated echo shapes of hard and soft sediment; modified after Burczynski (1999)	45
Figure 2-23:	Influence of depth on the division of the acoustic wave signature into the attack and decay phase	46
Figure 2-24:	Principal scheme of hydro-acoustic bubble detection in the water column	47
Figure 2-25:	Scheme of sound reflection at the acoustic turbidity layer	49
Figure 3-1:	Geographic localization of the reservoirs	53
Figure 3-2:	Topographic map of the Vossoroça reservoir at maximum water level	54
Figure 3-3:	Topographic map of the Capivari reservoir, the surface is shown for maximum water level	56
Figure 4-1:	Scheme of the overall measurement and data processing procedure	57
Figure 4-2:	Overview of the principle measurement steps, order and results; SBC	59
Figure 4-3:	Lateral view of the onboard echo sounder setup	62
Figure 4-4:	The mounted EA 400 echo sounder on the aluminum vessel	63
Figure 4-5:	Survey route in VR depicted against longitude and latitude; gray lines represent the sailed path, the black line is the reservoir outline	66
Figure 4-6:	Survey route in CR depicted against longitude and latitude, gray lines represent the driven path, the black line is the reservoir outline; hatched areas were too shallow for measurement or the GPS signal was lost during survey	66
Figure 4-7:	Data processing sequence for SBC approaches	69
Figure 4-8:	Principle of the definition of acoustic classes	70
Figure 4-9:	Principle of the single parameter correlation	70
Figure 4-10:	Example for the application of the box-count method	71
Figure 4-11:	Echogram in Sonar5 pro showing both frequencies with exemplary detected upper and lower sediment layer boundaries	73
Figure 4-12:	Schematic cross section through the sediment depicting the density gradients and the corresponding bottom picks	73
Figure 4-13:	3D illustration of the intensity from a sequence of pings hitting the sediment, including marked positions for the upper and lower sediment layer detection	74

Figure 4-14:	Exemplary echogram taken at Core site 6, diagonal traces are detected bubbles	75
Figure 4-15:	Bubbles and fishes in the same echogram (Ostrovsky, 2009).....	75
Figure 4-16:	Overview over the post-processing steps	77
Figure 4-17:	Design of the Mondsee Corer	83
Figure 4-18:	Foto of the grab sampler prepared for sampling	84
Figure 4-19:	Sediment sampling locations in VR depicted against latitude and longitude; cores are displayed with crosses while grab samples are represented as triangles	85
Figure 4-20:	Sediment sampling location in CR depicted against latitude and longitude.....	86
Figure 4-21:	Rendered design of the DPS-PS; design and construction by Gauger (2013)	91
Figure 4-22:	DPS after recovery with adherent sediment.....	92
Figure 4-23:	Injection of DPS solution in the head space vial.....	92
Figure 5-1:	(A) Percentaged dry weight distribution of grain sizes in core samples from VR; values for core 8 are doubtful due to handling errors during sample processing; (B) Percentaged dry weight distribution of grain sizes in VR grab samples.....	100
Figure 5-2:	Percentaged dry weight distribution of grain sizes in core samples from CR	100
Figure 5-3:	Granulometric lakebed characteristics at sampling locations in the south-western arm of VR, C# indicates the core numbers and G# the numbers of the grab samples.....	101
Figure 5-4:	Granulometric lakebed characteristics at sampling locations in CR, the numbers indicate the core numbers	102
Figure 5-5:	TC content in sediment samples in the VR, cores and grabs are named individually	103
Figure 5-6:	TC content in sediment samples in the Capivari reservoir; cores are named individually	104
Figure 5-7:	Correlation between the total carbon content and the LOI in all core samples from VR and CR; (N = 28; p<0.005).....	105
Figure 5-8:	Share of finest particle fraction plotted against LOI; all cores and grabs from CR and VR are included (N=45; p<0.001).....	106
Figure 5-9:	Correlation of TC with LOI based on a selection of cores from VR and CR with less than 80% share of finest particle fraction; (N = 20, p = 0.01).....	106
Figure 5-10:	Share of finest particle fraction depicted over TC; all cores and grabs from CR and VR are included	106
Figure 5-11:	TC depicted over bulk density from all cores in VR and CR; (N = 28; p<0.01)	107

Figure 5-12:	LOI depicted over bulk density from all cores in VR and CR; (N = 28; $p < 0.01$)	107
Figure 5-13:	Total carbon vs. the relative depth in A) Capivari reservoir and B) in the Vossoroça reservoir, VR = core samples	108
Figure 5-14:	Comparison of finest fraction share and sulfur content in relation to the relative depth; Contents of the upper 15 cm of the sediment sample material from VR & CR are included in the graph; the orange line illustrates the trends described	109
Figure 5-15:	Total phosphor content vs. relative Depth and reservoir specific linear correlation (CR: N = 18, $p < 0.05$; VR: N = 30, $p < 0.05$)	110
Figure 5-16:	Total iron content vs. relative Depth and reservoir specific linear correlation (CR: N = 18, $p < 0.05$; VR: N = 30, $p < 0.05$).....	110
Figure 5-17:	Total iron content vs. share of finest sediment fraction and reservoir specific linear correlation (CR: N = 18, $p < 0.05$; VR: N = 30, $p < 0.05$).....	111
Figure 5-18:	Biplot of the PCA results of a selection of sediment parameters	112
Figure 5-19:	Map showing the depth below the surface of the VR as a function of latitude and longitude in March 2011	115
Figure 5-20:	Histogram of the distribution of depth classes in CR.....	116
Figure 5-21:	Map showing the depth below the surface of the CR as a function of latitude and longitude in November 2012.....	116
Figure 5-22:	Visualization and distribution of the most prevalent slope classes in CR.....	117
Figure 5-23:	Slope polygon map, Slope polygons are defined by the class breaks from Table 5-4.....	118
Figure 5-24:	Sediment thickness distribution in CR, results based on the dynamic hydro-acoustic measurements and IDW interpolation.....	119
Figure 5-25:	Spatial share of sediment thickness classes in the CR	119
Figure 5-26:	Measured vs. interpolated sediment thickness values; Correlation of the ST values, N=16; $p < 0.01$	120
Figure 5-27:	Comparison of the three approaches for sediment thickness estimation in CR	120
Figure 5-28:	Depicted proportion of particles $< 63 \mu\text{m}$ vs. the attSv1/decSv1 values and the modeled curve based on the adapted Gompertz function.....	128
Figure 5-29:	Map of the modeled proportion of the grain size fraction $< 63\mu\text{m}$ in [%] for the Capivari reservoir	128
Figure 5-30:	Differences between modeled and measured sediment shares of the finest fraction	129
Figure 5-31:	Linear regression model of the TC vs E1; N=15; $p < 0.01$	130
Figure 5-32:	Interpolated total carbon contents in the sediment of CR, Interpolation was performed using IDW	131

Figure 5-33:	Modeled and measured TC contents in a ranked order.....	131
Figure 5-34:	Results of the “first echo division” method; 38 kHz, Configuration B, 100 W; orange bars represent the standard deviation within the ping sequences; the size of the black squares is the relative depth, the larger the deeper	132
Figure 5-35:	Results of the “first echo division” method; 200 kHz, Configuration B, 100 W; orange bars represent the standard deviation within the ping sequences, the size of the black squares is the relative depth, larger squares represent deeper positions	133
Figure 5-36:	Acoustic signatures of four representative cores; 200 Khz, Configuration B, 100 W; Sv Mean is the backscatter strength in dB, the distance 0.0 is the entrance point of the sound wave in the sediment.....	134
Figure 5-37:	Relative distribution of classified pings within hydro-acoustic classes over granulometric ranges; basis for the granulometric classes are the results shown in Figure 5-29	135
Figure 5-38:	Results of the First Echo Division method classification; 200 kHz, Configuration B, 100 W. Results are shown as single pings; The side maps (A,B and C) show selected areas in detail.	137
Figure 5-39:	200 kHz Echogram (configuration B) showing rising bubbles at coring site six. Tracked bubbles are marked with squares	138
Figure 5-40:	Extreme bubbling at the surface during core sampling at location 6 in the first campaign of phase two.....	139
Figure 5-41:	Number of detected bubbles at coring sites in relation to measured TC contents and the sediment thickness	141
Figure 5-42:	Location of the detected bubbles and water depth in the CR	142
Figure 5-43:	Diagram of illustrating the relation between sediment thickness, bubble occurrence and the relative share of the measurement point count.....	143
Figure 5-44:	The DPS-PS positioned on the floating platform at the side of the vessel in combination with an electric winch	145
Figure 5-45:	Positions of the placed DPS’s in Capivari reservoir, lost DPS’s are not presented.....	146
Figure 5-46:	Oxygen concentrations in the DPS; DPS 0 is not shown since no oxygen was measured in the first campaign	147
Figure 5-47:	Oxygen concentration in membrane bags vs. time, under laboratory conditions.....	148
Figure 5-48:	Dissolved methane concentrations in the pore water of the CR; DPS 1 must be discarded due to erroneous placement	149
Figure 5-49:	Methane concentrations of DPS 2 & DPS 7 against sediment depth	151
Figure 5-50:	Sulfate concentrations in the pore water of the CR; DPS 1 must be discarded due to erroneous placement; DPS 4 reaches a	

	maximum of 3.32 mg l ⁻¹ but is cut for a better resolution of the other graphs	152
Figure 5-51:	Slope inclination of the profundal area of Capivari reservoir is illustrated and combined with sediment thickness isolines.	154
Figure 5-52:	Flow chart of the carbon stock calculation	156
Figure 5-53:	Organic carbon stock in the CR [kg m ⁻²]; results of the IDW interpolation process; the maximum interpolation distance of 50 m caused the edges of some shallow areas to stay without value.	157
Figure 5-54:	Oxygen depth profiles at selected coring sites, the prevalent oxycline marks the boundary for fast and slow mineralization of organic matter, core 17 shows the vertical oxygen distribution after a storm event.	158
Figure 5-55:	TC vs. the maximum concentration of methane in the pore water; location 10 was discarded as an outlier, (r = 0.98, N = 5, p<0.01).....	159
Figure 5-56:	TC vs. the maximum concentration of methane in the pore water, (r = 0.98, N = 5, p<0.01)	160
Figure 5-57:	Density vs the maximum concentration of methane in the pore water; r = -0.78, N = 5, p<0.1	160
Figure 5-58:	Hydro-acoustic parameters of the 200 kHz freq., configuration B, 100 W vs. the maximum methane concentration in the pore water	163
Figure 5-59:	Overview of derived characteristics of the determined reservoir zones in Capivari reservoir	166
Figure 6-1:	Carbon stock distribution in the Capivari reservoir, including detected bubbles in the water column; the blue circles represent averaged results from funnel measurements by Kan et al. (2013)	170
Figure A1- 1:	Photos of the core samples from Capivari reservoir plotted over sediment depth, part 1	184
Figure A1- 2:	Photos of the core samples from Capivari reservoir plotted over sediment depth, part 2	184
Figure A1- 3:	Photos of the core samples from Capivari reservoir plotted over sediment depth, part 3	185
Figure A1- 4:	Photos of the core samples from Vossoroca reservoir plotted over sediment depth	186
Figure A2- 1:	Beam Pattern 200 kHz (both directions)	187
Figure A2- 2:	Beam Pattern 38 kHz longitudinal	187
Figure A2- 3:	Beam Pattern 38 kHz transversal	188
Figure A4- 1:	Conductivity depth profiles measured in Capivari reservoir during campaign two in phase two.....	189

Figure A4- 2: Temperature depth profiles measured in Capivari reservoir during campaign two in phase two.....	189
Figure A10- 1: Water level and air pressure changes depicted over the time of measurement campaign two, phase two (12.03.–17.03.2013).....	197
Figure A12- 1: Depth profiles of various analytes in DPS 1	200
Figure A12- 2: Depth profiles of various analytes in DPS 2	200
Figure A12- 3: Depth profiles of various analytes in DPS 3	201
Figure A12- 4: Depth profiles of various analytes in DPS 4	201
Figure A12- 5: Depth profiles of various analytes in DPS 5	202
Figure A12- 6: Depth profiles of various analytes in DPS 7	202
Figure A13- 1: Regression analysis of the weight loss trough 105 °C drying plotted over the proportion of particles, N=16; p<0.01.....	203
Figure A13- 2: Linear regression analysis for the estimation of the density in relation to the share of fine material; N=16; p<0.01.....	203
Figure A14- 1: Comparison of the measured and modelled results of the particle proportion at 18 coring sites in Capivari reservoir	204

List of Tables

Table 2-1:	List of the OECD trophic class limitations (OECD, 1982)	16
Table 2-2:	List of basic reactions of complete and incomplete methane formation, after Conrad, 1989	22
Table 2-3:	Approximate values for the penetration of sound impulses into silt and sand depending on the frequency (British Standard 6349-5:1991, 1991).	38
Table 2-4:	Overview of the effects of the main transducer characteristics and settings	39
Table 3-1:	Morphometry of Capiuari and Vossorooca reservoir	56
Table 4-1:	Echo sounder configurations during phase 1 survey in VR	63
Table 4-2:	Echo sounder configurations during phase 2 survey in CR	63
Table 4-3:	List of the echo features used for SBC; most features have various names in the literature, therefore the most common terms are listed	68
Table 4-4:	Exemplary table for the grouping procedure for different parameter settings during bubble detection	79
Table 4-5:	In-situ sediment description and analysis parameter	87
Table 5-1:	Sediment key parameter from cores taken in Capiuari Reservoir (N = 18)	98
Table 5-2:	Sediment key parameter from cores and grabs taken in Vossorooca Reservoir (N = 32)	98
Table 5-3:	Correlation matrix of the five input parameters	111
Table 5-4:	Class breaks for slope inclination	117
Table 5-5:	Correlations between sediment and acoustic parameters based on the results obtained from the core samples of Vossorooca reservoir; statistical significance is given for $r > 0.63$ ($p < 0.05$, $N = 10$)	122
Table 5-6:	Correlations between sediment and acoustic parameters based on the results obtained from the grab samples of Vossorooca reservoir; statistical significance is given for $r > 0.44$ ($p < 0.05$, $N = 21$)	122
Table 5-7:	Correlations between sediment and acoustic parameters (200 kHz, 100W) based on the results obtained from the core samples of Capiuari reservoir; statistical significance is given for $r > 0.47$ ($p < 0.05$, $N = 18$)	125
Table 5-8:	Correlations between sediment and acoustic parameters (200 kHz, 500W) based on the results obtained from the core samples of Capiuari reservoir; statistical significance is given for $r > 0.47$ ($p < 0.05$, $N = 18$)	125
Table 5-9:	Correlations between sediment and acoustic parameters (38 kHz, 100W) based on the results obtained from the core samples of Capiuari reservoir; statistical significance is given for $r > 0.47$ ($p < 0.05$, $N = 18$)	126

Table 5-10:	Correlations between sediment and acoustic parameters (38 kHz, 500W) based on the results obtained from the core samples of Capivari reservoir; statistical significance is given for $r > 0.47$ ($p < 0.05$, $N = 18$).....	126
Table 5-11:	Number of Bubbles detected at coring sites; 200 kHz, configuration A, 500 W.....	140
Table 5-12:	Bubble statistics for configuration A, 200, 500 W,.....	141
Table 5-13:	Bubble statistics for driven lines; Configuration B, 200 kHz, 100 W	143
Table 5-14:	Overview of the deployed DPS's; the water depth at the current location, the individual equilibration time and the type of the DPS is given.....	146
Table A3- 1:	Table showing the GPS-data import format for Sonar5 pro.....	188
Table A5- 1:	Concentrations of the calibration standards for ion chromatography ...	190
Table A5- 2:	Composition and concentrations of the calibration standards for gas chromatography.....	190
Table A7- 1:	Calculation table for the water quality index after OECD criteria	193
Table A8- 1:	Overview table of the sediment analysis parameter from Capivari reservoir	194
Table A8- 2:	Overview table of the sediment analysis parameter from core samples from Vossoroca reservoir.....	195
Table A8- 3:	Overview table of the sediment analysis parameter from grab samples from Vossoroca reservoir.....	196
Table A11- 1:	Technical specifics of DPS-generation I; after Gauger (2013).....	198
Table A11- 2:	Technical specifics of DPS-generation II; after Hölzlwimmer (2013) ...	199

List of Abbreviations

AAS	Atom Absorption Spectrometry
AMTT	Advanced Multiple Target Tracker
AUV	Autonomous Underwater Vehicles
BD	Bulk Density
BE	Burial Efficiency
BRIC	Brazil, Russia, India, China
CFD	Cross Filter Tracking
CR	Capivari Reservoir
CRP	Carbon Related Parameter
CV	Coefficients of Variation
DGPS	Differential Global Positioning System
DPS	Dialysis Pore water Sampler
DPS-PS	Dialysis Pore water Sampler Placing System
GHG	Green House Gas
IC	Inorganic Carbon
IDW	Inverse Distance Weighting
LACTEC	Instituto de Tecnologia para o Desenvolvimento
LAWA	Länderarbeitsgemeinschaft Wasser
LOI	Loss On Ignition
MTT	Multiple Target Tracking
OC	Organic Carbon
OET	Oxygen Exposure Time
OM	Organic Matter
PC	Principal Component
PCA	Principal Component Analysis
POC	Particular Organic Carbon
POM	Particular Organic Matter
PSU	Practical Salinity Units
SBC	SeaBed Classification
SED	Single Echo Detection
ST	Sediment Thickness
SVP	Sound Velocity Profile
SWI	Sediment Water Interface
TC	Total Carbon

TCD	Thermal Conductivity Detector
TIC	Total Inorganic Carbon
TIN	Triangulated Irregular Network
TL	Transmission Loss
TL	Target Loss
TOC	Total Organic Carbon
TVG	Time Varying Gain
VR	Vossoroca Reservoir
WBD	Wet Bulk Density

Table of Contents

1	Introduction	1
1.1	Dams	1
1.2	Methane, Atmosphere and Global trends	2
1.3	Reservoirs in Brazil.....	3
1.4	Problem: Quantification	4
1.5	Objective of the Thesis	6
1.6	Contribution of the Thesis.....	7
1.7	Structure of the Thesis.....	9
2	Scientific Background and State of the Art.....	10
2.1	The system reservoir	10
2.1.1	Morphometry	10
2.1.2	Sedimentation	13
2.1.3	Trophic State and Water Quality	16
2.1.4	Carbon in Reservoirs	17
2.2	Greenhouse Gases and Reservoirs	20
2.2.1	Creation of Methane	20
2.2.2	Methane Emission Pathways	24
2.2.3	Diffusive Flux.....	25
2.2.4	Ebullition	26
2.3	Fundamentals of underwater Acoustics.....	30
2.3.1	Underwater Sound Propagation and Propagation Losses	31
2.3.2	Echo Sounding.....	35
2.3.3	Interaction of Sound with Bottom and Sediment.....	39
2.3.4	Acoustic Bottom Classification	41
2.3.5	Acoustic Bubble Detection	47
2.4	Summary of the Fundamentals.....	51
3	Investigation Area	53

3.1	Vossoroca Reservoir (VR).....	53
3.2	Capivari Reservoir (CR).....	55
4	Materials and Methods.....	57
4.1	Sampling Strategy.....	57
4.2	Hydro-acoustic Survey.....	62
4.2.1	Equipment – EA 400 Single Beam hydrographic Echo Sounder.....	62
4.2.2	Bathymetry.....	64
4.2.3	Fixed Position Acquisitions (point measurements).....	67
4.2.4	Seabed Classification (SBC).....	67
4.2.5	Sediment thickness:.....	71
4.2.6	Bubble detection.....	74
4.2.7	General Data Processing.....	79
4.2.8	Data Correction and Quality Control.....	81
4.3	Sediment Survey.....	83
4.3.1	Cores & Grabs.....	83
4.3.2	Dialysis Pore Water Sampler (DPS).....	88
4.4	Further Surveyed Parameters.....	95
4.4.1	Secchi Disc.....	95
4.4.2	Water Quality Parameters.....	96
4.4.3	Temperature – Conductivity – Depth (CTD).....	96
5	Results and Interpretation.....	97
5.1	Sediment Investigations.....	97
5.1.1	Sediment Key Data.....	97
5.1.2	Granulometry and Sediment Distribution in the Reservoirs.....	99
5.1.3	Sediment Parameter Interrelations.....	105
5.1.4	Multivariate Approach.....	111
5.1.5	Synopsis.....	113
5.2	Hydro-acoustic Results.....	114
5.2.1	Bathymetry and morphometric Implications.....	114
5.2.2	Sediment Thickness (ST).....	118

5.2.3	Seabed Classification (SBC).....	121
5.2.4	Bubble Detection	138
5.2.5	Synopsis	144
5.3	Dialysis Pore Water Sampling	145
5.3.1	Gas Concentrations.....	147
5.3.2	Ion Concentrations	151
5.3.3	Synopsis	153
5.4	Composed Results	154
5.4.1	Slope Inclination vs. Sediment Thickness	154
5.4.2	Carbon Stock Calculation	155
5.4.3	Methane Concentration and Sediment Parameter.....	159
5.4.4	Methane Concentration and hydro-acoustic Behavior	161
5.4.5	Synopsis	164
6	Discussion	167
7	Outlook.....	171
	References	173
	Appendix	184
A.1	Photos of the core samples.....	184
A.2	Beam lobes of EA 400 echo sounder.....	187
A.3	The standard Sonar5 pro GPS import format	188
A.4	Temperature and conductivity depth profiles.....	189
A.5	Calibration standards for the ion and gas chromatography	190
A.6	Calculation for dissolved gases in water samples using headspace gas chromatography	191
A.7	Calculation of the water quality index	193
A.8	Sediment analysis results	194
A.10	Water level and air pressure data	197
A.11	Technical sheet of the DPS	198

A.12	Depth profiles of various analytes in the DPS	200
A.13	Regression analysis of the sediment density correction factors...	203
A.14	Model results for the proportion of particles in the sediment	204

1 Introduction

“The urgency to act on climate change, combined with the pressing need to build more reservoirs to meet electricity and water demands in many parts of the world, suggests that the time to overlook reservoir emissions has passed.” Mäkinen & Khan (2010)

Chapter 1 gives an introduction to the background and motivation of this work. The role of dams on a global scale and the situation of reservoirs in Brazil is explained. In the context of the creation of impoundments, the development of greenhouse gases, in particular methane, is presented. Finally, the objective and the structure of the thesis are outlined.

1.1 Dams

Dams have been built and used by humankind for a long time. As many other processes driven by anthropogenic forces, the construction and utilization of dams and reservoirs were significantly accelerated in the last 150 years. As a clear evidence more than 95% of total global investment capital in dam projects was invested after 1950 (Lempérière, 2006). The construction boom of impoundments around the world led to a number of more than 50,000 dams higher than 15 m and a damming of more than 50% of the rivers worldwide until today (WCD, 2000). The reservoirs impounded by those dams account for an area of about 500,000 km², which equals one third of the surface of earth's natural water bodies. Estimations of the overall storage capacity result in a number of about 7,000 km³ (WCD, 2000).

The reservoirs fulfill a variety of general purposes and distinct functions, from irrigation, water supply and energy production to recreation and flood protection (Lempérière, 2006). 80% of the dams are used for hydropower generation. While the first dams were once built in the industrialized western countries, today 60% of constructed and 90% of dams in construction can be located in developing countries. The actual trend in reservoir construction will probably lead to a doubling of the generation of TWh a⁻¹ (2,700 in the year 2004) in the next 100 years (WCD, 2000). This seems to be likely as only 17% of the global potential hydro-electric sites have been used (Barros et al., 2011). It can be assumed that the construction of new dams will primarily take place in the biggest developing countries like India, China and especially Brazil (WCD, 2000; Lima I et al., 2008).

Since Rudd, J. W. M. et al. (1993) first mentioned reservoirs as important sources of Greenhouse Gases (GHGs) the “climate neutrality” of hydroelectricity is in doubt and therefore has been a discussion topic of increasing importance within the scientific community. Methane seems to play a major role in terms of GHG emissions from anthropogenic surface water bodies which was stated to be in particular the case for the tropics (Lima I et al., 2008; Soumis et al., 2005).

The creation of impoundments leads to the disruption of biochemical cycles in riverine systems. Transported material becomes trapped and the fate of the organic compounds is changed (Friedl & Wüest, 2002), (Dean & Gorham, 1998). Organic matter, which reaches a reservoir is likely to be decomposed while methane is produced.

1.2 Methane, Atmosphere and Global trends

*„Anthropogenic greenhouse gas emissions have increased since the pre-industrial era driven largely by economic and population growth . From 2000 to 2010 emissions were the highest in history. Historical emissions have driven atmospheric concentrations of **carbon dioxide, methane and nitrous oxide**, to levels that are unprecedented in at least the last 800,000 years, leading to an uptake of energy by the climate system.“ Intergovernmental Panel on Climate Change (IPCC) (2014)*

The anthropogenic influence on the methane (CH₄) concentration in the atmosphere is obvious, as the concentration increased from 715 ppbv to recently 1770 ppbv (Conrad, 2009). The rate of the methane concentration rise has been calculated at around 2% per year ($\pm 0.5\% \text{ a}^{-1}$) (Rasmussen, R. A. & Khalil, M. A. K., 1981). The start of this increase can be dated to the pre-industrial times (Conrad, 2009). The climatologic importance of this development is based on the findings that CH₄ is contributing to around 30% of the total net anthropogenic radiative forcing (IPCC, 2007). Conrad (1989) stressed the relevance of wetlands on the global methane cycle by indicating them as the biggest individual source of methane. He stated that 69% of all CH₄ formation is due to microbial processes from methanogenic archaea which can be found in inundated areas.

The critical point is not primarily the anthropogenic influence on wet land methane production by itself, but the creation of vast areas of wet lands and dams around the world, which produce significant amounts of methane after inundation (Conrad, 2009; Bastviken et al., 2004a; Barros et al., 2011; Fearnside, 1997; DelSontro et al., 2010).

Already Ehhalt (1974) calculated the annual production of CH₄ from fresh water lakes to be 1.25–25 10¹²g CH₄ a⁻¹. The wide range of this assumption (factor 20) shows quite plainly that the uncertainties were extremely high. Even after more than three decades of research, the uncertainties of global methane flux calculations are still high. The fluxes range from 8–48 10¹²g CH₄ a⁻¹, which then had an uncertainty of 600% (Bastviken et al., 2004a). St. Louis et al. (2000) assumed the human-induced global warming in form of GHG emissions from reservoirs to be 4% of the global share.

Many researchers have published data about reservoir-specific GHG emissions as well as regional and global estimates, but still the real extend of GHG emissions from anthropogenic surface water bodies and especially from hydro-electric reservoirs is poorly understood (Barros et al., 2011; Mäkinen & Khan, 2010; Demarty & Bastien, 2011; Lehner et al., 2011; Bastviken et al., 2004a; Bastviken et al., 2011).

After about 20 years of scientific discussion and increasing data availability, the following basic findings and statements can be posted:

- reservoir age, location biome, morphometric features and chemical status play a major role for the emission of GHGs (St. Louis et al., 2000; Tremblay et al., 2004)
- higher emissions from lower latitudes and higher emissions from younger reservoirs can be found (Barros et al., 2011)
- even temperate reservoirs can have high emissions due to organic matter enriched inflows (DelSontro et al., 2010)
- extreme spatial and temporal variability of emissions (Mendonça et al., 2012; Maeck et al., 2013)
- reservoir sediments are hot spots of methane production (Maeck et al., 2013; Bastviken et al., 2004a; DelSontro et al., 2010)

1.3 Reservoirs in Brazil

Brazil is a remarkable country, not only because it is of the five biggest countries in land area, but also as a hot-spot of biodiversity (Conservation International, 2000). As one of the BRIC-states this South-American nation acts as one of the four primary engines of global economic growth (Brainard & Martinez-Diaz, 2009). With the Amazon as the largest river in the world including an enormous number of tributaries and tremendous amounts of fresh water resources in general, the country has one of the biggest hydropower potentials around the globe. The supply rate of 78.4% of the nation's electricity demand from an installed

hydropower capacity of 121.104 MW is astonishing (ANEEL, 2013). Those numbers underline the importance of hydropower and therefore, the importance of reservoirs in Brazil. South America in total and Brazil in particular has a relatively small number of dams larger 0.5 km³, to be counted among 459 from 6,862 dams worldwide (Lehner et al., 2011). Compared to the storage capacity of 1,012 km³ representing 17% of the global installed capacity, the number of dams in Brazil (6.6% of dams worldwide) is small (Lehner et al., 2011), leading to the statement that the reservoirs in Brazil are above global average size.

Besides a relatively large number of surveys in Brazil, the real emissions from reservoirs are poorly calculated, which can be also related to the above average size of the reservoirs (Caetano de Souza, 2008). In addition to the large size, most reservoirs feature a low ratio between the surface and the volume. Extensive surfaces generally lead to high primary production in water bodies and hence accelerate sedimentation and consequently methane production (Martens et al., 1998). High average temperatures leading to fast natural carbon cycles intensify this effect (Soumis et al., 2005).

1.4 Problem: Quantification

The ongoing discussion about GHGs from reservoirs focusses in most cases either on 1) the question of hydroelectric power plants compared to thermal power plants in regards of CO₂-equivalents emitted per kW/h produced or 2) on the question, whether one reservoir emits more GHGs than the original undisturbed habitat would have emitted.

While those questions are of great importance, still the answer to the problem of an unflinching quantification of GHG emissions from reservoirs seems to be a major task to be solved prior to the calculation of regional or global estimations.

Nearly all investigations of GHGs from reservoirs rely on two different approaches for their quantification, independent of the research group or location of the study area around the world (Tremblay et al., 2005; Delmas et al., 2005; Bastviken et al., 2008; Baulch et al., 2011; Chanudet et al., 2011). The first approach uses floating chambers for the measurement of diffuse fluxes from the water body to the atmosphere, while the second approach is based on the capturing of gas bubbles on the way up to the surface. Named after the main instrument of measuring this latter approach is referred to as “funnels” and it is used for the quantification of the volume and composition of gas originating from ebullition in the

sediment. However, both methods use technical installations covering a certain area for a distinct time and can therefore, be considered as point measurements.

Floating chambers exist in a variety of designs with various methods for the measurement of gas fluxes (DelSontro et al., 2010; Bastviken et al., 2004a; Duchemin et al., 1999). The same accounts for the funnels. Most of the measurement equipments are only capable of collecting a certain volume of gas which is quantified manually after a distinct time, generally around 24 h. Some types are more advanced and are able to measure the captured volume and release it. Those can be used for long term measurements (Maeck et al., 2013). However, they still have the disadvantage of a relatively small sampling area. This area is usually around 1 m² (Bastviken et al., 2004a; DelSontro et al., 2010). The relevant measurement area for floating chambers is even smaller (Abril et al., 2005; Sherman et al., 2012).

A general conformance of findings during the last decade is that GHG emissions have a high temporal and spatial heterogeneity (Chen et al., 2011; Casper et al., 2000; Bastviken et al., 2004a; Maeck et al., 2013; DelSontro et al., 2011; Eilers, 2004). Hence, other quantification approaches have to be developed or the existing approaches have to be improved (Demarty & Bastien, 2011; DelSontro et al., 2011).

The latest developments from DelSontro et al. (2011) and Maeck et al. (2013) have shown that new time and space integrating approaches are needed for a better understanding of emission dynamics. Both have found that emissions are not only varying in time and space, but that there are hot spots of GHG production and emission within a reservoir. This clearly impedes the accuracy of overall estimations of emissions from reservoirs (Lehner et al., 2011), as the likeliness of missing the hot spots or only measuring in hot spot areas is high, considering the average size of reservoirs around the world and especially in Brazil.

In this regards the echo sounder technology offers a high potential of spatial coverage combined with a good temporal resolution. Moreover, the survey of sediment features and thickness as well as the detection of bubbles is possible. This makes this technology a promising tool to solve the problem of methane emission quantification.

1.5 Objective of the Thesis

This thesis principally aims on the testing and improvement of integrative approaches for the methane hot spot detection. In these regards, a set of different methods was used. Figure 1-1 illustrates the general context of the *state of the art problems* which lead to the overall *research objective*. The principal objective is divided into investigation-subunits: *sediment distribution, processes in the sediment and ebullition*.

The subunits in Figure 1-1 represent groups of different measurement equipment, parameters and methodologies. The findings are connected on the one hand to temporal or spatial system understanding and on the other hand to carbon and methane related processes. The system understanding elaborated is integrated into the results of carbon and methane quantification and distribution.

The investigation of principal connections between reservoir characteristics like the complexity of the shape and morphometric lakebed features, with the sediment properties, aims at the enhancement of the system understanding. Furthermore, the pore water investigations provide small-scale information about the redox- and methane formation conditions. The time integrating momentum of sediment can be used to improve the temporal understanding of processes, which potentially influence the methane emissions over time. Data sets obtained from hydro-acoustic surveys allow the development of models, that connect this acoustic data to sediment features. The model results then are spatially interpolated and therefore extend the local findings to the entire reservoir. This information addresses the spatial interpretation of the results.

Finally, data analysis and map interpretation lead to the definition of characteristic zones of the reservoir. The different zones are characterized by information about the sediment granulometry, biogeochemical processes, sediment accumulation, carbon stock and bubble occurrence. The combination of these features allows conclusions about the methane production in each zone and additionally gives hints about the temporal behavior.

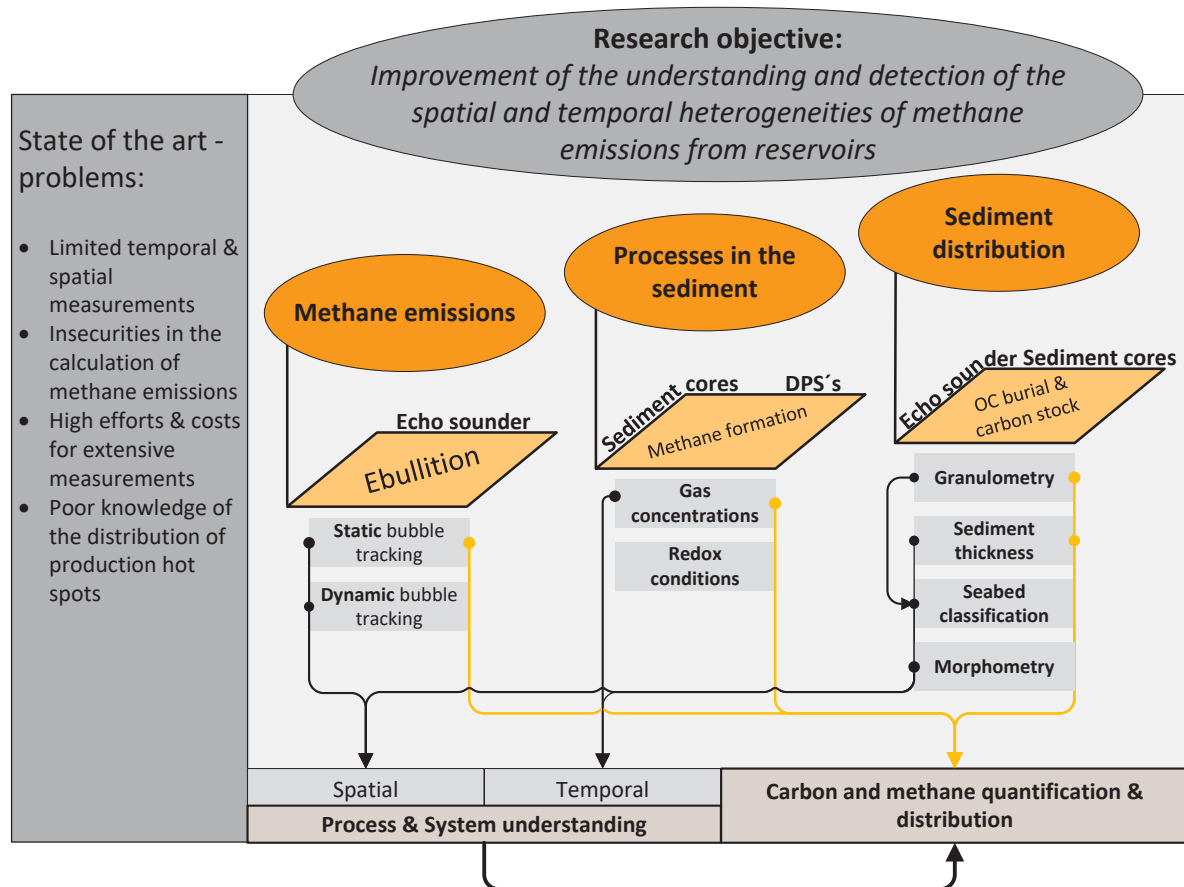


Figure 1-1: Overview scheme of the conducted research of this work.

1.6 Contribution of the Thesis

In succession of the objective of this thesis, this chapter summarizes the main scientific contribution of this work. The contribution is divided in a methodological part and a part, which contains the principal findings.

Methodological level:

- In regards to hydro-acoustic surveys and data interpretation, this work illustrates the possibility of new echo-feature combinations with methane-related parameters. The work provides an improved method for the determination of the sediment volume and furthermore the assessment of the carbon stock within a reservoir. It becomes possible to transfer the developed methodology and principal findings as a basis for further reservoir surveys. A significant reduction of necessary data for the detection of methane hot spots in other reservoirs is expected.

Moreover, the developed approach for the estimation of the sediment thickness, represents a valid method, which creates the opportunity to improve the calculation of the carbon stock of any reservoir.

- In the context of pore water investigations, this work describes an innovative sampling approach. A new placing mechanism was developed and tested in the field, which allows to reduce the overall effort and the costs for extensive pore water sampling. Within a flexible depth-range, it makes the utilization of divers or AUVs superfluous. Additionally, it creates the possibility to sample more locations in less time. The method is shown to produce valid results for gas and for ion concentrations.

Findings

- Sediment distribution and related heterogeneities were successfully assessed. Leading to the identification of significantly different zones in regards of sediment characteristics. The combination of obtained results provides information about the potential methane-formation conditions in the individual zones. This leads to an improved understanding of prevalent spatial emission patterns. Hence, future measurement campaigns can be adapted to this zonation and will produce emission data with increased reliability.
- Pore water investigations of gas contents and analyses of iron and sulfur contents in the sediment revealed a strong coherence. Transferred to the entire reservoir, the detected connection revealed a temporal component. Areas with changing redox conditions (proximal) feature lower iron and sulfur contents, while the short term methane production can still be high. Zones with permanent absence of oxygen (profundal) are able to produce similar amounts of methane, while the production is continuous. Consequently, the iron and sulfur content can be seen as proxy values for the temporal behavior of methane production. These findings will support the interpretation of temporally limited measurements, like funnel measurements.

The main overall contribution of this work is the enhanced interpretation of hydro-acoustic data. Due to the wide range of biogeochemical parameters and gas concentrations obtained, the echo sounder reveals a strong potential. Relatively cost saving hydro-acoustic surveys are now able to produce valuable information, which can be interpreted in the context of methane production. They also create the possibility to survey significantly larger reservoir surfaces.

Independent from the quantification of direct emission fluxes, one approach for the assessment of GHG emissions is the calculation of the entire carbon stock budget of a reservoir. Since this method is based on precise estimations of the carbon stock in the sediment, the findings of this thesis are able to substantially support this approach in the future.

1.7 Structure of the Thesis

In accordance to the declared objectives, this work is structured in five main chapters. For the understanding of the study, the scientific background and the State of the Art are described in chapter 2. This chapter is subdivided in three parts, addressing reservoirs as particular systems, the complex of GHGs and methane emissions as well as the fundamentals of hydro-acoustics.

Chapter 3 introduces the investigation areas and provides geographic, hydrological and ecological information about Vossoroca and Capivari reservoir.

The developed sampling strategy and used methods are explained in chapter 4. Whereas the methods are divided in the hydro-acoustic survey, the sediment investigation and a set of support parameters. Within the sediment survey, two principal parts are divided, the sediment sampling and the pore water investigations.

Chapter 5 reflects the general order of chapter 4 as it contains the results and their interpretations. However, the last part addresses in particular the results, which are based on combined findings of the three approaches.

In chapter 6 the presented results are discussed in the context of the actual scientific background and the defined research questions.

2 Scientific Background and State of the Art

Chapter 2 is divided in three major parts. They give background information about the basic processes in reservoirs and the creation of GHGs. Furthermore, the fundamentals of hydro-acoustic methods are explained. At the end of the chapter a summary of the scientific background, which is essential for the understanding of this work, is given.

2.1 The system reservoir

This chapter gives an essence of the most relevant processes and conditions to be considered when investigating a surface water reservoir. A particular focus is laid on the thematic context of the formation of GHGs respectively the processes leading to the formation or altering the formation conditions.

A detailed introduction regarding *Morphology*, *Sedimentation*, *Trophic State* and *Water Quality* as well as *Carbon in reservoirs* is given.

2.1.1 Morphometry

“Reservoir water chemistry is determined primarily by nutrient loading through hydrological processes, which in turn are affected by various factors including morphometry “ Park et al. (2014)

The term *morphometry* refers to the quantitative analysis of a form. In the context of reservoirs, it comprises features like size, surface-depth relation, the length and form of the outer shape line, slope distribution and the width of the banks including the drawdown area. Morphometry represents one of the fundamental characteristics influencing the processes within the system reservoir. The processes affected include sedimentation, resuspension, diffusion, mixing, sediment burial and outflow. In turn, these processes regulate many abiotic and biotic variables (Håkanson, 2005; Park et al., 2014; Kennedy et al., 1982).

General morphometric characteristics of reservoirs do not influence single defined reactions or processes, but they cause tendencies towards specific conditions and states.

It can be distinguished between two kinds of reservoirs:

- Reservoirs constructed in an areas with a relatively low elevation gradient. They need a long dam, creating a shallow reservoir.
- Reservoirs with high elevation differences within the flood area will allow the construction a relatively narrow but tall dam.

In general, reservoirs have a larger catchment than natural lakes resulting in a small *capacity to inflow ratio* ($C:I$). This leads to an higher influence of the catchment characteristics on the reservoir, such as high sediment and nutrient loads and as a result typically low transparency in the water body (Morris & Fan, 1998, 4.2; Likens, 2009, Likens, 2010). Reservoirs with high $C:I$ ratios maximal longitudinal gradients with high sedimentation rates can develop. The long residence times will lead to e.g. effective phosphorous retention. On the contrary low $C:I$ ratios imply an advectively dominated flow regime with less sedimentation (Kennedy, R., H. & Walker, W., W., 1990).

However, a wide range of shape configurations has a strong internal influence on the processes in the reservoir. For instance the hydraulic behavior and the sediment transport strongly depend on the shape configuration (Morris & Fan, 1998, 3.3.2; Gilbert, 2003; Håkanson, 2005). In this regard reservoirs exhibit a range of differences to natural lakes. For example, lakes tend to be shallow around the edges and deepest in the middle. Whereas, reservoirs deepen towards (profundal) the dam and have the shallowest parts at the upstream end (proximal) (Figure 2-1). Together with the elongated geometries the deepening towards the dam causes physical, water quality, and biological longitudinal gradients which are largely absent in lakes (Figure 2-1) (Morris & Fan, 1998, 4.2; Park et al., 2014).

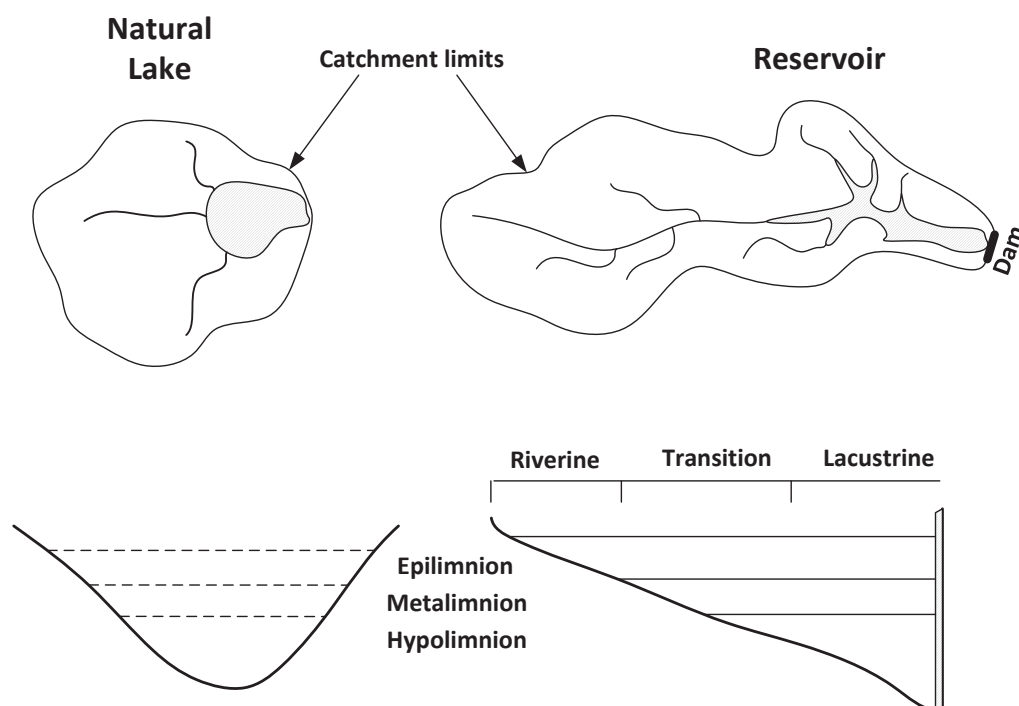


Figure 2-1: Exemplary reservoir configuration and depth distribution in comparison to a natural lake , the reservoirs show riverine behavior in the proximal and lacustrine characteristics in the profundal after Morris & Fan (1998).

The relation between the surface area and the volume of the reservoir influences the autochthonous production rates and mixing processes in the water column. If the surface is relatively large compared to the volume stored in the reservoir, high autochthonous production can occur due to an extensive phototrophic area. At the same time the stratification is strongly influenced by wind and thermal convection as the depth of the reservoir is low in comparison. Deep reservoirs with small surfaces may develop a more stable stratification and are prone to have limited autochthonous production. The stratification can lead to a sediment focusing in the deepest parts of the reservoir and to oxygen depletion in the hypolimnion (Morris & Fan, 1998, 4.3; Abraham et al., 1999).

By means of dividing the circumference of a reservoir by surface area the complexity of shorelines can be calculated (Park et al., 2014). The higher the resulting ratio, the larger is the share of sidearm area relative to the surface of the entire reservoir. An extensive area of sidearms will have various consequences for the processes in the reservoir. In general, long shore lines foster extensively vegetated littoral zones, however the typical strong water level fluctuations caused by the water usage, hinder the natural succession. The missing littoral- and aquatic vegetation leads to strong erosion along the banks, especially during drawdown phases. The steeper the banks along the reservoir outline, the higher is the erosion. High erosion rates will deliver fresh soil material and therefore nutrients to the reservoir (Nilsson, 2010). This sediment delivery is especially notable in small and mid-sized sidearms, where the fresh soil material changes the composition of the sediment.

The sidearms of a reservoir represent special areas with deviating patterns from the central water body. On the one hand, due to the shallow water depth, the water in the sidearms is prone to be stronger influenced by strong temperature fluctuations. On the other hand, the cover of the surrounding slopes protects the sidearms from direct wind impacts and therefore stabilizes the water stratification. Simulations have shown that the residence time in sidearms can be higher by several dimensions. These effects strongly develop if the singular sidearm does not have a direct inflow from the catchment. (Farrow & Patterson, 1994)

2.1.2 Sedimentation

“Half of all discharge entering large reservoirs shows a local sediment trapping efficiency of 80% or more.” Vörösmarty et al. (2003)

After a river is dammed, the reservoir created acts as a sediment trap (Rowan et al., 1995; Dean & Gorham, 1998; Vörösmarty et al., 2003). Only small shares of the sediment reaching the reservoir will leave the impoundment again. It is important to understand the basic patterns and driving forces for sediment distribution in a reservoir since those patterns have a strong influence on the hydropower schemes as well as biochemical processes like GHG production (Cesare et al., 2001).

The distribution of sediment in the reservoir depends on 1) the operation manner, 2) the size of deposited particles, 3) the shape of the reservoir and 4) the volume of the sediment deposited in the reservoir. After Annandale (2007) the shape of the reservoir can be seen as the major criterion for empirical deductions used for the understanding of sediment distribution.

Sedimentation occurs when a tributary enters the reservoir and hence decreases the flow velocity. The coarser fraction will settle fast after reaching the reservoir, while the finer fractions like clay and silt are transported towards the dam. According to the *Stokes' relation* (Eq. 1):

$$v_p = \frac{\Delta\rho}{\rho} \frac{g}{18\nu} D_p^2 \quad \text{Eq. 1}$$

Where $\Delta\rho$ ($kg\ m^{-3}$) represents the density difference between the particles and water. ρ is the density for water ($\approx 1000\ kg\ m^{-3}$), g ($9.81\ m\ s^{-2}$) is the gravitation acceleration, ν ($\approx 1-1.5\ 10^{-6}\ m^2\ s^{-1}$) is the viscosity of the water and D_p [m] is the diameter of the particles. Particles will settle if v_p is bigger than the speed of the upwelling water.

This division of the suspended loads is due to deviations in density and particle size (Morris & Fan, 1998, 9.11.2). As for example $\Delta\rho$ for inorganic particles is $\approx 1,700\ kg\ m^{-3}$ and for organic particles $\approx 20\ kg\ m^{-3}$ the organic fraction has the disposition to stay suspended even if the particle size is larger.

Sedimentation can be categorized to form four general longitudinal patterns: Delta, Tapering, Wedge and Uniform (Figure 2-2). All of those patterns can coexist and it is likely that in reality there will be an intermediate deposition pattern.

The filling of morphologic depressions including the deepest parts of the inundation zone (profundal) is an overall tendency.

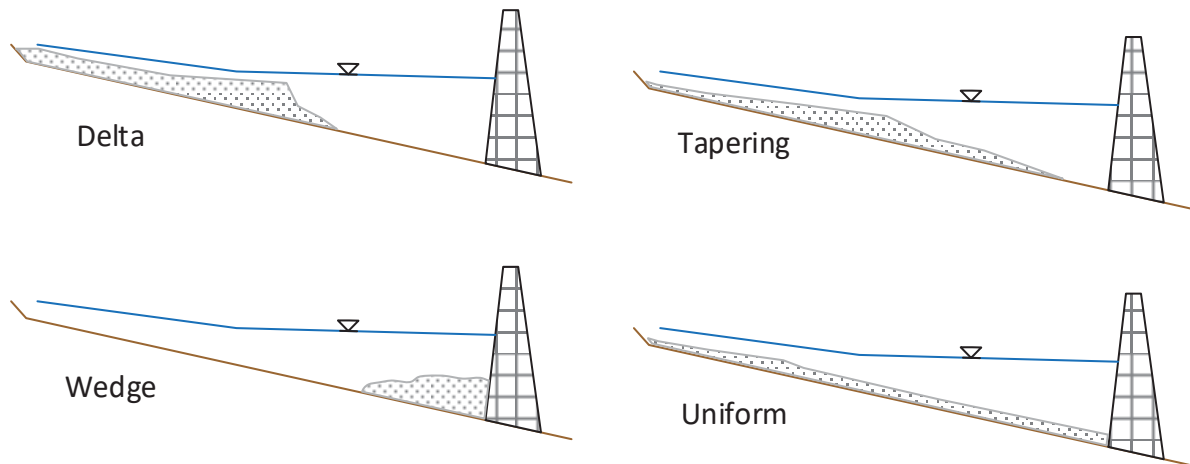


Figure 2-2: Basic sedimentation patterns after Morris & Fan (1998, 10.3).

Resuspension is the process of mobilizing formerly deposited particles. If the clay and silt proportion of the suspended loads entering the reservoir is high, resuspension and sediment gravity currents will be relevant processes forming deposition patterns (Evans, R., D., 1994; Cesare et al., 2001).

When the bottom shear stress exceeds a critical value at a relevant position, the sediment becomes remobilized. The critical shear stress is a function of the sediment properties, of which the water content and the average grain size are the two main parameters. Fresh, water saturated, recently deposited sediment can be remobilized easily, due to low cohesion within the sediment (Evans, R., D., 1994). The reservoir can be separated into three areas (Figure 2-3):

- erosion bottoms, where net accumulation is permanently prevented
- transportation bottoms, where the sediment is periodically resuspended
- accumulation areas, where no resuspension takes place

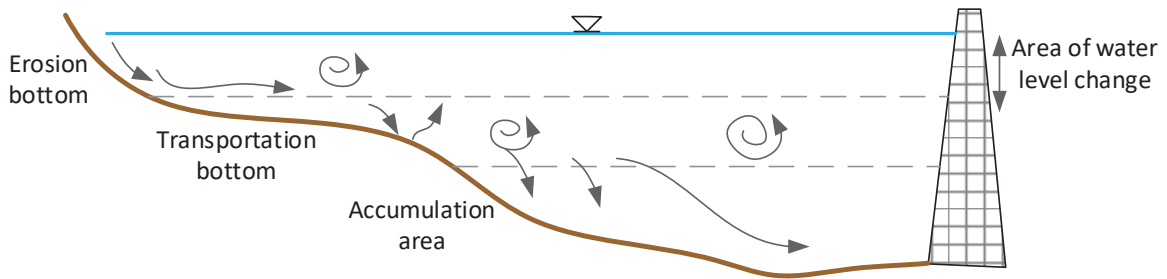


Figure 2-3: Zonation of sediment erosion, transportation and accumulation in a reservoir.

Resuspension (transportation) occurs especially during phases of turn-overs (seasonal circulation, storms) or during extreme water table drawdowns. When the water table is low, the deep water waves can reach formerly undisturbed sediment and initiate resuspension. Still, the deepest parts of the reservoirs are unaffected by resuspension under normal water level conditions. High conductivity or turbidity values measured in the hypolimnion (lower water layer) may indicate the influence of resuspension processes (Evans, R., D., 1994).

Long term sedimentation in the areas of erosion bottoms or transportation bottoms can only be possible if the continuous sediment supply reaching the reservoir and therefore the sedimentation rate overwhelms the wave energy. In this case sedimentation above the mud-energy-boundary is possible (McCave, 1971).

The named influences cause a vertical sedimentation gradient leading to higher sediment magnitudes in deeper areas (Evans, R., D., 1994). As one major driving force, turbidity currents are flowing water volumes with higher contents of fine material. The density differences cause the current to flow. These currents can already be formed by very low suspended-sediment concentrations around 1 g l^{-1} . They are capable of transporting suspended material downslope for relatively long distances, even if the general flow velocity of the surrounding water is close to zero (Cesare et al., 2001).

For the particular case of a tropic or sub-tropic reservoir, some basic assumptions can be made. The average sediment grain size is close to $63 \mu\text{m}$ (silt/clay fraction). The reservoir has a dendritic shape and is affected by strong water level changes which again cause strong shore line erosion. It can be expected to find high magnitudes of accumulated fine-sediment in depressions and the deeper parts of the reservoir (Hilton, 1985; Blais & Kalff, 1995). Whereas the steeper parts and areas close to the shore will inhabit only little amounts of sediment and if so, the grain size will be distinctively larger. The accumulated fine sediments (silt and clay) in depressions and deep zones are likely to have an elevated share

of organic material (Abraham et al., 1999; Horn et al., 2006). This coincides with the findings of Håkanson (2005) who states that the share of silt and clay fraction increases with higher depth in reservoirs.

Since the distribution of sediments in reservoirs is not analogue to sedimentation patterns in lakes and due to the higher complexity of reservoirs, little is known about the detailed sediment distribution in reservoir systems. When considering the large number of reservoirs of any size around the globe, the state of available information about storage volume losses and sediment thickness is even worse.

2.1.3 Trophic State and Water Quality

The available concentrations of nitrogen (N), phosphorous (P) and further nutrients are primary determinants of the trophic state and hence of the water quality. Similar to lakes, reservoirs can be seen as open systems, in which autotroph organisms (algae and macrophytes) convert inorganic carbon into organic matter. These organisms use solar radiation as an energy source and organic and inorganic compounds like oxygen, hydrogen, nitrogen, phosphorous, sulfur and silica as well as trace metals for primary production.

Following the Law of Minimum the C:N:P ratio determines the basic supply for algae and macrophytes and therefore the carrying capacity of the reservoir (Istvánovics, 2009). Since the solar radiation is the primary energy source for all autotrophic processes, the relative area of the reservoir is proportional to the productivity, leaving the volume as relatively unimportant in this regard (Nilsson, 2009). The transparency of the epilimnion (upper water layer) alters the amount of light penetrating the water and is itself determined by algae biomass density and suspended-sediment concentration (Likens, 2009).

The Organization for Economic Cooperation and Development defined widely accepted classes of trophic states and the according limits (OECD, 1982).

Table 2-1: List of the OECD trophic class limitations (OECD, 1982).

Trophic category	Mean total, P ($\mu\text{g l}^{-1}$)	Mean ($\mu\text{g chl-a l}^{-1}$)	Max. ($\mu\text{g chl-a l}^{-1}$)	Mean Secchi depth (m)
Oligotrophic	< 10	< 2.5	< 8	> 6
Mesotrophic	10–35	2.5–8	8–25	6–3
Eutrophic	> 35	> 8	> 25	< 3

Reservoirs in general and tropical reservoirs in particular, in comparison to natural lakes hold the property of a high eutrophication potential including a high bio productivity. This is due to constantly high insolation, high temperatures and therefore a year-round production. Furthermore, the dendrite formations with a large shore-line development, unstable thermal

stratification with high nutrient turnover rates and intensive operational water level changes are likely to intensify the eutrophication process (Gunkel & Sobral, 2013).

The mineralization of inundated soil and vegetation can lead to a high availability of nutrients (N, P) in the first phase after damming. Those mineralization processes will deplete the oxygen stock in the hypolimnion. Oxygen deficits slow down the decomposition and hence hasten the accumulation of fine organic sediments (Gunkel, 2009). The trophic state of the reservoir must be seen as an important parameter during the investigation of reservoirs, as it is strongly influencing the water quality. A rapid and strong eutrophication can lead to a loss of aquatic biodiversity, occurrence of cyanobacteria, mass development of macrophytes and for the following work especially relevant, an increased production of GHGs and methane in particular (Gunkel & Sobral, 2013).

2.1.4 Carbon in Reservoirs

“We propose that the extreme CH₄ ebullition in Lake Wohlen is ultimately attributable to very high sedimentation rates that result in limited oxic degradation of organic matter and rapid transfer of OC to deeper sediment layers.” Sobek et al. (2012)

This chapter will give a short overview about the relevant carbon related processes in a reservoir, describing the transport, accumulation and formation of organic carbon compounds. These processes will be regarded in the context of GHG formation.

Caused by the previously explained processes, impoundments disrupt natural biochemical cycles and thus, affects the households of nutrients and metals as well as carbon compounds (Friedl & Wüest, 2002; Dean & Gorham, 1998).

Even though the global annual amount of buried organic and inorganic carbon in reservoirs and lakes is huge compared to the oceans, only limited attention has been devoted to these components of the carbon cycle (Gudasz et al., 2010). Already Dean & Gorham, 1998 calculated the organic carbon (OC) burial of reservoirs (160–200 Tg a⁻¹) considerably higher than the burial rate from lakes (25–60 Tg a⁻¹) or even the oceans (60–130 Tg a⁻¹). It can be assumed that based on the increased number of reservoirs in the last decades the real amount of retained and buried OC is significantly higher. Therefore the understanding of carbon-related processes is essential for the assessment of reservoir behavior, not only on a global scale but particularly focusing on individual reservoirs.

Morris & Fan, 1998 described general longitudinal patterns of production and sedimentation of organic matter (OM) in a reservoir (Figure 2-4). Since the disposability of OM is a major variable for all carbon-coupled processes, it is elucidated in the first place.

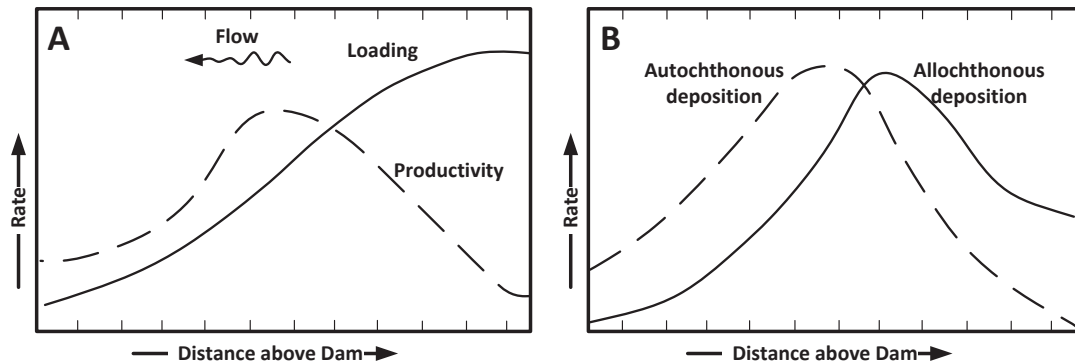


Figure 2-4: general longitudinal patterns of production and sedimentation of organic matter in a reservoir, after Morris & Fan (1998, 4.21).

Figure 2-4 (A) shows that the OM loading is highest at the inflow (proximal) of the feeding rivers. However, the peak of allochthonous OM sedimentation is located further downstream (Figure 2-4, B). Discharge peaks from the catchment lead to higher flow velocities and cause remobilization of material during strong rain events. Therefore, the accumulation rate of the relatively light organic particles in the proximal (area close to the inflow) of the reservoir is limited. In areas with lower flow velocities and less impact from storm events or after the so called “*plunge point*”, a sedimentation peak is assumed. The deposition of autochthonous OM is strongly related to the distribution of productivity. As general flow velocities in the middle of the reservoir tend to be low, the deposition peak can be found only slightly offset towards the outlet of the reservoir (Figure 2-4, B). Even if the universal tendencies shown in Figure 2-4 are the case, several authors stated that highest OM accumulation can be found in depressions, the old riverbed and the area towards the dam (Abraham et al., 1999; Blais & Kalff, 1995).

Besides the mechanisms controlling sedimentation, bio-chemical processes influence the type and amount of available carbon species from the epilimnion to the hypolimnion and the sediment. Figure 2-5 depicts an overview of relevant C-species in lake and reservoir ecosystems. Focusing on the composition and the processes of the sediment, the pathways from and to the benthos are the most relevant (Heyer & Kalff, 1998).

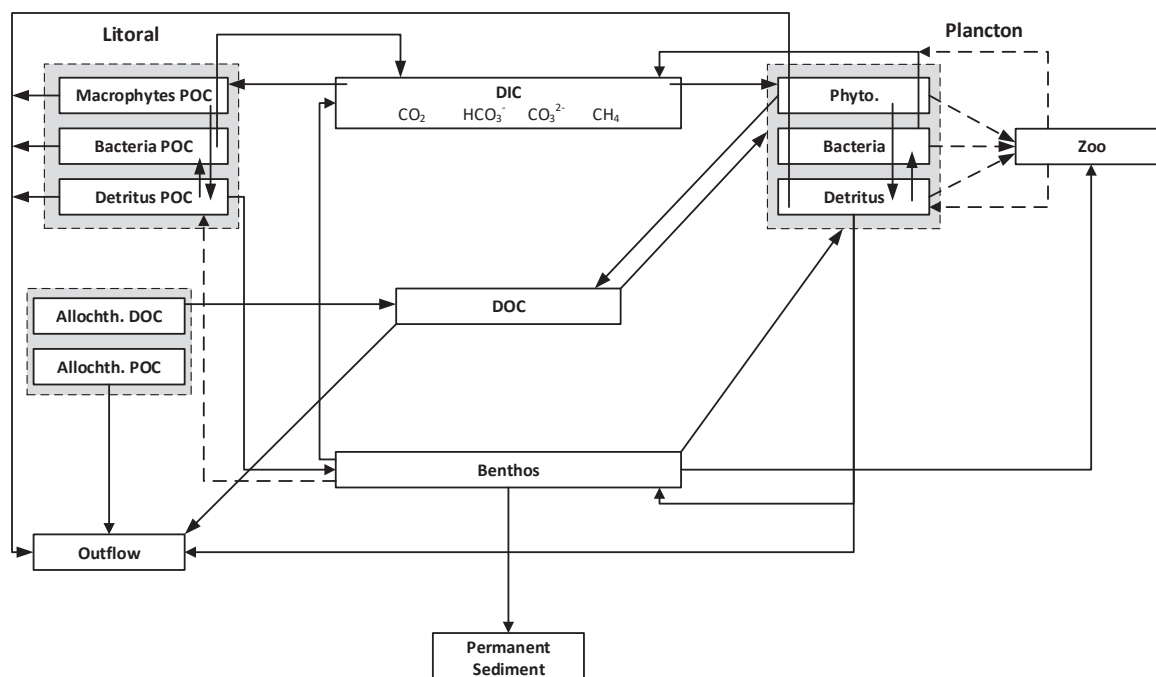


Figure 2-5: Carbon cycle in a surface water body; after Wetzel, R., G. (2001).

The mass flow of particular organic carbon (POC) from plancton and from the littoral which settles in deeper parts of the reservoir determines the range and type of mineralization and carbon burial in the sediment. Therefore, it is essential to have a closer look for a better understanding of GHG production conditions.

Sobek et al., 2012 stated that the potential of GHG production and hence emission can be directly attributed to high sedimentation rates ($\text{g OC m}^{-2} \text{ a}^{-1}$) leading to limited oxic degradation and fast transfer velocities of organic carbon (OC) to deeper sediment layers. Neither the primary productivity, nor the organic carbon degradation rate, the sedimentation rate or the bottom-water oxygen concentration as single parameters can give a satisfying explanation for OC burial (Bühler L., 2008). To quantify the input of degradable material, the *OC burial efficiency* (BE) (%), the ratio between OC gross sedimentation rate (potential OM sedimentation) ($\text{g OC m}^{-2} \text{ a}^{-1}$) and OC net sedimentation rate (effective OM sedimentation) ($\text{g OC m}^{-2} \text{ a}^{-1}$) can be calculated (Bühler L., 2008). The higher the BE, the higher is the GHG production potential of the particular sediment volume (Sobek et al., 2012).

One factor strongly influencing the BE is the oxygen exposure time (OET). If the OET is long (range of years) the BE will be lower than 15%. In the case of a range of days of OET, the BE approximates 95-100%. (Bühler L., 2008; Sobek et al., 2009)

Once the OET has a dominant influence on the amount of OC reaching the sediment, the depth of the oxycline becomes important. As explained in chapter 2.1.3 reservoirs with a certain nutrient and OM load tend to have a relatively deep hypolimnion. Thus, the vertical

distance each single OM-particle has to travel to reach the oxycline (water layer, which separates O₂-saturated from depleted water volumes) is significantly shorter than in a lake with oxic hypolimnion conditions (no oxycline present). If the OM reaches the oxycline faster, less OC will be mineralized and a higher share of the easily degradable compounds will be able to reach the sediment. After passing the oxycline the mineralization of OC will be extremely slow compared to the degradation in the oxic epilimnion (Bastviken et al., 2004b; Sobek et al., 2009). Under these conditions the major part of settling OC will fuel the anoxic degradation processes in the sediment. As especially the deeper parts of reservoirs are prone to have a major anoxic hypolimnion, this can lead to an extensive accumulation of OC in profundal zones (Sobek, 2009).

2.2 Greenhouse Gases and Reservoirs

Subsequent to the processes related to carbon in reservoirs, this chapter is about the processes in the sediment, which lead to the formation of methane. Additionally, the mechanisms of methane emission and the pathways, relevant for this work are described.

2.2.1 Creation of Methane

In reservoirs, the organic matter accumulating in the sediment is provided by autochthone primary production from either plankton or macrophytes or it is transported to the reservoir via the river inflows. Alternatively the OM reaches the reservoir directly through shore erosion and shore vegetation (Sobek, 2009). The most relevant part of the degradable material for biogeochemical processes in the sediment is the particulate organic matter (POM) (Mah, 1977).

The dissimilation of complex organic compounds takes place in several biochemical steps. The anoxic degradation in aquatic environments leads to the production of methane, in particular it can only be found in the sediment (Figure 2-6). Depending on the specific conditions of the sediment composition and the oxygen saturation in the hypolimnion even after some millimeters below the sediment water interface (SWI) the degradation processes and limited oxygen diffusion can lead to entirely anoxic conditions.

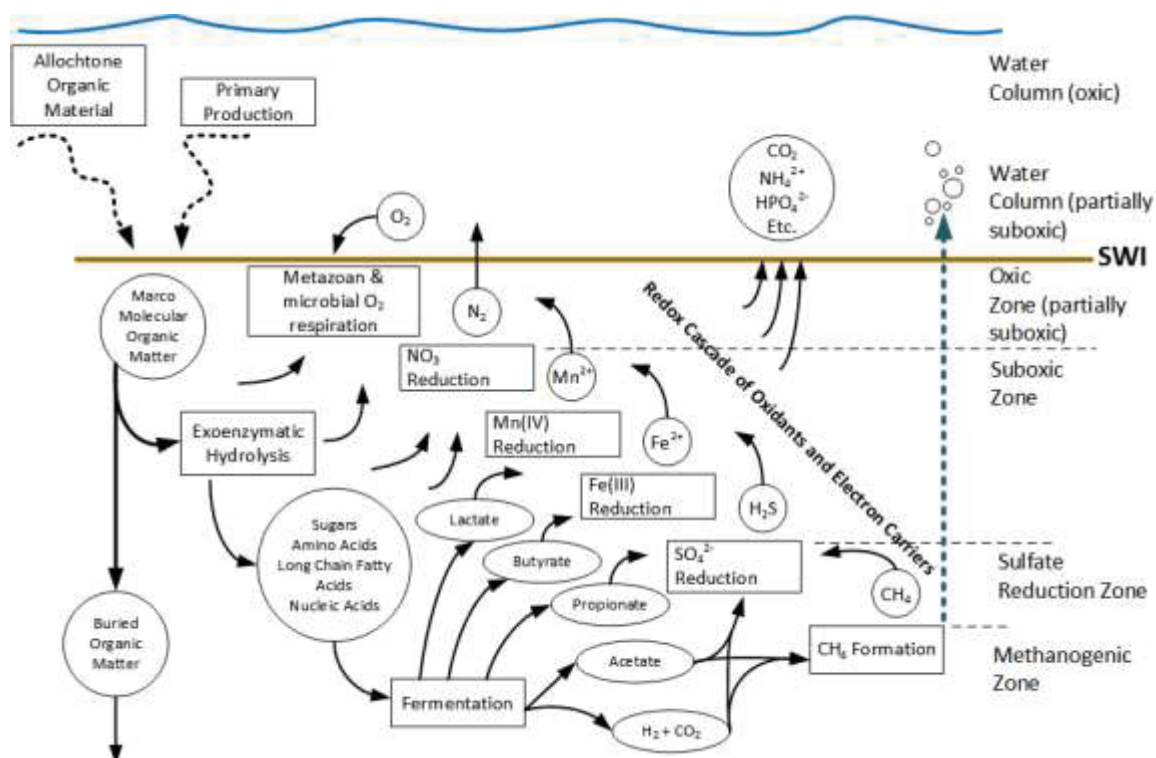


Figure 2-6: Model of the sediment related pathways of organic compounds; based on Jorgensen, 2000.

In the absence of oxygen or oxygen donors, the ultimate fate of complex organic compounds such as carbohydrates, lipids or proteins is their dissimilation and the formation of CH_4 and CO_2 . Heterotrophic organisms use the organic carbon as an electron acceptor and also as the primary source to build up biomass (Mah, 1977).

There are three principal methanogenic pathways which can be separated by the type of bacteria and by the intermediate products used for the final reaction steps (Okafor, 2011):

- Hydrogenotrophic methanogens only use hydrogen as an electron donor and carbon dioxide as an electron acceptor, some also have the capability to use formates as a source of both CO_2 and H_2 .
- Acetoclastic methanogens consume acetate, by splitting it into methyl and a carbonyl group.
- Methylotrophic methanogens grow on methylated compounds. They use them as an electron donor as well as acceptor or are reduced with H_2 .

The acetoclastic methane formation is known to be the most common process of the three pathways named above (Mah, 1977).

Figure 2-6 depicts the general sequence of anoxic degradation while the detailed reactions are condensed to the step “Fermentation”. Those steps of methanogenesis are listed in Table 2-2:

Table 2-2: List of basic reactions of complete and incomplete methane formation, after Conrad, 1989.

Complete degradation	Equation #
$4CO + 2H_2O \rightarrow 3CO_2 + CH_4$	Eq. 2
$4H_2 + CO_2 \rightarrow 2H_2O + CH_4$	Eq. 3
$4HCOOH \rightarrow 3CO_2 + 2H_2O + CH_4$	Eq. 4
$4CH_3OH \rightarrow CO_2 + H_2O + 3CH_4$	Eq. 5
$4(CH_3)_3NH_4 + 6H_2O \rightarrow 3CO_2 + 4NH_4 + 9CH_4$	Eq. 6
$2(CH_3)_2S + 2H_2O \rightarrow CO_2 + 4H_2S + 3CH_4$	Eq. 7
$CH_3COOH \rightarrow CO_2 + CH_4$	Eq. 8
<hr/>	
Incomplete Degradation	Equation #
$2CH_3CH_2OH + CO_2 \rightarrow 2CH_3COOH + CH_4$	Eq. 9
$4CH_3CHOHCH_3 + CO_2 \rightarrow 4CH_3COCH_3 + H_2O + CH_4$	Eq. 10

All three groups of methane producing archaea have in common that they depend on the substrate supply from associated anaerobic microbial communities (Okafor, 2011). These methanogens also have in common that even minimal concentrations of other terminal electron acceptors like nitrate or sulfate inhibit the process of methanogenesis in the sediment. Those alternative electron acceptors channel the electron flow to other thermodynamically more efficient bacteria for example sulfate reducers (Garcia et al., 2000). Best condition for methane production are found in environments with temperatures between 20 and 38 °C and highly reducing conditions, around $Eh \leq -300$ mV (Cicerone, 1988). Garcia et al., 2000, stated that the relatively narrow range of pH 6–8 marks the best growing conditions for the methanogens while other bacteria also show the adaption to grow in environments with pH values around 4, for example in peat bogs.

Besides the biogeochemical conditions, the net accumulation rate of sediment material has a major influence on the methane production rate (Aller, R., C., 2004; Sobek et al., 2012). As a general conceptual approach it can be predicted that if the sedimentation rate is constantly low, the relative expansion of oxic and suboxic, non-sulfidic reaction zones are favored. These reaction zones can be found in scales of 0.1–1 m below SWI. In contrast to those comparatively wide zones, high sedimentation rates will limit the oxic and suboxic zone to scales around 0.001–0.01 m. High sedimentation rates will lead to a relatively large preservation of carbon in the lower sediment layers while low sedimentation rates result in a dominance of low reactivity compounds and virtually no organic carbon is buried in the deeper sediment layers (Figure 2-7:). (Aller, R., C., 2004)

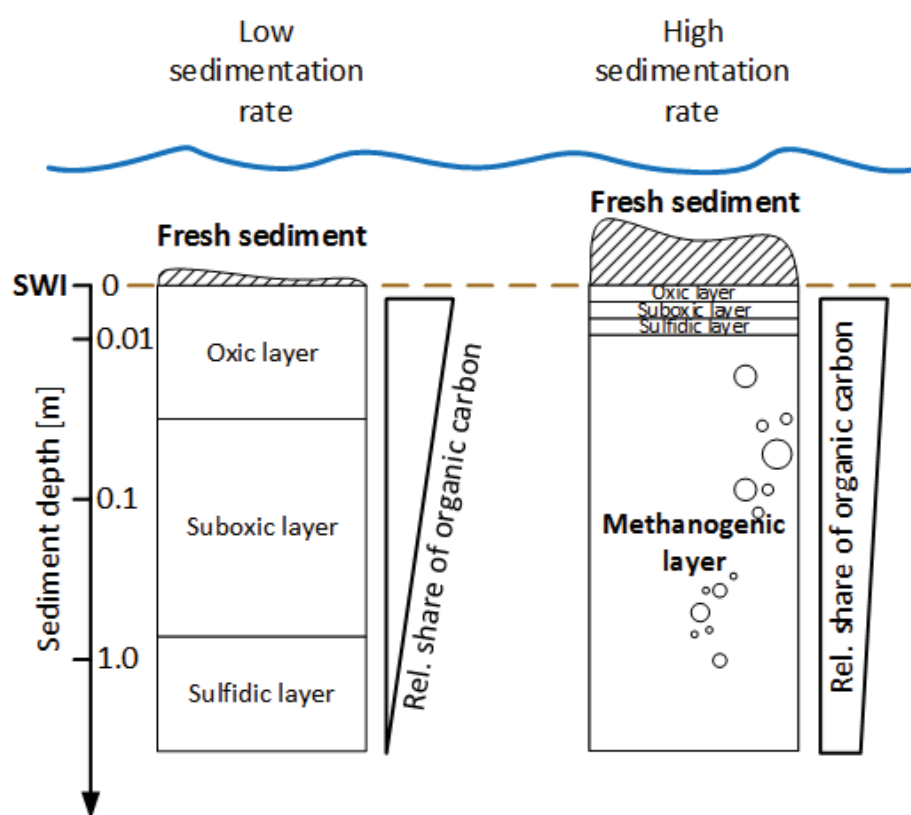


Figure 2-7: Dependence of the bio-chemical sediment conditions on the sedimentation rate

Since the solubility of methane in water is very low, the produced volumes can leave the sediment only via diffusion or bubble formation followed by ebullition (Garcia et al., 2000; Wiesenburg D. A. & Guinasso N. L., 1979).

2.2.2 Methane Emission Pathways

All GHGs produced in a reservoir have to be part of further reactions or they leave the reservoir. Since most of the GHGs (especially methane) are produced in the sediment during the decomposition of OM, they have to pass the water column to leave the reservoir. The different emission pathways as diffusion, ebullition and storage are described in the following.

Additionally to the mentioned pathways, methane can leave the reservoir by plant mediation in the littoral zone (Bastviken et al., 2004a). Due to the absence of aquatic vegetation at the study sites investigated in this work (see chapter 3), the plant mediated emissions are excluded from this study. The focus of this work is the creation, retention and rise of gas bubbles from the sediment, since they can be regarded as the dominant emission pathway in the tropics and subtropics (dos Santos et al., 2006). Generally, it can be stated that the ebullition pathway dominates the diffusive flux by nearly one order (Eugster et al., 2011; Maeck et al., 2013)

Figure 2-8 depicts a simplified concept of methane flux pathways, neglecting inflow and outflow effects. The reservoir can be separated in two principal layers, the oxygenated epilimnion and the anoxic hypolimnion overlying the sediment. They are separated by the oxycline, which is many times congruent with the thermocline. Parts of the methane produced in the sediment are emitted to the water column via diffusive flux from the sediment. Other parts of the methane leave the sediment in form of bubbles and large shares reach the water surface. Relatively small parts will be oxidized or re-dissolved (McGinnis et al., 2006). The methane, which is not leaving the sediment in form of bubbles, dissolves in the anoxic hypolimnion and builds up high methane concentrations and therefore a gradient from the bottom water to the surface. The methane diffuses along this gradient. Oxidation usually can be found between the epi- and the hypolimnion, since methane consuming bacteria can receive oxygen from the top and methane from the bottom. Methane that reaches the epilimnion via diffusion through this layer or by re-diffusion from bubbles can leave the reservoir at the water-atmosphere interface by diffusive flux.

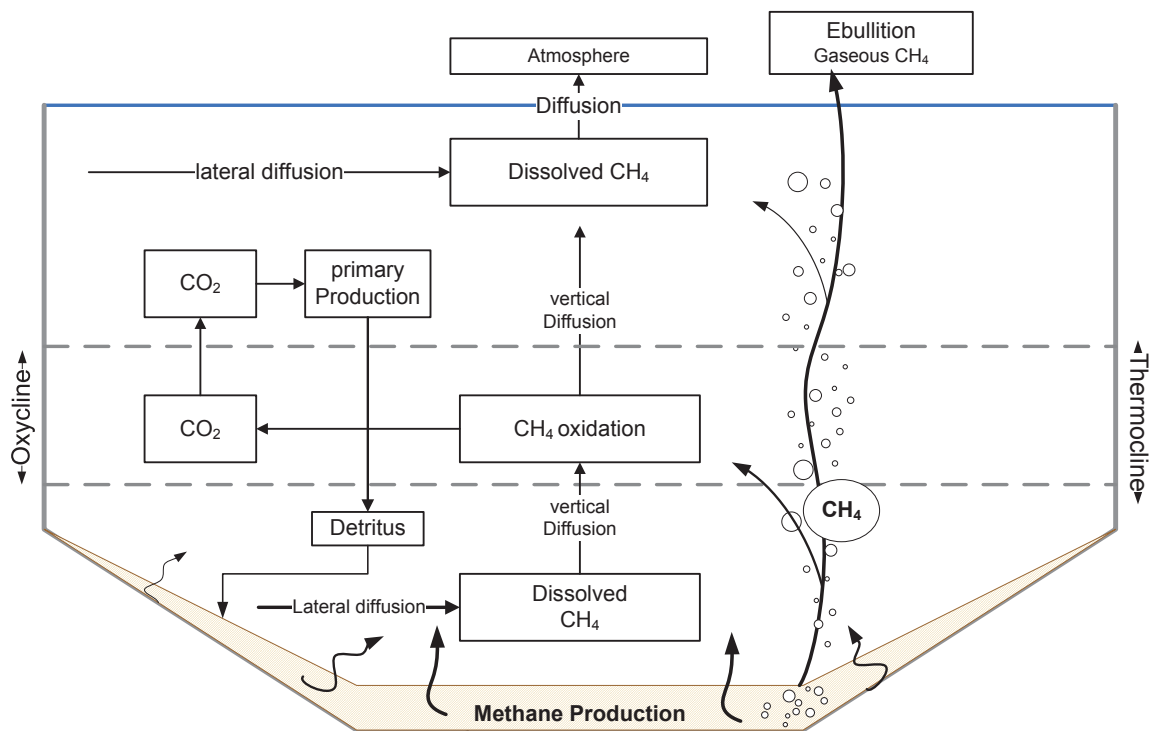


Figure 2-8: Simplified concept of methane emission pathways within the reservoir, the plant mediated pathway is excluded

2.2.3 Diffusive Flux

From the highly saturated hypolimnion the methane is transported towards the surface following the existing concentration gradient. Mainly responsible for the transport is turbulent diffusion. The methane can be unhindered transported through the hypolimnion until it reaches the anoxic-oxic boundary where methanotrophs start consuming the dissolved methane. Especially during phases of strong turbulence more methane can reach the surface without being oxidized to CO_2 . The flux from the water to the air phase depends mainly on whether the direct surface layer of the water is over-saturated and therefore has higher concentration than the air. Or, if the opposite is the case, the surface layer of the water will take up methane from the atmosphere. The flux is generally called F_{atm} and is typically calculated using the “*thin boundary layer*” method (Sherman et al., 2012). Important factors are: the concentration of the gas in the both phases, vertical distance and the turbulent diffusivity.

$$F_{atm} = k([C_{bulk\ water}] - [C_{bulk\ air}]) \quad \text{Eq. 11}$$

Where $C_{bulk\ air}$, and $C_{bulk\ water}$ are the concentrations of the gas (methane) measured in the atmosphere above the water and in the bulk fluid just below the water surface, respectively, and k is a wind speed-dependent gas transfer velocity, k ($m\ s^{-1}$). Most studies show that higher wind speeds will increase the gas exchange velocity significantly (Sherman et al., 2012). It can be stated that the diffusive flux has generally lower shares in the overall methane emission ($\pm 1\%$) than the degassing at the turbines ($\pm 49\%$) or direct fluxes from ebullition ($\pm 50\%$) (Maeck et al., 2013). But in contradiction to this they are much better investigated and understood in terms of temporal and special variability, since diffuse fluxes have been measured in a wide range of campaigns around the world (Abril et al., 2005; Tremblay et al., 2005; Bastviken et al., 2008).

2.2.4 Ebullition

Since the beginning of GHG emission related investigations in surface water bodies and especially in reservoirs, they focused on diffuse emissions over a long time. This is still reflected by the high number of publications and available measurement results of diffuse fluxes and a relatively low number of ebullition quantification studies. Ostrovsky (2003) noticed already the high spatial and temporal variability and moreover, the potential high fluxes caused by ebullition. Still, DeISontro et al. (2011) stated that: “...the spatial distribution of ebullition has not been systematically studied...”. Therefore, the dynamics related to ebullition in terms of stochastic and episodic variation still represent one of the central research gaps in the context of GHG emissions from reservoirs (Maeck et al., 2013).

Ebullition is normally measured using inverted funnel-shaped capturing constructions which are positioned in the water column (Figure 2-9).

Normally, a series of funnels is installed either next to each other in the same depth or in subsequent depth levels (Rosa et al., 2003). Hence, funnels can only provide limited depth-related information, since their positions are fixed and only a limited number of them can be deployed. The opening size of most funnels is ca. $1\ m^2$, in agreement to the uniformly recommended diameter of $0.7\ m$ (The World Bank, 2010). The general deployment time lies between a couple of hours and one day (Rosa et al., 2003; Bastviken et al., 2004a; Abril et al., 2005) even The World Bank (2010) recommends a deployment of up to several months.

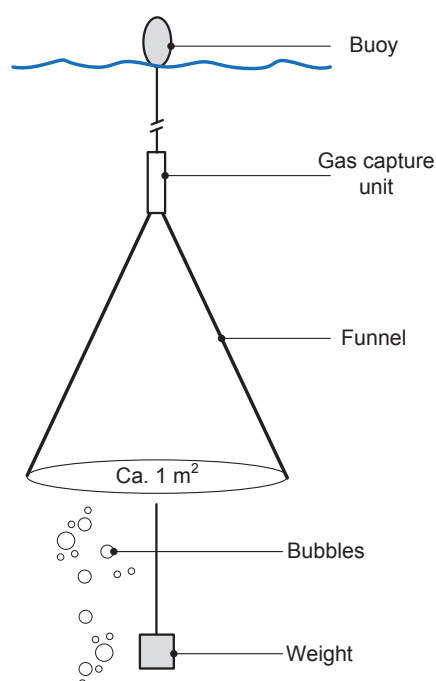


Figure 2-9: Basic design of a gas trap funnel

Only a few ebullition measurements with funnels were carried out producing long continuous time series of measurement (Maeck et al., 2013). The gas capturing unit of the funnel system was further developed and modified. A valve is installed at the top side of the capture unit which can be electrically controlled to release the gas. This made a multi-month deployment of the funnels possible. The number of valve openings was recorded with a data logger and could be related to the volume of the capture unit to calculate the gas flux. In addition to this, the internal clock gives time reference to the data allowing to recognize high and low emission phases.

Another opportunity of quantification of gas bubbles rising from the bottom of a water body to the surface is the use of echo sounding technology. Ostrovsky (2003) stated:

“Acoustic methods might be helpful to evaluate spatial variability of bubbles, which are strong scatterers of acoustic energy, in deep enough aquatic systems”.

DeISontro et al. (2011) developed, based on Ostrovsky et al. (2008) a method aiming to quantify ebullition by counting the number of rising bubbles and estimating their size using a single beam echo sounder. This led to an improved method of surface flux calculation from ebullition due to the capability of the echo sounder to detect bubbles in the entire water column ensonified by the sound waves. Additionally the area covered by these measurements can be manyfold larger compared to the limited number of square meters covered with funnels or chambers.

In the study from DeISontro et al. (2011) the funnels were mostly used for the determination of gas concentrations but not for the gas flux estimation. The results show a high spatial heterogeneity of bubble emissions and also a conjunction between potential sediment accumulation zones. Contrary to Abril et al. (2005), who claimed that major zones of bubbles production can only be found in depth lower than 10 m, other results show that methane bubbling from the sediment can be found also in greater depth (Ostrovsky, 2003; DeISontro et al., 2011; Wessels et al., 2010).

2.2.4.1 Formation of bubbles

Under certain conditions the produced methane from OM degradation can form bubbles in the sediment. The primary factor is the methane concentration in the pore water, which has to exceed the saturation level in order to form micro bubbles (Figure 2-10; A). For the accumulation of methane and hence the formation of bubbles, the diffuse flux from the sediment to the overlaying water cannot exceed the production in the sediment. If the partial pressure of all dissolved gases in the pore water is higher than the ambient pressure and the surface tension of the surrounding medium, bubbles can be formed.

Depending on the sediment properties the bubbles can grow in the interstitial spaces between the sediment particles. If those spaces are limited or the bubbles grow further, the particles can be displaced by the free gas (Figure 2-10, from B to C). Figure 2-10, D, depicts the situation for very fine sediments, dominated by silt or clay, where the pores are extremely small and hence the growing bubbles cause a displacement of the sediment. Bubble sizes measured by computerized tomography ranged between 0.4 and 5 mm (Abegg & Anderson, 1997) while bubble sizes up to radii of 11 mm were also observed (Anderson et al., 1998). Katsman et al. (2013) calculated that in muddy sediments a mature bubble can reach the size of around 11 mm equivalent spherical radius.

Decisive for the growth of the bubble is not only the surrounding sediment with its particular mechanical characteristics, but also the permanent support of dissolved methane. In a depth around 20 m a concentration of 6.5 mM was stated as sufficient for undisturbed bubble growth (Martens et al., 1998). Contrary to the shapes shown in Figure 2-10, bubbles with high volumes are likely to form non-spherical, amoeba-like shapes within the sediment (own observation from sediment cores; photos of cores are given in Appendix A.1).

Bubbles are known to build up coherent layers in sediments of high gas production (Lyons, 1996; Katsman et al., 2013; Sager et al., 1998). If the sediment contains a porous layer

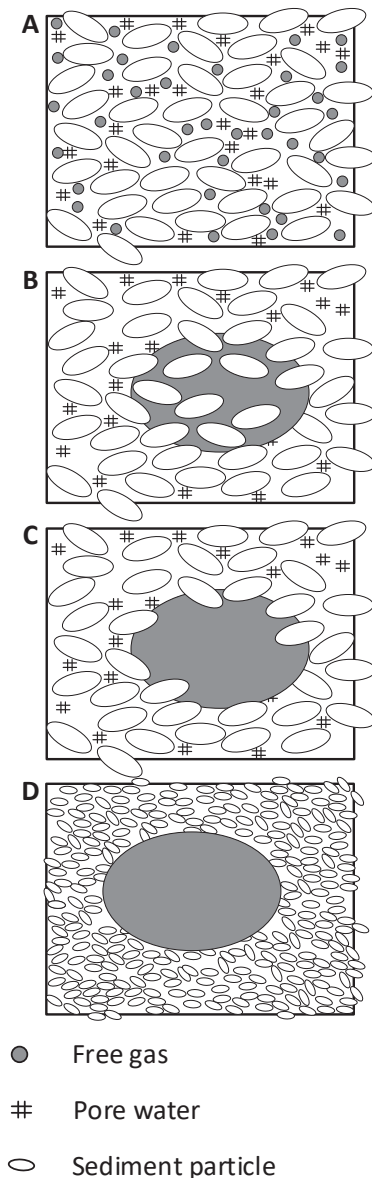


Figure 2-10: Different types of bubble formations in the sediment are shown; the sediment is displaced with increasing bubble size; modified after Anderson et al. (1998)

where gas accumulation can occur, it is likely that local spontaneous ebullition events will produce volcano-like pockmarks at the surface of the sediment (Wessels et al., 2010).

2.2.4.2 Rise of bubbles

The release of the bubbles created in the sediment depends on the production rate, outgassing frequency, the pressure respectively pressure changes and the mechanical features of the sediment (Katsman et al., 2013; Maeck et al., 2014; Scandella et al., 2011). The sediment is known to form preferential pathways, like vertically-aligned fractures after a series of bubble release events (Scandella et al., 2011; Katsman et al., 2013). Those conduits are assumed to facilitate the transport to the SWI. Conduit formation mainly occurs in fine sediment matrices (Choi et al., 2011). If conduits are present in the sediment the hydrostatic pressure moves into focus. Figure 2-11 visualizes in three steps the process of bubble release from the sediment.

It is initiated by a pressure drop caused by a decreasing water level. Figure 2-11 (A) shows the depth of active bubble formation (h) and the open conduit down to the point where the effective stress $\sigma' = \sigma - P_g$ reaches the tensile limit. Where P_g is the gas pressure and σ is the stress. Conduits always dilate if the effective stress is negative and is equal to the magnitude of the effective tensile strength (T). If the water level sinks (or even the atmospheric pressure) the pressure/stress in the entire sediment volume is reduced (Figure 2-11, B) (\rightarrow smaller σ), plastic cavity dilation allows

the bubbles to expand (decompress) until $P_g = \sigma + T$. During and after expansion the bubbles will leave the conduit and rise to the surface (Figure 2-11, C). Assuming that mechanic characteristics and methane production are constant the pressure situation is the dominant factor for the bubble release in fine grained sediments (Scandella et al., 2011; Maeck et al., 2014).

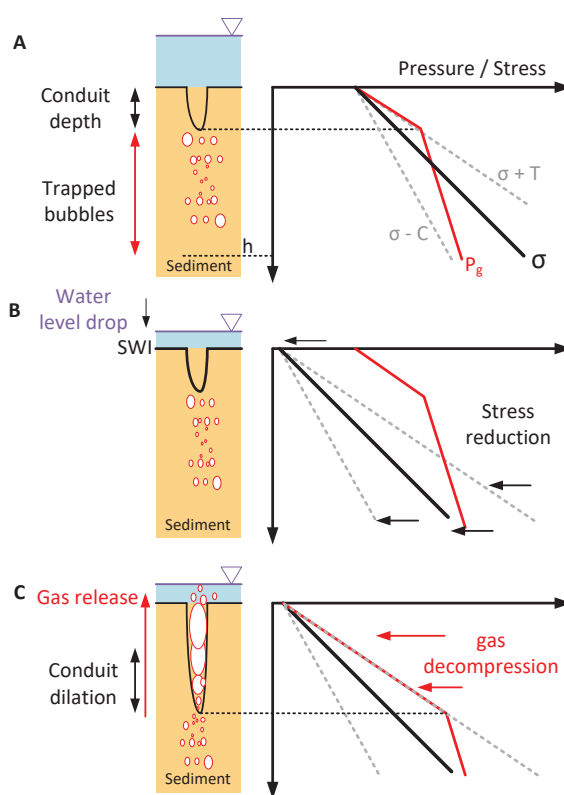


Figure 2-11: Modeled response of bubble release on pressure changes from a sediment with conduits, after Scandella et al., 2011.

During the rise the bubbles are affected by several physical and chemical processes. The bubbles can change their shape due to rising velocity and friction with the medium. The higher the volume of a bubble, the lesser it will maintain a round shape during the ascent. Bubbles with 1–3 ml volume already develop a variety of non-spherical shapes (Ostrovsky et al., 2008). The shape of the bubbles is relevant for the effective diffusion surface as well as for the backscatter strength of sound waves (Ostrovsky et al., 2008).

Bubbles which normally leave the sediment have a methane content between 5% and above 90% (Baulch et al., 2011; Maeck et al., 2014). Since the methane concentration in the bubble is higher than in the water column, the bubble will be affected by dissolution processes (Leifer & Patro, 2002). Hence, the bubble shrinks on the way to the surface and the methane content decreases. The dissolution is mainly controlled by 1) the depth of release and thus by the time the bubble is exposed to a medium with a concentration gradient and 2) by the volume and shape of the bubble.

The larger the volume the smaller is the surface in relation to the contained gas. Consequently, small bubbles will suffer higher losses of gas than large bubbles released at the same depth (Ostrovsky et al., 2008; McGinnis et al., 2006). McGinnis et al., 2006 calculated that a bubble from a depth of 26 m and 11 mm radius will transport ca. 90% of its methane content to the surface.

2.3 Fundamentals of underwater Acoustics

This chapter provides a general introduction to the physical nature of sound waves in an aquatic medium, including explanations of the decibel notation, signal behavior and propagation and possible applications in water bodies. Although there is a variety of applications and methods for distinct purposes, only the applications used in this work are elucidated. Since the basic knowledge of underwater acoustics is not common outside the hydrographs-community, basic facts and equations are explained.

2.3.1 Underwater Sound Propagation and Propagation Losses

Acoustic waves

Acoustic waves are longitudinal mechanical waves which are propagating in an elastic medium (i.e. gas, liquid or solid) via fluctuations of pressure and density and can be characterized by “frequency” or “wave length”. While frequency refers to the number of oscillations per time, one Hertz [Hz] is one wave cycle per second. The wave length is the distance between identical points within two adjacent wave cycles at a constant velocity. Therefore the frequency f [Hz] is inversely related to the wave length λ [m] (Eq. 12). Shortly stated as, the higher the frequency, the shorter the wave length.

Sound waves in water are transported relatively slow (ca. 1,500 m s⁻¹) compared to the speed of electromagnetic waves (ca. 300,000 km s⁻¹), but much faster than sound in air (300 m s⁻¹). The propagation of acoustic waves occurs with sound velocity c [m s⁻¹] (Eq. 13), depending on the density ρ [kg m⁻³] and the compressibility χ [Pa⁻¹] of the medium.

$$\lambda = \frac{c}{f} \quad [m] \quad \text{Eq. 12}$$

$$c = \sqrt{\frac{1}{\rho\chi}} \quad [m \text{ s}^{-1}] \quad \text{Eq. 13}$$

The sound intensity I [W m⁻²] of a plane wave depends on its pressure amplitude p_0 [Pa], density ρ [kg m⁻³] of the propagation medium and sound velocity c [m s⁻¹].

$$I = \frac{p_0^2}{2\rho c} \quad [W \text{ m}^{-2}] \quad \text{Eq. 14}$$

Sound intensity is defined as the average energy flow per surface unit perpendicular to the direction of propagation and time. As sound waves spread spherically, intensity decreases with growing distance from the source. The product of intensity I [W m⁻²] and surface A [m²] results in the sound power P [W] (Eq. 15) which is received by the surface (Lurton, 2010, 20–30).

$$P = I \cdot A = \frac{p_0^2 A}{2\rho c} \quad [W] \quad \text{Eq. 15}$$

Sound velocity

The speed of sound mainly depends on the characteristics of the transmitting medium. For water, the sound velocity strongly depends on the density. The density in turn is influenced by the temperature T , the hydrostatic pressure (depth dependent) and the salinity. The higher the density, the faster the sound travels through the water. General sound speeds in water can range from around 1400 m s^{-1} (cold, salt free water) up to 1500 m s^{-1} as a standard value for sea water. Higher sound speeds can only be reached under extremely high pressures in depths of more than 3000 m (Leroy, C., C. et al., 2008). In fresh water, the speed of sound can be assumed to be around 1480 m s^{-1} .

The sound velocity can be calculated by using the comparatively simple model by Medwin (1975) (Eq. 16), which accounts for the impact of the named parameters and provides a sufficient accuracy up to depths of 1000 meters.

$$c = 1449.2 + 4.6 T - 0.055 T^2 + 0.00029 T^3 + (1.34 - 0.01 T)(S - 35) + 0.016d \quad [\text{m s}^{-1}] \quad \text{Eq. 16}$$

c identifies the sound velocity [m s^{-1}], T is the temperature [$^{\circ}\text{C}$], d is the depth [m] and S is the salinity [PSU] (Lurton, 2010).

The decibel scale

The name decibel [dB] goes back to Alexander Graham Bell who was the inventor of the modern telephone. One decibel is the tenth of one *bel*. The decibel is a logarithmic unit expressing the ratio between two different values of a physical quantity, in this case intensity. One of these values is used as the reference, which in under water acoustics, is a pressure of $p_{ref} = 1 \text{ }\mu\text{Pa}$. The measured intensity can be expressed in decibel as the absolute pressure level p_{dB} of the physical quantity (Eq. 17). The unit decibel is appropriate to be used for sound measurements, since the logarithmic scale allows to represent a huge range of values created by the fast decrease of sound intensity caused by spherical spreading and absorption (Lurton, 2010, 20–30).

Following Eq. 18 the sound level L can either be calculated by using the ratio of two sound powers P_1, P_2 [W], two intensities I_1, I_2 [W m^{-2}] or two pressure amplitudes p_1, p_2 [Pa].

$$p_{dB} = 20 \log \frac{p}{p_{ref}} \quad [\text{dB}] \quad \text{Eq. 17}$$

$$L = 10 \log \frac{P_1}{P_2} = 10 \log \frac{I_1}{I_2} = 10 \log \frac{p_1^2}{p_2^2} = 20 \log \frac{p_1}{p_2} \quad [dB] \quad \text{Eq. 18}$$

Geometric spreading loss

All sound waves which are transmitted through water emanating from a point source, e. g. the transducer of an echo sounder, spread in all possible directions, forming a sphere (Figure 2-12). Since energy is conserved the intensity of the wave diminishes exponentially with range. This means that the ratio of the intensities at two ranges is proportional to the inverse ratio of the sphere surfaces at those ranges (Eq. 19).

$$\frac{I_2}{I_1} = \frac{A_1}{A_2} = \frac{4\pi R_1^2}{4\pi R_2^2} = \left(\frac{R_1}{R_2}\right)^2 \Leftrightarrow 10 \log \frac{I_2}{I_1} = 10 \log \left(\frac{R_1}{R_2}\right)^2 = 20 \log \left(\frac{R_1}{R_2}\right) \quad \text{Eq. 19}$$

The transmission loss (TL) of a sound wave is calculated through the comparison of the intensity I of one signal at a distinct range R with the intensity I_{1m} of the signal at a 1 m distance from the source and is defined as

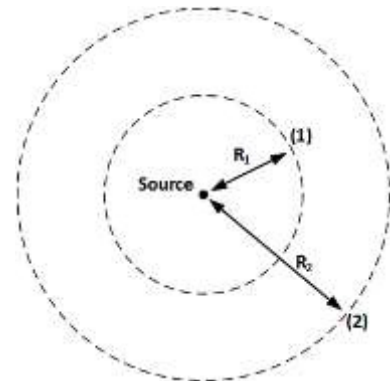


Figure 2-12: Spherical spreading, after Lurton, 2010, 20–22.

$$TL = 10 \log \frac{I_{1m}}{I} \quad [dB] \quad \text{Eq. 20}$$

According to Eq. 21, the transmission loss of an acoustic wave caused by spherical spreading can therefore also be expressed as:

$$TL_{spread} = 20 \log \left(\frac{R}{R_{1m}}\right) \quad [dB] \quad \text{Eq. 21}$$

A widespread simplification of the formula is $TL_{spread} = 20 \log R$ with no reference to the unit distance. For practical reasons this expression also will be used from this point on. (Lurton, 2010, 22–23)

Correction of spreading losses - Time-Varying Gain

If alternating targets with different distances to the transducer are to be detected without biasing the received signal, the signal intensity has to be corrected. To ensure that identical reflecting targets cause the same echo strength independent of their distance to the echo sounder, the transmission loss due to geometric spreading can be corrected using a function called Time-Varying Gain (TVG) (Figure 2-13) (Tęgowski et al., 2006). For spherical spreading, there are different TVG functions depending on the target type. For volume targets $TVG = 20 \log R$ is applied (Eq. 23). For surface targets and point targets, however,

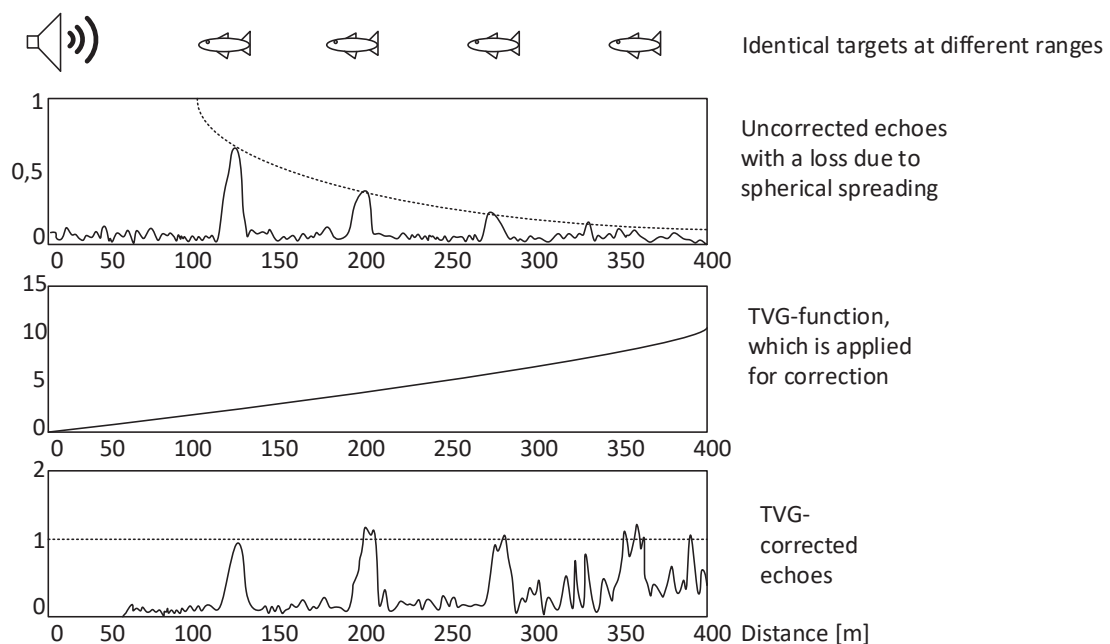


Figure 2-13: Principle of Time-Varying Gain (TVG), after (Lurton, 2010).

$TVG = 30 \log R$ and $TVG = 40 \log R$, respectively, have to be used for correction.

On the one hand, applying the TVG function can compensate the intensity losses of different ranges. On the other hand, it has to be kept in mind that the TVG correction will also increase the noise of the signal. The signal-to-noise ratio stays unchanged through this correction (Lurton, 2010, 251–253).

Absorption losses

In addition to decreasing intensity through spherical expansion, the intensity of the sound wave will be affected by the absorption of energy caused by the medium water. Both frictional dissipation and heat induce that the signal is attenuated constantly. This is expressed through an attenuation coefficient α [dB km⁻¹] (Eq. 22). Since all investigations in this work were carried out particular in shallow waters (max. depth 45 m), for practical reasons the equation will refer to α [dB m⁻¹]:

$$TL_{abs} = \alpha R \quad [dB] \quad \text{Eq. 22}$$

Correction of spherical spreading and absorption losses

For reasons of clarity, the physics of the hydro acoustic part of this work are kept as simple as possible and therefore other existing losses like scattering will be ignored due to the subordinate relevance and signal distortion. For the purposes of this work it is assumed that the target loss (TL) mainly consists of spherical spreading and attenuation (Eq. 23). Therefore the data obtained was corrected from those effects.

$$TL = TL_{spread} + TL_{abs} = 20 \log\left(\frac{R}{R_{1m}}\right) + \alpha R \quad [dB] \quad \text{Eq. 23}$$

2.3.2 Echo Sounding

Set-up of an echo sounding system

The echo sounder system used for this survey consists of five principal parts. The central element is the transceiver, it generates high-voltage electrical pulses (100 – 1000 W) which are sent to the transducer. It also contains the communication and processing rack for the data exchange with the computer.

The produced electrical impulses are sent to the underwater located transducer. It mainly consists of two arrays of piezoceramic elements, one for each frequency (38 and 200 kHz) and a sonic-permeable polymer hull for mechanic protection. Through deformation of the piezoceramic elements the

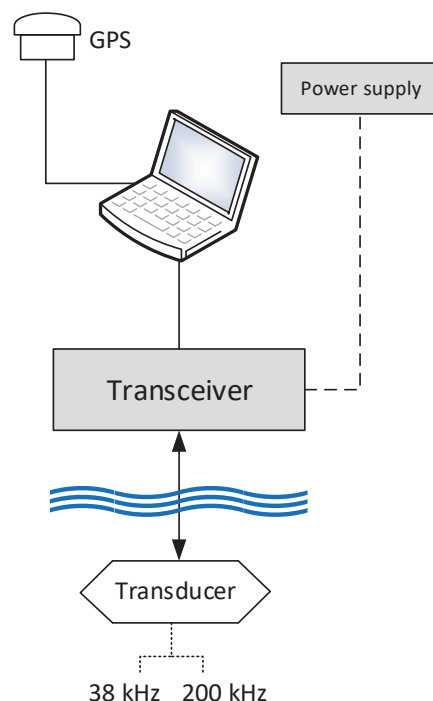


Figure 2-14: Set up of the EA400 echo sounding system.

electrical pulses are transformed into sound waves. Typical beam angles of those impulses vary from 2.75° to 20° (Buchanan, 2009). This principle works as well the controversially, which means that the transducer is also able to receive returning sound waves (echoes) and to convert them into electrical pulses. The received pulses (pings) are sent back to the transceiver where they are processed in real time. The processed data is stored and visualized on the notebook (Airmar Technology Corporation, 2012). The EA400 software tags every single ping with a time stamp and the available GPS position information.

Principle of measurement

Based on the physical background explained, the water depth under the echo sounder as well as some characteristics of the reflecting medium can be derived. The character of the return signal is dependent on the function of the transducer (frequency, pulse length, power input), the angle of incidence and the reflective properties of the bottom material encountered within the footprint of the sound wave (Buchanan, 2009). Depending on these parameters the acoustic signature of the sound wave is changed.

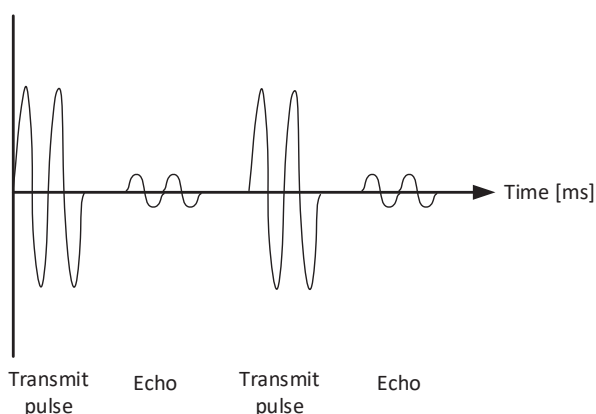


Figure 2-15: Echo sounding sequence, showing the transmitted pulse and the following echo.

The depth can be measured by emitting sound pulses into the water and measuring the time until the echo reaches the transducer again. The depth in [m] is half of the distance the sound travels during time t with speed c (Eq. 24). Those pings have a distinct duration (pulse length τ) and are emitted with a distinct frequency [ping s^{-1}] (ping rate). In this manner all obstacles which are capable of reflecting sound waves can be detected on the way between the transducer and the bottom.

$$d = \frac{tc}{2} \quad [m] \quad \text{Eq. 24}$$

The sound wave, while travelling through the water, bounces back from every object or boundary (density or phase difference). In general the echo lasts for a longer period than the original pulse length. In form of intensity modulations it contains information about the echo strength of any object or surface. The horizontal resolution is a function of travel speed and

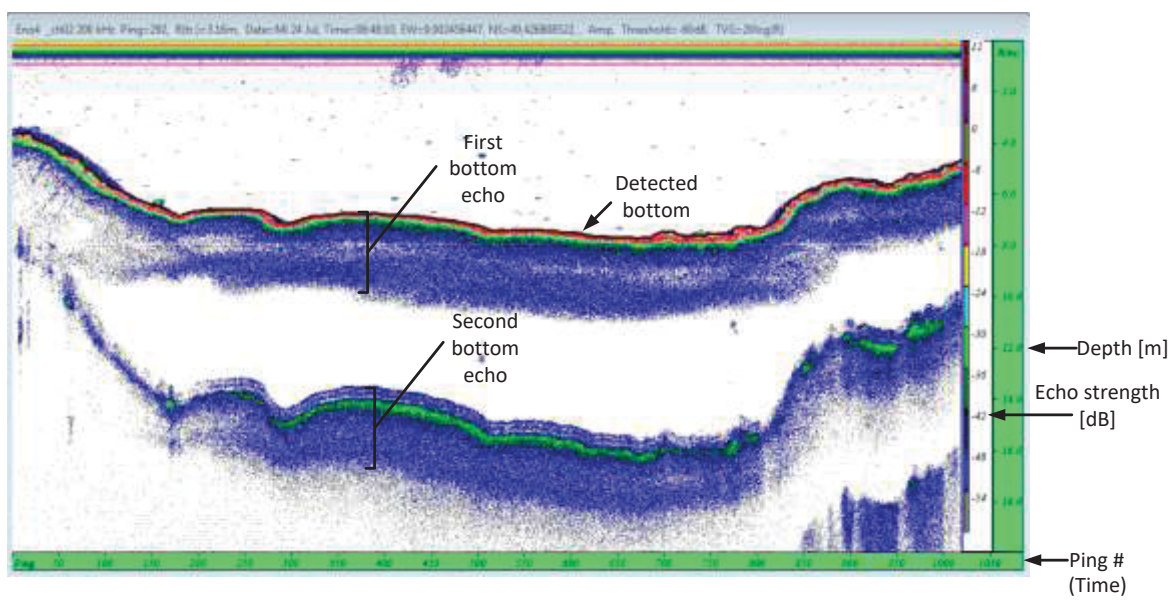


Figure 2-16: Example of an echogram; Sonar5 pro, colors represent the echo strength in dB referring to an adaptable scale, the black line depicts the identified bottom.

ping rate, while the vertical resolution complies with the wave length, meaning that a higher frequency allows a higher resolution.

The echo strength is a logarithmic measure for the intensity of the echo in relation to the intensity of the original sound wave at a one meter distance of the transducer. This echo information is available for further processing and can be visualized in form of an echogram (example shown in Figure 2-16).

The echogram shows the recorded pings juxtaposed from left to right with increasing numbers on the x-axis, whereas the y-axis indicates the time the echo needs to return and hence the depth in [m]. After having emitted a signal of pulse length τ [ms], the echo sounder is waiting for echoes. For intervals of the pulse length duration τ , the sounder measures the echo strength of the returning impulse and the elapsed time since the moment the signal has been emitted by the sounder. This information is stored in samples, which can be visualized in the echogram as pixels, colored depending on the echo strength (Buchanan, 2009).

The software compiles the echogram by slicing each ping in a number of samples (time slices) while each sample is represented by a pixel in the echogram. The intensity value of each sample defines the color of the pixel and the frequency defines the possible resolution and therefore the minimal size of each pixel.

A 200 kHz echogram shows more details (resolution ± 1 cm) than a 38 kHz echogram (resolution 4–5 cm) of the same situation (Airmar Technology Corporation, 2012) (Figure 2-17). Higher frequencies are able to detect smaller objects but they consequently suffer from a higher attenuation than low frequency waves. Hence, the low frequencies are able to penetrate sediment significantly deeper. Examples of penetration depths are given in Table

2-3. Hydro-acoustic methods can be used for the identification of the bottom types, fish biomass or buried objects. One specific application is the detection of gas bubbles.

Table 2-3: Approximate values for the penetration of sound impulses into silt and sand depending on the frequency (British Standard 6349-5:1991, 1991).

Frequency [kHz]	Penetration [m] for silt	Penetration [m] for sand
10	2.0 to 5.0	0.5 to 1.5
15	1.0 to 3.0	0.5 to 1.0
50	0.5 to 2.0	0.1 to 0.5
100	0.1 to 1.0	0.0 to 0.5
200	0.0 to 0.2	0.0 to 0.1

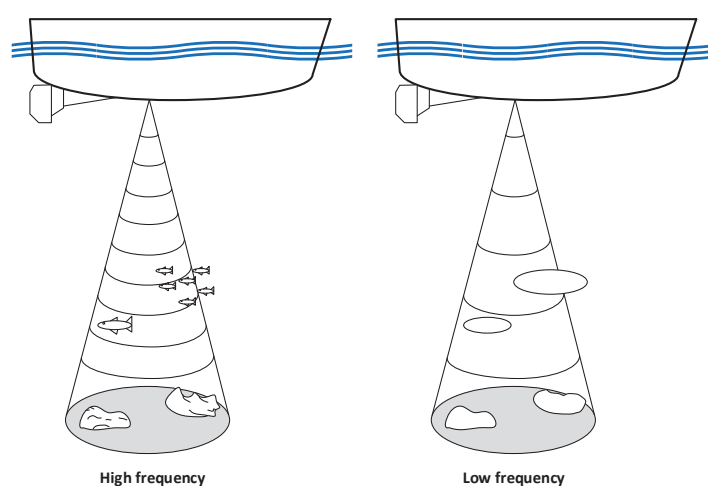


Figure 2-17: Differences between high and low frequency resolution, concerning the detection of obstacles.

Transducer configuration

Whereas the two frequencies, 38 and 200 kHz as fix part of the hardware cannot be altered, a variety of transducer configurations can be adapted to the needs of the survey. These parameters and their influence on the acoustic pulse will be addressed in the following. Table 2-4 gives an overview of the principal effects of the different transducer settings.

Transmitting power

The transmitting power P [W], put in every ping has to be appropriate for the purposes of the survey intended. The power of the pulses has to be sufficient to guarantee that the signal is not lost at the deepest parts which can also be covered with soft sediments reducing the reflectivity. At the same time the power may not be too high so that clipping effects would be caused in shallow parts of the investigation area, which can feature harder bottoms producing strong echoes (Collins & Rhynas, 1998; Lurton, 2010, 189–190).

Pulse duration

The pulse length τ [ms] describes the duration of power transmission and is proportional to the amount of energy transmitted into the water. Hence, a short pulse length delivers less energy through the water and into the bottom. Depending on the transmitting power a very short pulse length can lead to a loss of information. Disadvantages of long pulse lengths lay within the resolution of the signal. Long τ -values will cause the samples (parts of the pings) to increase in size, thus the resolution deteriorates. Furthermore, long pulses can lead to a signal blending, which means that the echo of a previous pulse is returning to the transducer before the emission of the subsequent pulse itself has been fully completed. This can lead to a loss of information.

Ping rate

The ping rate does not influence the properties of the echo signal itself. The rate influences the ratio of measurements per time respectively sailed distance. It should be chosen dependent on the vessel speed, the striven resolution and also to avoid unnecessary large data volumes (Collins & Rhynas, 1998).

Table 2-4: Overview of the effects of the main transducer characteristics and settings.

Parameter:	Low/short	High/long
Frequency	Resolution low, high penetration depth	Resolution high, low penetration depth
Transmitting power	Energy consumption low	Increased penetration depth
Pulse length	Detailed images, less energy per ping	Reduced resolution, can increase penetration depth
Ping rate	Less resolution per distance; small data volumes; less noise in shallow water	Best resolution per distance, can cause noise

2.3.3 Interaction of Sound with Bottom and Sediment

“Reflective properties of bottom, determined by the method of multiple echoes measurements are strongly correlated with mechanical characteristics of bottom sediments” Orłowski (1984)

Sound waves hitting an interface between two different media (e.g. water and sediment) are reflected. At those acoustic impedance discontinuities one part of the sound wave’s energy is reflected directly, while the rest is transmitted into the next medium. The ratio between the transmitted (or refracted) and the reflected part of the wave depends on the impedance contrast between the two media. The impedance of a medium is defined as the product of its

density ρ [kg m^{-3}] and the sound velocity c [m s^{-1}] in this medium (Eq. 25) (Lurton, 2010, 372–379).

$$\text{acoustic impedance } Z = \rho \cdot c \quad [\text{kg m}^{-2} \text{s}] \quad \text{Eq. 25}$$

The share of energy thrown back by direct reflection increases with stronger impedance contrasts. For normal incidence ($\vartheta_1 = 0$; see

Figure 2-18), which was the case for all measurements in this work, the reflection coefficient V can be calculated as follows (Eq. 26) (Lurton, 2010, 402–403). Where Z_i is the impedance of the medium.

$$\text{reflection coefficient } V = \frac{Z_2 - Z_1}{Z_2 + Z_1} = \frac{\rho_2 c_2 - \rho_1 c_1}{\rho_2 c_2 + \rho_1 c_1} \quad \text{Eq. 26}$$

Reflection and scattering at surfaces

An absolutely plane surface would cause the whole energy to be reflected specularly with an angle θ_r analogously to the angle of incidence, but in the opposite direction (Figure 2-18, A). However, since no surface in nature is totally plane, in particular no sediment interfaces, there is not only coherent reflection. Irregular or rough interfaces, like the bottom of a lake, only reflect a part of the energy in specular direction (coherent reflection), while the other part of the energy is scattered in all directions. This phenomenon is called diffuse reflection or (surface) scattering (Figure 2-18, B) (Brouwer P., 2008; Lurton, 2010, 372–379; Orłowski,

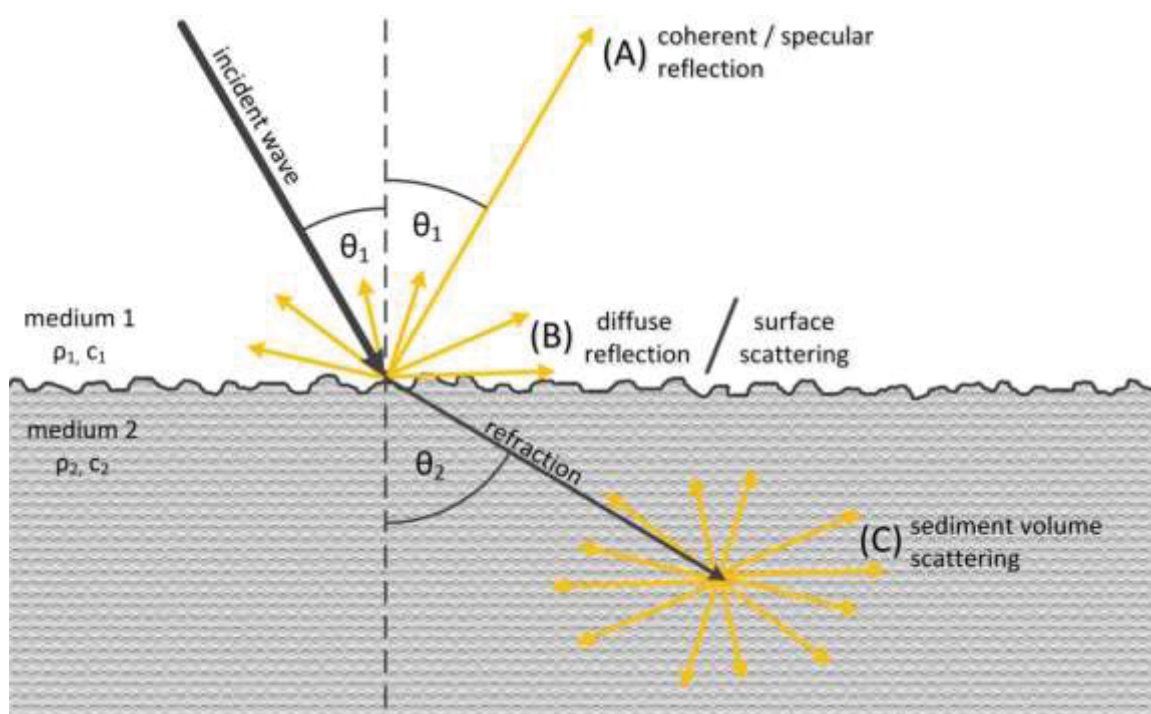


Figure 2-18: Refraction, reflection and scattering due to the interaction of sound with the sediment.

1984).

The ratio between diffuse and specular reflection depends on the roughness of the interface. The rougher a surface, the higher is the scattered fraction. For a correct understanding of the term *roughness* it is important to set the spatial irregularities of a surface in relation to the wave length λ . A rough surface for the 200 kHz frequency can look plane in terms of the reflection of a 38 kHz sound wave (Lurton, 2010, 476–477).

Scattering inside the sediment

Scattering does not only occur on surfaces of impedance irregularities, but also inside the sediment. Thus, the sediment volume scattering depends on sediment roughness and heterogeneities inside the sediment. Stones and shells which are buried in the sediment or free gas forming bubbles in sediment scatter the sound wave and hence the energy which is penetrating the sediment (Figure 2-18, C). Sediment volume backscattering can contribute significantly to global backscattering strength (Orlowski, 1984; Lurton, 2010, 98–101).

2.3.4 Acoustic Bottom Classification

Based on the physical circumstances echo sounding systems are able to obtain information about the seabed (bottom) acoustic *hardness* (acoustic reflection coefficient) and acoustic *roughness* (backscatter coefficient) since this information is encoded in the echo signal. This information can be analyzed and helps to detect e.g. suitable routes for communication cables, benthic habitats like coral reefs and sea weed populations or gas bubbles bound in the sediment (Hamilton, 2001).

Concerning sediment classification, model-based methods and empirical methods can be distinguished. Model-based approaches run on a higher complexity level and require much data based knowledge. Nevertheless, they have the advantage that they directly calculate physical properties of sediment from echo signals. In comparison, empirical methods are easy to implement. They are based on the correlation between echo features such as echo shape or echo energy and sediment properties (Hamilton, 2001; Amiri-Simkooei et al., 2011).

For empirical approaches it is essential to recover physical samples of the lakebed. The direct match of digital signal features and the corresponding lakebed samples is called “*ground truthing*”. The results of sediment classification are in most cases only valid for the equipment used and are hard to transfer to other hardware configurations (Hamilton, 2001). Two empirical methods, often implemented in commercial classification software, are the “first echo division method” (implemented in QTC View, BioSonics VBT Seabed Classifier)

and the “first/second bottom ratio method” (implemented in BioSonics VBT Seabed Classifier, Roxann, Echoplus) (Hamilton et al., 1999). The classification and characterization of sediments within this work are also based on these methods. After an explanation of bottom ensonification the mentioned methods will be explained.

Phases of Bottom ensonification

The principle of “bottom ensonification phases” is essential for the understanding of these methods. Due to its wave front curvature each ping ensonifies the lakebed in different phases resulting in phase-specific reflection shapes and areas (Figure 2-19). These phases can be distinguished by the time which has passed after entering the bottom. The first phase “*attack*” begins, when the pulse reaches the ground. During this phase the ensonified area has the shape of a circle whose diameter is increasing with time. After the duration of exactly one pulse length (1τ [ms]), the back slope of the pulse reaches the lakebed and the second phase “*decay*” starts. From the center of the circle a hole with increasing diameter is formed. As a consequence the ensonified area has the shape of an annulus whose diameter also increases with time. The third phase begins when the front of the pulse reaches the boundaries of the ideal beam pattern. At this moment the annulus stops growing and becomes thinner from the middle. This phase lasts until the pulse has completely entered the bottom and the annulus has disappeared (Hamilton, 2001; Burczynski, 1999). Therefore the third phase is named “release phase”.

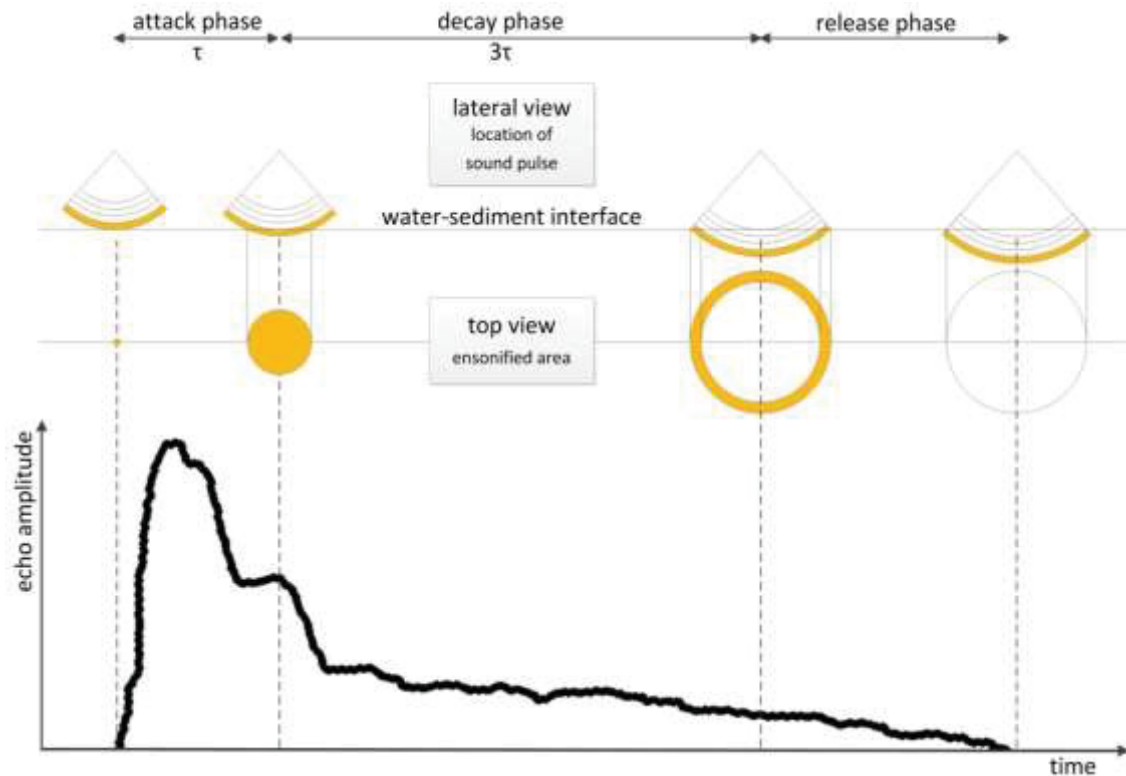


Figure 2-19: Interaction of a ping with the lakebed - The three phases of bottom ensonification depending on the position of the sound pulse inside the sediment (lateral view) with the resulting shapes of the ensonified areas reflecting from the bottom (top view).

First echo division method and first/second bottom ratio method

According to the distinguished phases during the penetration of the lakebed by a sound wave, the shape of an echo can be divided into three parts (Figure 2-20). The first part complies with the attack phase (duration: one pulse length from the point of bottom detection) and the second with the decay phase (duration: three pulse lengths from the end of attack phase). The last part of the echo is called release phase. It is not used for classification.

The section of the echo, which is created during the attack phase, is mainly caused by surface reverberation (reflection). The energy of this part of the echo ($E1'$) can be used as a measure for acoustic hardness or reflectivity. The detection of this part is very sensitive to the pitch and roll movement of the survey vessel. The section of the echo which is created during the decay phase is caused by both, surface and volume reverberation (scattering). As scattering depends on bottom roughness, the energy of this part of the echo ($E1$) is generally described as acoustic roughness (Figure 2-20). The energy of the attack ($E1'$) and decay phase ($E1$) is estimated by the integration of the bottom echo amplitude squared

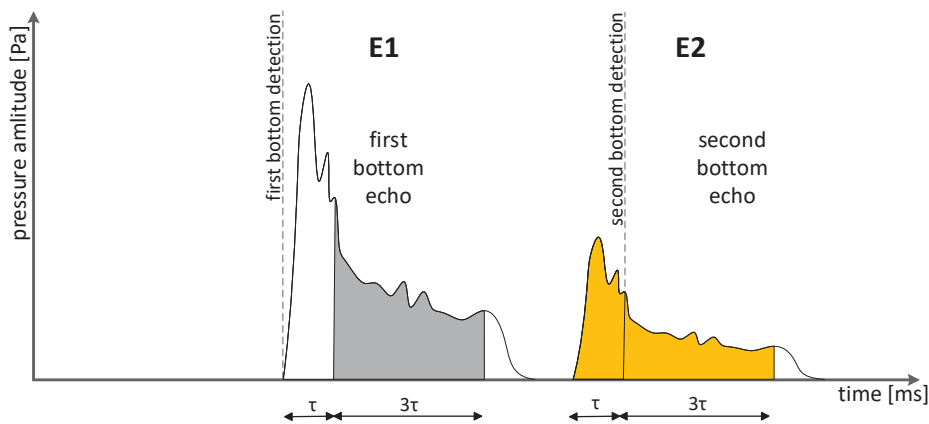


Figure 2-20: Exemplary acoustic wave showing the integrated areas of the wave signature for the “First / second bottom ratio method”; the first part is the attack phase, the second the decay phase and last part of the echo is called the release phase

(Voulgaris & Collins, 1990; Burczynski, 1999; Balk et al., 2011).

The principle of the *first/second bottom ratio method* (Figure 2-20) which was developed by Orlowski, 1984) is quite similar to the one of the *first echo division method* (Figure 2-21).

The second part of the first echo ($E1$) as a measure for sediment roughness is defined in the same way as in the *first echo division method*. In contrast, the whole energy of the second bottom echo ($E2$) is used as a measure for bottom hardness or rather reflectivity.

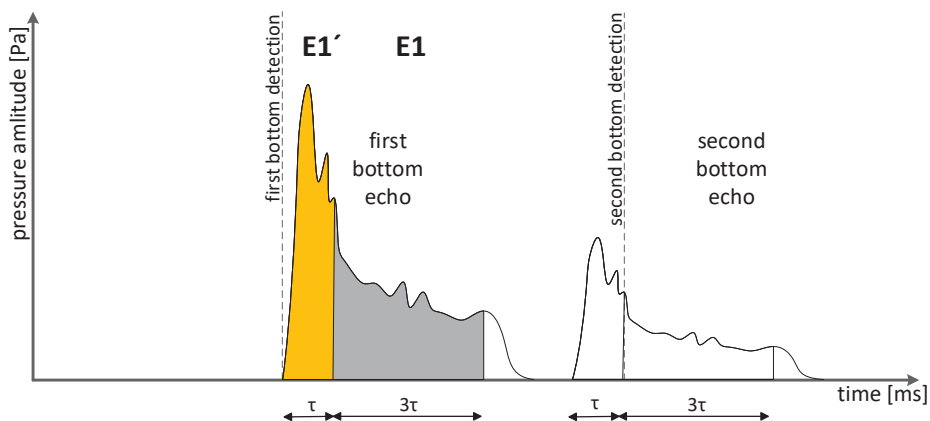


Figure 2-21: Exemplary acoustic wave showing the integrated areas of the wave signature for the “First echo division method”.

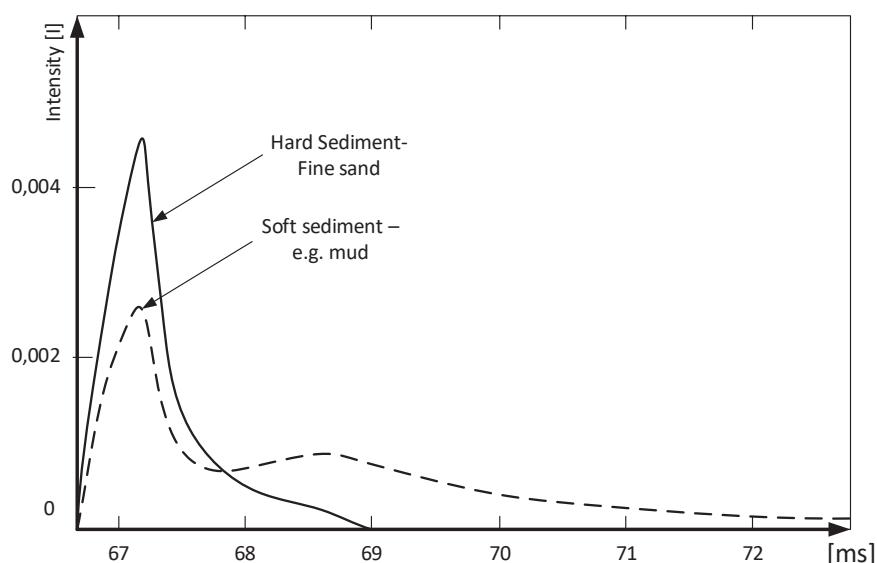


Figure 2-22: Simulated echo shapes of hard and soft sediment; modified after Burczynski (1999)

This value can be diminished in the case of high roughness (Burczynski 1999).

Although $E1'$, $E1$ and $E2$ are referred to sediment hardness and roughness respectively, it must be considered that those parameters are only acoustic values resulting from the interaction of a penetrating sound wave with bottom. In this respect it is only a simplifying basic assumption that flat hard sediments cause strong specular reflection, while soft or rough sediments are responsible for intense scattering. Figure 2-22 shows exemplarily simulated echo shapes for soft and hard sediment. The signature of a homogeneous relatively hard sediment (in this case fine sand) shows, that most of the energy is reflected within a first high intensity peak. The echo of the soft sediment is characterized by a low first peak and a longer lasting reverberation, indicating that the pulse is able to penetrate the sediment leading to scattering in the deeper parts of the lakebed.

Influence of depth

The basic assumption for the division of the echoes for bottom classification is, that pulse-returns during attack and decay phase originate from reverberation at the surface or within the sediment. It can be assumed that most contributions to the echo energy of the attack phase originate from specular reflection and surface scattering and those during the decay phase are due to sediment volume backscattering.

This assumption is correct, as long as the beam footprint and the pulse footprint have the same extent. However, this is the case for one distinct distance between the transducer and

the bottom (Figure 2-23, situation 2) depending on the pulse length and the beam angle. In shallower water the pulse footprint is larger than the beam footprint (beam limited regime, Figure 2-23, situation 1), whereas in deeper water the beam footprint is larger (pulse-limited regime, Figure 2-23, situation 3).

If the regime is pulse-limited, in the case of deeper water, the edges of the beam footprint are only ensonified during decay phase, causing that specular reflection and surface scattering from this expanse (forming an annulus) contribute to $E1$, while it would be normally contributing to $E1'$ during situation 2. This leads to an oversampling of the decay phase. Whereas, the contrary appears, if the regime is beam-limited. In this case, during the attack phase there is sediment volume scattering even from the edges of the beam footprint. However, as depth increases, the ensonification of the peripheric regions of the beam footprint delays progressively. As a consequence of this the return of this region retards as well, resulting in a dilation of the echo shape. (Hamilton, 2001; Lurton, 2010, 329–332)

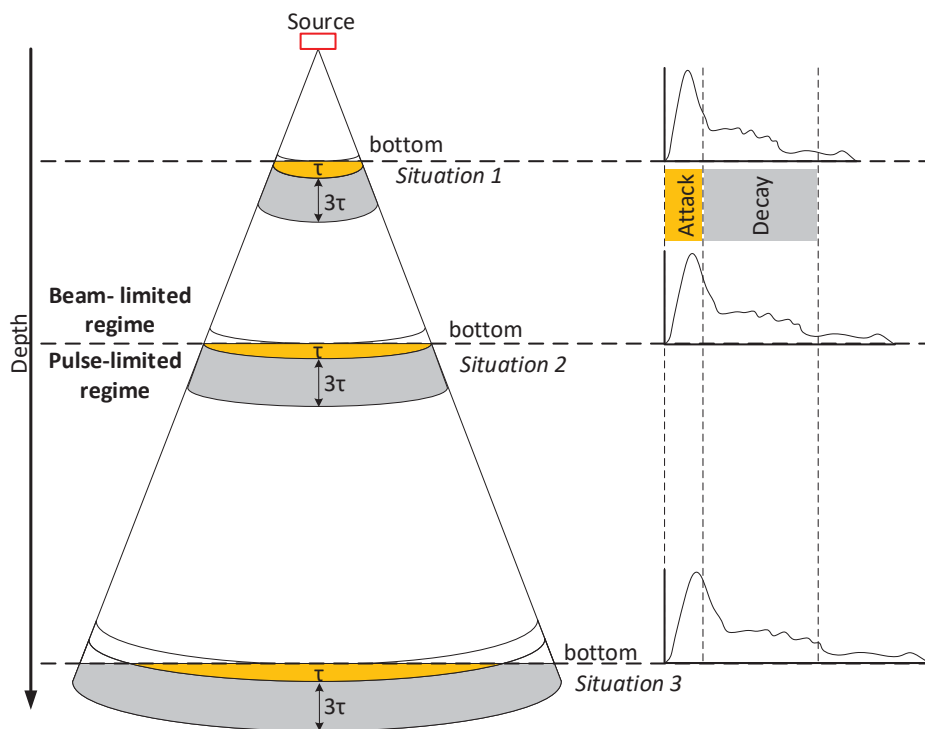


Figure 2-23: Influence of depth on the division of the acoustic wave signature into the attack and decay phase.

2.3.5 Acoustic Bubble Detection

The general advantage of hydro-acoustic remote sensing technologies is the ability to scan relatively large areas and acquire data from extensive water and sediment volumes at the same time. Since the detection of gas bubbles can be parallelly performed, echo sounding is a relatively time- and cost-effective technique (Ostrovsky, 2003; DeISontro et al., 2011). Therefore, these methods represent valuable alternatives for standard point measurements during the detection of methane stored in the sediment or the quantification of bubbles rising to the surface (Ostrovsky et al., 2008). This chapter will support the basic understanding for the hydro-acoustic detection of bubbles in the water column. Moreover it will describe possible approaches for the detection of free gas in the sediment.

2.3.5.1 Bubbles in the water column

The hydro-acoustic detection of bubbles in the water column seems to be a promising extension of options to gas traps and video or photo detection, since those are only suitable for restricted areas.

Gas bubbles and the swim bladders of fishes can be detected by the echo sounder because of their large density difference compared to water (Figure 2-24).

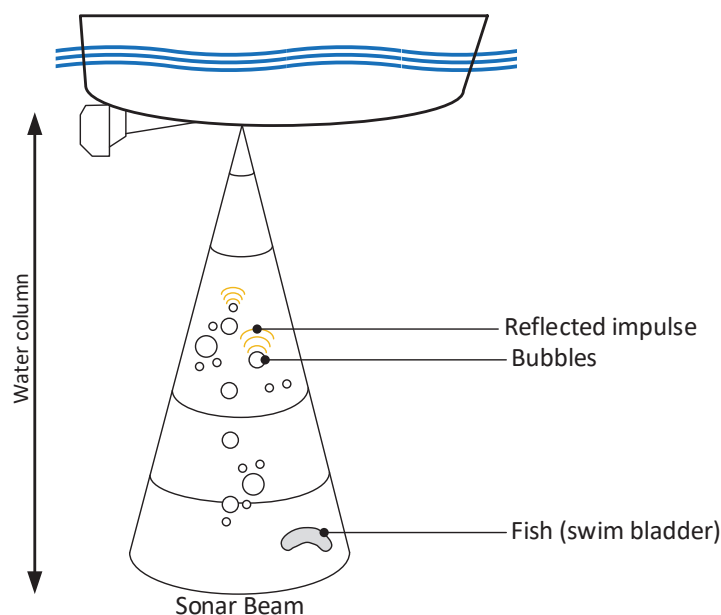


Figure 2-24: Principal scheme of hydro-acoustic bubble detection in the water column

Gas bubbles are strong scatterers of acoustic energy (Vagle & Farmer, 1992). By applying a suitable parameter setting of the echo sounder, even the exact quantification of bubbles (targets) and their characteristics like size and volume is possible (Ostrovsky, 2003, Ostrovsky, 2009a). Ostrovsky et al. (2008) published the empiric relation between σ_{bs} (backscattering cross section in m^2) and the volume of the bubbles V (in ml). It can be described by a logarithmic equation Eq. 27 or alternatively by Eq. 28. This equation is valid for a bubble volume range from 0.005 to 20 ml. This range covers nearly all naturally occurring bubble sizes in reservoirs, since methane bubbles from soft muddy sediments normally vary between 0.1 ml and 0.38 ml respectively an equivalent radius of (r_{eq}) 1.3 mm to 4.5 mm (McGinnis et al., 2006; Ostrovsky et al., 2008).

$$\log(\sigma_{bs}) = (0.745 \pm 0.013) \log(V) - (4.467 \pm 0.016) \quad \text{Eq. 27}$$

$$\sigma_{bs} = 3.409 \cdot 10^{-5} V^{0.745 \pm 0.013} \quad \text{Eq. 28}$$

The equation can also be expressed as:

The target strength (TS) is proportional to the volumes of the bubbles. It can be calculated by:

$$TS = 10 \log(\sigma_{bs}) = 7.45 \log(V) - 44.67 \quad \text{Eq. 29}$$

Even smallest bubbles, which could be expected during surveys in reservoirs with soft sediment, are larger than the maximum size for resonance considering the two relevant frequencies 38 and 200 kHz. Hence, those bubbles cannot resonate at the chosen sonar frequencies and thus Eq. 27 – Eq. 29 are valid for the entire water column. Very small bubbles of around 0.005 ml will have a TS of ca. -66 dB while bubbles with a volume of 10 ml cause strong reflection with TS ranges around -36 dB (Ostrovsky et al., 2008).

However, the difference in backscattering between gas bubbles and fish bladders is very small and thus causes problems distinguishing them. Thus, the certain recognition and quantification of gas bubbles in the water column are more difficult (Ostrovsky et al., 2008). Nevertheless, some differences are noticeable: 1) bubbles rise vertically to the surface whereas fish generally leave almost horizontal tracks (Ostrovsky, 2009a, Ostrovsky, 2009b)

and 2) the mean target strength of gas bubbles is weaker than the TS of swim bladders. Due to the average volume of bubbles ($r_{eq} = \text{ca. } 2.85 \text{ mm}$; 0.01 ml) they can be distinguished from fish which have swim bladders with much larger volumes. Whereas targets with a stronger signal than -44 dB usually are fish, targets with a TS from -66 to -50 dB typically are bubbles (Ostrovsky, 2009a). It has to be noted that the higher the volume of the bubble the flatter the shape and hence less spherical the bubble will be. This can be explained with the changing ratio of surface tension versus the mechanical stress from the rise. In small bubbles the surface tension dominates, but becomes weaker the larger the bubble is. Therefore, this allometry of bubbles limits the proportional relation of r_{eq} and σ_{bs} to the named range ($0.005 - 20 \text{ ml}$).

2.3.5.2 Bubbles in the sediment

While bubbles in the water column can normally be detected as single targets the bubbles in the sediment can only be detected as collectives or layers.

Coarse sediments like gravel and sand have only a very limited bubble holding capacity. Due to low cohesion between the particles as well as relatively big pore spaces and hence a high number of preferential ways for bubbles to leave the sediment (Ostrovsky et al., 2008), they lack the capacity of producing relevant volumes of accumulated gas. In addition, coarse sediments tend to have low shares of bio-available organic carbon and hence are mainly unimportant for the formation of GHGs. Consequently, coarse sediment ($> 2 \text{ mm}$ diameter) is not considered further this work.

Consequently, the focus of the detection of bubbles in the sediment lies on soft muddy and organic rich sediments. They have the bio-chemical capacity to produce relevant amounts of

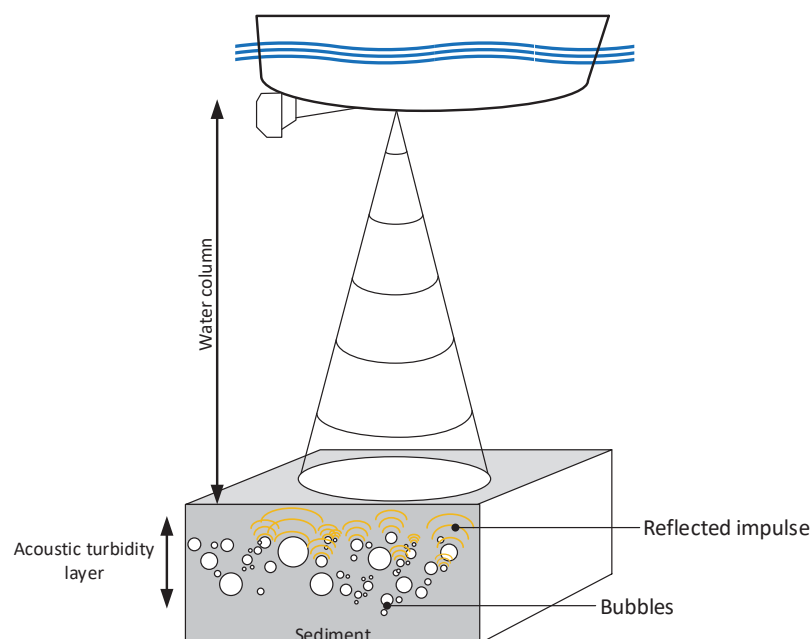


Figure 2-25: Scheme of sound reflection at the acoustic turbidity layer.

gases and also sufficient cohesion to capture the formed bubbles. The collective of bubbles in the sediment appears like a so-called “*acoustic turbidity layer*” (Figure 2-25).

Since the detection of single bubbles is not possible, the general attenuation of the sediment volume of one area has to be related to ground truthing sediment samples (Lyons, 1996), leading to a seabed classification (SBC) process. The context of sediment features and hydro-acoustic behavior is explained in the following.

The overall reflection of an ensonified compact sediment volume is stronger than the reflection from soft sediment. High intensities of reflected signals are caused by strong acoustic impedance contrasts. The contrast is derived from the impedance of both media, here water and sediment (Eq. 30). The stronger the impedance contrast between two media, the higher the reflected part. For normal incidence ($\theta_1 = 0$), which is mostly given in single beam echo sounding applications, the reflection coefficient V can be calculated as follows (Eq. 31) (Lurton, 2010, 80–82).

$$\text{acoustic impedance } Z = \rho \cdot c \quad [kg \ m^{-2} s^{-1}] \quad \text{Eq. 30}$$

$$\text{reflection coefficient } V = \frac{Z_2 - Z_1}{Z_2 + Z_1} = \frac{\rho_2 c_2 - \rho_1 c_1}{\rho_2 c_2 + \rho_1 c_1} \quad \text{Eq. 31}$$

A strong reflection leads to less attenuation and therefore to higher dB values measured by the transducer. It can be expected that the $E1$ values are significantly higher from gas-bearing sediments compared to sediments with the same granulometric and chemical features without gas bubbles (Holland & Gerig, 2006). The $E1'$ value especially of the 200 kHz frequency (less sediment penetration) is likely to be less influenced by bubble occurrence in the sediment, since most bubbles are assumed to be found in deeper sediment layers (10 – 60 cm) due to increasing cohesion with sediment depth (Jain & Juanes, 2009).

2.4 Summary of the Fundamentals

The system reservoir

- Reservoirs are more complex biochemical reactors than natural lakes
- They trap most of the material entering the reservoir.
- The complexity of the shape strongly influences the sedimentation processes and the formation of internal gradients.
- Sediment deposition also depends on flow velocities, which establish vertical transportation gradients.
- The trophic state of a water body directly influences the available amount of organic matter and hence sedimentation processes.
- The burial efficiency plays a major role for the accumulation of organic matter in the sediment. Stratified reservoirs tend to have higher burial efficiencies than mixed ones.
- The profundal acts as a permanent sink for sediments and consequently represents a potential zone of methane production.

Greenhouse gases in reservoirs

- Methane formation only takes place in the sediment, under the absence of oxygen or oxygen donors.
- The SWI creates steep gradients of oxygen concentrations within the range of millimeters.
- The availability of organic substrate determines the productivity of the methane producing archaea. Higher sedimentation rates lead to increased methane production.
- The correct quantification of diffuse fluxes to the atmosphere is still challenging and often limited to small areas.
- Ebullition is found to be the major pathway of GHG directly leaving the reservoir. The ebullitive emissions feature high spatial and temporal heterogeneities.
- Fine grained sediments are capable of producing large-sized bubbles, while coarse materials can only hold small bubble volumes. The moment and the amount of ebullition depends on changes of the hydro-static pressure.
- The larger the size of a rising bubble, the more gas is transported to the surface. Bubbles from deeper areas suffer increased re-diffusion, hence less methane reaches the surface.

Hydro-acoustic fundamentals

- The resolution of an echo sounder depends on the frequency and the pulse length. Higher frequencies and shorter pulse lengths reach better resolutions.
- Lower frequencies are able to penetrate sediment deeper. The penetration depth of the sound wave depends on the attenuation of the sediment volume.
- Objects or boundaries, which cause a strong impedance contrast cause intense echoes and are therefore easy detectable. Homogeneous sediment volumes produce less attenuation.
- Hydro-acoustic waves can be used for the detection and classification of sediment types. Each echo can be divided in distinct phases. The integration of the intensity of each phase (attack or decay) can be correlated with features of the sediment.
- Due to the low density of gas, bubbles have a strong influence on the hydro-acoustic behavior of sediment volumes, hence they can be detected.
- Likewise, bubbles in the water column are strong scatterers. The number, rising velocity and size can be detected.

3 Investigation Area

This chapter presents geographic, environmental and technical background information of the two investigated reservoirs.

All four measurement campaigns of this study were carried out in the south east of Brazil. The first two in Vossoroça Reservoir took place in March 2011 and November–December 2011. The field campaigns in Capivari Reservoir were conducted afterwards in November–December 2012 and March 2013. According to the Köppen-Geiger climate classification, both reservoirs belong to a region which is classified as *Cfa*: C, temperate climate ($T_{hot} > 10^{\circ}\text{C}$ & $0^{\circ}\text{C} < T_{cold} < 18^{\circ}\text{C}$); f, without dry season and with a, hot summer ($T_{hot} > 22^{\circ}\text{C}$) (Peel et al., 2007).

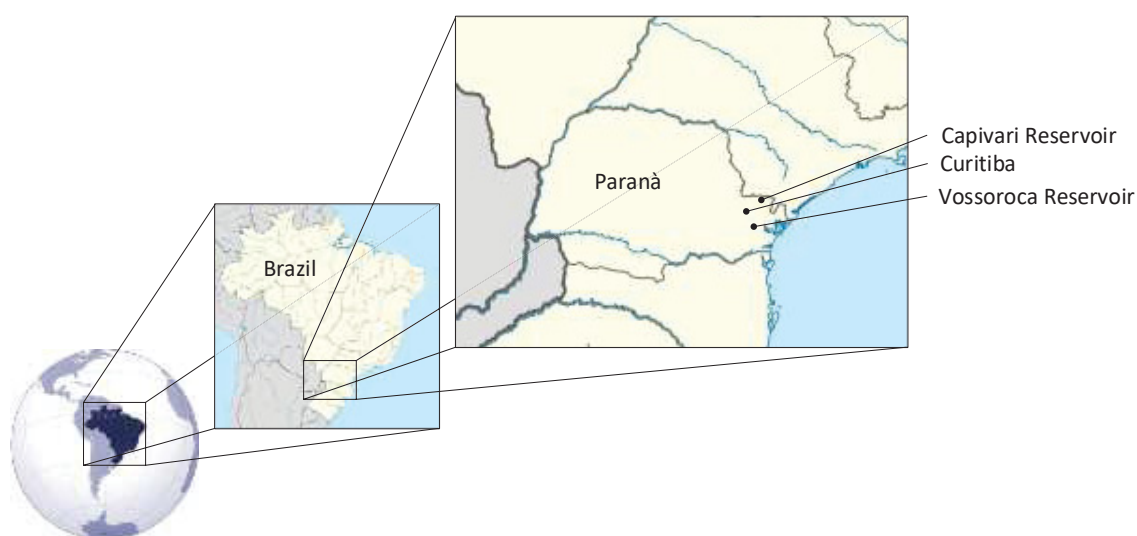


Figure 3-1: Geographic localization of the reservoirs.

3.1 Vossoroça Reservoir (VR)

The Vossoroça reservoir is located in the state of Paraná, approximately 50 km southeast of the city of Curitiba in the “Serra do Mar” mountain range at approximately 833 masl. The climate is subtropical with monthly average temperatures between 13°C in June and 21°C in February. The annual rainfall is about 1,900 mm, the climate is subtropical.

The reservoir which covers an area of about 5 km^2 and has a capacity of $33.6 \times 10^6 \text{ m}^3$ (Republic of Brazil, 1969) was created in 1940 to regulate the water flow in the hydroelectric power plant Chaminé located 7 km downstream. It is fed by various small streams and rivers whereby the largest of which is Rio João with an average discharge of $3.5 \text{ m}^3 \text{ s}^{-1}$. The average water depth is about 8 m, the maximum depth is about 17 m. The catchment area of

the reservoir has a size of 151 km² (Republic of Brazil, 1969) and is predominantly rural. The immediate surrounding area of the reservoir is used for recreation and is mostly covered with Atlantic forest including the native Paraná pine tree (*Araucaria angustifolia*). The upstream area of the catchment is mainly used by agriculture. Major parts of the reservoir are under protection since it belongs to the environmental protection area of Guaratuba.

A summary of the basic data of Vossorooca reservoir is listed in Table 3-1.



Figure 3-2: Topographic map of the Vossorooca reservoir at maximum water level.

3.2 Capivari Reservoir (CR)

Capivari reservoir is located 40 km northeast of the state capital Curitiba at a latitude of about 2°S of the tropic of Capricorn (Figure 3-3). To the east the water body verges on the Serra do Mar mountain range that separates it geographically from the Atlantic Ocean that is about 80 km away. The reservoir was constructed in 1970 for the operation of the Governador Parigot de Souza Hydroelectric Power Station (Borges et al., 2008) The surface covers now an area of 13.1 km² at an altitude of 788 masl. Its average depth is calculated at 13.6 m while the deepest parts reach 45 m during maximum water level. With a volume of 178 Mm³ and a medium flow of 19.4 m³ s⁻¹ the detention time is around 107 d. The main contributor to the surface inflow is the Capivari River with a share of around 90%, Tapera River and Rio dos Patos contribute with small shares. Receiving water is the Cachoeira River on the eastern side of the Serra do Mar, from where the water flows into the ocean (Materon B. & Maurer E., 1979). A summary of morphometric data of Capivari reservoir is listed in Table 3-1.

The climate is comparable to the situation in Vossoroça. On average annual precipitation amounts to 1,400 mm, with high quantities of rainfall year-round (Peel et al., 2007). The natural vegetation in the rural catchment area of around 1,200 km² consists of Atlantic rainforest.

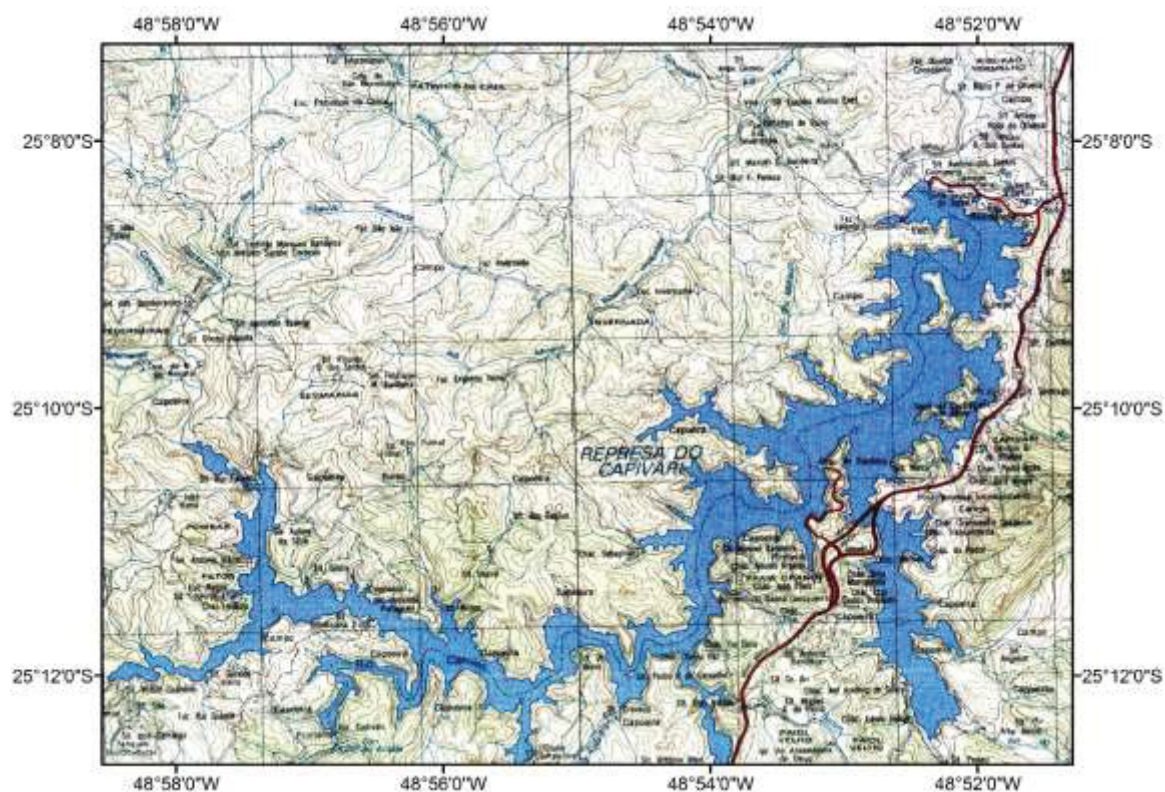


Figure 3-3: Topographic map of the Capivari reservoir, the surface is shown for maximum water level.

Table 3-1: Morphometry of Capivari and Vossoroca reservoir.

Characteristic	Capivari Reservoir	Vossoroca Reservoir
Maximum length	18 km	5.9 km
Maximum width	1.3 km	1 km
Average width	Ca. 0.45 km	Ca. 0.25 km
Maximum depth	45 m	17 m
Average depth	13.6	8 m
Surface area	13.1 km ²	5 km ²
Volume	178 x 10 ⁶ m ³	33.6 x 10 ⁶ m ³
Mean residence time	107 days	110 days
Catchment size	1,200 km ²	151 km ²
Complexity	10.2	11.5
Age	44 a	74 a

4 Materials and Methods

This chapter outlines the survey approach by presenting the equipment used, the measurement techniques and the processing steps of the conducted survey. Important processes, configurations and data treatment steps are explained in detail. Since a variety of measurement techniques were used to produce the results presented in this work, especially the overview figures should help to enhance the comprehension of the investigation procedures.

First the sampling strategy is described, followed by the different measurement approaches.

4.1 Sampling Strategy

This section explains the general approach and basic ideas of the strategy behind the sampling done in this work.

The sampling strategy was elaborated based on the objective definition of this work (chapter 1.5). To develop a systematic approach for an extensive investigation of the GHG production and related parameters in a reservoir, hydro-acoustic methods are combined with physico-chemical sediment parameters and gas measurements. Next to the correlation of acoustic with granulometric and chemical sediment features their spatial distribution and therefore the recognition of patterns within the reservoir is investigated. Here, the methodological approach of the combination of point measurements with spatial surveys constitutes the central procedure.

Figure 4-1 shows the general procedure of data treatment. Point measurements were carried out including all measurement types. Next, the results were statistically analyzed in order to

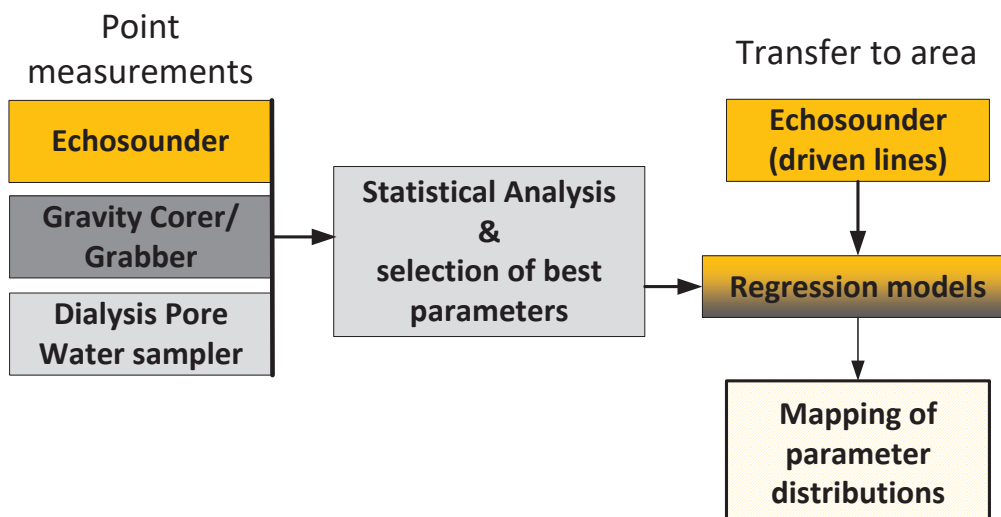


Figure 4-1: Scheme of the overall measurement and data processing procedure.

find potential relations and including all measured parameters. While the granulometric sediment parameters are used as the reference for acoustic ground truthing, further investigations for the detection of correlations were carried out. A selection of promising correlations were used to be transposed from point information to areal information (driven survey). Based on the echo sounding results of the entire reservoir and the correlation terms, the particular sediment features can be transferred into spatial maps. In combination with analyzed morphological features and detected sediment thickness distribution in the reservoir, conclusions can be drawn in regards to the allocation of GHG production.

The data surveys and measurements were separated in two phases. Each phase again was parted in two field campaigns.

In the first phase, sediment sampling- and hydro-acoustic methods have been tested in two campaigns on the Vossoroca Reservoir (VR). Results were analyzed and used for method adaption and improvement (Figure 4-2).

To improve the data density and also the feasibility of the survey the point sampling during phase one was focused on the western arm and the central part of the reservoir (Figure 4-19). These two parts were assumed to be representative for the entire reservoir.

In a second phase during two campaigns a detailed investigation of the Capivari Reservoir was conducted. Data from VR serves for comparison and as additional input data for e.g. correlations, as the general conditions (climate, land use in the catchment, altitude, geologic background, etc.) and reservoir characteristics are directly comparable (see chapter 3).

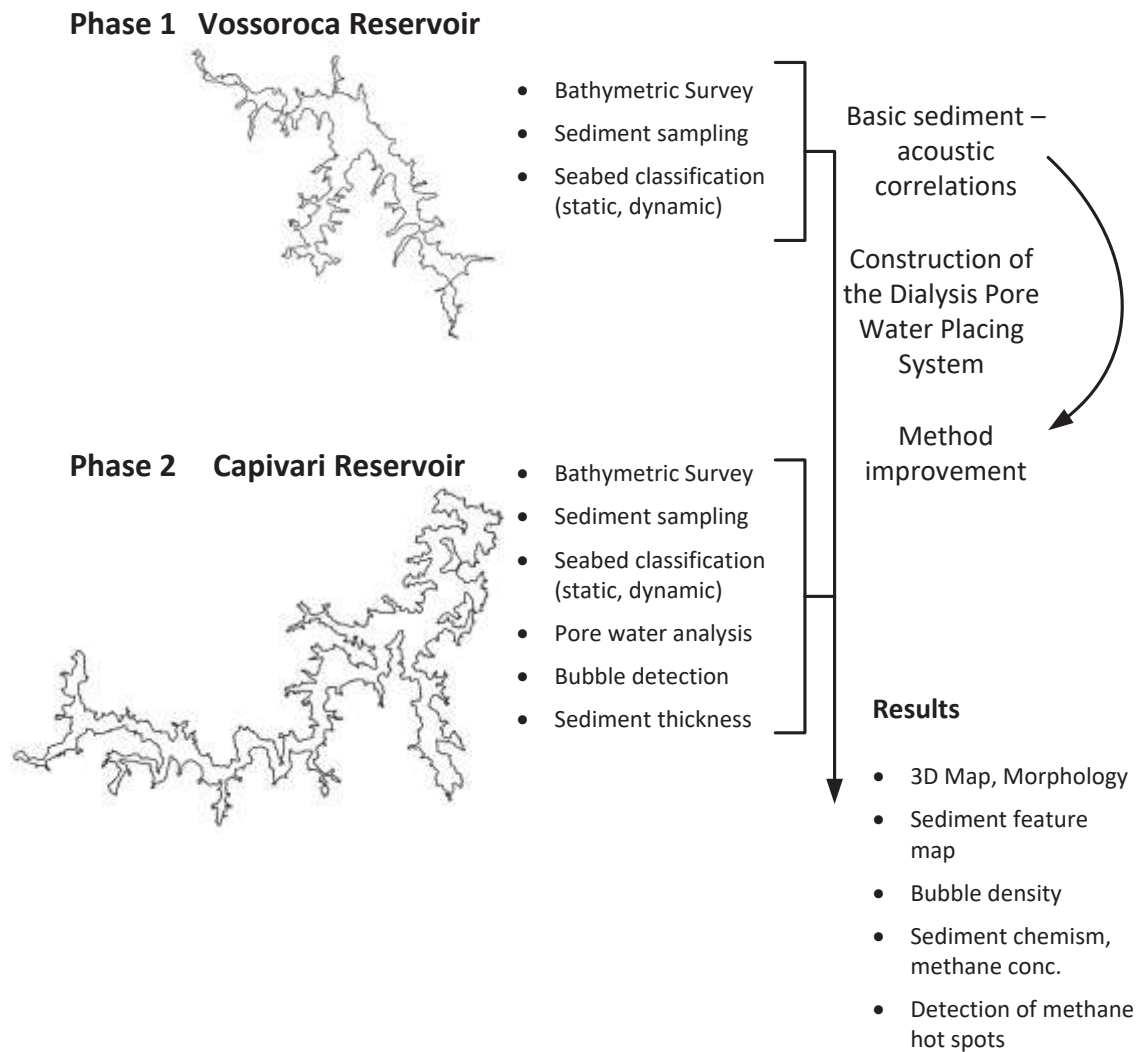


Figure 4-2: Overview of the principle measurement steps, order and results; SBC.

Hydro-acoustic Measurement Strategy

The followed approach for the hydro-acoustic measurements is a combination of static and dynamic surveys.

The water column and the sediment were scanned with the echo sounder while the vessel was either fixed to one position (sediment sampling sites) or while the boat was driving along the transect lines. In both reservoirs the bathymetric survey was carried out for the entire lake except for the very shallow parts (less than 1.50 m). In those parts no proper echo signal could be received and the risk of running aground was too high.

The sediment was sampled at the exact same positions as where the static measurements were carried out to assure that the sediment samples were taken within the footprint of the echo sounder beam in order to substantiate the relation between echo sounding results and the obtained sediment parameters. Static measurements also feature the advantage that sounding errors caused by boat motion or cavitation (bubbles under the transducer) can be avoided. Therefore, these results represent a basis for later verification for the outcomes of the dynamic measurements.

At each point a sequence of transducer configurations (pulse length, power input) was used during the ensonification phases. Hence, a range of different sampling parameters is available for the seabed classification (SBC) and further analysis. Details of the hydro-acoustic data acquisition for both reservoirs are explained in chapter 4.2.

Sediment sampling strategy

Since it is not possible to conduct physical spatial sediment sampling, the general approach of characterizing sediments in water bodies is limited to point measurements.

Sediment samples were recovered using a van Veen sampler (US Environmental Protection Agency (EPA), 2001) and a Mondsee Corer (Niederreiter, 2012). In this context the quality for hydro-acoustic ground truthing using grab samples compared to core samples was assessed.

In this work the sediment characteristics and parameters serve as a link between the hydro-acoustic parameters and estimated methane production. To obtain the best possible results, a wide range of different sediment parameters was measured.

The parameters can be classified in two groups:

- The first group represents the parameters which can be directly related to hydro-acoustic behavior of the sediment, including granulometry, bulk density and gas concentration.

- The second group includes the sediment parameters which can only indirectly be related to the acoustic response of ensonification. Those parameters are the content of total iron [g kg^{-1}], total Mn [mg kg^{-1}], Loss on ignition (LOI) [%], total Sulfur [%] and total Carbon (TC) [%] in the solid phase of the sediment. The analysis of these parameters aims on the assessment of geo-biochemical conditions in the reservoir causing distinct reflectivity patterns of the sediment, which can be correlated to the hydro-acoustic signals and thus being transferred to the entire reservoir.

In addition to this, the pore water was investigated taking into account the following parameters: dissolved CO_2 , N_2O , CH_4 , O_2 , NO_3^- , NO_2^- , SO_4^{2-} and F^- in mg l^{-1} . The survey of pore water concentrations in in-situ situations in relatively deep reservoirs is generally limited to the use of divers or Autonomous Underwater Vehicles (AUVs). These procedures are time demanding and produce high costs. Therefore, a new instrument for the placement and recovery of Dialysis Pore water Sampling devices (DPS's) was developed and constructed (chapter 4.3.2.1). The Dialysis Pore water Sampler Placing System (DPS-PS) was successfully tested in CR. The results are included in this work.

4.2 Hydro-acoustic Survey

In this chapter the equipment used during the surveys, the different methodological approaches as well as the data processing steps are explained. The detection of seabed features is separated in the *fixed position acquisition* and the *dynamic seabed classification*. Furthermore, the determination of the sediment thickness and the detection of gas bubbles are described.

4.2.1 Equipment – EA 400 Single Beam hydrographic Echo Sounder

This section explains the basic setup of the hydro-acoustic equipment during all surveys conducted for this work.

Mounted on a five meter class aluminum vessel the transducer of the echo sounder was installed star board looking down with an incidence angle of 0° . The transducer was fixed on a steel frame to ensure maximum stability against the resistance in the water and also to minimize natural vibration. To avoid that the sound waves from the transducer interfere with bubbles from cavitation or the vessel hull, the draught was set to 68 cm. The draught value was included in the EA 400 processing software to produce correct depth values. To minimize the difference between the transducer and GPS position and to receive a better signal due to a higher receiving position of the antenna, the GPS receiver was mounted close to the transducer on a 2 m pole. Figure 4-3 shows the setup from a lateral perspective and

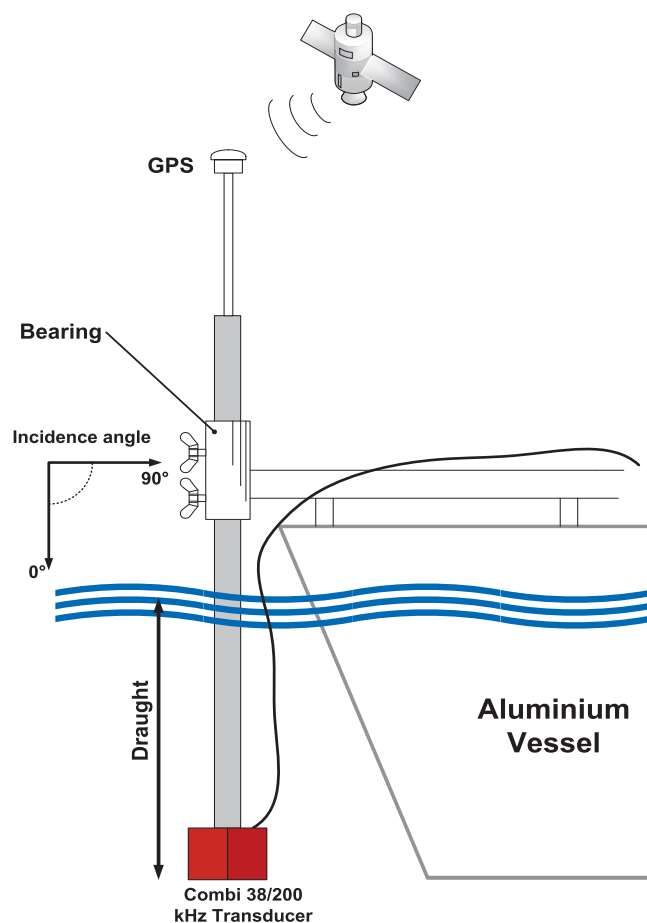


Figure 4-3: Lateral view of the onboard echo sounder setup.

Figure 4-4 a picture of the mounted equipment from the front.

During this work the transducer was exclusively used in the downward alignment. Both possible frequencies were used for vertical scanning. While the 200 kHz frequency has an opening angle of 7° in longitudinal and transverse direction forming a symmetric beam lobe (see Appendix A.2), the 38 kHz frequency beam opens 13° in longitudinal and 21° in transversal direction forming a asymmetric beam lobe (see Appendix A.2). The transceiver is able to produce impulses with a power input from 100 W to 1000 W and pulse lengths (τ) from 0.256 to 2.048 ms for the 38 kHz frequency and 0.064 to 1.024 ms for the higher 200 kHz frequency. The used configurations during the different surveys are listed in Table 4-1 and Table 4-2.



Figure 4-4: The mounted EA 400 echo sounder on the aluminum vessel.

Table 4-1: Echo sounder configurations during phase 1 survey in VR.

		Frequency		Configuration			
		A	B	C	D		
Power input [W]		100	100	100	100		
Pulse length [ms]	38 kHz	0.256	0.512	0.256*	0.256*		
Pulse length [ms]	200 kHz	0.256	0.512	0.064	0.128*		

* Configuration was not applied to core 1 and core 2 in VR

Table 4-2: Echo sounder configurations during phase 2 survey in CR.

		Frequency		Configuration					
		A	B	C	D	E	F	G	H
Power input [W]		100	100	100	100	500	500	500	500
Pulse length [ms]	38 kHz	0.256	0.512	1.024	2.048	0.256	0.512	1.024	2.048
Pulse length [ms]	200 kHz	0.064	0.128	0.256	0.512	0.064	0.128	0.256	0.512

4.2.2 Bathymetry

“A common misconception is that the deepest areas of a lake are the best locations for sediment coring.” Eilers (2004)

The bathymetric survey was planned and conducted aiming on the creation of a depth map of both reservoirs (phase one and two). The resulting 3D-depth map does not only serve the purpose of the information of depth distribution within the reservoir, it represents the foundation for morphologic interpretation of the results, hydraulic calculations (not part of this work) and more detailed parameters like the inclination of slopes. Furthermore, it plays an important role during the determination of sampling locations for the placement of DPS and sediment coring or grab sampling.

The data and experiences from the first phase (VR) were assessed to improve the echo sounder configuration during phase two (CR). This was done to produce the best possible data base for the correlation of echo features with sediment parameters.

During the survey in phase one the ping rate was set to 15–20 pings s^{-1} which proved to be too high, since some interference with plankton or ringing effects in shallower areas were detected. The ping rate was reduced to 5–10 pings s^{-1} during phase two of the survey. Other echo sounding configurations were kept constant during the two surveys. Driving speed during the surveys varied between 1.2 and 1.8 $m s^{-1}$, leading to a resolution of 18–36 pings m^{-1} during phase one and 6–18 pings m^{-1} during phase two. In dangerous situations caused by tree logs or rocks in the water the vessel speed was reduced.

In regards to the echo sounder configuration, Poulain et al. (2011) published an optimal input power of 400 W and a pulse length of 0.512 ms for seabed classification.

In opposition to Poulain the configurations for the dynamic surveys in this work were chosen differently. The input power was set to 100 W and the pulse length for the 200 kHz frequency was set to 0.256 ms, while the 38 kHz frequency was emitting pulses of 0.512 ms length.

The input power was modified since the maximum estimated survey depth in both reservoirs was expected not to exceed the depth of 50 m. A power input of 400 W would have reduced the potential survey area to the parts of the reservoirs with a minimum depth of 5 m due to the saturation effect (Poulain et al., 2011). This would have led to a significantly reduced potential investigation area and therefore to reduced results. The settings refer to configuration B, in Table 4-1 and Table 4-2, chapter 4.2.1.

In addition the lower power input was expected to produce sufficiently strong impulses to gain echoes with a good signal to noise ratio. Furthermore, the daily measuring routine (up to 7 hours of measurement) could be performed using only one car battery for the echo

sounder and one for the peripheral equipment (notebook, other sensors) simplifying the survey operation. One crucial setting is the pulse length, which was chosen the same for the 38 kHz frequency since it is closer to the 70 kHz used during the survey conducted by Poulain. Hence, a basis for comparability is given.

Since the objective of this work is not only to perform a standard SBC but also to detect bubble occurrences in the sediment, the hydro-acoustic resolution plays a major role regarding the expected results. Accordingly, the pulse lengths of the 200 kHz frequency was chosen shorter to allow a better depth resolution in the echograms.

The survey raster was separated into two different parts. One part was driven close to the shore line of both reservoirs while the other route followed a zig-zag course (Figure 4-5 & Figure 4-6). The outer line was sailed to ensure the data acquisition even in the shallow parts which is often forgotten during comparable surveys. The zig-zag course was sailed to obtain the best possible result regarding spatial coverage. In narrow branches or winding parts of the reservoirs the course was adapted to the local situation. The EA400 software was set to save raw-data files every 100 mb and additionally *.xyz files with a time stamp and the depth information.

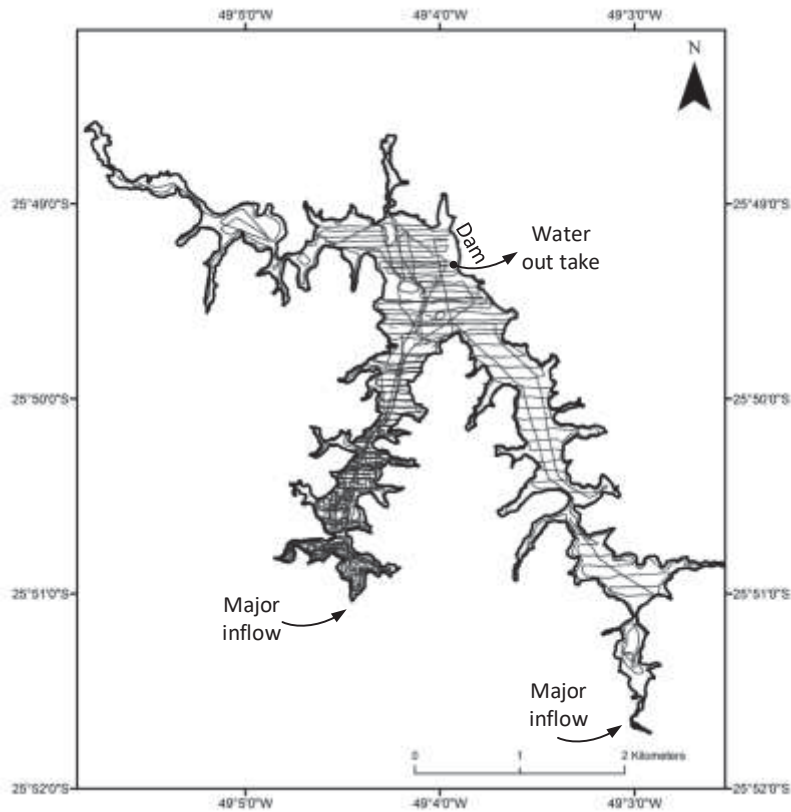


Figure 4-5: Survey route in VR depicted against longitude and latitude; gray lines represent the sailed path, the black line is the reservoir outline.

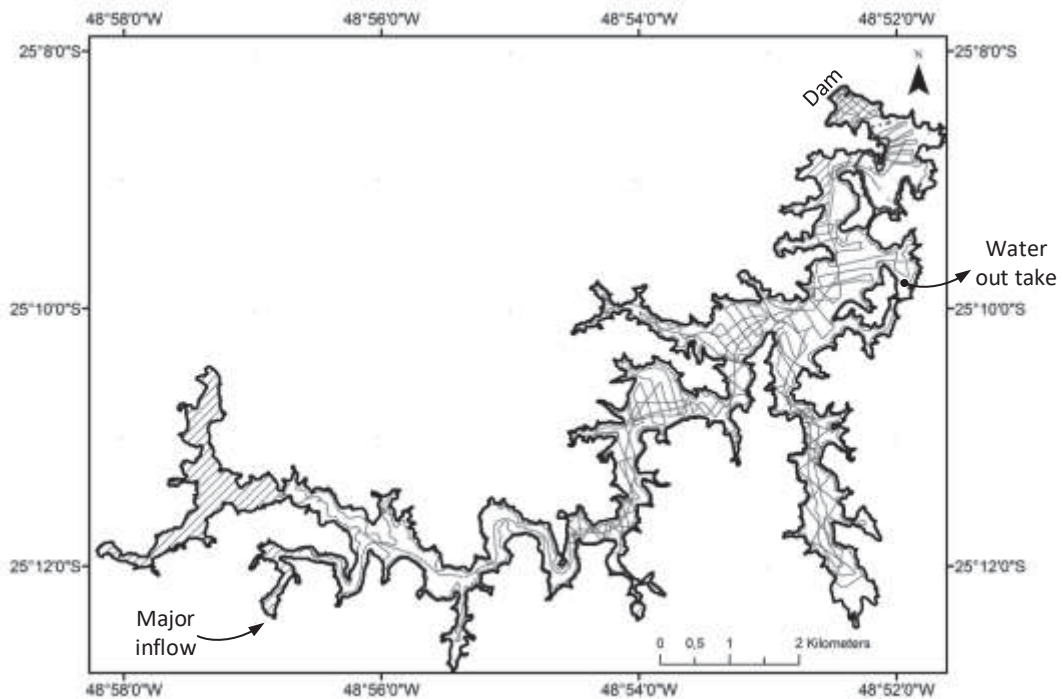


Figure 4-6: Survey route in CR depicted against longitude and latitude, gray lines represent the driven path, the black line is the reservoir outline; hatched areas were too shallow for measurement or the GPS signal was lost during survey.

Creation of the 3D models

After the correction of the bathymetric data (chapter 4.2.8) the two data sets were imported in ArcGIS 10.2 as multi point information. In several processing steps a regular raster was interpolated using Inverse Distance Weighting (IDW). This raster was processed to a contour data set which again was the basis for the Triangulated Network (TIN). Due to missing spatial high resolution data, the Reservoir outline was taken from satellite images (Google Earth). Image scenes were chosen where the water level was approximately the same as during the surveys.

4.2.3 Fixed Position Acquisitions (point measurements)

At all positions where sediment samples were planned to be taken, static hydro-acoustic measurements were conducted before the sediment was disturbed. Positions are presented in chapter 4.3.1 (Figure 4-19 & Figure 4-20).

After fixing the vessel to one position the bottom was ensonified. During ensonification phases all movement onboard was stopped to avoid a variation of the incidence angle due to shaking of the boat. Due to the fact that incidence angle variations on fine sediments have a limited effect on the backscatter strength, the impact from very small waves on the results can be neglected (Brouwer P., 2008).

Various combinations of pulse lengths and power inputs were used to cover and determine the best possible configurations considering the later SBC and bubble detection. In comparison to Poulain et al. (2011) the spectrum of combinations was significantly expanded. Used combinations of the configuration settings are given in Table 4-1 and Table 4-2. For each single configuration the sediment was ensonified for as much time as it was necessary to obtain a minimal number of 300 pings per configuration. Likewise with the dynamic survey all data was stored as *.raw files and *.xyz files.

4.2.4 Seabed Classification (SBC)

Seabed classification is the process of automatic or semi-automatic seabed type detection based on a number of training examples. The hydro-acoustic data alone cannot produce any added value to the spatial investigation of sediments in a reservoir. Therefore, the “*ground truthing*” is an inevitable presupposition for the interpretation of hydro-acoustic information. Based on the analysis of the sediment information in combination with the hydro-acoustic sediment features a classification system can be developed (Orlowski, 1984; Freitas et al., 2008).

In this work the following features were used for classification:

Table 4-3: List of the echo features used for SBC; most features have various names in the literature, therefore the most common terms are listed.

Feature	Other titles	Explanation
attSv1	E1'	"Hardness"
decSv1	E1	"Roughness"
attSv1 + decSv1	E1' + E1	Entire fist bottom echo
attSv2		Attack of the 2 nd bottom echo
decSv2		Decay of the 2 nd bottom echo
attSv2 + decSv2	E2	"Hardness"; Entire 2 nd bottom echo
attSv1 / decSv1	E1' / E1	Relation between Attack and Decay
decSv1 / (attSv2 + decSv2)	E1 / E2	
FD (linear, non-linear)		Fractal dimension, Echo shape parameter

This wide range of possible echo features was developed and used to assess the best possible classification combinations beyond the already used standard combinations (see chapter 2.3.4). In this work all hydro-acoustic data was processed and analyzed using the software Sonar5 pro (Balk et al., 2011). Figure 4-7 shows the general survey and processing sequence for the performed SBC leading to two different approaches for SBC.

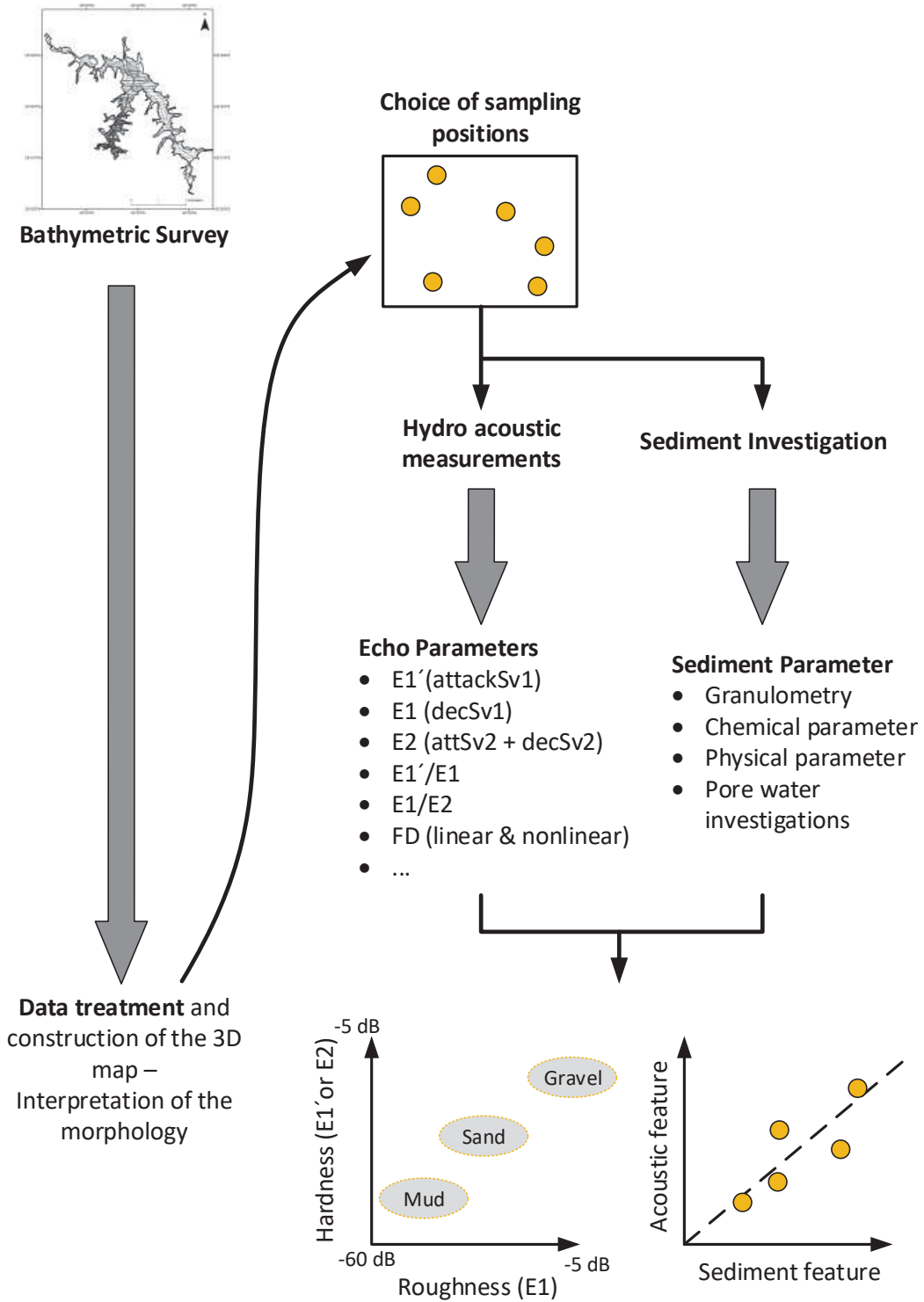


Figure 4-7: Data processing sequence for SBC approaches.

4.2.4.1 SBC- approaches

Approach 1: Clustering via echo features

Sediments with different compositions and characteristics will cause a variation in the detected echo parameters, these features can be used to produce sampling clusters, grouping the same sediment types together. Two acoustic parameters are used for this approach of classification. The most common combination is “hardness” (attSv1 (E1')) and “roughness” (attSv2 (E1)) as defining values (Burczynski, 1999). The main purpose of this procedure is to use acoustic parameters which allow the best possible separation of the displayed sediment samples in the diagram and hence a clear definition of sediment types (Figure 4-8). This can be obtained not only by the combination of “hardness” and “roughness” features as in the “first echo division” method (Burczynski, 1999). Although this approach is well known and in many cases promising, further echo features can be used.

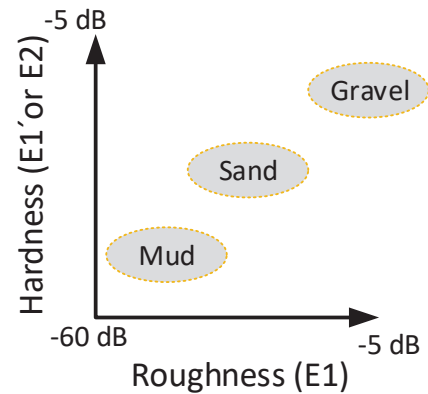


Figure 4-8: Principle of the definition of acoustic classes.

Approach 2: Correlation of echo- with sediment parameters

The second general approach is the statistical analysis of the echo features including the obtained sediment parameters. A classification becomes possible if correlations between an echo feature and a sediment parameter are found.

As applied in Anderson & Pacheco (2011) sediment parameters such as granulometry, density and loss on ignition can be used for correlation. In this study the range of investigated correlations was significantly extended (see chapter 5.2.3). The resulting equations are the basis for a classification of the data points from the dynamic survey. In this manner the sediment properties of unknown substrates can be calculated.

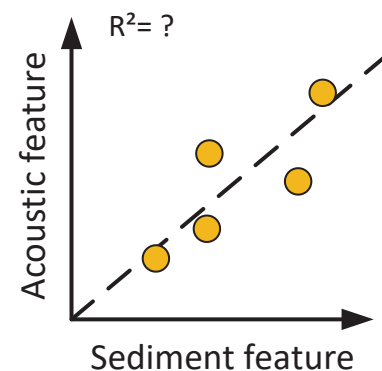


Figure 4-9: Principle of the single parameter correlation.

4.2.4.2 Fractal Dimension as an additional echo parameter

The Fractal Dimension (FD) is a parameter which can be used for the analysis of textures (Soille & Rivest, 1996). Hence in the context of SBC it serves for the analysis of the echo shapes and therefore creates information about the backscatter characteristics of the sediment. To obtain this information each echogram was analyzed, the bottom detected and the Mean Volume Backscattering Strength (MVBS or Mean Sv) for all pings calculated in Sonar5 pro . The resulting curve was flattened using a 3x3 filter to smooth small range variations. Calculated *Range* and *Mean Sv* values were exported, starting at the “bottom pick” ending at the end of the *decaySv1*. Data was loaded to OriginLab software and visualized. All graphs were produced in the way to maintain a constant side relations between the x and the y axis. This was done since the scaling of the curves effects the box-count results (Soille & Rivest, 1996). Graphs were stored as *.jpg files and loaded to the software Fractalyse 2.4 (Research Centre Th MA – Universit  de Franche-Comt , P. Frankhauser). For the fractal dimension analysis the box count method was chosen with an exponential box size and a fixed grid algorithm (Figure 4-10), based on the methodology published by van Walree, P., A. et al., 2005. The results from the FD-estimations were stored for linear and for non-linear estimations. The created FD values were used for sediment – acoustic correlations.

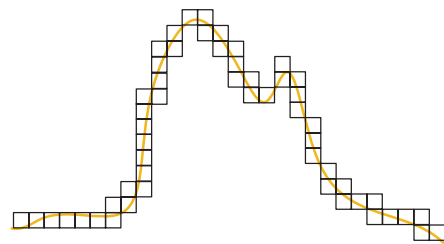


Figure 4-10: Example for the application of the box-count method.

4.2.5 Sediment thickness:

Several methods for the estimation of sediment thickness in lakes or reservoirs are available. The first and oldest method is to use sediment coring to determine the thickness of the actual sediment. This technique is generally a save approach since the exact sediment magnitudes can be measured. The interfaces between the pre- and post-impoundment layers are often distinct. Gravity or vibrational cores are used. Disadvantages are relative high handling and working efforts to recovery sufficient core samples as well as the general problem that only spatial restricted point information can be obtained. Hence, the spatial interpolation of the sediment information may constitute a problem. Additionally, if the sediment layer is thick it is likely that the core is not long enough to sample the entire vertical layer and reach the former lakebed.

The second approach is called “*Topographic Differencing*”. Here, the difference between the pre-impoundment and today lake bottom is calculated (Ortt, JR. & Richard, 2000; Jakubauskas & deNoyelles, 2008). This information is processed and a distinct 3D

representation of the accumulated sediment is the result. An advantage is the ability to produce sediment thickness information for the entire reservoir. However, this method normally suffers from the poor quality of pre-impoundment maps, be it the missing information about the map coordinate system and transformation of the insufficient resolution due to an inappropriate spatial scale of the map.

The third option is the “*Acoustic Estimation*” of the sediment thickness. This approach uses two different acoustic frequencies. The high frequency is used to detect the sediment water interface and the lower frequency detects the interface between the sediment layer and the next consolidated sediment layer (pre-impoundment layer). The feasibility was described by Dunbar et al., 2000 and Jakubauskas & deNoyelles (2008). Acoustic Estimation features the same advantage as the Topographic Differencing, since it is possible to collect data for the entire reservoir.

The first option was discarded as the available corer has a maximum sampling depth of 80 cm and it could be expected to find sediment thicknesses up to several meters (Kansas Water Office, 2008). Topographic Differencing was conducted for the CR but due to the fact that the original map has a vertical resolution of 5 m the differentiation of sediment layers smaller than this is invalid. Therefore, the third option was chosen for the estimation of sediment thickness in the Capivari Reservoir. Details of the methodology and the detailed approach are explained in the following.

Thickness calculation

Based on the fact that the 38 kHz frequency is able to penetrate the sediment deeper than the 200 kHz frequency (see chapter 2.3.3), a methodology for the estimation of the sediment layer was developed. For the calculation of the magnitude of the sediment layer the upper limit was derived from the 200 kHz frequency bottom detection. This data is already available from the bathymetric survey. The definition and hence the detection of the lower sediment interface is more complicated as the density difference between layers can be less distinct. In addition the reflected strength (T_s) of the echo signal does not reach the same level for all sediment types and locations. Therefore, a determined threshold for the detection of the interface cannot be derived. Instead of a fixed threshold for the lower interface detection, the echogram data is analyzed and the particular highest reflection pixel cluster is marked as the sediment layer interface (Figure 4-11). Figure 4-13 illustrates the sediment reflectivity and detection of the upper and lower boundaries in a 3D graph.

The bottom detection in Sonar5 pro is not able to produce satisfying results, hence all data was controlled and adapted manually. In some cases the detected interface composes of an

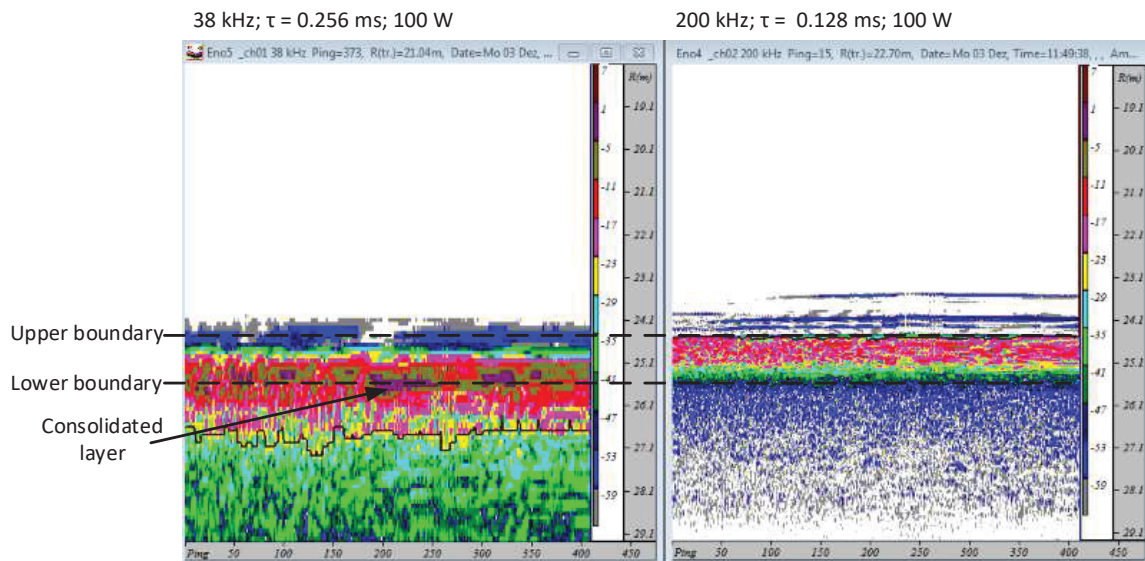


Figure 4-11: Echogram in Sonar5 pro showing both frequencies with exemplary detected upper and lower sediment layer boundaries.

array of vertical distributed pixels, resembling the same Sv-values, than the mean depth between these pixels is chosen as the corresponding interface.

This method is a promising approach to define the thickness of a sediment layer until a density boundary (Figure 4-12). If accumulations of sediment are present and more than one stratum within the sediment layer is detected, the lower most clearly distinctive boundary is chosen as the limit of accumulated sediment (see dark violet pixel in Figure 4-11).

It cannot be derived if the detected boundary is exactly the pre-impoundment layer or a posterior developed consolidated stratum. However, in the context of understanding the principal reservoir processes discussed in this work, the expressiveness of this method is sufficient. In the following, the term “*sediment thickness*” will refer to the here defined sediment layer.

The marked layer bottom is stored as a *.bottom-file and depth values together with coordinates are exported for processing in ArcGIS. Layer-depth values (200 & 38 kHz) at the same coordinates are

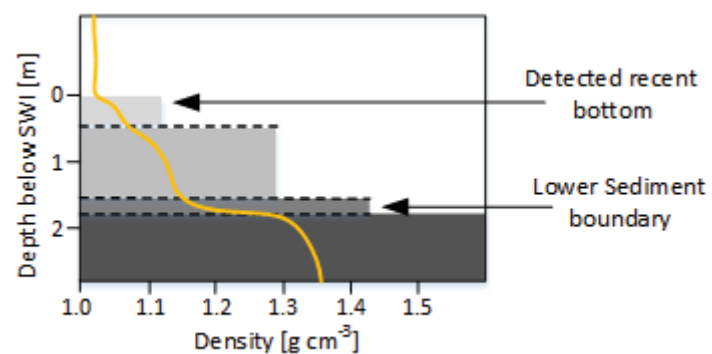


Figure 4-12: Schematic cross section through the sediment depicting the density gradients and the corresponding bottom picks.

subtracted resulting in the magnitude of the sediment overlay. To obtain a sediment map of the entire reservoir this information is interpolated using IDW. In order to verify the validity and reproducibility of the conducted method, the sediment thickness at the 18 coring sites is evaluated and a cross validation with the interpolated raster is performed.

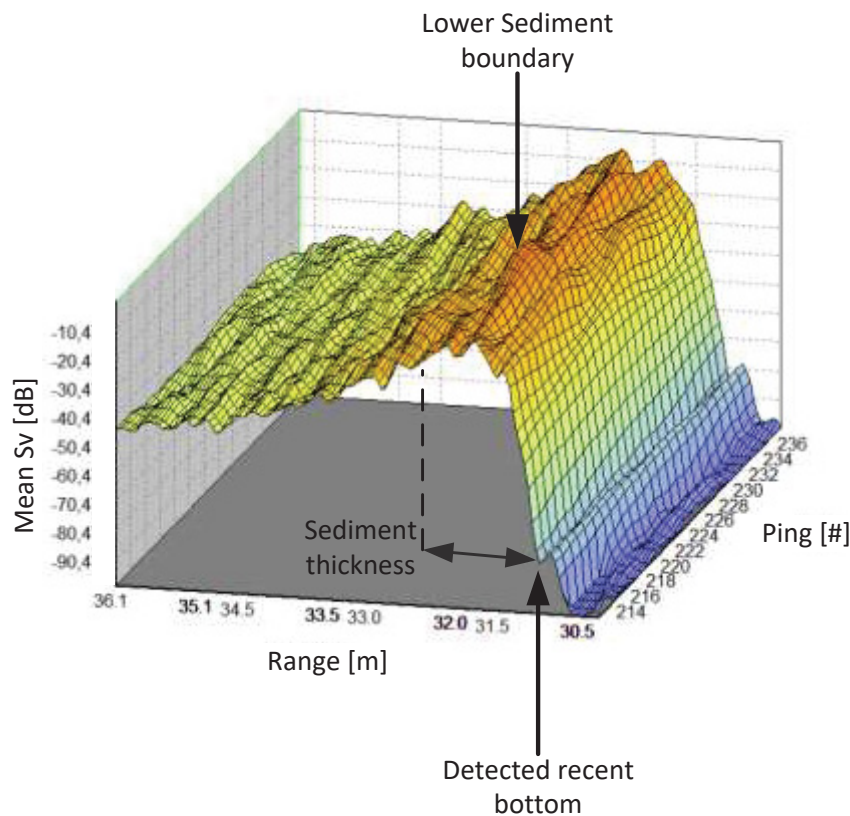


Figure 4-13: 3D illustration of the intensity from a sequence of pings hitting the sediment, including marked positions for the upper and lower sediment layer detection.

4.2.6 Bubble detection

Visual approach

Hydro-acoustic methods can deliver an important input for the detection of bubbles with improved spatial and temporal resolution. Therefore, the quantification of ebullition can be significantly enhanced compared to non-acoustical approaches (Ostrovsky, 2003; Ostrovsky et al., 2008; DelSontro et al., 2011). However, this approach entails other complications

which are irrelevant for bubbles quantification with funnels. For instance, a fish gets seldom caught in a funnel to be counted as methane gas.

To avoid measurement complications and erroneous results it is inevitable to define basic parameters for the gas bubble detection.

For this purpose, based on bubbles visible in the echogram a first approach was made and then the settings were applied for the whole reservoir. An echogram was selected where the bubbles were clearly visible to facilitate the definition of the right parameters for the gas bubble detection. The sampling site of core 6 was selected (Figure 4-14). Here the tracks in the echogram caused by rising bubbles strongly resemble the situation depicted in example echograms of Ostrovsky (2009a) (Figure 4-15).

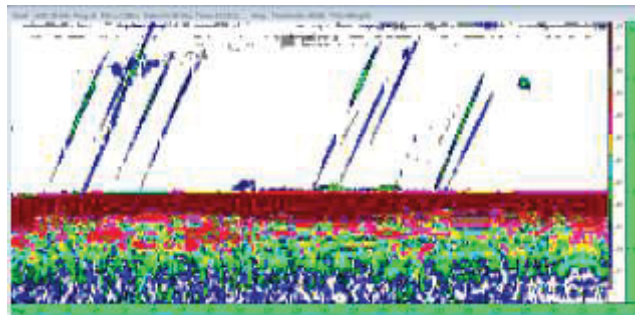


Figure 4-14: Exemplary echogram taken at Core site 6, diagonal traces are detected bubbles.

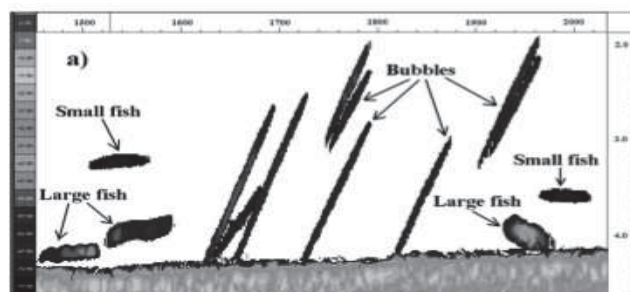


Figure 4-15: Bubbles and fishes in the same echogram (Ostrovsky, 2009).

Different approaches to bubble tracking in Sonar5 pro

Sonar5 pro provides versatile tools to detect, track and analyze bubbles within echograms. The basic procedure relies on the combination of successive targets from different tracks (Balk et al., 2011). The three options are given in the following:

Manual Tracking: This approach allows the user to manually draw a rectangle around visibly identified tracks to define the targets. Since manual identification of all single tracks is time demanding this approach is only suitable for relatively small amounts of data.

Cross Filter Tracking (CFD): The CFD is based on image analysis and uses the Single Echo Detection (SED) echogram to trace clusters of samples or pixels with a specific decibel value. The methodology works similar to the Manual Tracking except that the identification-rectangles around the tracks are detected automatically.

Multiple Target Tracking (MTT): For bigger amounts of data the automatic tracking method provides numerous parameter settings for tracking either using the Simple MTT or the advanced MTT. The implementation of the advanced MTT is most promising, but also very challenging. It allows the most precise detection of bubbles. In this work the AMTT was used based on the procedure established by DelSontro et al. (2011). Since DelSontro et al. (2011) used a different echo sounder system (120 kHz, split beam) the procedure was adapted for the EA400 system used for this study. In the following, the steps of the bubble detection are explained in detail.

Bubble detection using the Advanced Multiple Target Tracker (AMTT)

This section explains the multiple processing steps for the AMTT tool implemented in Sonar5 pro. Figure 4-16 gives an overview over the processing steps during the AMTT procedure based on Balk et al. (2011). The descriptions of the major steps are divided over the following subchapters.

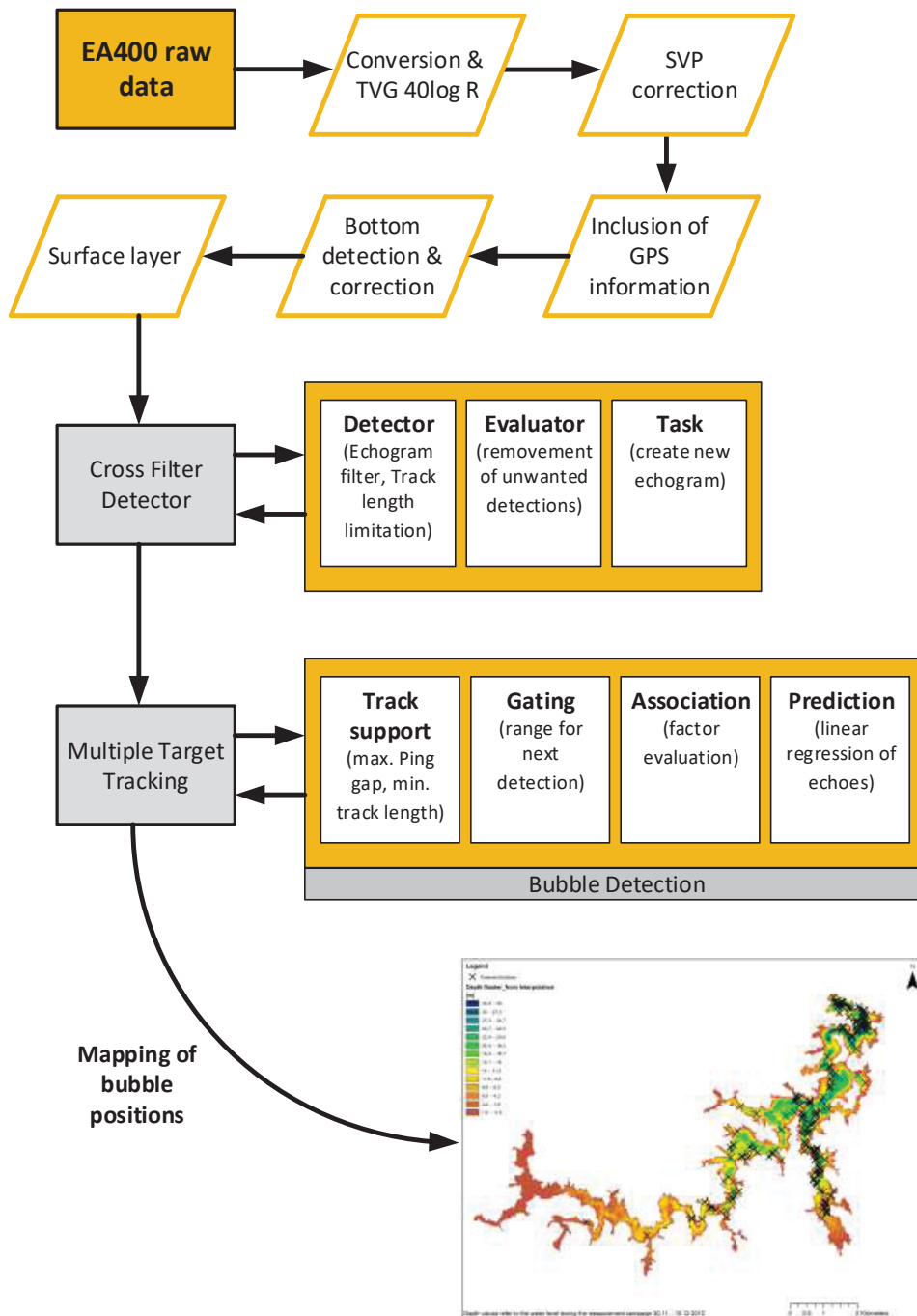


Figure 4-16: Overview of the bubble detection post-processing steps.

Setup for the application of the AMTT

Cross Filter Detector (CFD): The CFD is applied to the echograms in advance to the tracking process. Based on image analysis the CFD is programmed to detect targets in the AMP-echogram.

Sonar5 pro is capable of visualizing two types of echograms. One is the “standard” echogram showing the color-encoded amplitudes of each pixel. It is referred to as “AMP-echogram”. The other option is the visualization of single echo detections (SED).

The AMP-echogram is suitable for shallow water applications with low signal to noise ratios. Executing the detector, evaluator and “task” steps a new single echo detection (SED) - echogram is created. It becomes filtered by the detector in the next step. The foreground filter equally distributes the echo intensity so that peaks are removed and are not detected as single echoes. The background filter was set to a low level with the mean-filter method to ensure that only echoes with small variations in echo intensity were detected as tracks. Unwanted detections are removed by the evaluator. Track length were limited to a number of 5–75 pings. In the last step the SED echogram was created while the gaps in the tracks were automatically filled.

Advanced Multiple Target Tracker: The AMTT consists of four basic elements: Track supporter, Gating, Association, and Prediction. They can be used for the configuration of various parameters for target tracking. Using the Track supporter the minimum track length and the maximum ping gap can be set. This defines the numbers of echoes that may be missing before the next target is detected. The Track supporter functions as a filter, defining new tracks or rejecting echoes as noise. By conducting the “Gating”, the range to the next echo detection is defined and was set to 0.1 m starting from the first ping. The Gating step “predicts” the location of the next echo because, as stated in the manual, “*the future is very well known in post-processing*”, Balk et al. (2011). As a last step, the application of a linear regression in the *Prediction* estimates the subsequent positions of the echoes by: “*applying a straight best fit line through the last N echoes in the track*”, Balk et al. (2011).

Fish and bubble baskets: Bubble as well as the fish baskets are created in advance of the tracking together with the automatic storage of various sample data from the detected targets. Here the number of echoes, the target strength (Ts), water depth and sample location is stored. In order to separate the bubbles from possibly detected fish the minimal rising velocity was defined as 0.1 m s^{-1} .

Static bubble detection at core sites

At the static measurement sites (Core 1–18) bubble detection procedures were conducted for all eight configurations for both frequencies (see chapter 4.2.1, Table 4-2). Different settings regarding the echogram threshold and the limitation of the target strengths were applied and the results were grouped to evaluate the performance of the settings (Table 4-4).

To determine the best configuration for bubble detection clusters were build. The rising velocity of 0.1 m s^{-1} was chosen as one criterion. The other two clusters were limited by target strength. For each configuration and cluster the number of detected bubbles was stored including the individual visual evaluation of the measurements in the echogram.

Table 4-4: Exemplary table for the grouping procedure for different parameter settings during bubble detection.

	Vz < -0.1 cm/s only								-75.00 < TS < -45.00								TS < -45.00							
AMP-echogram threshold: -100	Σ bubbles								Σ bubbles								Σ bubbles							
Configuration	A	B	C	D	E	F	G	H	A	B	C	D	E	F	G	H	A	B	C	D	E	F	G	H
Σ bubbles																								
AMP-echogram threshold: -80	Σ bubbles								Σ bubbles								Σ bubbles							
Configuration	A	B	C	D	E	F	G	H	A	B	C	D	E	F	G	H	A	B	C	D	E	F	G	H
Σ bubbles																								

Bubble detection in echograms of the dynamic survey

Following the evaluation of the best configuration settings in Sonar5 pro these were used for the detection and analysis of the echograms obtained during the dynamic surveys. Other than for the analysis at the sediment sampling sites, only configuration B was available for the bubble detection at the driven lines. After detecting all possible bubbles the coordinates were imported to ArcGIS for further interpretation and mapping.

4.2.7 General Data Processing

All data imported to Sonar5 pro has to be converted from the *.raw data format to the *.uuu Sonar5 pro specific format. At the beginning of this process it has to be decided, if the data is going to be used for volume analysis (volume targets), like sediment features or for the detection of bubbles. For the first approach it is necessary that the echogram is corrected using the $\text{TVG} = 20 \log R$ function while the bubble detection works with the $\text{TVG} = 40 \log R$ function. For details on TVG corrections see Chapter 2.3.1.

Moreover, the echogram specific range settings have to be defined as well during the converting process. For the purpose of SBC as a minimum the range was set to two times the maximum depth detected in the individual echogram plus a fixed value of 5 m. The double depth is important to ensure that the information of the second bottom echo is still part of the converted echogram. The additional depth provides sufficient extra range for the

volume information of the second bottom detection. Accordingly, if the maximal water depth in an echogram is 20 m, the converter range will be set to 45 m.

For the bottom detection in Sonar5 pro, the “*image analysis*” method was selected. The filter height and filter width for both, the pre-filter and post-filter were set to 1 pixel. As a threshold, for the bottom detection a value of -36 dB was chosen. Consequently, the first sample with an echo strength of -36 dB or higher is detected as bottom. This value was defined after manual visual bottom detection. After the automatic bottom detection, the produced bottom line was inspected and corrected manually if necessary (semi-supervised bottom detection). Based on the detected bottom, attack and decay values were exported as .txt files.

For the SBC the amplitude echogram base threshold was generally set to -90 dB. Since a higher range in the echograms does not have a negative effect on any bubble detection process the same configurations could be used for this purpose as well, even if half the maximum range would be sufficient. Regarding the threshold in the amplitude echogram the basic conversion parameters are different. For bubble detection a very low threshold of -120 dB was chosen to ensure that all detectable targets are visible.

Due to the fact that Sonar5 pro is unable to include the GPS information directly to the echogram, all GPS data was processed and converted to the standard Sonar5 pro import format (see Appendix A.3). Afterwards it could be imported and via the second-based timestamp the coordinates could be related to the single pings of each echogram. During this step, Sonar5 pro created automatically *.NAV files which makes it possible to link the GPS data continuously to the corresponding echogram. After this step, for all echogram analysis besides the bubble detection, the *bottom line* has to be detected. By altering the file format from *.uuu to *.uuuQ Sonar5 pro automatically stores the alteration of information after a successful detection of the bottom line. For bathymetric as well as SBC approaches the bottom line is inevitable, since it represents the position of the beginning of the consolidated sediment. For the bathymetry the depth value will be exported and for SBC the detected bottom is the beginning of the sediment feature analysis.

4.2.8 Data Correction and Quality Control

Sound velocity correction

Since the sound velocity in the water is one of the essential factors influencing the results of hydro-acoustic measurements, it has to be exactly determined.

The sound velocity in water depends on temperature, hydrostatic pressure (depth dependent) and salinity. Due to the fact that the sound velocity was set to constant (1500 m s^{-1}) in the EA 400 software during the surveys, a sound velocity correction had to be performed in the post processing. In this case the following sound velocity model by Medwin (1977) was used (Eq. 32). Where c is the sound velocity [m s^{-1}], T is the temperature [$^{\circ}\text{C}$], z is the depth [m] and S is the salinity [PSU].

$$c = 1449.2 + 4.6 T - 0.055 T^2 + 0.00029 T^3 + (1.34 - 0.01 T)(S - 35) + 0.016z \quad \text{Eq. 32}$$

The salinity of the reservoir was calculated from conductivity values, assuming that a conductivity of $1 \mu\text{S cm}^{-1}$ complies with a concentration of 0.53 mg l^{-1} NaCl (Karrasch & Eeckert Gesellschaft für Wassertechnologie mbH, 2014). According to this relation, for example the mean conductivity of $32 \mu\text{S cm}^{-1}$ measured in VR reservoir complies with a salinity of 16.96 mg l^{-1} or rather 0.01696 PSU.

For each week of the survey in VR a temperature-salinity profile was taken using a HORIBA® multi-sensor. Results were used as input to Eq. 32) (profiles are shown in Appendix A.4). During the phase-two surveys at CR a CastAway™ CTD from YSI was available facilitating the recording of the temperature and conductivity for the entire depth. Hence, SVPs could be included in the correction on a daily basis.

Water level changes:

Bathymetric measurements always refer to one water surface level. As the water level in reservoirs can change in relatively short periods (within one day), the water level during each survey is required for post processing. Especially, if one bathymetric survey demands multi-day measurements it is important to refer all obtained data to the same reference water level.

Vossoroca reservoir:

At VR an official water-gage is missing. Hence a fix point with reference to the water level was needed. A concrete pillar close to the shore at the ramp was chosen as reference point. The top point of this pillar was geo-referenced with a DGPS network resulting in a positioning accuracy of around one centimeter.

The daily mean water level of the VR was determined by measuring the distance between the water level and the top of the pillar (834.74 m above sea level) and the actual water level. As reference height for the bathymetric survey, the highest mean water level during the survey (833.78 m above sea level) was chosen.

Capivari reservoir:

Since CR feature an official water-gage the recording of the daily water levels was less effort. The water levels were recorded two times each day, before and after each survey. Like in VR the highest water level during the two campaigns was also used as the bathymetric reference level. In CR the correction of the water levels was especially essential since the level between campaign one and two changed about 4.5 m.

Extreme values and error signals

All results processed in Sonar5 pro were exported as *.txt files. Besides the hydro-acoustic corrections and compensations no data quality control was undertaken until this process step. Hence, the data (bathymetric and SBC) was processed using Matlab R2011b to perform further calculations and quality control. Sonar5 pro gives -999 values if a pixel does not have any value. To avoid the inclusion of these values in the calculation of further echo feature values, they were deleted from the data matrix. Furthermore, logic limits were set for each echo feature value to exclude extraordinary deviations. After this control the data was exported and analyzed.

4.3 Sediment Survey

This chapter explains the two principal sampling techniques regarding sediment investigations, applied in this work. First, the core and grab sampling is illustrated, including the different relevant measurement parameters. Second, methodological details about the developed measurement approach, for the dialysis pore water sampling are given.

4.3.1 Cores & Grabs

Core sampling

For the core sampling a gravity "Mondsee"-corer by the manufacturer Uwitech was used (Niederreiter, 2012). The corer (Figure 4-20) basically consists of a steel carrier for replaceable, cylindric 86 mm diameter PVC tubes of different lengths (60 cm and 80 cm tubes were used). For core sample recovery, the corer was lowered rapidly into the water from the side of the boat using a steel rope winch. The device also features a locking mechanism which is indicated in Figure 4-20. By locking the tube, the mechanism ensures that no sample material is lost or washed out during the pull-phase. The impact on the seabed triggers the release of the elastic band and allows the plastic ball to lock the PVC tube the moment the tube is being withdrawn from the sediment. An airtight lip seal at the tube's top traps supernatant water from the sediment-water interface inside the PVC tube. It also causes the buildup of negative pressure in the tube during the rise to the surface. Hence, the sediment is unlikely to leave the tube as long the lip seal is closed. This mechanism is especially useful if the locking mechanism has a malfunction. To lock up the PVC tube for transportation a rubber plug has to be used while the tip of the corer is still under water.

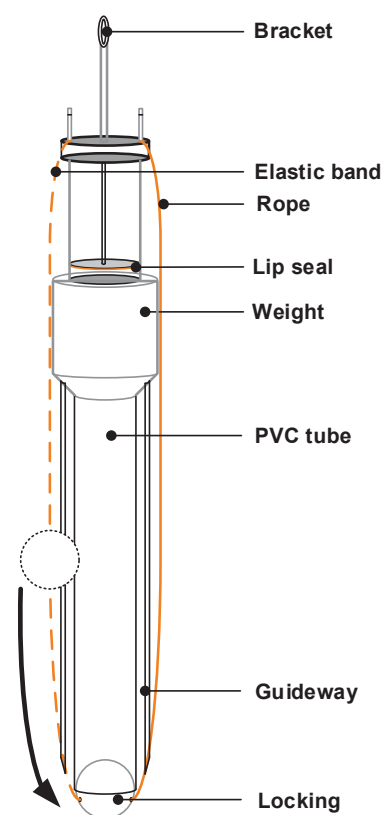


Figure 4-17: Schematic design of the Mondsee Corer.

After sampling, basic physical and chemical water parameters were obtained from the supernatant water. The sediment sample volume is about 3 liters using the 80 cm tube. Depending on the sediment composition, the most cores had a length of around 40–50 cm.

As a main advantage to other sampling techniques the coring provides a mostly maintained integrity of the sediment and a greater penetration depth. Structural features like stratification can still be identified in the opened cores. In addition, the washout of the fine fraction during recovery can be reduced to a minimum and the entire sample has only limited contact to the atmosphere (US Environmental Protection Agency (EPA), 2001, 3–11). One drawback is a higher expenditure of time and equipment compared to grab sampling. Multiple sampling attempts are often necessary for the obtainment of a proper core. There were difficulties drawing cores in sloping ground, probably resulting from hard sediments, insufficient corer weight or not hitting the sediment surface orthogonally.

Grab sampling

In addition to core sampling, grab samples were taken using a Petersen Grab Sampler (US Environmental Protection Agency (EPA), 2001, 3–5). It consists of two metal jaws which are held open (Figure 4-18) by a latch until the sampler hits the seabed. The jaws are then unlocked. Up to 1 liter of sediment is sampled by pulling up the grabber. The device was then retrieved, opened and the sediment material was transferred by hand into a Whirl-pak® for save and air tight storage.

The van Veen grabber can be operated faster than the Mondsee corer, since sampling preparation is simple. The grabber does not require a winch. Best results are obtained in soft, oozy sediment but the grabber is not restricted to it. Steep slopes and rocky seabeds are harder or impossible to sample, as the device tilts during sampling or rocks prevent the jaws from closing. In contrast to the Uwitech corer, only about the top 15 cm of the deposits are sampled and the fine fraction can be lost as it gets washed out during recovery. No supernatant water can be sampled.



Figure 4-18: Foto of the grab sampler prepared for sampling.

Vossoroca reservoir

During the surveys in phase one 10 core samples and 21 grab samples were retrieved. The sediment samples were taken in depth between 2 m and 17 m which equates nearly to the deepest spot in the reservoir. The positions of the sampling sites are illustrated in Figure 4-19.

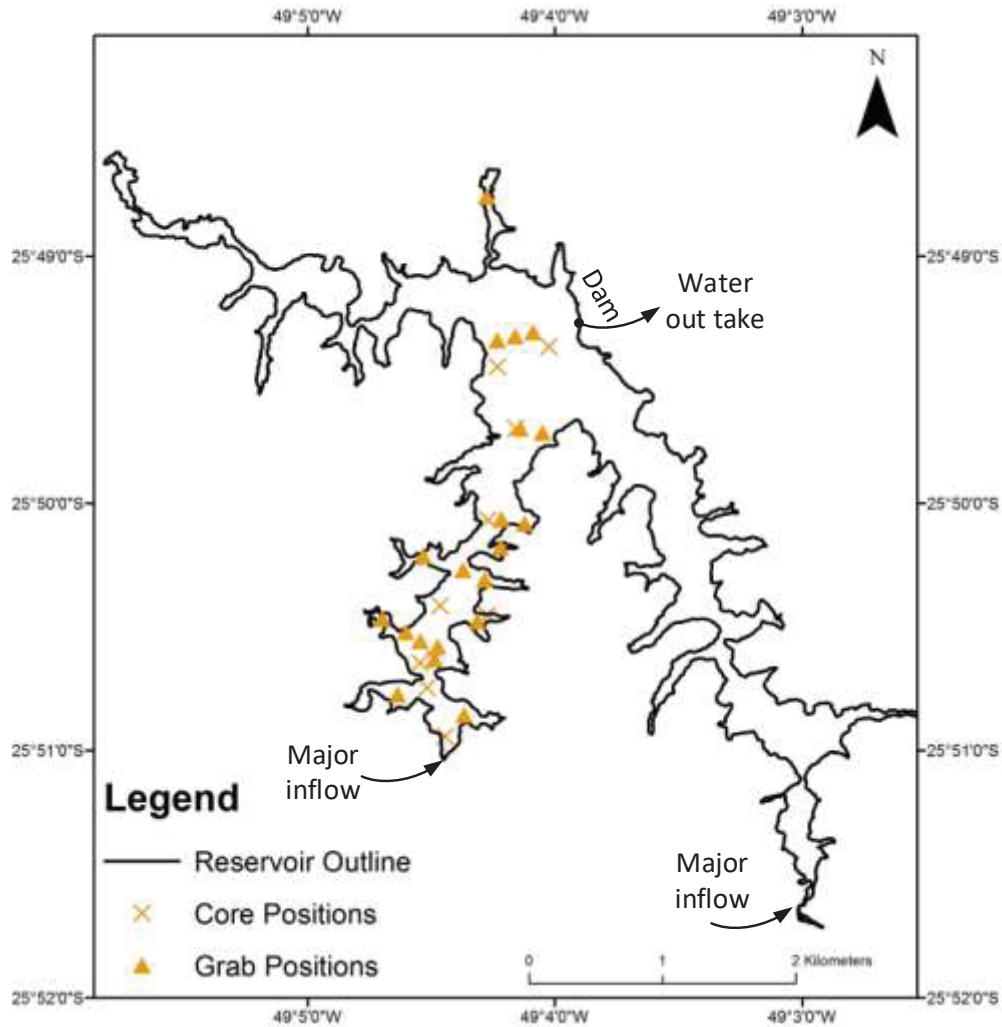


Figure 4-19: Sediment sampling locations in VR depicted against latitude and longitude; cores are displayed with crosses while grab samples are represented as triangles.

Capivari reservoir

In both surveys together 18 Core and one Grab sample were taken from water depth between 2 and 35 m. The Grab sample was taken, since the recovery of a proper core sampling was impossible. The positions of the sampling sites are depicted in Figure 4-20.

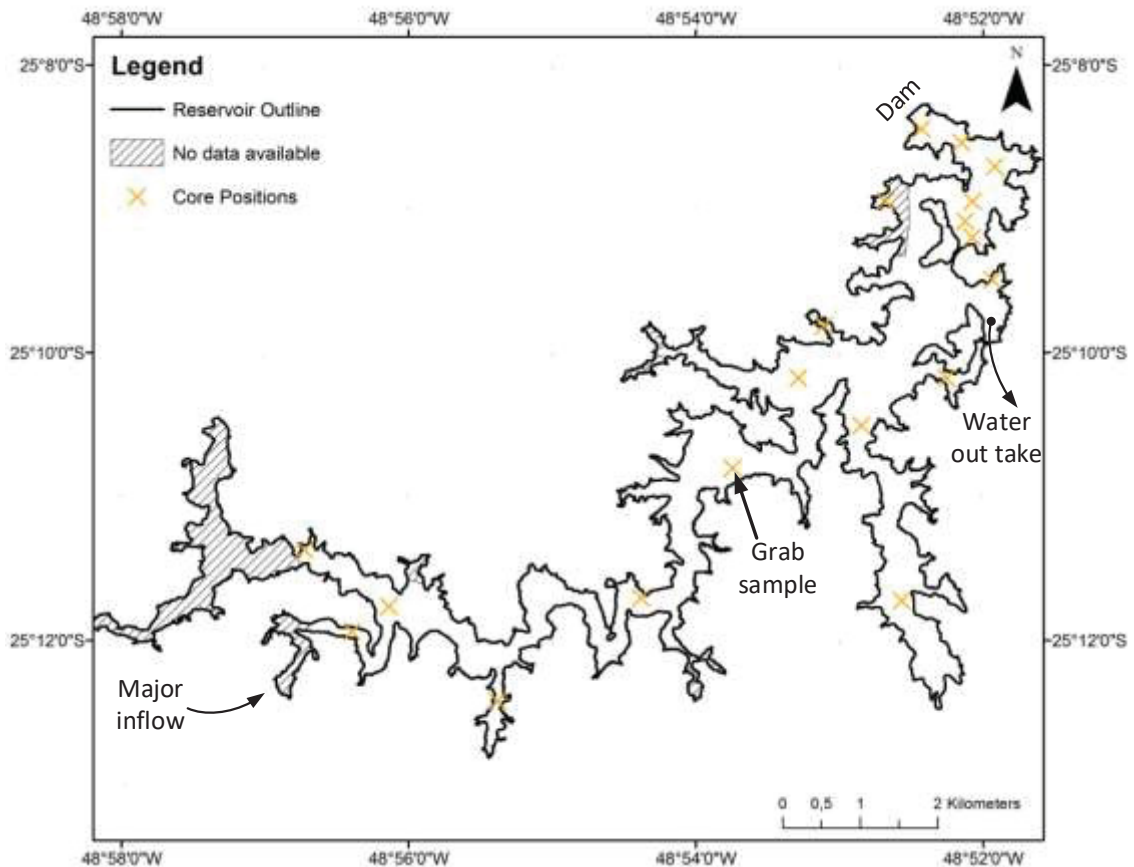


Figure 4-20: Sediment sampling location in CR depicted against latitude and longitude.

4.3.1.1 In-situ sediment analysis

Before the sediment was investigated the supernatant water was measured for temperature, conductivity and pH value. These measurements were performed still on the boat, directly after recovering the cores.

As a first step of sediment investigation, the core samples were cut in half and were optically examined with regard to the qualitative aspects listed in Table 4-5, whereas the last five aspects were rated on a scale from 0 to 4.

Some samples had clearly visible boundaries and were therefore divided in different layers. The number of layers per core reaches from 1 to a maximum of 5. A representative sample from every layer in each core was taken and named “total”. All material from the layers and “totals” were sieved separately as described in chapter 4.3.1.2.

Table 4-5: In-situ sediment description and analysis parameter.

Sediment feature	Characteristics
Odor	Intensity and quality of the samples smell
Color after Munsell:	determined with a Munsell Soil Color Book
Dominant structural feature	Description of visible structures
HCl-reaktion	Optical/acoustical observations of a chem. reaction after HCL (concentration of 10%) application
pH-value	determined with a Hellige-Troug pH test kit
Components	all material that could be identified with hands and the naked eye
Disturbances	pores or other errors in the sample
Darkness	(0 = bright, 4 = dark)
Dryness	(0 = wet, 4 = dry)
Elasticity	(0 = plastic, 4 = elastic)
Stratification	(0 = badly stratified, 4 = well stratified)
Sharpness of boundaries	(0 = no boundaries, 4 = sharp boundaries)

4.3.1.2 Granulometry

The sediment material from core and grab samples was wet sieved through four sieves with a mesh size of 2 mm, 0,5 mm, 0,25 mm and 0,063 mm to determinate the consistency of each Sample according to DIN 52098:2005-06 (Deutsches Institut fuer Normung e.V (2005). Lake water was used for the sieving of all samples. The sieving divided the samples into pea gravel (> 2 mm), coarse sand (0.5 mm), medium sand (0.25 mm) and fine sand (0.063 mm). Silt and clay passed through the 0.063 mm sieve. In order to determine the mass of the silt and clay fraction the volume of this suspension obtained from sieving was recorded. This value was used to calculate the real mass share of the silt and clay fraction, which was necessary since only a share of the suspension was dried and analyzed in the laboratory.

4.3.1.3 Wet Bulk Density (WBD)

Using a cylindrical soil sample ring (3.5 cm diameter, 4.5cm depth) a density sample was taken from each layer, whenever possible. The density samples were stored at minimum 4°C and were weighted on a special accuracy scale in the laboratory. Due to the destruction of the integrity of the sediment matrix the wet bulk density was only sampled from core samples. The WBD is calculated by Eq. 33 (derived from Avnimelech et al., 2001):

$$\text{Wet bulk density [g cm}^{-3}\text{]} = \text{Weight wet sample} / \text{total sample Volume} \quad \text{Eq. 33}$$

4.3.1.4 Chemical parameters (C, Fe, Mn, P)

In order to measure the carbon and sulfur content, an Eltra CS 2000[®] Carbon Sulfur Determinator was used. The samples were grinded to a flour-like consistency as preparation of the measurements. 250 mg of each sample were burned in an induction furnace at 1,800°C together with 700 mg of iron and 1,800 mg of Wolfram. The formed combustion gas is transported by an inert gas stream to an infrared sensor which detects the CO₂ and SO₂ content of the sample. Since it was expected that grain sizes bigger than fine sand do not contain significant contents of carbon or sulfur, only the smallest particle size fraction was analyzed for total carbon and sulfur.

Total phosphorus was measured as phosphate by molybdate blue analysis, according to DIN 38405-11 Deutsches Institut fuer Normung e.V (2007).

Total iron and total manganese contents were determined by atom absorption spectrometry (AAS).

4.3.1.5 Organic compounds (LOI)

To determine the loss of ignition 1–5 g of the air dried samples were grinded using a pestle and burnt for at least two hours in a muffle oven at 550°C. The burning time was not chosen to be longer since the LOI was predicted to be under 20% (Heiri et al., 2001). The share that has been used for the LOI equates to around 15% to 30% of the total dried sample weight. The weight of the sample has been measured before and after burning to calculate the loss. The Results are noted as percentages. The LOI was calculated after Eq. 34 (Heiri et al.,

$$LOI_{550} = \left(\frac{DW_{105} - DW_{550}}{DW_{105}} \right) * 100 \quad \text{Eq. 34}$$

2001).

Where DW_{105} is the dry weight at 105°C and DW_{550} the dry weight after 550°C and 2.5 hours in the Muffeloven.

4.3.2 Dialysis Pore Water Sampler (DPS)

As Teasdale et al. (1995) stated, dialysis pore water samplers (DPS) bear a number of advantages with regard to bio-chemical sediment investigation. The DPS were adapted to and specialized for different purposes in the last decades (Hesslein, 1976; Lewandowski et

al., 2002; Thomas & Arthur M., 2010; Schubert, C. J. et al., 2011). The applications reach from the measurement of concentration gradients of heavy metals and redox conditions to the calculation of diffuse fluxes of gas from the sediment to the water body (Urban et al., 1997; Thomas & Arthur M., 2010). Since DPS deliver valuable information about the biochemical processes and concentrations in a mostly undisturbed sediment, this sampling technique still has its place in modern environmental science. However, after many years of use and further development, most sediment DPS still have to be manually introduced to the sediment by divers or research submarines which makes the DPS relatively expensive in use and time-demanding in terms of preparation and placement. Otherwise, the measurements are limited to very shallow areas of the water bodies.

In addition to the placement efforts, the treatment of DPS before and after recovery is complicated and costly as the DPS have to be kept in oxygen-free atmosphere before placement and have to be analyzed in a glove box afterwards (Lyons et al., 1979; Teasdale et al., 1995; Dattagupta et al., 2007). Addressing these major drawbacks of DPS, the intention was to develop a DPS placing system (DPS-PS), which would allow the precise placement of DPS in water with a depth of up to 40 m and assessing the biases of on-board measurements and possible methodological improvements. The DPS-PS was designed not only to place one type of DPS, but should also be capable of placing DPS with variable chamber sizes and design factors. As mobility of equipment has become an important requirement, the DPS-PS design should allow all components to fit in a single aluminum box making it transportable in airplanes. The system was tested with a set of eight peepers investigating gas concentrations and redox conditions in the sediment. From pre-survey investigations, it could be assumed that the predominant sediment type found in CR is a rather soft mixture of silt and clay. Measurements were carried out during phase two.

4.3.2.1 Placement system concept and construction

With the objective of avoiding the described effects and still be able to generate a fast workflow placing the peepers, an innovative placing system was developed (Hözlwimmer, 2013). To keep the assembly as simple as possible, components are made from a rapid construction kit of prefabricated aluminum profiles resulting in a compact mechanism, which can be transported and used on a 5 m aluminum boat (Figure 4-21).

The inside of the housing bears two pairs of guide rails on either side, made from polyethylene. These provide a robust and dirt-proof vertical guidance for two sleds, which are connected through a pull-eye mechanism, featuring a 1:2 translation.

A hydraulic cylinder specified to max. 40 cm extension drives one sled upwards while the other sled is pulled downwards, resulting in an 80 cm travel of the peeper sled. Including a 10% safety margin, 74 cm long peepers can be safely pushed into the sediment (Hözlwimmer, 2013). Two foldable aluminum-framed PVC stands on both sides assure that the entire DPS-PS keeps an upright position and does not sink into the sediment. The surface of the stands can be adapted to the expected sediment hardness. The softer the sediment the more elements can be attached and folded out.

The pressure for the sled movement comes from a manual hydraulic pump located on the boat. The pump and cable system is capable of delivering 200 bar maximum pressure equaling 500 kg down force of the peeper sled.

Before placing the peeper into the sediment, it has to be fixed in the holding mechanism, which can be adjusted to any desired penetration depth. The use of the hand pump for pressure generation secures that the DPS penetrates the sediment in small steps. With every stroke of the hand pump, the pressure in the cylinder increases and pushes the peeper deeper into the sediment. After applying approximately 80 bars, the peeper reaches the maximum depth and the previously adapted holding mechanism releases it at exactly the configured sediment depth. For harder sediment, a higher pressure is needed, hence the DPS-PS can be equipped with additional weight to generate appropriate counter weight.

After placing, a relief valve at the manual pump releases the pressure. Then, elastic straps automatically counteract the extension of the cylinder and move the sled back to the starting position. The whole placement system can now be recovered using a car battery- powered electric winch.

The DPS itself looks similar to former designs (Winfrey & Zeikus, 1977), but is made from 15 individual aluminum compartments assembled using a 2-component epoxy resin. 15 chambers for a length of 60 cm result in an effective vertical resolution of 4 cm. On the bottom end, a stainless steel tip is bonded to the body allowing easy sediment penetration (Figure 4-21).

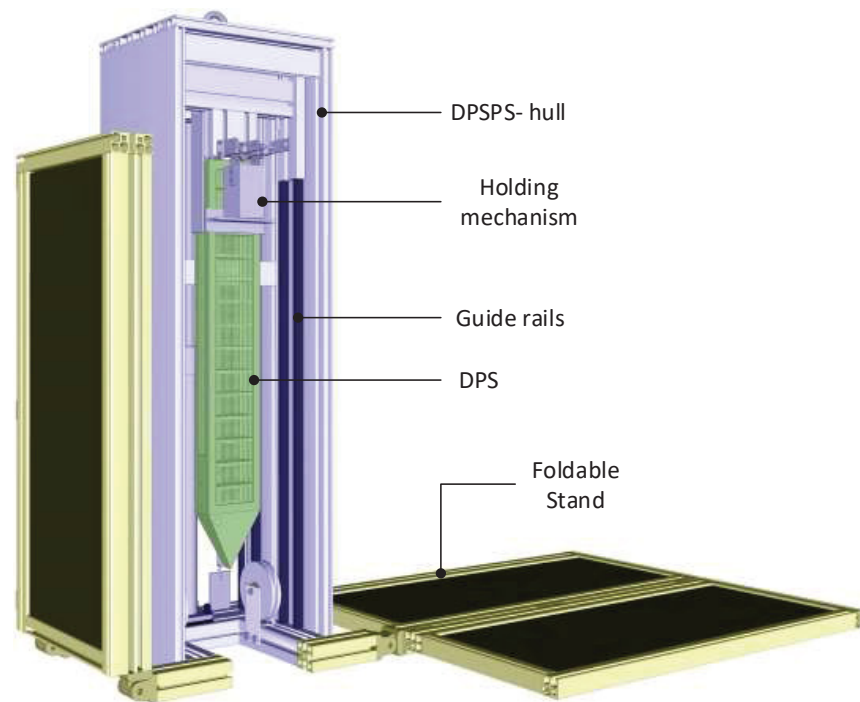


Figure 4-21: Rendered design of the DPS-PS; design and construction by Gauger (2013)

Two closure frames bear a steel mesh protecting the inner membrane tubes. One of the frames is permanently fixed while the other one can be removed providing access to the inner compartments. According to specific measurement demands the peepers allow various membranes to be chosen. The DPS-PS is also capable of deploying peepers of various designs. The chamber size and therefore the depth resolution can be altered, as long as the outer dimensions of the peeper stay the same.

4.3.2.2 Sample preparation and Peeper Placement

For the preparation of the DPS, a regenerated cellulose membrane tube (ZelluTrans; Carl Roth GmbH, Karlsruhe, Germany) with a molecular weight cut off (MWCO) between $1.99265 \cdot 10^{-23}$ kg and $2.32475 \cdot 10^{-23}$ kg, which is equivalent to a pore size of ~ 4 nm (US Environmental Protection Agency, 2005), and a thickness of $20 \mu\text{m}$, was cut into segments of 10 cm length. Each of the segments was then closed on one end with a polyamide 6.6 cable strap and filled with distilled water. Care was taken to avoid air bubbles inside the membrane tube and thus keep it as free of oxygen as possible. After filling, the other end was closed with a cable strap. Each bag then contained a volume of ~ 50 ml. Membrane bags were usually prepared on the day or the day before placement and stored inside a polyethylene

bag filled with distilled water. Shortly before placement, one bag was positioned inside each chamber of the DPS and the housing was closed securely with a polyamide 6.6 cable strap.

Placing procedure

The prepared DPS was clamped in the DPS-PS. The DPS-PS was then lowered with the help of an electric winch until the tension in the steel cable lessened by the DPS-PS reaching the sediment surface. The dialysis sampler is pushed vertically into the sediment by the hand-driven hydraulic system. Ultimately, after recovering the DPS-PS, a buoy was attached to a rope connected to the DPS for marking the location of the peeper and for recovery after the equilibration time. Caution has to be given to the length of the rope as wave action can loosen or even pull out the DPS from the sediment if the rope is too short, leading to biased results. The length of the rope rl can be calculated after (Hilgert et al., 2014), (Eq. 35):

$$rl = d + 1 + \ln(d) \quad \text{Eq. 35}$$

Where d represents the water depth in [m] at the current position. If the water body is affected by rapid water level changes, like in reservoirs, the maximum water level at the current position can be used as d .

Peeper recovery and sample treatment

The peepers were recovered by manually pulling them out of the sediment and up to the surface using the ropes attached to the buoys. After the peeper was retrieved back on the boat, handling was to be conducted as fast as possible to prevent diffusion of oxygen into the membrane and methane to the atmosphere which would accordingly falsify sample analysis. For the whole sampling procedure of 15 chambers, about 25 minutes were needed. The executed sampling sequence included photo documentation, in situ oxygen and temperature measurements, and headspace sampling for further gas and ion analysis.

After recovery of each peeper, the first step was to take photos to document the position of the adherent



Figure 4-22: DPS after recovery with adherent sediment.



Figure 4-23: Injection of DPS solution in the head space vial.

sediment marking the sediment water interface (SWI) Figure 4-22.

The SWI was most times clearly visible by sediment. Then, the cable straps were cut off and the DPS opened. Due to the highest expected gradients and hence the fastest diffusion, the oxygen concentration and temperature were measured beginning from chamber 15 (lowermost chamber) using a medical syringe sensor (Oxygen Microsensor; PreSens®, Regensburg, Germany). The syringe has the benefit that the bag does not need to be opened and therefore air contact of the sample stays at the minimum. Before insertion of the syringe, the bags were cleaned from sediment particles to avoid intrusion of particles from the outer surface into the sampling solution. In the next step, a sample of 10 ml volume was taken with a syringe (Omnifix® 10 ml; Braun, Melsungen, Germany) fitted with a metal cannula (100 Sterican®; Braun, Melsungen, Germany) from the membrane bag and transferred to a 20 ml headspace brown glass vial filled with ambient air. To let the air escape from the vial, a second cannula was placed in the rubber septum of the vial cap. To prevent degradation of methane through microorganisms, the vial was previously prepared with 0.1 ml of a preserving agent (0.6% HgCl₂ solution) (Bartram & Richard, 1996). For each sample, a fresh syringe was used and during all measurements, the membrane bags were protected from direct sunlight. Vials were afterwards stored dark and cool at 4°C until analysis.

4.3.2.3 Measurement (Head space analysis)

The chromatographic analysis was performed by LACTEC (Institute of Technology for Development) in Curitiba, Brazil. This had the advantage, that the samples could be analyzed relatively fast after sampling as well as that the existing experience of the laboratory personnel guaranteed reliable results.

Gas chromatography

Detection and quantification of the gaseous analytes, methane (CH₄), nitrous oxide (N₂O), carbon dioxide (CO₂), oxygen (O₂) and nitrogen (N₂) was carried out with a multi-channel static headspace gas chromatograph (Trace GC Ultra®; Thermo Scientific, Waltham, USA). The gas chromatograph was interconnected with three different detectors. For the detection of methane and indirect detection of carbon dioxide a Flame Ionization Detector (FID), for nitrous oxide an Electron Capture Detector (ECD) and for oxygen and nitrogen a Thermal Conductivity Detector (TCD) was in use. The latter two gases were identified by default and did not have relevance for the study.

For analysis, samples were preheated at 90°C and 2 ml portions were manually inserted with a polypropylene syringe into a storage loop and subsequently introduced into the Hayesep N packed columns (2000×0,5 mm; VICI AG International, Schenkon, Switzerland) through valves. The FID detector used helium as carrier gas. The makeup gas had a flow rate of 30 ml min⁻¹, as fuel gas helium was used with a flow rate of 10 ml min⁻¹ and the airflow was adjusted to 350 ml min⁻¹. For the ECD detector nitrogen was used as carrier gas at a constant pressure of 250 kPa. Column temperature for both columns was 90°C. For the detection of carbon dioxide with the FID detector a methanator system was used. In the methanator, carbon dioxide was catalytic reduced to methane under excess hydrogen. Eq. 36 shows the basic reaction in the methanator.



Actually many of the samples exceeded the highest standard of the calibration curve for CO₂, hence in some cases peak areas could not be integrated entirely. Thus, the integrated area is not fully accurate. CH₄ was quantified with the FID until it exceeded the highest possible standard, then it was switched to the TCD for highest concentrations. Due to the high methane concentrations, the column was flushed after each sample to evade artifacts from former measurements. Therefore, carrier gas was used, conducting chromatographic analysis without sample injection.

The calibration of the chromatograph was done using nine different standards with varying concentrations (details in Appendix A.5). Final processing of the obtained data was carried out with ChromQuest™ (Version 5; Thermo Scientific, Waltham, USA).

Results were given in ppm respectively percent in the gas phase and had to be converted, according to Henry's law, into the concentration in the aqueous phase (see Appendix A.6).

Ion chromatography

For the detection of fluoride, chloride, bromide, nitrite, nitrate, phosphate and sulfate a single-channel ion chromatograph (Dionex ICS-9000®; Thermo Scientific, Waltham, USA) interconnected with a conductivity cell with DS5 detection stabilizer (Thermo Scientific, Waltham, USA) was used. Samples of 10 µl were injected into the chromatograph and separated on a Dionex IonPac AS23® carbonate eluent anion-exchange column (4×250 mm; Thermo Scientific, Waltham, USA) protected by a Dionex IonPac AG23® guard column (4×50mm; Thermo Scientific, Waltham, USA). All samples taken directly out of the membrane tube in the DPS were free of any particles, therefore a pretreatment was not necessary. Hence anions should have been detected, carbonate eluent was used to carry the sample through the chromatograph. The flow rate was 1 ml/min. As regenerate for the Dionex MMS 300 Suppressor (4cm; Thermo Scientific, Waltham, USA) dilute sulfuric acid was used. The peak integration was done with Chromeleon (Version 7; Thermo Scientific, Waltham, USA). The calibration was done with seven ion-specific standards (Appendix A.5). Concentrations obtained by measurement of both ion and gas chromatography were corrected for the volume of the preserving agent by equation A6- 10 (see Appendix A.6).

4.4 Further Surveyed Parameters

4.4.1 Secchi Disc

The visibility depth was assessed once a day during the surveys of phase two using a Secchi disc. Since the Secchi depth is linear correlated to the algal biomass in the water column the obtained values are used for the calculation of the trophic state of the reservoir (Carlson, R., E., 1977). In combination with received water quality data from the inflows and the reservoir itself (provided by LACTEC) the water quality index was calculated using Eq. 37 (Länderarbeitsgemeinschaft Wasser (LAWA), 2001).

$$INDEX = \frac{Ind_{Chl} * W_f + Ind_{SD} * W_f + Ind_{P_{SP}} * W_f + P_s * W_f}{\sum W_f} \quad \text{Eq. 37}$$

Where “*Ind*” stands for index and the subscript for the individual parameter. W_f is the weighting factor. The individual parameters are: *Chl* = Chlorophyll-a [$\mu\text{g l}^{-1}$]; *SD* = Secchi-depth [m]; P_{sp} = Total Phosphorous during spring [$\mu\text{g l}^{-1}$] and P_s = Total Phosphorous during summer [$\mu\text{g l}^{-1}$]. The detailed calculation can be found in Appendix A.7.

The water quality index was calculated due to its relevance in the context of GHG emissions. Gunkel & Sobral (2013) stated that there is a direct relation between water quality and potential GHG production. Accordingly, this information can serve as a secondary parameter to understand the behavior of the reservoir. An oligotrophic reservoir in contrast to a highly productive eutrophic one would not be expected to produce relevant amounts of methane (Abe et al., 2009b).

4.4.2 Water Quality Parameters

For the acquisition of basic water parameters a U-53 Multiparameter Water Quality Checker from HORIBA was used. With the multiprobe temperature ($^{\circ}\text{C}$), pH, conductivity ($\mu\text{s cm}^{-1}$), dissolved oxygen (mg l^{-1}), turbidity (NTU) and depth (m) were measured. In phase one and phase two regular vertical profiles were measured collecting data at 1 m intervals until the lakebed was nearly reached. In phase one the obtained results were used for the echo correction calculations. Whereas in phase two the vertical sampling was taken over by the CastAway®-CTD due to faster data acquisition.

All data was tagged with GPS positions and time stamps.

4.4.3 Temperature – Conductivity – Depth (CTD)

During phase two at all sample points the CastAway®-CTD was used to obtain information about the vertical temperature and conductivity distribution in the reservoir. The main purpose of this measurements is the correction of sound speed in the water column, but it also serves to understand the actual stratification situation in the reservoir. Exemplary results are given in Appendix A.4.

5 Results and Interpretation

Reflecting the methodological structure of this study, this chapter is divided into four parts. The first three parts contain the results from the sediment, hydro-acoustic and pore water investigations. Each part primarily focuses on the method-specific findings. However, if it serves the explanation of the findings or is necessary for the understanding, data from the other methods are included. In the last part “*composed results*” more complex interpretations and results are developed including the selected data from the previous three subchapters, which is most relevant for answering the overall research questions.

5.1 Sediment Investigations

This section gives a synopsis of the sediment investigation results. They are presented in singular perspectives as well as in the context of other sediment features and their spatial distribution in the reservoirs. The selection of sediment features discussed, focuses on the formation of GHGs and the context of hydro-acoustic measurements, even though many other single features were investigated.

5.1.1 Sediment Key Data

For the comparison of the sediment conditions in VR and CR the key parameters are given in Table 5-1 and Table 5-2. In addition to the differences of the two reservoirs described in chapter 3, basic statistics of the sediment samples are listed here. The entire sediment analysis results are given in Appendix A.8.

The sediment composition of both reservoirs is similar in most regards. The granulometry ranges in comparable limits since the mean share of the finest fraction differs only by 6.8%. The same accounts for the coarser grain size fractions. While the highest bulk density measured in Capivari reservoir is slightly higher (1.8 g cm^{-3}) than in VR, the maximum total carbon content and also the upper limit of the LOI reaches higher contents in VR (6.5% and 18.7%, respectively). Sulfur concentrations in the sediment have nearly the same value ranges and feature high coefficients of variation (CV). This generally may be caused by low concentrations and the associated measurement inaccuracies. Total concentrations of iron, phosphor and manganese exhibit higher values in the sampled sediment volumes in CR.

Table 5-1: Sediment key parameter from cores taken in Capivari Reservoir (N = 18), CV is the coefficients of variation

	Mean	Max.	Min.	Standard Deviation (SD)	CV
Depth [m]*	13.7	32.5	0.4	8.8	0.6
LOI [%]	13.3	16.5	8.3	1.7	0.1
Total Carbon [%]	2.7	4.2	1.3	0.6	0.2
Bulk Density [g cm ⁻³]	1.3	1.8	1.1	0.1	0.1
Sulfur [%]**	0.05	0.14	0.01	0.03	0.7
Phosphor [mg kg ⁻¹]	1395	1837	965	279	0.2
Mn [mg kg ⁻¹]	635	1296	336	242	0.4
Fe [g kg ⁻¹]	68.2	93.4	53.9	11.4	0.2
Proportion of particles <63µm [%]	78.3	99.9	34.7	17.5	0.2
Proportion of particles <250µm >63µm [%]	14.7	43.2	0	13	0.9
Proportion of particles <500µm >250µm [%]	4	19.5	0	4	1
Proportion of particles <2mm >500µm [%]	2.2	14.1	0	2.2	1
Proportion of particles >2mm [%]	0.5	2.6	0	0.6	1.2

*Depth range only refers to the sediment sampling locations

** Values are rounded to two decimal places

Table 5-2: Sediment key parameter from cores and grabs taken in Vossoroca Reservoir (N = 32), CV is the coefficients of variation

	Mean	Max.	Min.	Standard Deviation (SD)	CV
Depth [m]*	8.8	15.6	2.1	3.6	0.4
LOI [%]	12.1	18.7	2.9	4.4	0.4
Total Carbon [%]	2.8	6.5	0.4	1.3	0.5
Bulk Density [g cm ⁻³]	1.2	1.6	1.1	0.2	0.2
Sulfur [%]**	0.03	0.13	0	0.03	0.87
Phosphor [mg kg ⁻¹]	822	1344	224	329	0.4
Mn [mg kg ⁻¹]	341	488	190	71.3	0.2
Fe [g kg ⁻¹]	42	68.3	11.4	12.6	0.3
Proportion of particles <63µm [%]	71.5	99.9	0	32.6	0.5
Proportion of particles <250µm >63µm [%]	10.2	95.2	0.1	17.6	1.7
Proportion of particles <500µm >250µm [%]	8.6	36.8	0	11.2	1.3
Proportion of particles <2mm >500µm [%]	8.1	42.5	0	12.9	1.6
Proportion of particles >2mm [%]	1.7	15	0	3.2	1.9

*Depth range only refers to the sediment sampling locations

** Values are rounded to two decimal places

In-Situ Sediment analysis – a first insight into the sediment composition

The in-situ analysis was conducted for all core samples from VR and CR. The distinction of layers in the cores was mainly based on the color and the water content of the sediment. Colors range from light ochre over brown tones to darker black and blue hues and were determined using the Munsell color chart. The number of layers ranged from one to five layers per core, also in dependence to the length of the taken cores. Since grab samples have a disturbed structure these cannot be subdivided into layers. Most cores show gas inclusions. The bubbles are present in various configurations. From randomly distributed large (> 2 cm diameter) single bubbles to homogeneously distributed small (< 4 mm diameter) bubbles. A tendency can be observed: The larger the volume of the bubble, the less spherical the shape.

This effect is particularly visible in soft sediments with high shares of silt and clay (Boudreau, B., P. et al., 2005; Sollberger et al., 2014).

In all samples investigated, neither optical nor acoustical reactions with 10% HCl were observed, proving the complete absence of carbonates. The odor of many samples tend to have a smell of H₂S especially after the appliance of HCl, indicating the presence of sulfides. Smells of the samples ranged from earthy and metallic to putrid. Putrid odors were mostly present in sediment samples featuring blackish-bluish colors. The pH values range from 4.5 to 7, while most samples show pH values in the acidic range around 5–5.5. The sediment samples feature a wide range of elasticity with a vertical differentiation, visible in the core samples. The upper parts of the cores have higher elasticity while the deeper layers tend to be dryer and hence have low elasticities. Dryness is vertically oppositional distributed. Upper layers are highly water saturated in contrast to lower dryer layers.

5.1.2 Granulometry and Sediment Distribution in the Reservoirs

Figure 5-1 (A & B) shows the granulometry results as percentaged dry weight from VR sediment samples. In phase one of the research, grab and core samples were taken and hence are depicted next to each other. Figure 5-2 then shows the corresponding results from CR. Here, only core samples are represented. The range of grain size distributions of both reservoirs appears to be generally similar. In both reservoirs no sediments could be found consisting of pure sand or gravel.

Differences can be found in the share of the coarser material in the grab samples compared to the core samples. This can be due to the fact that, on the one hand the grab sampler is capable of sampling sediments with higher densities, which can be caused by the presence

of consolidated clay, sand and gravel mixtures. On the other hand, the grabber is prone to lose some fine material through washing of particles during the recovery.

Noteworthy is the discrepancy in grain size distribution between the different samples, independent from the reservoir or the sampling technique. As already addressed, high shares of coarse material can be found, contrasting that at least every second sample taken, has a silt-clay fraction share higher than 90%. Some samples even reach close to 100% silt and clay fraction (e.g. Figure 5-1, B: core 4, 7, 8, 18, 20 and 22).

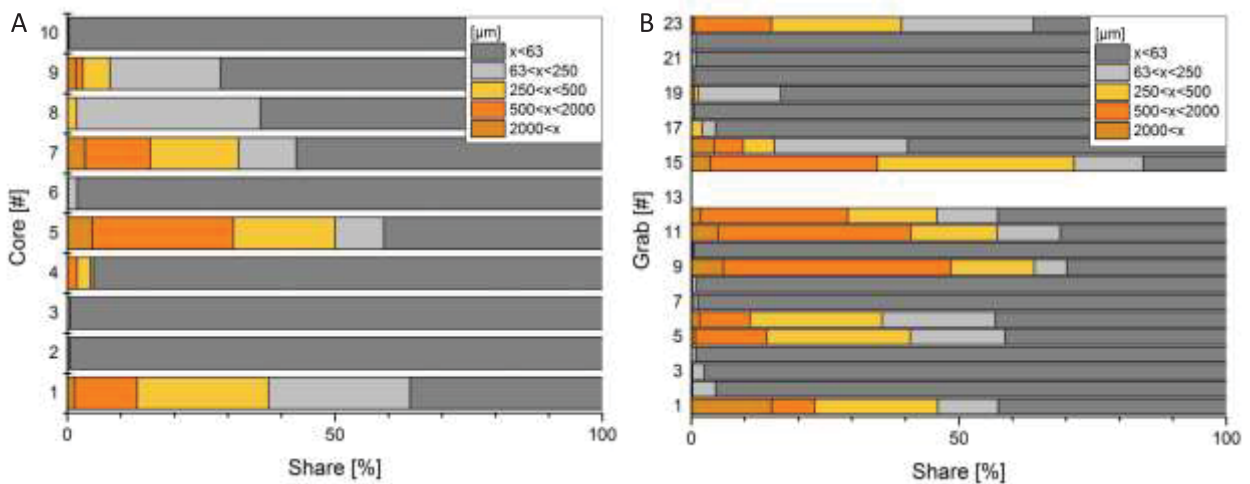


Figure 5-1: (A) Percentaged dry weight distribution of grain sizes in core samples from VR; values for core 8 are doubtful due to handling errors during sample processing; (B) Percentaged dry weight distribution of grain sizes in VR grab samples.

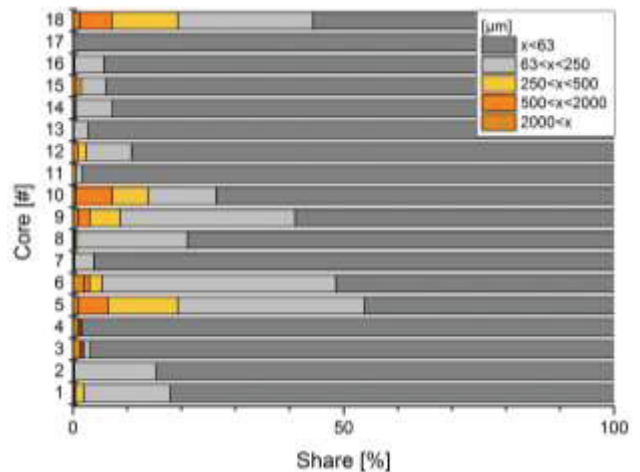


Figure 5-2: Percentaged dry weight distribution of grain sizes in core samples from CR.

Considering the sediment distribution within the reservoirs, in particular within the south-western arm of the VR and the entire CR analog patterns can be observed. The granulometric characteristics of the sediment samples distributed over the area of the reservoirs are presented in Figure 5-3 and Figure 5-4. The pie charts represent the composition of the sampled lakebed at the current position. Shown values are weighted shares of all layers analyzed and hence represent an average of the entire vertical grain size distribution of the sampled volumes. Exact coring depths and photos of the cores are given in Appendix A.1. Due to the destruction of the sediment structures no images of the grab samples are presented.

Two overall tendencies of the sediment distribution in the reservoirs can be observed. The first is the presence of coarser material in the proximals and the second is the predominant gradient from the inflow to the deeper areas with increasing shares of fine material (Figure 5-3: G4, C10; Figure 5-4: Core 1, 2, 3, 4, 7 and Core 15).

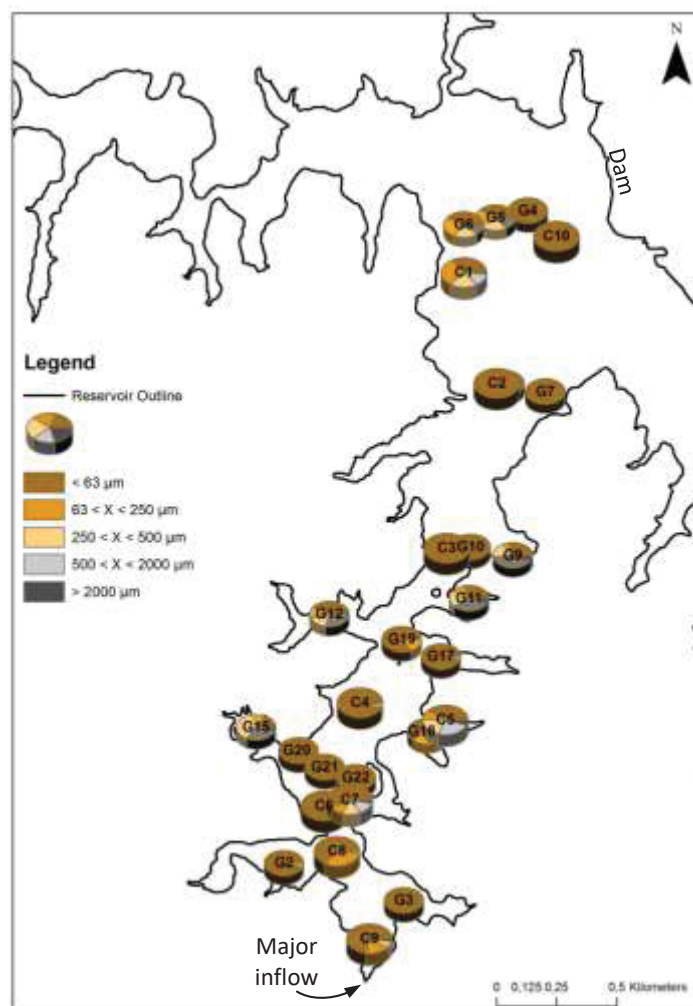


Figure 5-3: Granulometric lakebed characteristics at sampling locations in the south-western arm of VR, C# indicates the core numbers and G# the numbers of the grab samples.

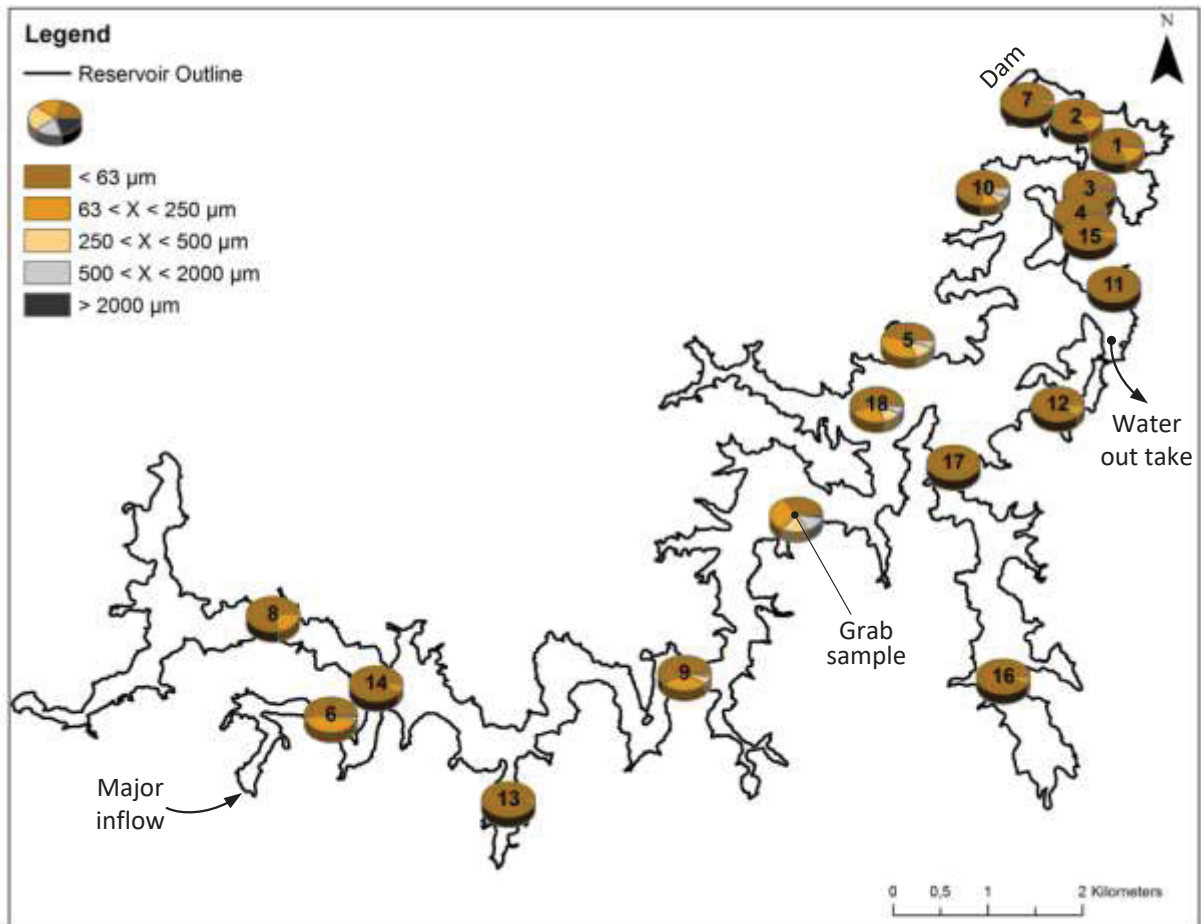


Figure 5-4: Granulometric lakebed characteristics at sampling locations in CR, the numbers indicate the core numbers.

Small branches of the reservoirs feature higher shares of coarse sediment (Figure 5-4: C5, G9, G12, G15; Figure 5-4: Core 5 and Core 10). The same accounts for shallow areas or plateaus within the main parts of the reservoirs (Figure 5-3: C1, G5, G6; Figure 5-4: Core 18 and the grab sample). Larger branches or sidearms do not evince the same pattern, but rather show sediment compositions similar to the main arm (Figure 5-4: Core 13, Core 16 and Core 17).

It has to be kept in mind that CR is nearly ten times larger than VR. Hence for comparison of locations, morphology and topologic characteristics of the single sampling sites the real distances have to be considered. Regarding the shown maps (Figure 5-3 & Figure 5-4) the entire south-western arm and center part of VR is approximately the size of the south-eastern sidearm in CR.

The variation between sediment compositions of neighboring samples already gives a presentiment of the heterogeneity of the sediment distribution in the two reservoirs. Therefore, it is difficult to generally derive the sediment characteristics from the position in

the reservoir. Diligent investigations and a more detailed understanding of the distribution and accumulation mechanisms are necessary.

As a further relevant parameter of sediment distribution and characterization, the total carbon (TC) of the sample material, is depicted in Figure 5-5 and Figure 5-6. Like for the granulometry, here again similarities between the two reservoirs can be found. High TC values are present in the proximal areas of the reservoirs as well as in the profundal close to the dam. Some sidearms and plateaus feature lower TC values. A first comparison of the grain size distribution and the TC indicate the contradiction of high TC values in the coarse material as well as in samples consisting of high shares of fine material. This will be

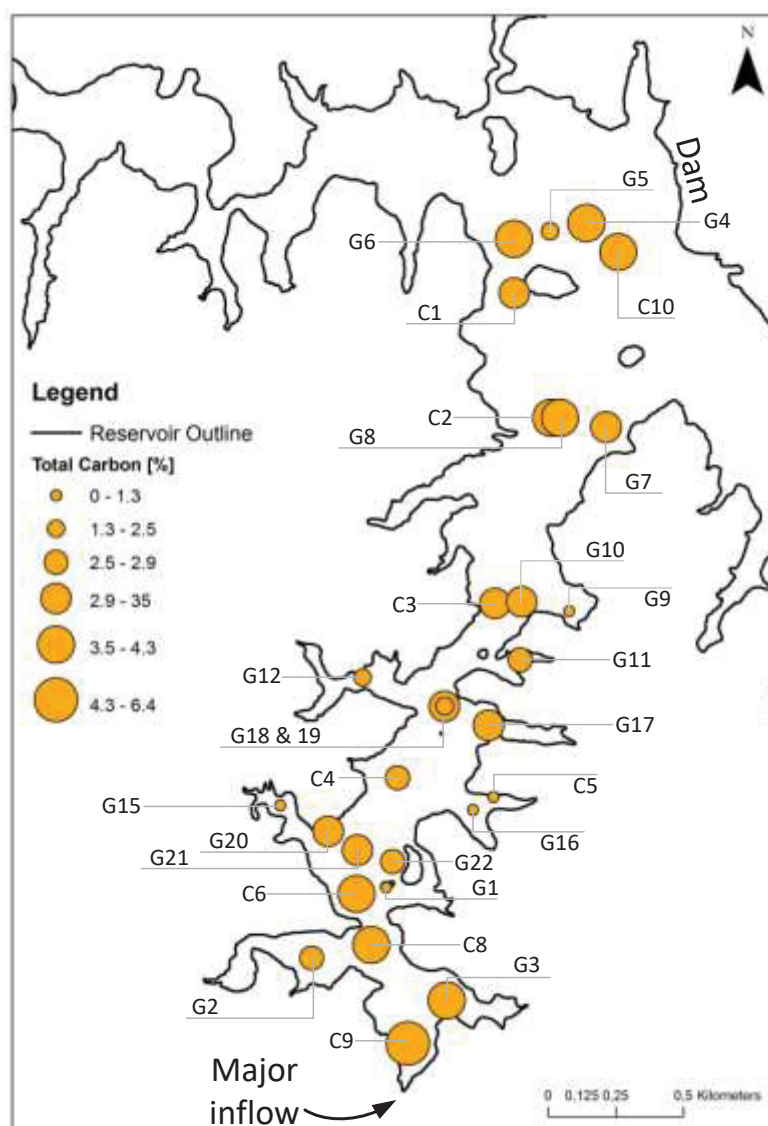


Figure 5-5: TC content in sediment samples in the VR, cores and grabs are named individually.

investigated in the following section of this work.

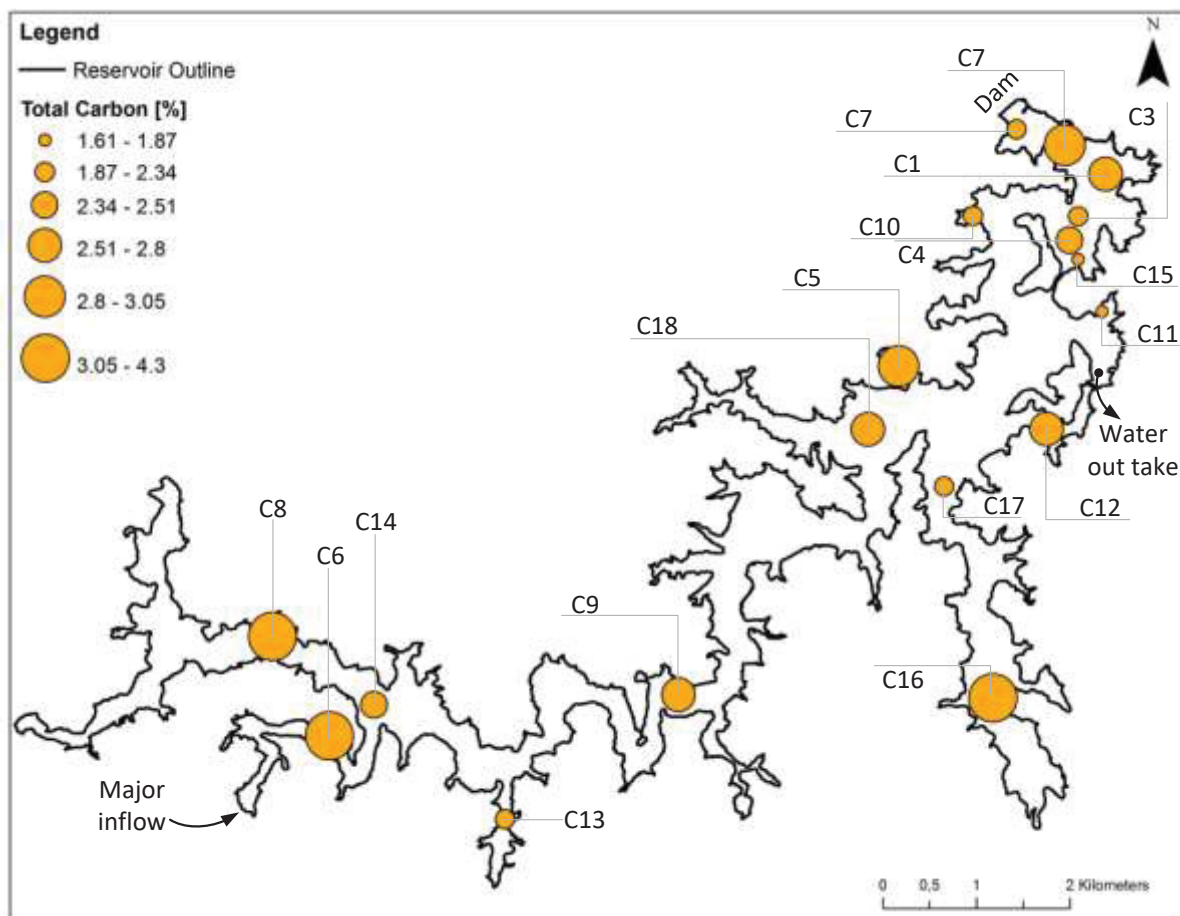


Figure 5-6: TC content in sediment samples in the Capivari reservoir; cores are named individually.

5.1.3 Sediment Parameter Interrelations

This section evaluates the correlations between sediment parameters aiming on the recognition of interrelations. The focus lies on the carbon-related correlations as well as on the particle distribution.

While the carbon-related parameters are important for the biochemical degradation processes and hence for the GHG production in the sediment. The granulometric distribution is one principal factor influencing the density and thus the hydro-acoustic properties of the sediment. It is a principal concern to determine the relationship of physical and granulometric parameters with carbon related parameters. Hence, the loss on ignition and total carbon in conjunction with their interrelation with other parameters is regarded first, looking at the strength of their relationship.

Prior to the regression analyses, all sediment data sets were checked for normal distribution. Data was tested for normal distribution using the Shapiro-Wilk and Kolmogorov-Smirnov tests. With a confidence level of 5%, p-values of around 6.2 for the Shapiro-Wilk and 0.77 for the Kolmogorov-Smirnov test were reached, conforming the normal distribution of the data sets.

The normal distribution cannot be rejected for all sediment parameters, if the values included in the analysis are referring to the same sediment depth (here upper 15 cm). Consequently the following analyses are statistically legitimate.

For understanding the relation between the TC and LOI, it is started from the assumption that the sampled volumes represent the entire spectrum of the sediment types in the reservoirs and also that the errors during the measurement of the LOI are independent from the errors which may occur measuring the TC. The linear regression calculation results in a Pearson r-value of 0.76 (N = 28; $p < 0.01$) (Figure 5-7). Thus, a significant positive correlation between the two parameters can be stated. Significant correlations between these parameters were also published by Vos et al. (2005).

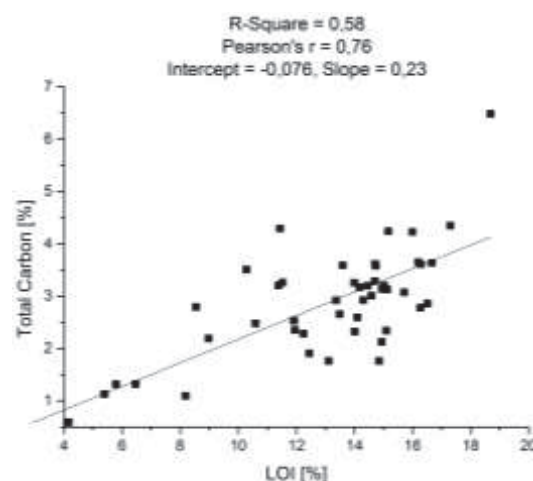


Figure 5-7: Correlation between the total carbon content and the LOI in all core samples from VR and CR; (N = 28; $p < 0.005$).

In this study, due to the absence of any HCl reaction it can be presumed that no inorganic carbon (IC) is present in any sample and that the TC is a very close approximation of the total organic carbon (TOC). This assumption is strongly supported by Ortt, JR. & Richard (2000), who found a correlation of 0.98 between TC and TOC in the absence of IC.

Comparing the sediment composition with carbon related parameters (CRPs), the finest fraction is exemplarily used as a representative value for the entire granulometric distribution. The LOI shows a different behavior than the TC (Figure 5-8 & Figure 5-9). While the proportion of particles $< 63 \mu\text{m}$ stands in a significant positive correlation to the LOI, no clear relation to the TC can be derived. Consequently, the LOI–TC relation must be biased by the clay and silt share in the sediment. To control influence of the silt and clay fraction on the LOI, the TC is again plotted against the LOI, under exclusion of all samples with a silt and clay share of more than 80%. Figure 5-10 shows a highly significant correlation with $r = 0.92$ ($N = 20$, $p = 0.01$). Consequently, the LOI is clearly influenced by high shares of silt and clay. This suggestion is corroborated by Craft et al. (1991) and Vos et al. (2005)

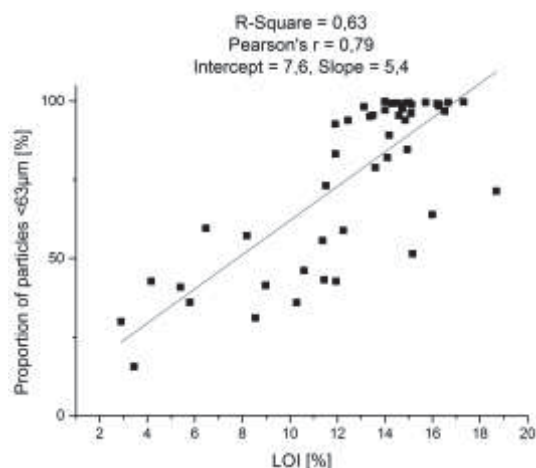


Figure 5-8: Share of finest particle fraction plotted against LOI; all cores and grabs from CR and VR are included ($N=45$; $p<0.001$).

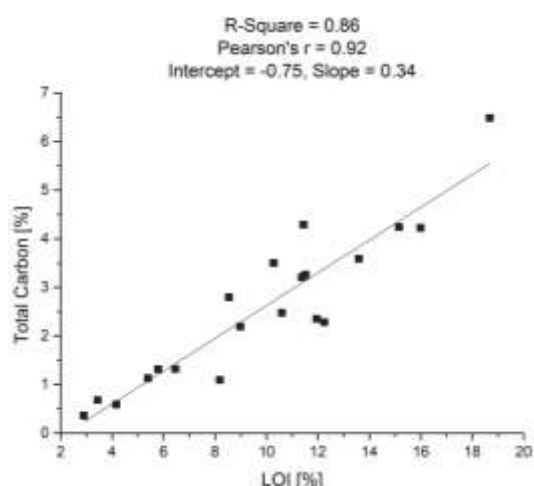


Figure 5-10: Correlation of TC with LOI based on a selection of cores from VR and CR with less than 80% share of finest particle fraction; ($N = 20$, $p = 0.01$).

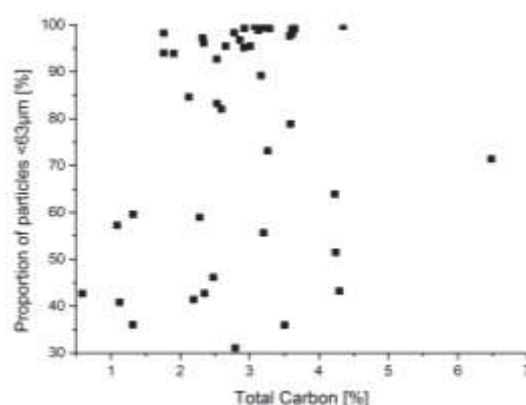


Figure 5-9: Share of finest particle fraction depicted over TC; all cores and grabs from CR and VR are included.

As a primary value for the interpretation of SBC-data the density is of importance. Since the bulk density (BD) could not be determined for the grab samples, only the results of the core samples are presented.

The presence of OC represents one general precondition for the formation of CH₄ bubbles. Based on the assumption that the bulk density of the sediment notably changes with the existence of free gas bubbles (Leifer & Patro, 2002; Sager et al., 1998; Anderson et al., 1998) in the sediment matrix, a relation between OC and density can be assumed.

In Figure 5-12 and Figure 5-11 the relations between density and both CRPs are shown. Both correlations are significant and therefore a direct connection between the bulk density and the presence of organic matter in the sediment can be derived.

Organic compounds always feature lower densities than mineral particles and consequently, a general coherence with the bulk density can be assumed. Yet, the share of OM in the sediment in both reservoirs is between 2–6% and hence the influence on the density is relatively low.

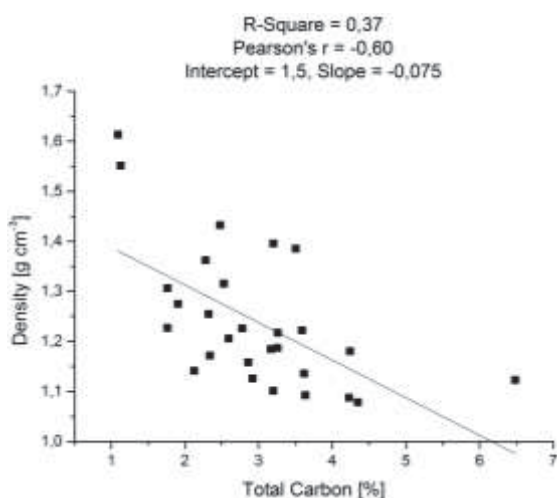


Figure 5-12: TC depicted over bulk density from all cores in VR and CR; (N = 28; $p < 0.01$).

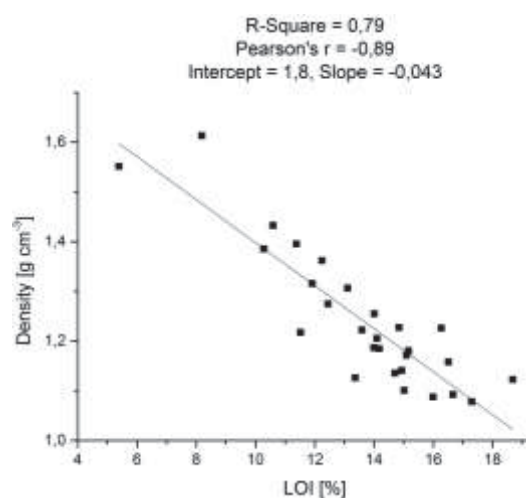


Figure 5-11: LOI depicted over bulk density from all cores in VR and CR; (N = 28; $p < 0.01$).

The values of the LOI scatter less and hence the Pearson r is, with a value of -0.89 considerably stronger correlated than the -0.60 from the BD–TC relation. However, both regression analyses support the same suggestion. The higher the organic content of the sediment, the lower the bulk density. This stands in accordance to several findings in the literature (Sobek et al., 2012).

Depth-dependence of sediment features

Aiming on the understanding of principal processes in the reservoirs an important aspect is the distribution of sediment parameters in relation to the water depth. For the comparison of the depth-dependent data from both reservoirs the local depth was recalculated to *relative depth*. The actual local depth was set into relation to the maximum depth of the corresponding reservoir. Thus, the deepest measuring points can be grouped together likewise the points from shallow areas, independent from the general depth difference of the two reservoirs.

Total Carbon:

Figure 5-13 (A and B) compares the relative depth at the sampling locations with the TC content in both reservoirs. They coincide with the highest TC values found in the shallowest areas of the reservoir, which in these cases are equal to the proximal. Furthermore, it can be observed that after relatively low TC values in the mid-depth range an increase in the carbon content in the deepest parts of the reservoir is present. Joining the information from Figure 5-5 and Figure 5-6 with Figure 5-13 A and B, areas with similar carbon content ranges can be defined. The reservoirs can be separated in the proximal, the middle part, the profundal and the sidearms. Yet, it has to be stated that not all of the sampled sidearms show the same behavior (Figure 5-6: Core 5, 13 and 16). Some side arms show high TC values while others feature values at the lower end of the entire spectrum. It is suggested that this is due to erosion processes on the one hand and direct introduction of organic material from the surroundings on the other hand. Strong erosion leaves only the bare soil with relatively low

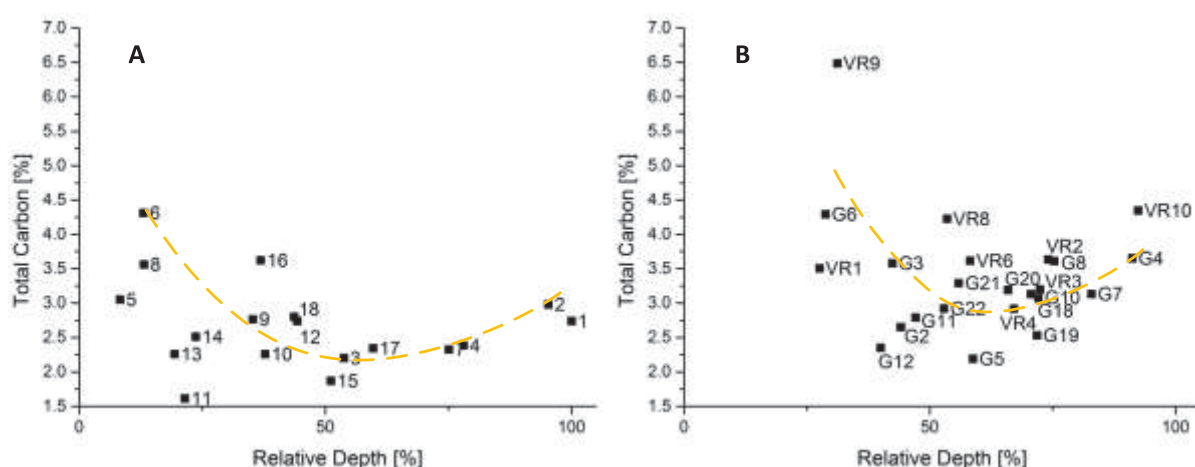


Figure 5-13: Total carbon vs. the relative depth in A) Capivari reservoir and B) in the Vossoroca reservoir, VR = core samples.

TC contents around 2–2.5%. While the accumulation of organic rich material introduced from the shore vegetation increases the TC value significantly.

Sulfur & Proportion of Particles:

Comparing the allocation of the finest particle fraction with the content of sulfur, a contrary trend can be observed (Figure 5-14). While the share of the finest fraction has a high variability with an increasing average slope up to a relative depth of about 50%, the sulfur content is stable on a low level until 60% relative depth, followed by an increasing slope. Both patterns suggest that between 50–60% a switch-over of conditions takes place. The depth corresponds to a depth of around 18 m in CR and 11 m in VR. Finest particles accumulate and the sulfur content constantly increases. The switch-over can be attributed to the presence of the oxycline, which is located in a depth of 11–15 m in Capivari reservoir.

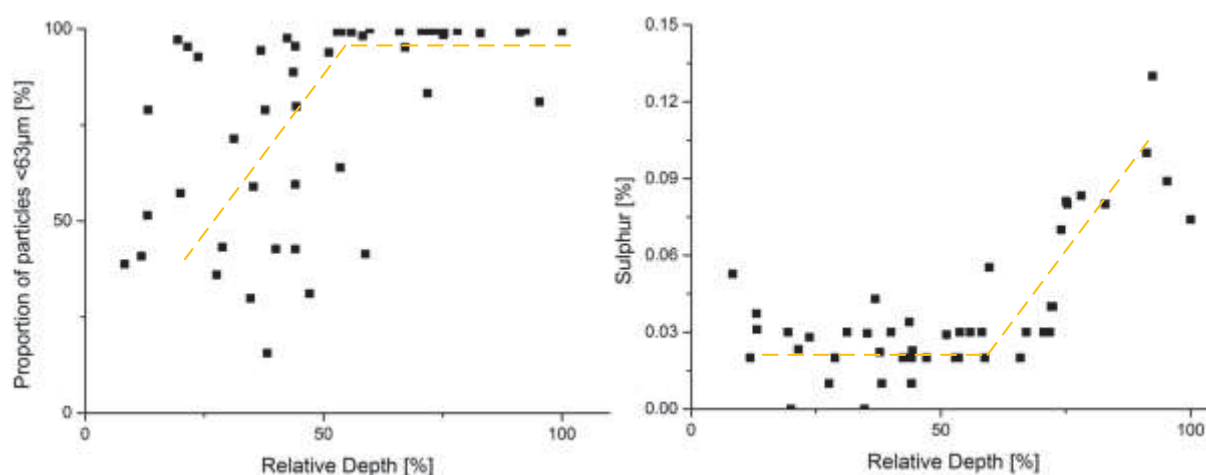


Figure 5-14: Comparison of finest fraction share and sulfur content in relation to the relative depth; Contents of the upper 15 cm of the sediment sample material from VR & CR are included in the graph; the orange line illustrates the trends described.

Iron & Phosphor:

The distribution of total iron content and total phosphor depicted over the relative depth is given in Figure 5-16 and Figure 5-15. Both graphs show a similar behavior between the two reservoirs. Capivari reservoir possesses higher Fe_{tot} and P_{tot} contents independent from the depth of the sediment sample. Iron and phosphor reveal comparable trends, regarding the inter- and intra-reservoir behavior. Regression analysis results indicate similar relations and slopes, leading to significant positive correlations with r-values between 0.60 and 0.88 (CR: $N = 18$, $p < 0.05$; VR: $N = 30$, $p < 0.05$).

Based on the fact that Fe_{tot} and P_{tot} are distributed in a comparable manner, Fe_{tot} is selected as a representative for both parameters due to the higher r-values. The relation of Fe_{tot} and the particle distribution is evaluated in Figure 5-17. There is a weak tendency that the lowest Fe_{tot} -values are found in coarser sediment. Even if the correlations are still in a significant range, the variation of the values is high, particularly if the results for higher shares of the finest fraction are regarded. Above 90% of finest fraction there is no clear tendency to be derived and hence the Fe_{tot} and P_{tot} content can be seen as almost independent from the particle composition. However, very coarse sediments feature relatively low contents of iron.

The found results are in accordance to the iron contents published by Passier & deLange (1998). The elevated contents of iron in deeper parts of the reservoir can be explained by the absence of oxygen, lower redox-potentials and hence the permanent fixation of iron bound to sulfur (FeS or FeS_2).

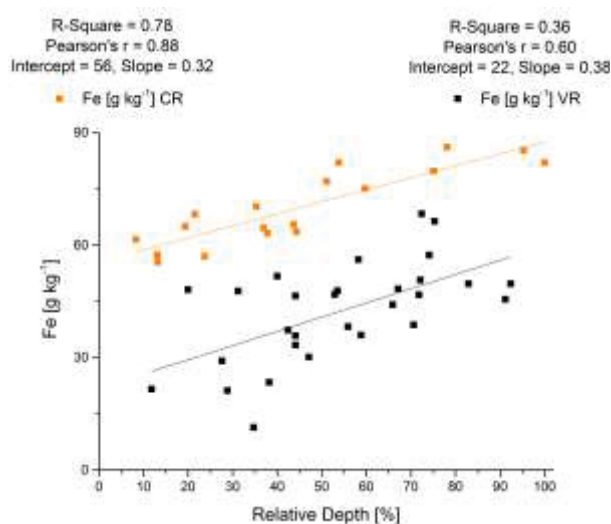


Figure 5-16: Total iron content vs. relative Depth and reservoir specific linear correlation (CR: N = 18, $p < 0.05$; VR: N = 30, $p < 0.05$).

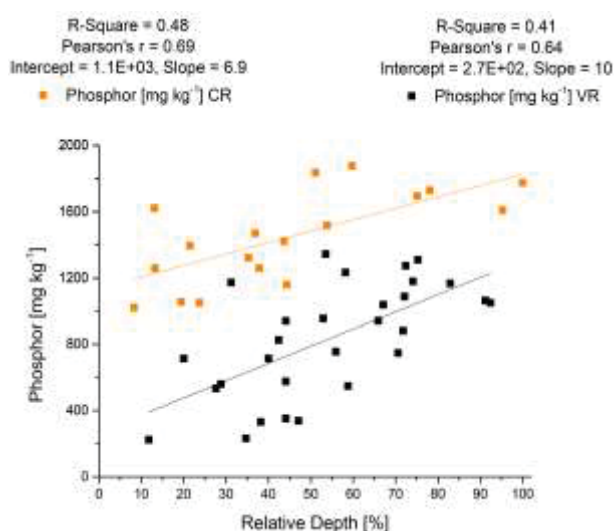


Figure 5-15: Total phosphor content vs. relative Depth and reservoir specific linear correlation (CR: N = 18, $p < 0.05$; VR: N = 30, $p < 0.05$).

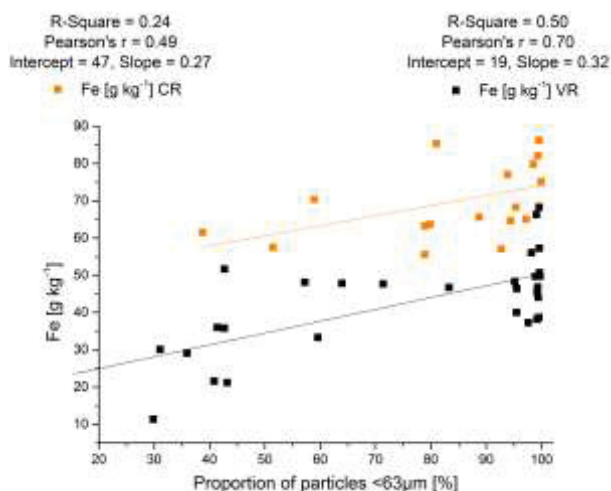


Figure 5-17: Total iron content vs. share of finest sediment fraction and reservoir specific linear correlation (CR: N = 18, $p < 0.05$; VR: N = 30, $p < 0.05$).

5.1.4 Multivariate Approach

In order to assess relations between more than one sediment parameter, sets of supposedly related parameters are used as input data for a Principal Component Analysis (PCA) (Grant, 1990). The normal distribution of the relevant values was confirmed (chapter 5.1.3) and consequently a PCA is possible. The PCA was conducted using OriginLab 9.0. The correlation matrix for the PCA is given in Table 5-3.

Table 5-3: Correlation matrix of the five input parameters

	LOI	Total carbon	Density	Depth	Proportion of particles < 63µm
LOI	1	0.69	0.59	0.55	-0.87
Total carbon	0.69	1	0.11	-0.07	-0.58
Density	0.59	0.11	1	0.62	-0.61
Depth	0.55	-0.07	0.62	1	-0.61
Proportion of particles <63µm	-0.87	-0.58	-0.61	-0.61	1

The Biplot shows the two extracted principal components (PC) and the loadings of the input parameters (Figure 5-18). PC1 is mainly composed of the coefficients of the eigenvectors from the LOI (0.53) and Density (-0.53), while the PC2 is dominated by the eigenvectors of total carbon (-0.72) and the particle share < 63 µm (0.53).

Density and LOI are well explained by the PC1 while the TC has a tendency to be explained by the PC2.

Two distinct outcomes of the PCA can be described. First, the density opposes the LOI and second, the share of the finest fraction is grouped together with the relative depth.

The relation between density and LOI was already statistically described in chapter 5.1.3. It can be explained by the fact that the

LOI includes the influence of the grain size distribution (Figure 5-8) and also the total carbon content (Figure 5-10). The position between both vectors in the biplot underlines this coherence. Consequently, the LOI has a strong correlation with the granulometric features determining the density. Since high values of both, the TC and the share of the finest fraction are prerequisites for the formation of bubbles, the strong relation to sediment density becomes clear.

The grouping of the silt and clay fraction and the relative depth is explained by the dependence of sedimentation processes respectively resuspension. High particle shares of silt and clay are mainly found in the deeper areas of the hypolimnion, where flow velocities and therefore the impact from shear stress is low.

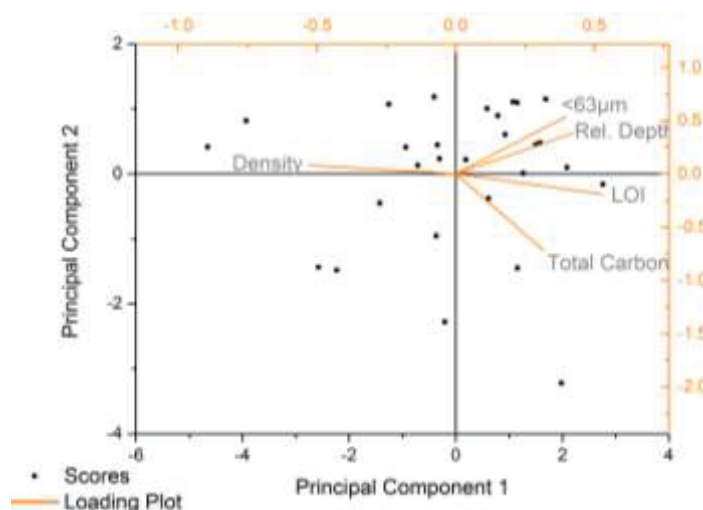


Figure 5-18: Biplot of the PCA results of a selection of sediment parameters.

5.1.5 Synopsis

Summarizing the central results of the *sediment sampling analysis*, the following aspects can be named:

- The evaluated distribution and behavior of the sediment is very similar in both reservoirs. The formation of significantly different zones in regards of sediment characteristics, in the reservoirs is identified. A first demarcation indicates the following demarcation: inflow (proximal), outflow (profundal), small sidearms and inner areas with intermediate depth (plateaus). Proximal and profundal feature the highest contents of TC.
- The LOI cannot be used as a direct substitute for the TOC. It is rather a mixed parameter combining the share of silt and clay and the OC content. Under exclusion of samples with shares higher than 80% silt and clay fraction, the LOI is strongly correlated with the OC content.
- In the absence of inorganic carbon, the total carbon equals the total organic carbon (TC = TOC).
- TC and LOI have a high potential to explain the density changes of the sediment, since both feature significant correlations with the density values.
- Fe_{tot} , P_{tot} show the same behavior regarding distribution and concentration gradients in the sediment.
- Due to the depth distribution of the silt and clay fraction and the sulfur content a switch-over zone is suggested. At an average relative depth of 50-60% an increase, respectively accumulation is observed. This corresponds to a depth of around 18 m in CR and 11 m in VR.

5.2 Hydro-acoustic Results

In this section both reservoirs will be addressed, but more information is given about the Capivari reservoir, referring to the sampling strategy of this work (chapter 0). Results from Vossoroça reservoir will serve as a data pool for comparison. However, most of the hydro-acoustic research was conducted in CR and therefore this reservoir plays the central role in the detailed investigation in the rest of this study. Based on the bathymetric results the depth distribution of the reservoirs was derived. The creation of a 3D-surface of the CR allowed the calculation of the slope distribution, which is suggested to stand in a direct context with sediment focusing. This analysis is ensued by the detection and illustration of the sediment thickness, exemplifying zones of sediment accumulation. After a validation of this approach, the SBC is used for spatial interpolation of selected sediment parameters, which are related to the formation of GHGs. Finally, the outcomes of the static and dynamic bubble detection are visualized and set into context with the underlying sediment.

5.2.1 Bathymetry and morphometric Implications

This chapter and its subchapters contain the principal results from the bathymetric data ascertainment and the results derived from the resulting 3D-reservoir model. The reservoir topography including depth and slope distribution are delineated.

Depth interpolation

Vossoroça Reservoir

Interpolated results of the bathymetric survey in the VR are shown in Figure 5-19. If regarded in detail the old riverbeds in both southern arms can be recognized. The profundal lies in front of the restricted zone west of the dam. Here the maximum depth reaches 17 m. The south-western arm is characterized by the feature that, in contrast to other large arms, the inflow area is relatively deep. This is caused by the effect that the main river enters the reservoir in a small water fall, causing the minimum depth of around 2–3 m at this inflow.

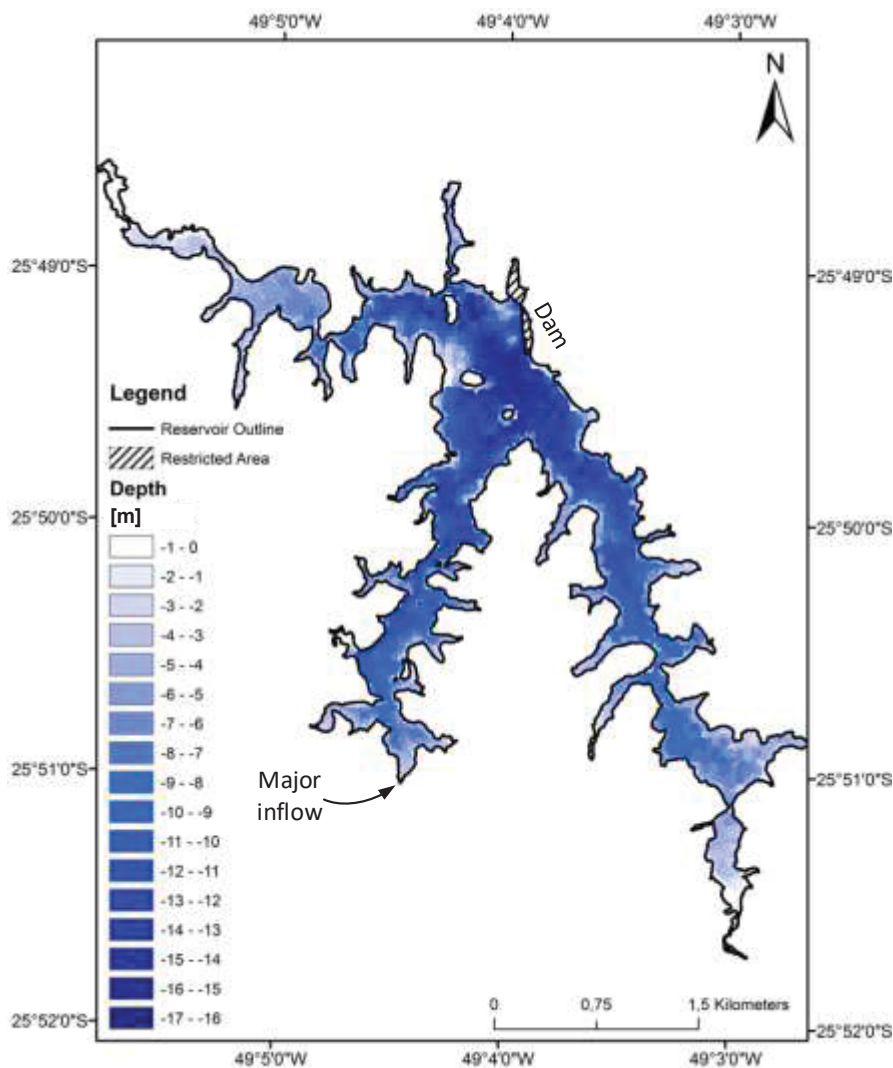


Figure 5-19: Map showing the depth below the surface of the VR as a function of latitude and longitude in March 2011.

Capivari Reservoir

Like the old lakebed in VR, the former run of the Capivari River can still be distinguished from the rest of the lakebed in CR (Figure 73). Here the deepest area is located in the northern part in front of the dam. During the survey of the bathymetric data the water level did not allow sailing in the south-western inflow areas since the water depth was lower than 1.8 m and old uncut trees were encountered regularly. The histogram in Figure 72 gives information about the depth distribution in CR.

At the time of measurement 50% of the reservoir had a depth lower than 7 m. Only 4% of the reservoir are deeper than 25 m. It has to be mentioned that the values shallower than 1.5 m were generated during the interpolation process since those areas are too shallow for an exact measurement. In the histogram the hashed areas from the map are not included, thus in reality, the share of shallow areas is slightly larger.

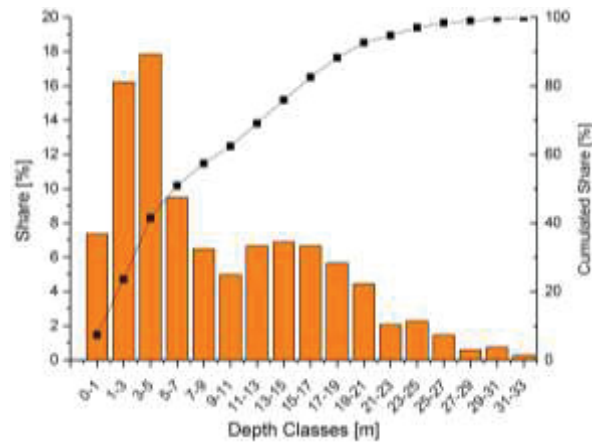


Figure 5-20: Histogram of the distribution of depth classes in CR.

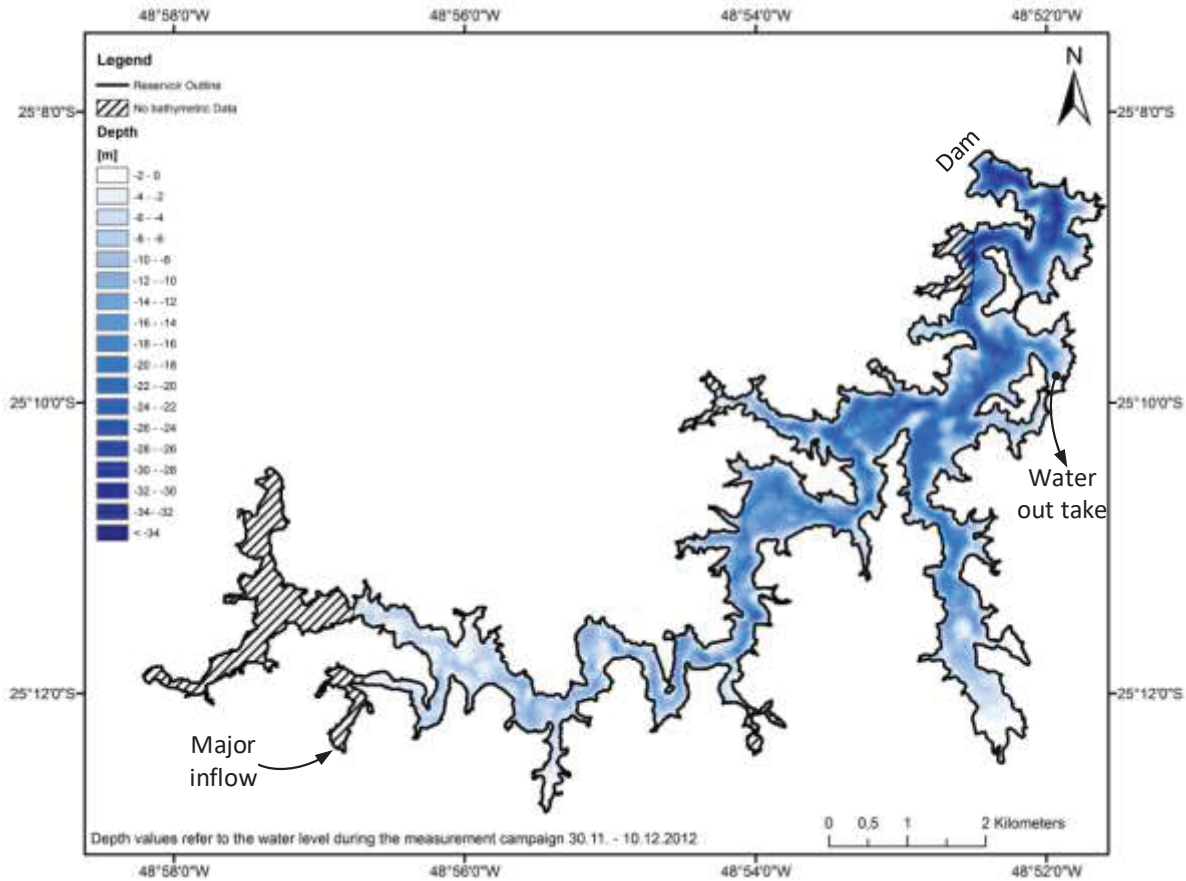


Figure 5-21: Map showing the depth below the surface of the CR as a function of latitude and longitude in November 2012.

Slope calculation

The slope distribution was calculated with regards to the potential coherence with the sediment distribution and the influence on SBC.

Based on the bathymetric data a Triangulated Irregular Network (TIN) was constructed. The TIN served as the data basis for the calculation of slope polygons using ArcGIS 10.2.2. For the construction of equi-inclined slope polygons break values were consigned. The values are given in Table 5-4.

Since a large range of slope inclinations is present in the reservoir, the classes were chosen from 0°–55° including the very steep slopes.

Figure 5-22 shows the distribution of the most abundant four slope classes and illustrates the corresponding inclination. About 52% of the lakebed in CR has a slope between 0–7.5° (class 1 & 2). Around 16% of the area can be added to the extremely steep areas with inclinations above 17.5° (classes 5–

Table 5-4: Class breaks for slope inclination

Class Breaks [°]	Slope Class #
0	0
5	1
10	2
15	3
20	4
25	5
30	6
35	7
40	8
45	9
50	10
55	11

11). These areas are illustrated in tones of orange in Figure 5-23 while flat or less inclined areas are represented by darker tones of gray. It can be observed that the steepest areas follow the old riverbed and are located particularly at the undercut slope sides. The closer to the dam and hence the higher the water depth, the more abundant the strongly inclined reservoir banks become. The wider parts of the reservoir feature plateaus on the slip-off slope side.

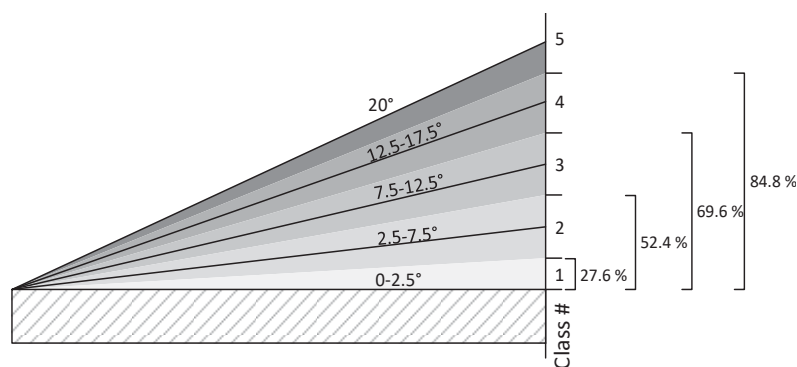


Figure 5-22: Visualization and distribution of the most prevalent slope classes in CR.

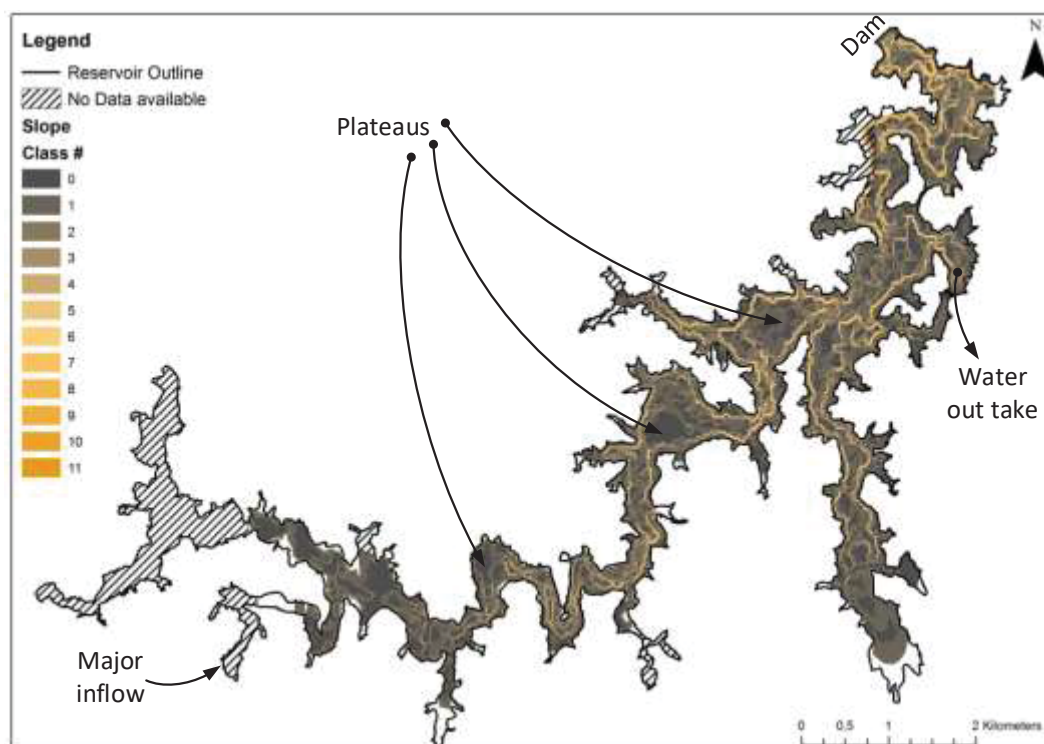


Figure 5-23: Slope polygon map, Slope polygons are defined by the class breaks from Table 5-4.

5.2.2 Sediment Thickness (ST)

Based on the differences between the processed bottom lines (38 & 200 kHz), the sediment layer thickness was calculated and then interpolated (IDW), it is illustrated in Figure 2-24. An area of 11.1 km² was calculated. In accordance with the literature, the results show a sediment accumulation in the old riverbed and potential former depressions (Blais & Kalff, 1995; Gilbert, 2003). Highest interpolated thicknesses reach 3 m while the most abundant magnitudes stay below this value. Due to the interpolation process, extreme values are lost. At some single points, magnitudes of up to 3.8 m were calculated, but since these measurement points have a share of less than 0.001% of the total point number, their loss can be neglected. A tendency can be derived, the ST reaches only minimum values in the outer reaches of the reservoir close to the shore line. Clear coherence to the water depth can be derived. In accordance to Gilbert (2003) plateau areas and shallow parts are not capable of accumulating significant amounts of sediment.

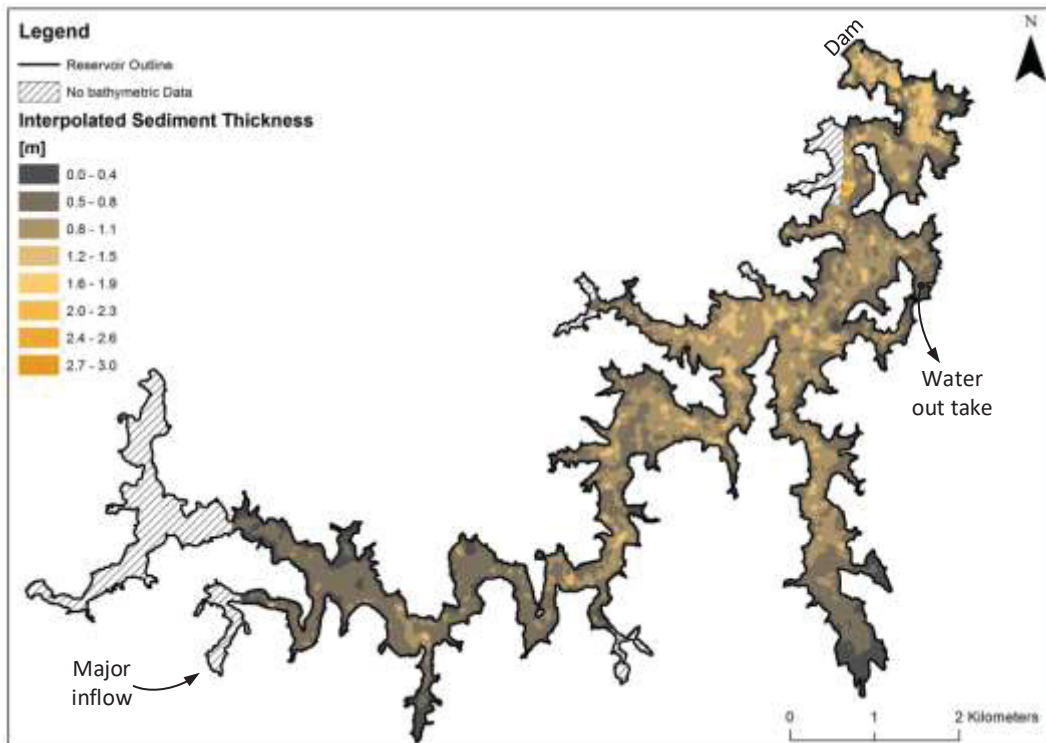


Figure 5-24: Sediment thickness distribution in CR, results based on the dynamic hydro-acoustic measurements and IDW interpolation.

It can be stated that the sediment overlay classes from 0.4–0.9 m contribute to around 70% of the entire reservoir lakebed surface (Figure 5-25). Areas with no overlay at all to a thickness of 0.1 m of sediment cover contribute to 0.8 km² (7%) of the entire lakebed surface. This can be attributed to the steep slopes and drawdown areas along the shore line. These findings match the results from Anderson (2010).

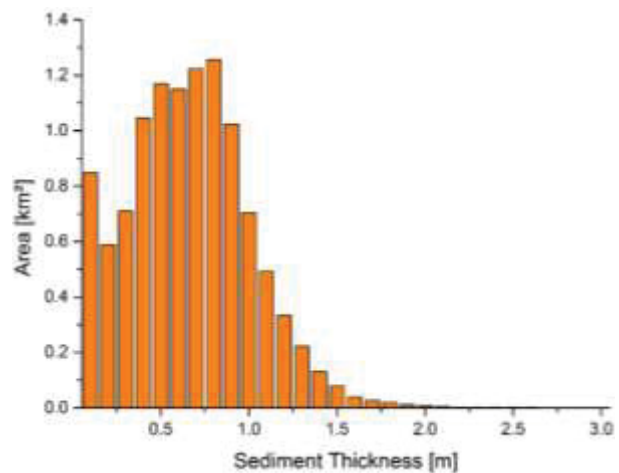


Figure 5-25: Spatial share of sediment thickness classes in the CR.

To control the quality of the sediment thickness interpolation and also the precision of the applied model for the data points of the driven survey, a cross validation was conducted. The estimated ST values from the coring sites were used as independent subsamples. Due to the fact that, the same methodology was used at the static measurement sites and that none of these points is included in the data set of the driven lines, they may represent the validation data set. The cross validation shows a high grade of correlation ($r = 0.92$; $N = 16$; $p < 0.01$) and a linear relation between the interpolated and measured values (Figure 5-26). The calculated slope value of the regression (1.1) is very close to the expected value of 1.0. These results suggest that the spatial interpolation is a versatile tool producing values within a valid range. Although the results from this method cannot be ultimately controlled (limited coring depth), an approximation of the validity is done.

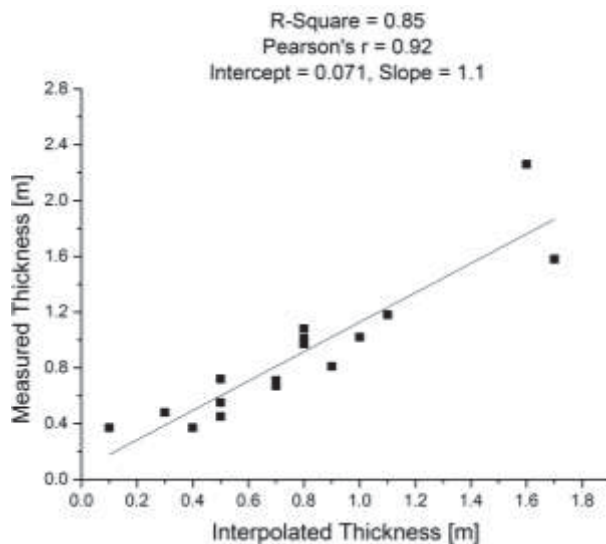


Figure 5-26: Measured vs. interpolated sediment thickness values; Correlation of the ST values, $N=16$; $p < 0.01$.

Since the maximum core penetration depth was 75 cm, an exact sediment layer determination was not possible at most sites (core tubes shorter than ST). Still, the hydro-acoustic ST values can be set in relation to the absolute core penetration depths. Figure 5-27 gives an overview about the differences between the sediment depths values obtained from the three approaches. Generally, the results for sediment thicknesses around 0.3–0.5 m tend to have a high correlation between all three values. Larger interpolated or measured sediment depths cannot be reflected by the coring depths. However, there is a tendency that the core penetration at locations with higher ST values is deeper. This can be explained by the fact that high sediment thicknesses are only

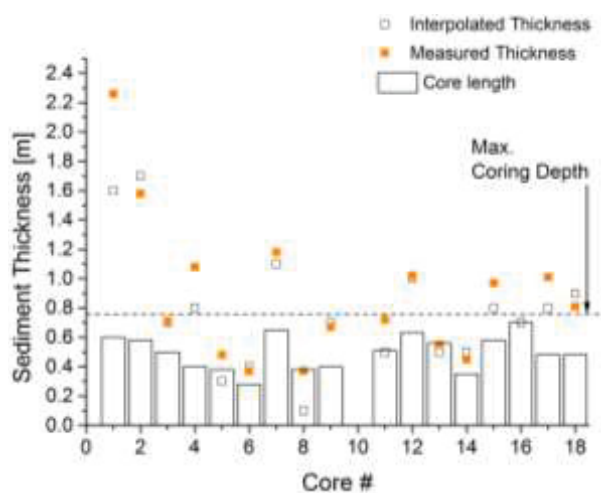


Figure 5-27: Comparison of the three approaches for sediment thickness estimation in CR.

reached through high sedimentation rates, which in Capivari reservoir means an accumulation of soft sediment. Hence, at these locations the corer can easily penetrate the sediment. Additionally to the softer sediment, the water depth at these sites tend to be higher (Figure 5-24), as most of the sediment accumulates in the deeper regions. Therefore, it is suggested that the coring device has a prolonged acceleration phase during the fall and thus can penetrate the sediment deeper.

5.2.3 Seabed Classification (SBC)

Following the hydro-acoustic measurement strategy, two general methods of seabed classification were conducted. The first aims on the creation of correlated acoustic – sediment parameter pairs, while the second method targets the clustering of sediment samples in groups of the same hydro-acoustic behavior. Results of both approaches are presented in the following.

5.2.3.1 Approach one – creating sediment-acoustic pairs

For this approach the results from the SBC are divided into two parts, due to the underlying methodology. The results obtained during the dynamic and stationary are separated. In addition the results obtained from the phase one measurements (VR), which were the basis for the methodological adaptations in phase two, are presented separately from phase two results (CR).

Stationary SBC results

As described in the methodology part (chapter 4.2.3) the stationary SBC was carried out with a set of configurations, alternating the pulse length (τ) and/or the input power. Incidence angle, frequencies and further parameters were kept constant. Due to a very high number of conducted single correlations, 896 pairs for the Vossoroca and 2,560 combinations for Capivari reservoir, only the most promising correlations between the SBC-features and the sediment parameters are presented.

Hydro-acoustic data was tested for normal distribution using the Shapiro-Wilk and Kolmogorov-Smirnov tests. With a confidence level of 5%, p-values of around 5.7 for the Shapiro-Wilk and 0.76 for the Kolmogorov-Smirnov test were reached, conforming the normal distribution of the data sets. Consequently the following analyses are statistically legitimate.

SBC in the Vossoroça Reservoir

To assess the use of the hydro-acoustic parameters for lakebed characterization and prediction all combination of the relevant parameters were correlated. Table 5-5 and

Table 5-6 list the Pearson r-values for the core samples and the grab samples. The 38 and 200 kHz frequencies are shown next to each other for a direct comparison. R-values above the significance level are highlighted (Core samples: $p < 0.05$ for $r = 0.63$, $N = 10$; Gab samples: $p < 0.05$, $r = 0.44$, $N = 21$). For both sample types the average performance of the lower frequency is clearly higher. In addition, the correlation with core samples reach higher levels of conformance. The best detectable parameter is the “*density*”, which independently of the hydro-acoustic parameters reaches average r-value of 0.62 and maximal r-values of 0.89. High correlations are also reached between the particle composition and most hydro-acoustic parameters. Here the best pair, % < 63 μm vs. E1, reaches an r-value of 0.91. Comparably high correlations are not reached within the group of grab samples (best value: $r = 0.60$).

Compared to the quality of the correlations between cores and hydro-acoustic parameters, the correlations with the grab samples are clearly less significant. Based on these findings from Vossoroça, the use of grab samples was substituted by core samples in phase two (apart from one sample).

Table 5-5: Correlations between sediment and acoustic parameters based on the results obtained from the core samples of Vossoroça reservoir; statistical significance is given for $r > 0.63$ ($p < 0.05$, $N = 10$).

kHz	density		Total P		LOI		% < 63 μm		Total C	
	200	38	200	38	200	38	200	38	200	38
E1`	0.10	0.85	0.06	0.62	0.10	0.71	0.17	0.81	0.12	0.50
E1	0.42	0.54	0.43	0.64	0.42	0.44	0.82	0.91	0.05	0.05
attdecSv1	0.25	0.87	0.07	0.66	0.25	0.71	0.30	0.88	0.12	0.38
attSv2	0.43	0.24	0.57	0.07	0.32	0.24	0.67	0.17	0.04	0.53
decSv2	0.11	0.89	0.17	0.63	0.13	0.73	0.25	0.79	0.12	0.51
attdecSv2 (E2)	0.15	0.88	0.29	0.59	0.09	0.74	0.33	0.71	0.09	0.51
attSv1/decSv1	0.24	0.47	0.19	0.23	0.16	0.42	0.63	0.25	0.05	0.47
decSv1/attdecSv2	0.45	0.22	0.51	0.15	0.44	0.33	0.84	0.15	0.08	0.62

Table 5-6: Correlations between sediment and acoustic parameters based on the results obtained from the grab samples of Vossoroça reservoir; statistical significance is given for $r > 0.44$ ($p < 0.05$, $N = 21$).

kHz	Total P		LOI		% < 63 μm		Total C	
	200	38	200	38	200	38	200	38
E1`	0.37	0.27	0.16	0.27	0.18	0.52	0.11	0.14

E1	0.56	0.56	0.37	0.38	0.48	0.54	0.25	0.28
attdecSv1	0.37	0.42	0.21	0.34	0.19	0.60	0.11	0.18
attSv2	0.14	0.04	0.11	0.08	0.05	0.02	0.02	0.05
decSv2	0.30	0.36	0.12	0.31	0.12	0.54	0.08	0.18
attdecSv2 (E2)	0.27	0.33	0.12	0.28	0.11	0.51	0.07	0.16
attSv1/decSv1	0.53	0.22	0.14	0.09	0.37	0.07	0.21	0.10
decSv1/attdecSv2	0.60	0.14	0.37	0.27	0.57	0.07	0.25	0.13

SBC in the Capivari Reservoir

The procedures of the seabed classification followed the methodology in Vossoroça, but with the addition that more parameters were investigated during phase two. The results of the SBC for the two frequencies are given in separate tables (Table 5-7 –

Table 5-10). The 200 kHz frequency produces higher correlations compared to the results from the 38 kHz. This stands in accordance to Anderson & Pacheco, 2011. No clear tendencies can be derived comparing the results of the different input powers 100 and 500 W. The 500 W – correlations tend to have less pairs with significant correlations but some feature higher r-values. In comparison to the literature values from Anderson & Pacheco, 2011 the overall correlations are less significant since no parameter combination reaches values above 0.81. This can be the case because the investigated reservoirs in the literature are morphologically less complex and show uniform structures and gradients. However, the highlighted correlation pairs demonstrate the possibility of SBC in both investigated reservoirs.

Although the correlations between the fractal dimension and various sediment parameters presented by Anderson & Pacheco (2011) are promising, the best correlations obtained in this work including the fractal dimension, reach only an r-value of 0.59 (Table 5-9). Accordingly, the fractal dimension was discarded for the detailed analysis of the correlations and hence further results are not presented in this work.

Under the perspective, that outliers are not yet excluded from the regression calculations, a potential of significantly higher correlations is given, if results are regarded and adapted in detail. This is done for selected parameters as a preparation for the spatial interpolation. The selected correlation pairs for the spatial interpolation are highlighted in orange (Table 5-7 and Table 5-9).

Table 5-7: Correlations between sediment and acoustic parameters (200 kHz, 100W) based on the results obtained from the core samples of Capivari reservoir; statistical significance is given for $r > 0.47$ ($p < 0.05$, $N = 18$).

	E1`	E1	attdecSv1	attSv2	decSv2	attdecSv2 (E2)	attSv1/ decSv1	decSv1/ attdecSv2	FD linear	FD non linear
density	0.53 (A,B)	-0.53 (D)	-0.39 (D)	0.48 (B)	0.47 (B)	0.47 (B)	-0.60 (B)	0.38 (B)	-0.39 (B)	-0.29 (B)
Total_P	-0.53 (B)	0.59 (D)	-0.36 (B)	-0.43 (B)	-0.43 (B)	-0.42 (B)	0.52 (B)	-0.49 (C)	0.58 (B)	0.59 (B)
LOI	-0.32 (B)	0.38 (D)	0.58 (D)	-0.18 (B)	0.52 (D)	0.46 (D)	0.54 (B)	-0.36 (B)	0.26 (B)	-0.33 (D)
% < 63µm	-0.55 (A)	0.81 (C)	0.44 (D)	-0.54 (B)	-0.46 (B)	-0.46 (B)	0.71 (B)	-0.67 (C)	0.53 (B)	0.46 (B)
Total_S	-0.41 (B)	0.51(C)	0.51 (C)	0.25 (A)	0.26 (D)	0.23 (D)	0.55 (B)	-0.34 (C)	0.53 (B)	0.46 (B)
Total_C	0.39 (C)	-0.37 (C)	0.42 (B)	0.38 (C)	0.40 (C)	0.4 (C)	-0.36 (C)	0.54 (C)	-0.45 (D)	-0.53 (C)
D_90_V	0.13 (D)	0.25 (C)	0.13 (B)	-0.24 (D)	-0.14 (A)	-0.14 (A)	0.12 (B)	0.41 (C)	0.21 (A)	0.32 (D)

Table 5-8: Correlations between sediment and acoustic parameters (200 kHz, 500W) based on the results obtained from the core samples of Capivari reservoir; statistical significance is given for $r > 0.47$ ($p < 0.05$, $N = 18$).

	E1`	E1	attdecSv1	attSv2	decSv2	attdecSv2 (E2)	attSv1/ decSv1	decSv1/ attdecSv2	FD linear	FD non linear
density	0.45 (B)	-0.61 (D)	0.29 (A)	0.53 (B)	0.42 (A)	0.43 (A)	-0.51 (B)	0.42 (D)	-0.4 (A)	-0.42 (C)
Total_P	-0.55 (B)	0.61 (D)	-0.36 (A)	-0.44 (D)	-0.45 (B)	-0.45 (B)	0.55 (B)	-0.53 (D)	0.51 (B)	0.53 (B)
LOI	-0.27 (B)	0.39 (D)	0.38 (C)	-0.41 (B)	0.43 (D)	0.38 (C)	0.58 (B)	-0.49 (B)	0.21 (A)	0.2 (C)
% < 63µm	-0.34 (A)	0.54 (C)	0.32 (D)	-0.61 (B)	-0.47 (A)	-0.48 (A)	0.47 (A)	-0.56 (B)	0.50 (A)	0.38 (B)
Total_S	-0.45 (B)	0.42 (D)	-0.26 (A)	-0.23 (D)	0.24 (C)	0.25 (C)	0.67 (B)	0.34 (B)	0.34 (B)	0.37 (D)
Total_C	0.46 (B)	-0.38 (C)	0.35 (A)	0.32 (A)	0.33 (B)	0.33 (B)	-0.35 (A)	0.52 (C)	-0.58 (C)	-0.46 (B)
D_90_V	0.26 (A)	0.33 (D)	0.24 (A)	-0.46 (C)	-0.23 (A)	-0.21 (A)	-0.2 (D)	-0.35 (A)	0.16 (B)	-0.31 (D)

Table 5-9: Correlations between sediment and acoustic parameters (38 kHz, 100W) based on the results obtained from the core samples of Capivari reservoir; statistical significance is given for $r > 0.47$ ($p < 0.05$, $N = 18$).

	E1`	E1	attdecSv1	attSv2	decSv2	attdecSv2	attSv1/ decSv1	decSv1/ attdecSv2	FD linear	FD non linear
density	0.47 (B)	-0.59 (C)	-0.12 (D)	0.58 (B)	-0.42 (D)	0.41 (B)	-0.52 (B)	0.40 (C)	-0.44 (A)	-0.59 (B)
Total_P	-0.65 (B)	0.44 (C)	-0.50 (D)	-0.53 (B)	-0.57 (B)	-0.59 (B)	0.51 (B)	-0.54 (C)	-0.60 (D)	0.28 (B)
LOI	0.20 (D)	0.28 (C)	0.3 (D)	-0.27 (B)	0.33 (D)	0.25 (D)	0.29 (A)	-0.11 (A)	0.17 (A)	0.30 (C)
% < 63µm	-0.42 (A)	0.51 (B)	0.3 (C)	-0.44 (B)	0.37 (D)	-0.31 (B)	0.58 (A)	-0.4 (A)	0.61 (A)	0.49 (A)
Total_S	-0.42 (B)	0.23 (B)	-0.22 (C)	-0.42 (B)	-0.20 (C)	-0.27 (C)	0.36 (B)	0.25 (B)	0.27 (A)	0.54 (A)
Total_C	0.42 (C)	-0.56 (B)	0.38 (A)	0.47 (C)	0.31 (A)	0.31 (A)	-0.48 (B)	0.52 (B)	0.49 (C)	-0.32 (D)
D_90_V	0.36 (D)	0.44 (B)	-0.31 (A)	0.22 (B)	0.22 (B)	-0.15(A)	-0.24 (D)	-0.27 (A)	0.22 (D)	0.35 (D)

Table 5-10: Correlations between sediment and acoustic parameters (38 kHz, 500W) based on the results obtained from the core samples of Capivari reservoir; statistical significance is given for $r > 0.47$ ($p < 0.05$, $N = 18$).

	E1`	E1	attdecSv1	attSv2	decSv2	attdecSv2	attSv1/ decSv1	decSv1/ attdecSv2	FD linear	FD non linear
density	0.29 (A)	-0.63 (C)	-0.44 (B)	0.34 (A)	-0.33 (D)	0.26 (A)	-0.36 (A)	0.33 (D)	-0.63 (A)	-0.25 (A)
Total_P	-0.57 (A)	0.31 (B)	-0.32 (A)	-0.56 (A)	-0.45 (A)	-0.47 (A)	0.40 (A)	-0.43 (C)	-0.45 (C)	0.48 (D)
LOI	0.23 (C)	0.33 (B)	0.57 (C)	-0.35 (A)	0.33 (C)	0.29 (C)	0.49 (A)	-0.17 (B)	0.29 (A)	0.43 (B)
% < 63µm	0.49 (D)	0.70 (B)	0.60 (D)	-0.41 (A)	0.40 (D)	0.39 (D)	0.46 (A)	-0.49 (B)	0.53 (A)	0.2 (B)
Total_S	-0.48 (A)	0.34 (B)	0.32 (C)	-0.57 (A)	-0.33 (A)	0.34 (A)	0.43 (A)	-0.33 (B)	0.17 (B)	0.33 (D)
Total_C	0.32 (A)	-0.49 (B)	0.17 (A)	0.35 (A)	0.41 (D)	0.39 (A)	-0.29 (B)	0.53 (A)	-0.43 (B)	-0.51 (D)
D_90_V	0.30 (D)	0.52 (B)	0.40 (B)	-0.20 (A)	0.40 (B)	0.14 (D)	0.10 (A)	-0.26 (B)	0.57 (C)	0.33 (A)

Dynamic SBC – the entire reservoir

Based on the regression models from the static measurements the corresponding sediment parameters are calculated for the entire reservoir. Since TC and the particle distribution show significant correlations as well as a predictive function for the GHG production of the sediment, both are chosen for the modeling. Although, higher correlation values are presented in Table 5-7 –

Table 5-10, only correlation pairs including hydro-acoustic values obtained with configuration B are analyzed in detail. Around 177,000 point values of the dynamic hydro-acoustic measurement were processed with the given models.

Particle Distribution

The best r-values representing the particle composition ($\% < 63\mu\text{m}$) of the sediment, combined with a hydro-acoustic parameter from a linear regression model is found for configuration C, 200 kHz ($E1$ vs. $\% < 63\mu\text{m}$; $r = 0.81$). As the objective of the SBC is not only the evaluation of the potential sediment prediction in a static mode, but also the transfer to the dynamic survey, the best correlation of configuration B has to be used. Hence, the next highest r-value from configuration B ($attSv1/decSv1 \times \% < 63\mu\text{m}$; $r = 0.71$) serves for further analysis. A linear regression is not capable of resembling a model, which can properly represent the plateau evident between 90–100% proportions of the finest fraction (Figure 5-28). Therefore, based on the inability of the original linear regression model another model function, the *Gompertz Function* (Seber, G. A. F. & Wild, C. J., 2005) was adapted. It is originally a sigmoidal function for population growth, but is capable of modelling the hydro-acoustic sediment behavior. The function is given in Eq. 38.

$$y = ae^{(\log(\frac{xc}{a}) * e^{(-k * X)})} \quad \text{Eq. 38}$$

Where a is the amplitude (asymptote), xc is the center and k the coefficient; lower bounds are $a > 0.0$ and $k > 0.0$. The resulted curve is shown in Figure 5-28. This model is used to predict the sediment values for “ $\% < 63\mu\text{m}$ ” resulting in the following equation:

$$\% < 63\mu\text{m} = 97.9 * \text{EXP}(\text{LOG}(0.35/97.9) * \text{EXP}(-4.3 * L3)) \quad (r^2 = 0.83) \quad \text{Eq. 39}$$

The modeled values represent the data basis for the interpolation (IDW) to predict the share of the finest fraction in the entire reservoir. Results are demonstrated in Figure 5-29.

Having in mind the presented results from the sediment distribution (chapter 5.1.2), described gradients are reflected well in the interpolated raster. Higher shares of fine sediment are found in the deeper areas of the reservoir and coarser material is located in the proximal and in some sidearms. Especially narrow sidearms show high shares of coarse material.

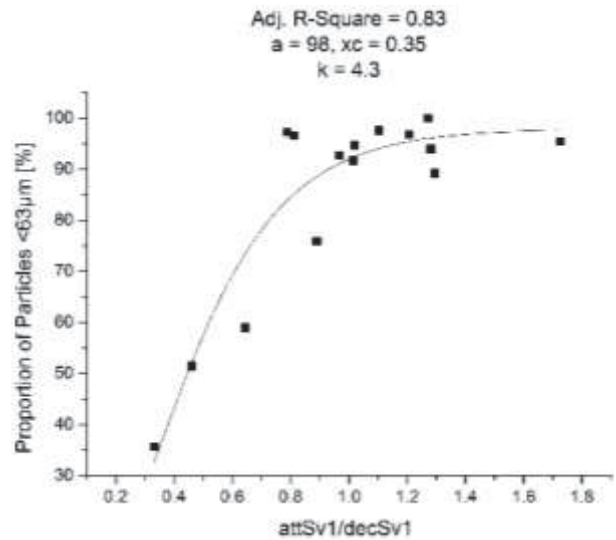


Figure 5-28: Depicted proportion of particles < 63 µm vs. the attSv1/decSv1 values and the modeled curve based on the adapted Gompertz function.

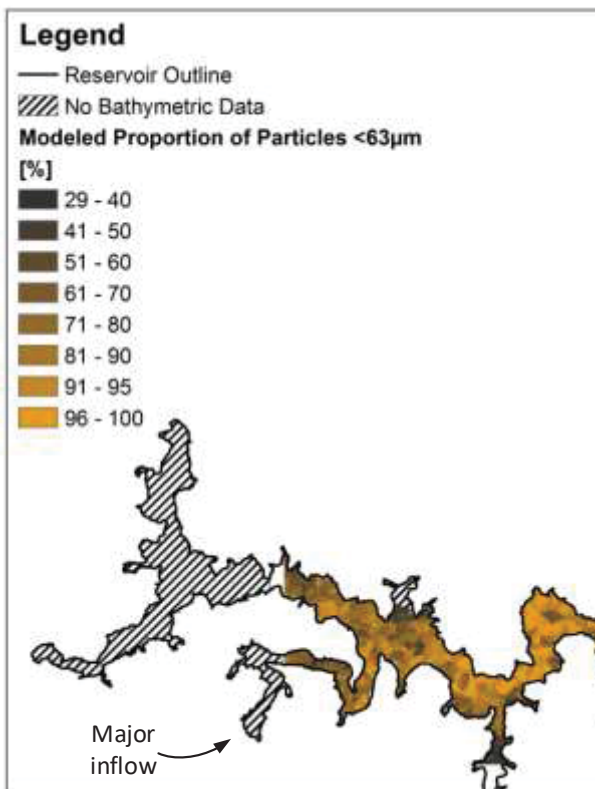


Figure 5-29: Map of the modeled proportion of the grain size fraction < 63µm in [%] for the Capivari reservoir.

To validate the interpolated results, a cross validation is performed. Ranked values from the granulometric measurements, the mean values from the classified interpolated polygons with upper and lower contour line limits and the extracted interpolated pixel values at the corresponding coring site, are set in relation. Polygons based on contour lines show different topologic shapes compared to the local pixel values. Hence, not all polygons and pixels feature the same sediment composition, if regarded on a small scale (30 x 30 m). In Figure 5-30 the orange points represent the measured values, from the static sediment thickness estimation, which are compared to the interpolated polygon- and pixel-based values. The modeled values, especially the pixel values accurately reproduce the real share of finest fraction in a range from 85–100%. The average pixel-based deviation for this range is 6.7%. If the outlier from rank 16 is excluded from the average, a deviation of 3.4% is reached. The value extraction from contour-based topologies reaches a slightly lower precision with a deviation of 8.8%. Yet, apart from the outlier the overall performance is worse. For areas with higher shares of coarse material the variation between the modeled values for the pixel-based extraction is 25.7% respectively 27.5% for the contour-based values. Besides a systematic, model based over estimation of the modeled values below 85% finest fraction (see Appendix A.14), these model results can be predicated by the location of the sampling sites. If sidearms are extremely narrow (Core 5; 6 & 13) the interpolation is not able to represent the entire sediment gradients due to the minimal pixel size (30 x 30 m). The heterogeneity of the sediment in this areas is higher than the resolution of the raster. Moreover, it is suggested that the hydro-acoustic behavior of the sediment influences the model results. In particular, the presence of gas bubbles can shift the hydro-acoustic apparition of the sediment (Anderson et al., 1998). This is discussed in detail in chapter 5.2.3.2.

Total Carbon:

Selected from Table 5-7–Table 5-10 the best r-value representing the TC in the sediment is found for the pair *TC* x *E1* (38 kHz, 100W). The overall correlation from the linear regression

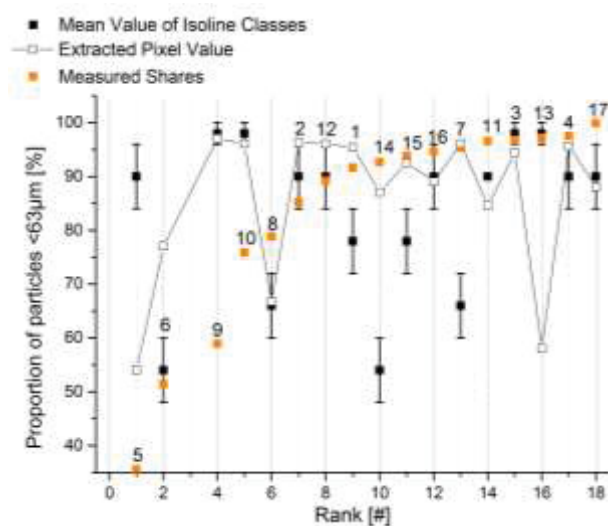


Figure 5-30: Differences between modeled and measured sediment shares of the finest fraction.

resulted in an r-value of -0.56. Since this value represents only a correlation on a relatively low significance level, the input values were regarded in detail. Due to potentially biased hydro-acoustic values, caused by inclination of the lake ground and relatively high waves during the static hydro-acoustic measurements, two of the input values (Core 12 & 15) were excluded. Afterwards, a new regression was calculated (Figure 5-31). This linear regression leads to the model of Eq. 40.

$$\%TC = 1.3 + (-0.06 * E1) \quad (r = -0.74) \quad \text{Eq. 40}$$

Based on this formula the TC values for all hydro-acoustic measurement points were calculated. The results from interpolation (IDW) are presented in Figure 5-32. The map shows that the proximal, the profundal and the sidearms generally feature the highest carbon contents. Lower contents can be dedicated to the plateau areas. However, a high small-scale spatial heterogeneity can be observed. It is suggested that the hydro-acoustic values are not strongly influenced by depth, since both deep and shallow areas are classified with high carbon values (compare Figure 5-21 and Figure 5-32). To evaluate the goodness of the interpolation a cross validation was conducted with the original sediment samples.

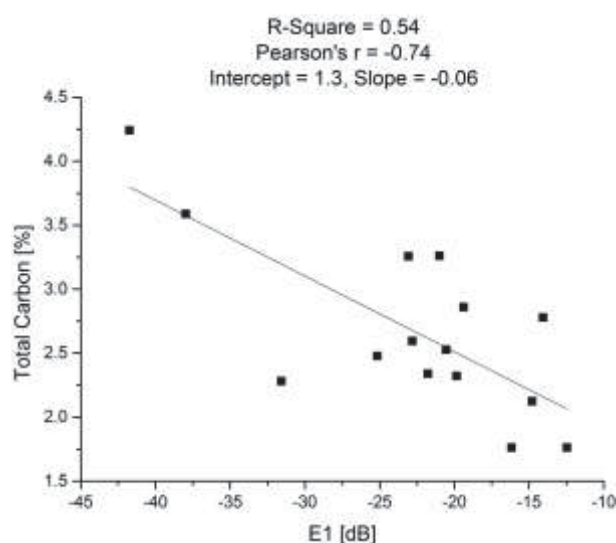


Figure 5-31: Linear regression model of the TC vs E1; N=15; $p < 0.01$.

The comparison of the measured and modeled results is given in a ranked order in Figure

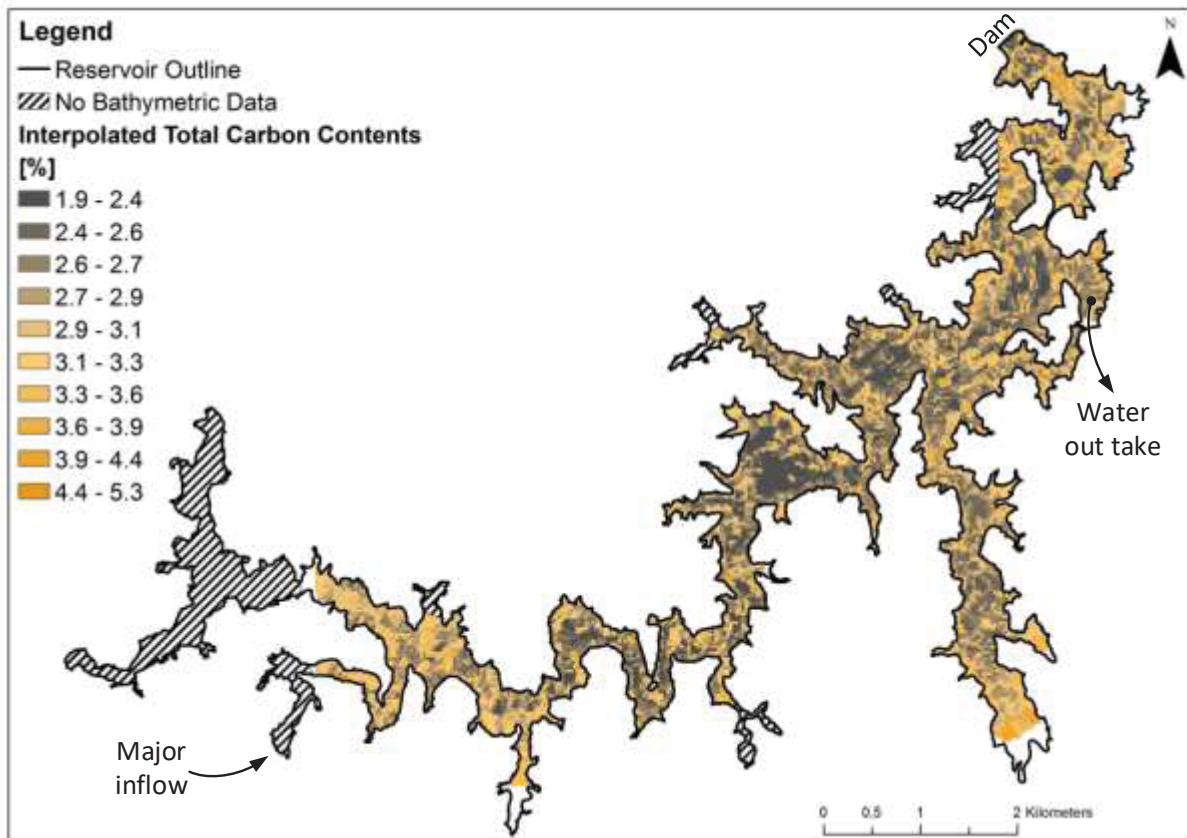


Figure 5-32: Interpolated total carbon contents in the sediment of CR, Interpolation was performed using IDW.

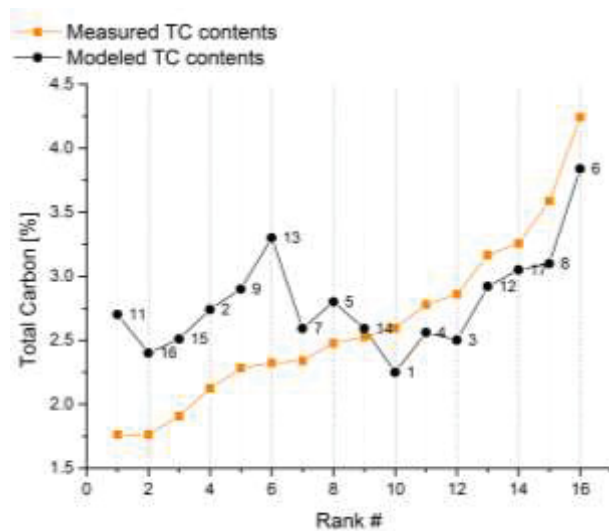


Figure 5-33: Modeled and measured TC contents in a ranked order.

5-33.

Here the modeled values are extracted from the interpolated pixels at the coring positions. The average deviation from the granulometric results is 17% (SD $\pm 0.45\%$ total carbon).

If the strongest scatterers (Core 9, 11 & 13) are excluded, a deviation of 13% (SD $\pm 0.36\%$ total carbon) is reached. Especially the lower content ranges tend to have stronger deviations, while the general TC-distribution is represented well based on the modeled results. From the individual deviations of the sampling sites, it can be concluded that the modeling of the TC in the sediment is less accurate in small sidearms. Whereby open, more homogeneous areas of the lakebed are represented with sufficient accuracy.

5.2.3.2 Approach two – producing sediment clusters

This approach aims on the classification of sediment types by creating groups of same acoustic behavior. As the result of a preselection process, the *first echo division method* was chosen as the most promising approach.

Results from both frequencies are presented (Figure 5-34 and Figure 5-35). In accordance to Figure 4-8, chapter 4.2.4.1 hard, strongly reflecting sediment types are normally located in the range of -5 – -15 dB (high hardness and roughness values). Sediments with weaker reflectivity are ordered in the lower left part of the diagram. Generally, fine, muddy sediments are located in the range of -25 – -50 dB.

The results from the 38 kHz frequency show that most core samples are located relatively close together. No sample is located in the standard-range of soft sediment. One distinct group can be separated from the other samples, due to the high attSv1 values combined with relatively low decSv1 values (Core 5, 6, 8 & 9). This distinction is caused by the elevated bulk densities of the named cores. All four samples feature increased shares of coarse material (Figure 5-2 and Figure 5-4). The attack phase of the 38 kHz frequency with a pulse length of 0.512 ms (configuration B) is influenced by the sediment features in the first

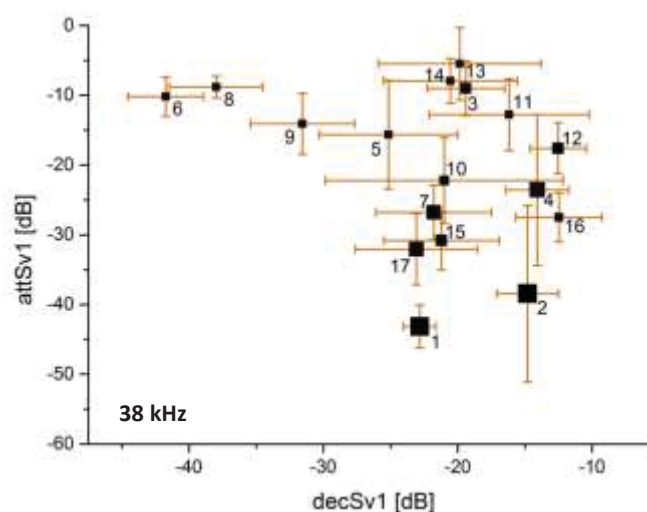


Figure 5-34: Results of the “first echo division” method; 38 kHz, Configuration B, 100 W; orange bars represent the standard deviation within the ping sequences; the size of the black squares is the relative depth, the larger the deeper.

76 cm of the ensonified sediment. Echoes show higher intensities, if a compacted sediment layer is present. Alternatively a reflecting layer of aligned bubbles may cause the same effect (Anderson et al., 1998).

In comparison to the 38 kHz-sample-allocation, the 200 kHz is able to cluster the samples in more distinct groups (Figure 5-35). The ability to clearly separate the sediment samples due their acoustic behavior, is a primary prerequisite for a successful classification. Thus, the seabed classification is conducted based on the 200 kHz frequency values.

Taking into account the obtained knowledge of the sediment characteristics of each core sample and additionally keeping in mind the basic assumption of the allocation of hard and soft sediments, clusters are defined.

Cluster “A” is delimited on the basis of the following supposition. Since no gravel or coarse sand exists as sediment in the entire Capivari reservoir, the only possible reason for a significantly increased reflection of both, hardness and roughness, is the presence of a dense acoustic turbidity layer (bubbles) in the upper part of the sediment. Due to the fact that core 13 is separately located from other samples, it must feature relevant differences and hence was allocated to an own cluster ($\text{attSv1} > -18 \text{ dB}$; $\text{decSv1} > -20 \text{ dB}$). Group “B” is delimited on the basis of high attack values combined with low decay values ($\text{attSv1} > -24 \text{ dB}$; $\text{decSv1} < -24 \text{ dB}$). It contains the same samples like the one group, described with the 38 kHz frequency. Group “C” takes the part of the dedicated soft, muddy sediment, since it is defined by lower attack and decay values ($\text{attSv1} < -25 \text{ dB}$; $\text{decSv1} < -20 \text{ dB}$). The rest of the samples are set as “unclassified”.

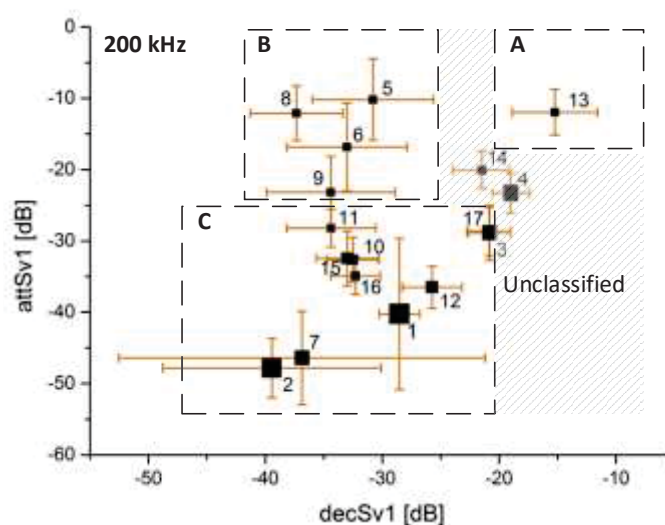


Figure 5-35: Results of the “first echo division” method; 200 kHz, Configuration B, 100 W; orange bars represent the standard deviation within the ping sequences, the size of the black squares is the relative depth, larger squares represent deeper positions.

Both frequencies show the same patterns in regards to depth influence (size of the black squares Figure 5-35). Sediment in deeper areas of the reservoir produce a clearly lower attack value. The decay value is unaffected by the depth distribution. Depth dependence of the acoustic response can be due to low bulk densities and high fine particle shares which are found in the morphologic depressions of the impoundment. The effect of depth on the

acoustic signal itself is not further investigated. It is assumed, that the described corrections (chapter 2.3.1) are sufficient to produce correct results within the given depth-ranges in the reservoirs.

To explain the differences of the chosen groups in detail, Figure 5-36 illustrates the acoustic signatures of exemplary core samples. The x-axis [m] should be read analogue to traveling time of the sound wave. While 0 cm is the point where the wave enters the sediment. S_v – mean is the average reflected intensity (backscatter) from the sediment volume. It combines the energy from coherent (specular) reflection and the volume scattering. Sound reflected during the volume scattering reaches the transducer later than sound waves reflected by specular reflection, therefore the given depth in Figure 5-36 should not be regarded as an exact measure.

Core 5 and 13, both feature strong reflectivity during the attack phase, which equals 19.6 cm of sediment depth for the 200 kHz frequency and a pulse length of 0.128 ms. As shown in Figure 5-35, core 13 has a significantly stronger reflection intensity during the decay phase (following $3 \cdot 19.6$ cm). This can be explained by strong reverberation caused by bubbles (Naudts et al., 2008).

The compact structure of core 5 appears as a flat surface for the 200 kHz frequency (specular reflection), whereas the reflecting horizon of the bubbles of core 13 appears rough. Hence, the $decSv1$ (roughness) value of core 13 is increased. A close investigation of core 13 showed that this core contained large bubbles within the upper 5 cm of the sediment. Most other cores showed the presence of larger bubbles exclusively in deeper sediment layers (10–15 cm or deeper).

Cluster “C” is represented by core 2 and 12. Both show a comparable behavior. They feature no steep peak during the attack phase nor high values during the decay phase. Instead, the signal signature is extended over a relatively long distance (time). This can be due to extensive scattering within the sediment volume. Lower energy levels are caused by sound

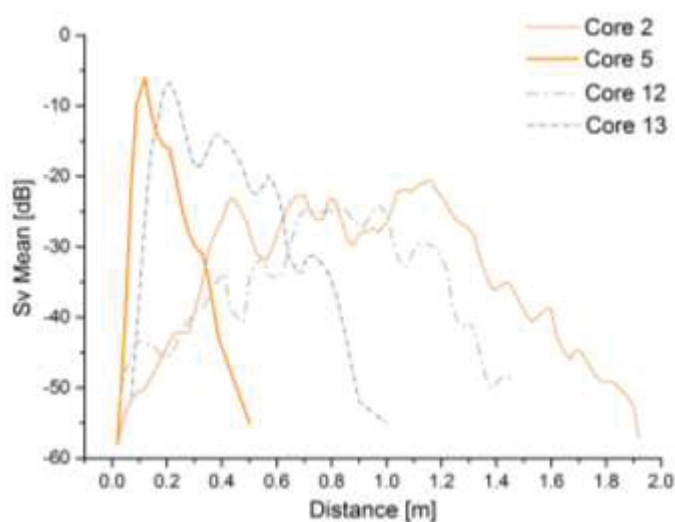


Figure 5-36: Acoustic signatures of four representative cores; 200 KHz, Configuration B, 100 W; S_v Mean is the backscatter strength in dB, the distance 0.0 is the entrance point of the sound wave in the sediment.

attenuation in the sediment, which can be caused by randomly distributed bubbles in the sediment.

After group A, B and C are defined, all 177.000 pings of the dynamic survey are classified based on the described decibel group limits. Nominal values, in this case the sediment classes, cannot be interpolated. Therefore, Figure 5-38 shows the single pings in accordance to the determined acoustic classes.

As could be derived from Figure 5-35, class A holds the smallest share of all classified pings. It is restricted to small areas, often in direct vicinity with unclassified echoes (Figure 5-38, side map A and B) This can be explained by the fact that both share the same range of decay values. The occurrence of class A can be assigned to intensive sediment accumulation areas. For comparison see Figure 5-24, chapter 5.2.2.

Pings assigned to class B are primarily located in the proximal as well as in the sidearms of the reservoir. These finding stand in accordance to the granulometric results from the sediment samples taken in this areas. The sediment in these parts is distinguished by the elevated share of coarse material entering the reservoir via the inflow or erosion (Core 5, 6, 8 and 9; Figure 5-2, chapter 5.1.2).

In the deeper areas of the main reservoir and the central parts of the larger sidearms, most pings are assigned to class A. This again corresponds to the previously described characteristic of the sediment type, assigned to this class. These areas feature soft sediments with high water contents and low bulk densities. Reflectivity can still be comparatively high due to the presence of bubbles in the sediment (Lyons, 1996; Naudts et al., 2008).

Figure 5-37 depicts the affiliation of the defined hydro-acoustic classes

versus the interpolated granulometric raster. It shows that around 60% of the pings assigned to class B represent a sediment with 84% of finest fraction or lower. This finding agrees with the assumption that this class is assigned to relative compact sediments with elevated densities. Pings assigned to class A present an intermediary distribution in regards to the

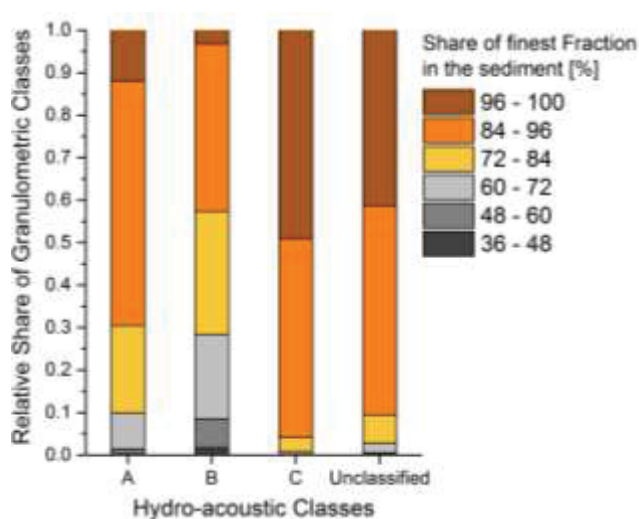


Figure 5-37: Relative distribution of classified pings within hydro-acoustic classes over granulometric ranges; basis for the granulometric classes are the results shown in Figure 5-29.

sediment composition, which contrasts the expectation of gas loaded soft sediment (e.g. core 13). Consequently, the seabed classification approach is not capable of differentiating consolidated, flat sediment from soft sediment with high bubble counts in the upper centimeters. The granulometric range of class C fits the expectations, since pings were assigned to soft and relatively fine-grained sediment, producing relatively low attack and decay values.

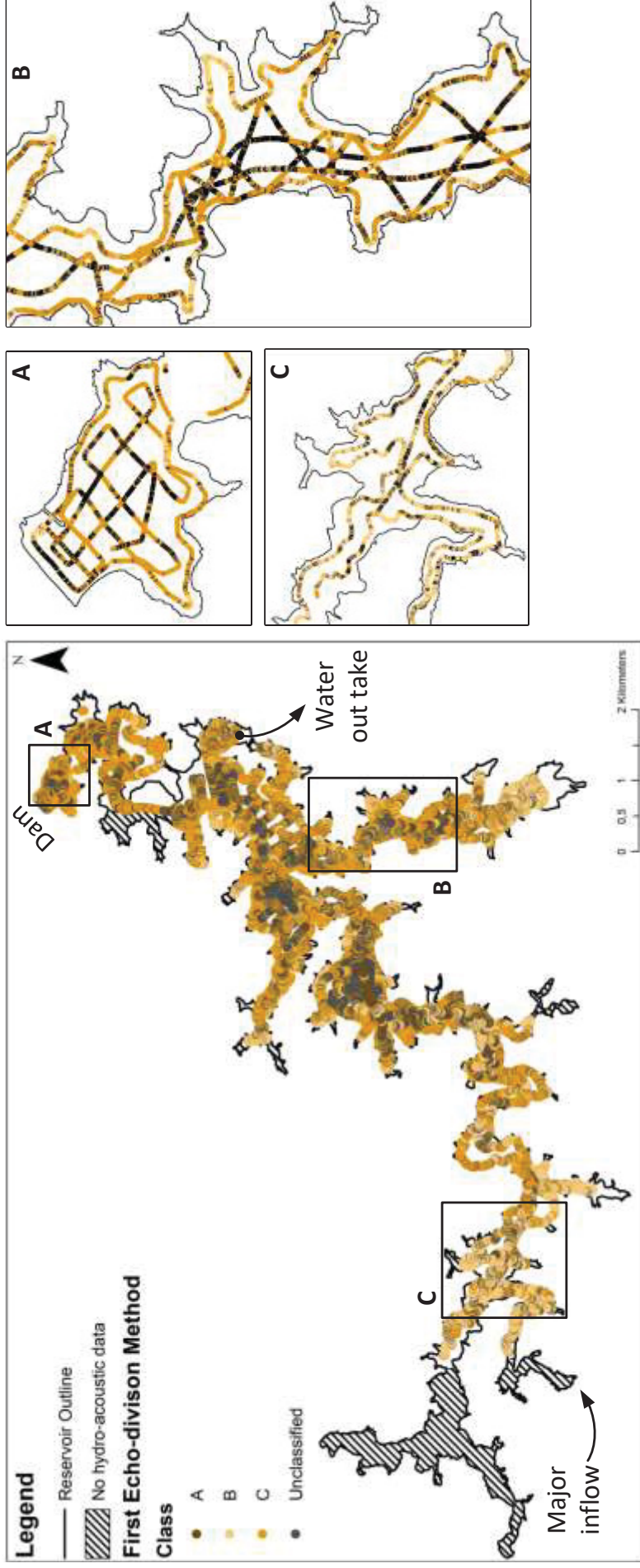


Figure 5-38: Results of the First Echo Division method classification; 200 kHz, Configuration B, 100 W. Results are shown as single pings; The side maps (A,B and C) show selected areas in detail.

5.2.4 Bubble Detection

„Estimates of ebullitive emissions can be obtained together with an assessment of its uncertainty assuming that measured values deviate from mean emissions as the result of spatial random variations and random measurement errors.“ IEA Hydropower Agreement (2012)

Rising bubbles from the sediment were first detected in the static mode to assess the bubble flux at the coring sites. Subsequently, bubbles were detected along the driven tracks of the bathymetric survey. For the static approach results are only presented for core 1–9 due to the fact that during the second campaign in phase two of the survey, no bubbles were rising during static measurements.

5.2.4.1 Static bubble detection

The feasibility of bubble detection was already proven in the literature (Ostrovsky et al., 2008; Ostrovsky, 2009a; Vagle et al., 2010; DeSontro et al., 2011) and was successfully conducted during the phase two surveys. Figure 5-39 shows rising bubbles at coring site six

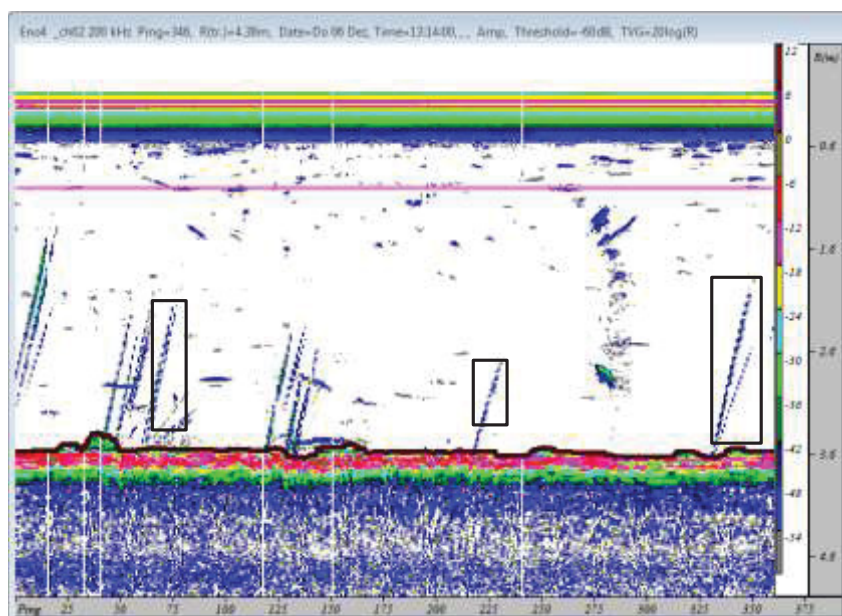


Figure 5-39: 200 kHz Echogram (configuration B) showing rising bubbles at coring site six. Tracked bubbles are marked with squares.

with rectangles representing the marked bubbles. During the second campaign at CR the water level was rising as well as the atmospheric pressure, causing increased hydro static pressure on the sediment. Therefore, the ebullition was reduced to a minimum (Scandella et al., 2011). Information about the water level and atmospheric pressure is given in Appendix A.10. The physical background is explained in chapter 2.2.4.2.

At coring site six the extensive permanent presence of bubbles reaching the surface was used to optimize the detection configurations of the Sonar5 pro Software. The rising bubbles gave the opportunity to directly verify the detected bubbles with the presence of bubbles at



Figure 5-40: Extreme bubbling at the surface during core sampling at location 6 in the first campaign of phase two.

the surface. Extreme bubbling was observed during sediment coring (Figure 5-40).

In general, there are significant differences between the 38 and 200 kHz frequencies. Whereas bubbles could be very well detected with the 38 kHz frequency producing reasonable results. Bubbles were also detected with the 200 kHz frequency, yet giving many inexplicable results. With the 200 kHz frequency up to 300 bubbles per echogram were detected where bubbles could neither be seen at the surface nor were detected with the 38 kHz frequency. The most influencing software parameters concerning bubble detection using a single-beam echosounder are certainly the settings of *ping gap* and *rising velocity*. If the ping gap is set too low some echoes that might still belong to the same track may not be detected. On the other side, if the ping gap is set too high, too many echoes are combined into one track. The configuration of the rising velocity can have similar effects on the bubble detection.

Starting configurations of Sonar5 pro were chosen after literature (Ostrovsky et al., 2008; Ostrovsky, 2009a; DelSontro et al., 2011). With all configurations (A–D, 100 & 500 W) at all sampling sites 98 bubbles were detected. As a general result, the short pulse length configurations A and B are best suited for bubble detection, regarding the resolution and level of detail, at the 38 and the 200 kHz frequency. By contrast, configurations C and D with longer pulse lengths resulted in poor detection quality. Especially for the 38 kHz frequency the echograms of the configurations C and D showed a high level of background noise. Since the target strength for rising bubbles is generally low, the background noise strongly influences the detection quality. The power input of 500 W consumed more battery power, but also resulted in a higher resolution of the echograms. That made configuration A with 500 W at 200 kHz the best configuration for the bubble detection during point measurements. Using this configuration, 30 bubbles could be tracked. In total, five out of ten sampling sites showed ebullition during the survey. In particular, at core 1, 6 and 8 many bubbles were tracked (Table 5-11). Comparing these results with sediment parameters it is noticeable that bubbling especially occurred at sampling sites where the TC content is elevated (Figure 5-41). The figure shows that bubbles are only detected at sites where the TC value is above-average (TC mean = 2.9%). Moreover, Figure 5-41 illustrates that bubbles in the proximal rise from carbon rich sediments, whereas in the profundal bubbles are detected over sediments with relatively low TC values.

At sampling site 5 no bubbles could be detected due to very shallow conditions, although TC content is relatively high. Coring sites 3, 4 and 7 did not show any bubble activity, they also feature the lowest total carbon contents (Figure 5-41)

Table 5-11: Number of Bubbles detected at coring sites; 200 kHz, configuration A, 500 W.

Site: Core #	1	2	3	4	5	6	7	8	9	Grab 1
Number of bubbles	10	1	0	0	–*	9	0	8	2	0

**site at Core 5 was too shallow to obtain reasonable results*

Regarding the acoustic values of the detected bubbles from configuration 200 kHz, A, 500 W (Table 5-12), the mean rising velocity is 18.2 cm s^{-1} and the mean TS is -63.2 dB . The rising velocity and the detected TS values agree with available values from the literature (Ostrovsky, 2003, Ostrovsky, 2009a). These values are very similar to the values obtained when considering all configurations. Only the number of echoes per track is higher using configuration A 500 W. This can be ascribed to the increased resolution with shorter pulse length, which enables a more accurate detection. The investigations show that the rising velocity and detectability of the bubbles were independent from the depth (minimum depth 3–

4 m), consequently the used method can be transferred to the acoustic data from the driven lines.

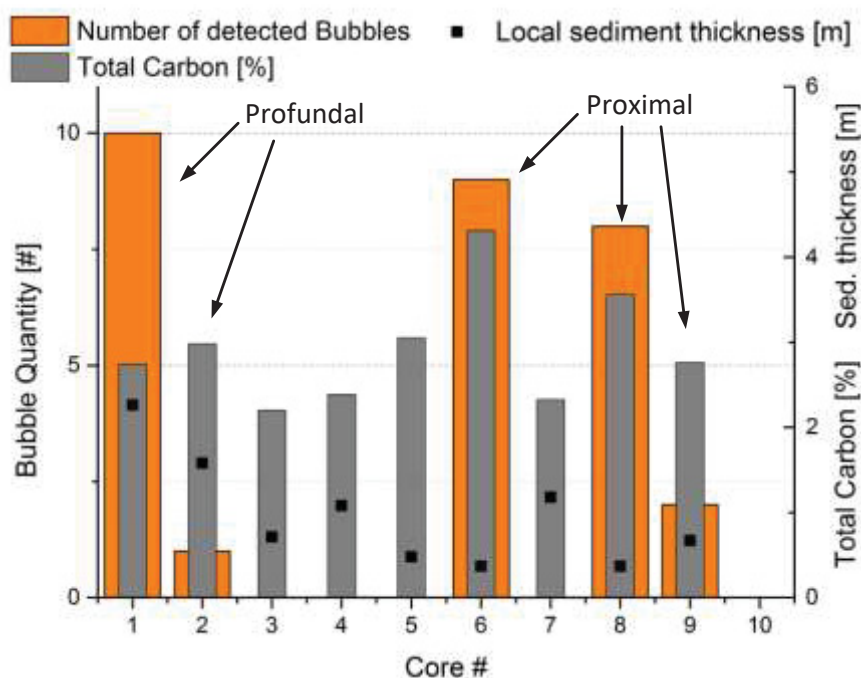


Figure 5-41: Number of detected bubbles at coring sites in relation to measured TC contents and the sediment thickness.

Table 5-12: Bubble statistics for configuration A, 200, 500 W, compared to average values from the remaining configurations.

	Configuration A		All configurations	
	Mean	Median	Mean	Median
Rising velocity [cm s ⁻¹]	18.20	19.00	18.64	20.00
Target strength [dB]	-63.20	-62.17	-62.88	-61.34
# Echoes	16.13	9.50	11.49	7.00

5.2.4.2 Bubble detection at driven lines

The same Sonar5 pro configurations, which were approved during the evaluation of the static measurements, are used for the bubble detection on the driven routes. In total 262 bubbles were detected with the 38 kHz frequency. In contrast to the findings from the static measurements, the same settings applied for the 200 kHz frequency resulted in the detection of nearly no bubbles. A map of the detected bubbles (38 kHz) is shown in Figure 5-42. Highest bubble densities are located in the profundal and the south-eastern sidearm of CR.

In the shallow areas only some single bubbles could be detected. The mean depth of the detected bubbles is 17.3 m (Table -5-13).

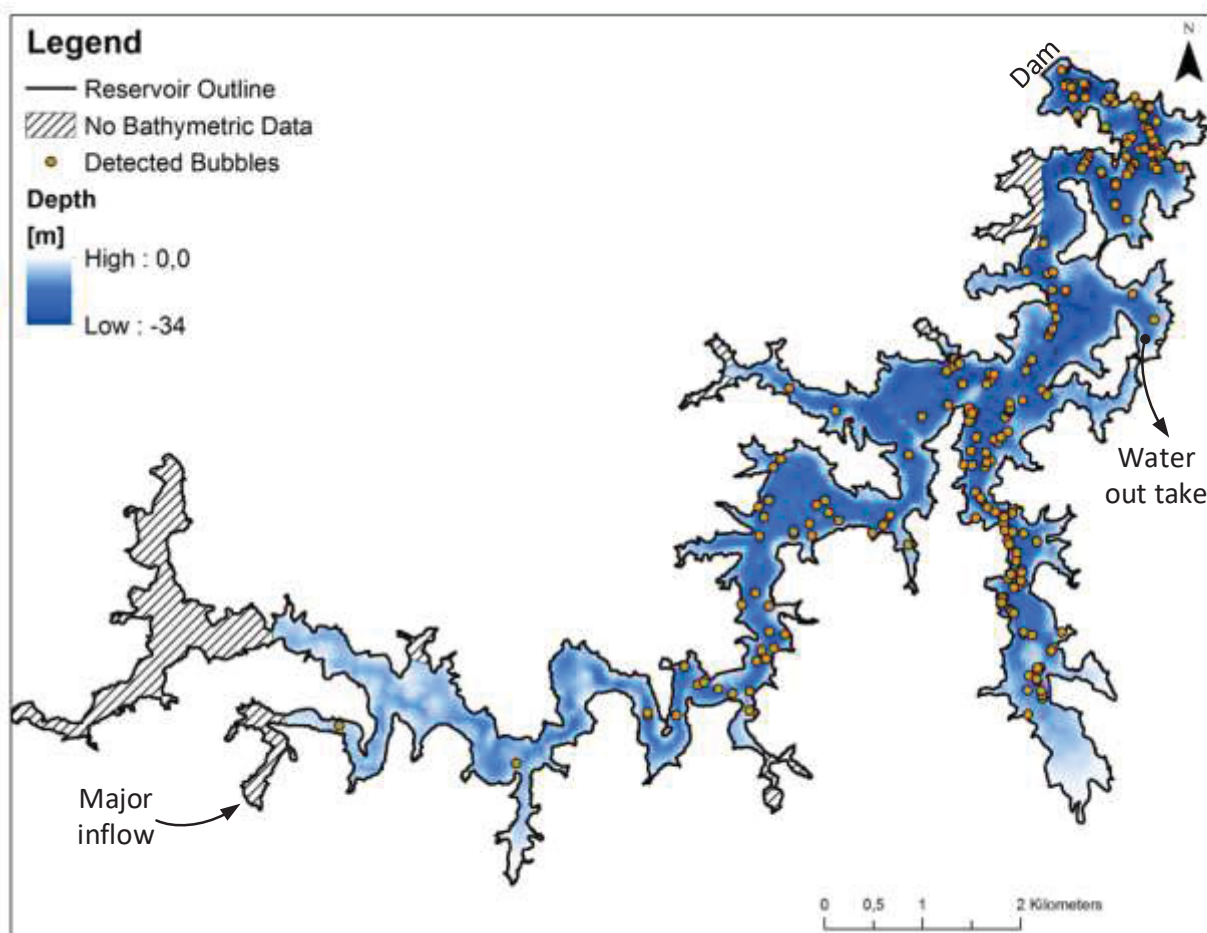


Figure 5-42: Location of the detected bubbles and water depth in the CR.

Including only depths greater than 8 m, the water depth cannot be regarded as a valid factor for the distribution of the detected bubbles. The accumulation of sediment is suggested to have a stronger influence on the bubble occurrence. Hence, the relation between sediment thickness, bubble occurrence and the relative share of the measurement point count is investigated (Figure 5-43). Including the number of measurement points, the relation to the distribution of the sediment thickness has a major effect on the interpretation of the bubble occurrence. Since bubbles can only be detected in the water column under driven lines there is no direct connection to the interpolated area of the different sediment thickness classes.

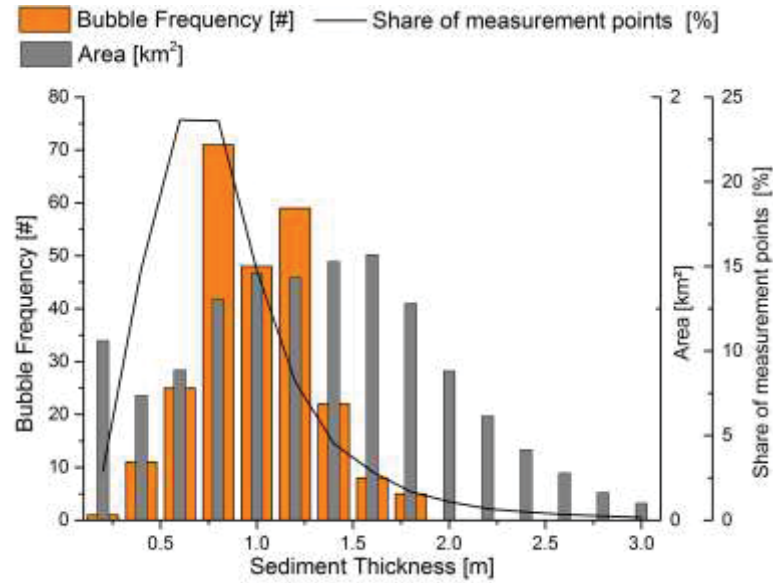


Figure 5-43: Diagram of illustrating the relation between sediment thickness, bubble occurrence and the relative share of the measurement point count.

The comparison of the three factors shows that bubbles primarily occur in areas with increased sediment overlay. Highest bubble frequencies are reached in areas with 0.8–1.2 m of sediment overlay. It can be expected that high bubble densities can be encountered above areas of thicker sediment as well, but the ratio of points representing this area is disproportionately low. On the contrary, the areas of low sediment thickness show very little bubble detection counts, although both the spatial share and the point representation is relatively high. Therefore, it is suggested that the presence of bubbles in the water column can be attributed to the accumulation of sediment.

Table -5-13: Bubble statistics for driven lines; Configuration B, 200 kHz, 100 W.

	Mean TSc [dB]	Start depth [m]	Target depth [m]	Water depth [m]	Vz first last [cm/s]	Mean Vz [cm/s]
Mean	-56.7	9.9	9.5	17.3	14.5	16.4
Median	-55.6	8.3	7.9	16.7	13.0	15.0

5.2.5 Synopsis

- Depth distribution and morphologic characteristics are relative similar between the two reservoirs.
- 52% of the CR lakebed have a slope inclination lower than 7.5°. Extremely steep slopes are limited to regions in the drawdown area or along the old riverbed, forming ridges.
- Sediment thickness reaches maxima in the deepest areas and is influenced by the inclination of the lakebed. Sediment thickness values from the driven survey strongly correlate with static results and with core samples in the range of their possible length.
- Static SBC approaches show significant correlations between hydro-acoustic and sediment parameters in both reservoirs. The selected sediment features could be spatially reproduced by interpolating the modelled sediment values. However, mapping of the spatial heterogeneity of the sediment characteristics in small-scale morphologic features like narrow branches, is complicated.
- Clustering of the sediment samples based on the first echo division method resulted in a good distinction of three sediment classes. However, the distinction of gas-loaded volumes at the sediment surface and compacted sediments, appears difficult. In the absence of dense acoustic turbidity layers, the hydro-acoustic response of granulometric differences can be reproduced by the classification. Accordingly, sediment classes can be detected and parts of the reservoir can be assigned to distinctive sediment types.
- Bubble detection was successfully conducted. Bubble distribution in the reservoir depends mainly on the accumulation of sediment. The higher the accumulation, the more bubbles will be produced. Bubbles are mostly found in areas deeper than 8 m with an average depth of 17 m.
- Short term bubble detections at coring sites show dependencies between TC contents and bubble numbers.
- Two spatial methane production patterns are derived. The proximal produced bubbles in carbon rich sediments with a low magnitude, while the profundal shows ebullition of bubbles over sediments with lower carbon content, but high sediment thicknesses.

5.3 Dialysis Pore Water Sampling

Considering that the technical devices for the DPS sampling approach conducted in this work, were specifically developed and constructed, the objective of this chapter is on the one hand to show the validity of the produced results and on the other hand present information about the behavior of relevant gas and ion species in and above the sediment.

During phase two of the study DPS were placed in the sediment of CR. In the first campaign the DPS-PS handling still had to be elaborated since the entire system was newly developed. Therefore, only two DPS's were placed without complications, which could have altered the results. One of these DPS's was stolen or lost during the equilibration time (not listed). The other DPS could be recovered and analyzed. In the second campaign the DPS-PS handling was improved and the placement was facilitated due to an electric winch and a floating platform attached to the side of the boat (Figure 5-44.)

Seven DPS's were placed during the survey and one was again lost or stolen (Figure 5-45). Table 5-14 gives an overview over the DPS's deployed during both campaigns. The design of the DPS was developed in cooperation with Hölzlwimmer (2013) details and technical specifications are given in Appendix A.11. Since the technical differences between Generation 1 and 2 are mainly relevant for the handling in the field, they are not discussed in detail.

The principal purpose of the DPS-approach is the investigation of the redox conditions, gas concentrations and chemical gradients in the sediment. The findings from this investigation, then can be related to the production of GHGs. Since the sediment at the corresponding



Figure 5-44: The DPS-PS positioned on the floating platform at the side of the vessel in combination with an electric winch.

locations was additionally scanned with the echo sounder and core samples were taken, it was possible to extend the findings by putting them in the context of the results from the additional measurement approaches.

Table 5-14: Overview of the deployed DPS's; the water depth at the current location, the individual equilibration time and the type of the DPS is given.

DPS Number	Type	Equilibration Time [h]	Water Depth [m]
DPS 0	Generation I	144	32
DPS 1	Generation I	214	18
DPS 2	Generation I	216	17
DPS 3	Generation II	190	12
DPS 4	Generation II	186	20
DPS 5	Generation II	145	11
DPS 6	Generation II	peeper missing	12
DPS 7	Generation II	147	17

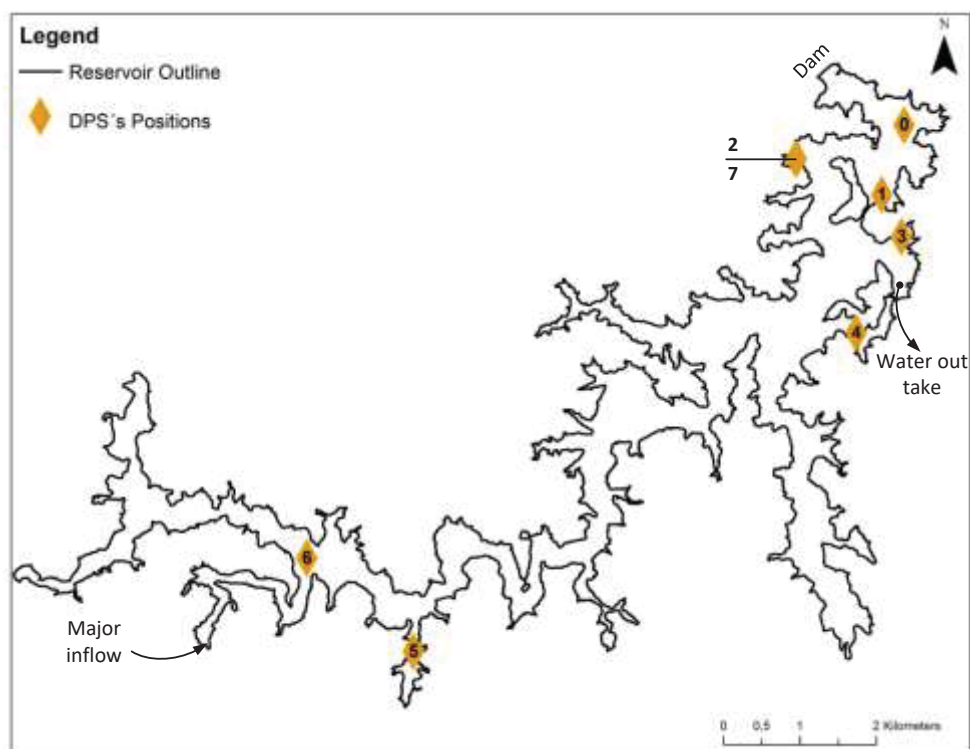


Figure 5-45: Positions of the placed DPS's in Capivari reservoir, lost DPS's are not presented.

5.3.1 Gas Concentrations

This chapter describes the results from the gas chromatography analyses of the head space samples. Four gases were measured (O_2 , CO_2 , N_2O and CH_4) but only the methane and oxygen concentrations are discussed in detail. Nitrous oxide concentrations were not detectable or close to zero. The number of valid carbon dioxide measurements was limited due to the fact that some of the samples were not in the range of the calibration and therefore had to be excluded. All results are shown in Appendix A.12.

Oxygen:

As a primary prerequisite for the methane formation the absence of oxygen is crucial. Hence, the oxygen concentration gradients measured in the sediment are presented in the first place. Based on general expectations, the oxygen concentration below the SWI tends to be zero. Figure 5-46 depicts the measured O_2 -concentrations in the overlaying water, through the SWI and below. Besides the DPS 2, all DPS's show concentrations below 1 mg in the first chamber under the SWI, with a decreasing tendency. The results from DPS 2 must be regarded as individually biased. Due to a power shortage on board the oxygen measurement was interrupted for around 30 min.

It must be assumed that significant re-diffusion has taken place. The interruption is marked with an arrow in Figure 5-46. Also for the interpretation and the correct understanding of the oxygen concentrations of the other DPS's the re-diffusion is a highly relevant factor. Especially the lower chambers with no dissolved oxygen are exposed to strong diffusion gradients during the onboard measuring. To control the effect of re-diffusion, additional experiments were conducted in the laboratory.

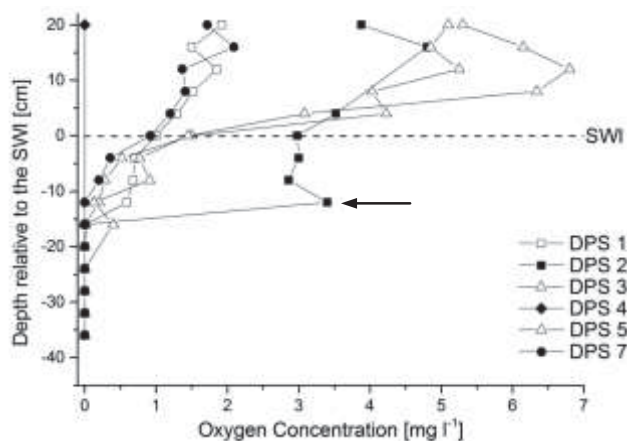


Figure 5-46: Oxygen concentrations in the DPS; DPS 0 is not shown since no oxygen was measured in the first campaign.

Error Control Experiments

For the measurement of the oxygen diffusion rate through the air-exposed celluloses membrane, a laboratory experiment was conducted. Eleven bags of the same membrane material as used during the field campaigns, filled with air-saturated deionized water, were submerged in helium-stripped deoxygenated water. The gradient of oxygen concentration was then measured over time. After reaching a concentration of 0 mg l⁻¹, four bags were exposed to ambient air and the increase in oxygen inside the bags was recorded analogously.

To ensure that the measured increase in oxygen concentration was only caused by diffusion, the membrane bags were kept intact. The oxygen concentration was measured using the same equipment as in the field (Oxygen Microsensor; PreSens), which allows measurement by only introducing a needle into the bags. Hence, biasing of the results can be neglected. In Figure 5-47 the re-diffusion into the bags is presented. The curves represent the beginning of an asymptotic approximation to the air saturation.

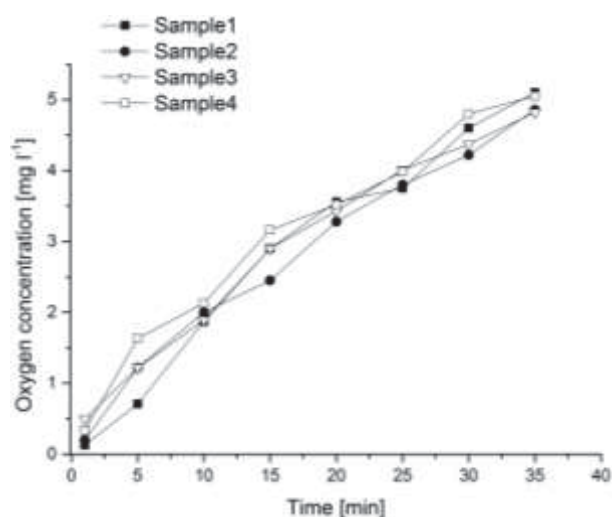


Figure 5-47: Oxygen concentration in membrane bags vs. time, under laboratory conditions.

Comparing the laboratory re-diffusion rate with the measured concentrations from the DPS's, it becomes clear that the DPS-values are considerably lower. The first five chambers from the lower most end in the direction to the SWI are oxygen free, in spite of the fact that measuring in the field took around 2 min per chamber. Under laboratory conditions a permeation flux of 0.2 mg min⁻¹ and hence a concentration of 2 mg l⁻¹ after 10 min is reached. These results lead to the conclusion that the stay of the membrane bags in the sediment led to clogging of the membrane pores. The clogging slows down the re-diffusion. This effect was already observed by Brandl & Hanselmann, 1991 and Jacobs, 2002.

In this context the power breakdown during the measurement of DPS 2 gives a hint of the pre-recovery oxygen concentrations of the remaining DPS's. An additional hint gives the oxygen concentration in DPS 4. During the campaign it was assumed that the DPS was not properly placed because during recovery of the DPS the resistance of the sediment was very low. Hence, it was assumed that the DPS 4 was not placed deep enough in the sediment. To save time only two chambers were measured for oxygen. Both have a concentration of 0

mg l⁻¹. Since both measurements were performed without any delay, they give back the exact concentration from the corresponding chambers. If the re-diffusion speed of DPS 2 is transferred to the other DPS no chambers below the SWI and most likely not above the SWI contained any oxygen. This stands in direct accordance to the results from DPS 4 and independently measured O₂- concentrations in the supernatant water of the recovered cores (data not shown). The sediment overlaying water was generally oxygen free. Findings stated by Uhlmann & Horn (2001) are in agreement.

Methane:

The production of methane is limited to permanent oxygen-free ambients. Therefore, in most cases methane is primarily produced within the sediment. The prevalent gradients of methane concentration in the overlaying water and underneath the SWI are depicted in Figure 5-48. The methane concentration stays close to zero in the chambers above the sediment and increases below the SWI. In deeper chambers, increasing concentrations were measured. From the development of the individual concentrations it is assumed that the local dissolved methane concentration reaches a plateau in the depth of around 40–50 cm. The exact calculation of the solubility of methane in the sediment is not trivial. Yet, including the principal factors, pressure and temperature the obtained concentrations are at the limits of solubility (Duan et al., 1992). The presence of gas bubbles in nearly all core samples

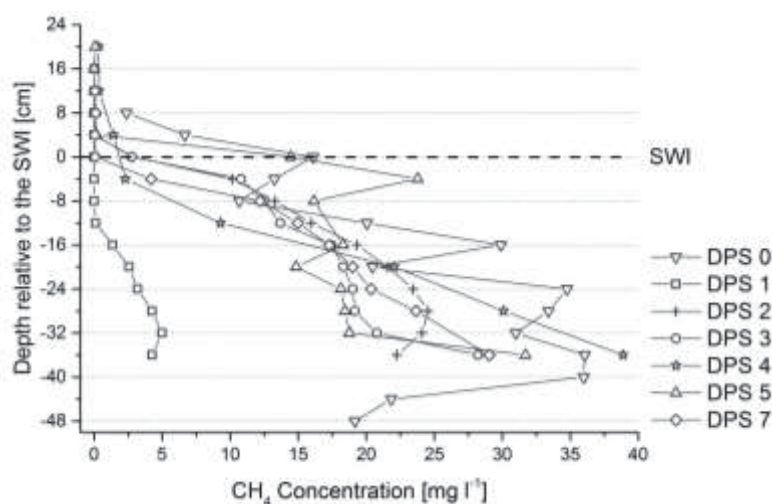


Figure 5-48: Dissolved methane concentrations in the pore water of the CR; DPS 1 was discarded due to erroneous placement.

underlines these findings.

Compared to literature results, the measured values are reasonable. Adams & Baudo (2001) published pore water concentrations in the range of 18 mg l⁻¹ in an Italian lake. Higher concentrations are reported from Abe et al., 2009a, who investigated the CH₄ concentrations in the upper most centimeter of the sediment in a tropical reservoir. Concentrations around 40–48 mg l⁻¹ were observed.

The team of Tundisi (2013) measured the methane concentrations in the sediment of Capivari reservoir at some of the DPS-sites surveyed in this work, with a different technique. The technique is described in Sidagis Galli C. et al. (2009) and Abe et al. (2012). At two comparable sites (DPS 0 and DPS 5), the methane concentrations measured by Tundisi in the first 4 cm of the sediment ranged from 24–25.5 mg l⁻¹. The own results from the DPS measurements show a range from 15–16 mg l⁻¹ at the corresponding positions. Taking into account that the sediment volumes sampled were not exactly the same (distance of some meters) and that around a month lay between the measurements, the results seem to be in agreement. The differences could be caused by local variation of available organic carbon or also by water level changes.

Thus, it can be stated that the methane concentrations obtained from the measurement technique presented in this study do not suffer from the same diffusion effects found for oxygen measurements. It is suggested that the measured concentrations are not primarily dependent on the water depth at the sampling position, as the deeper locations not necessarily show the higher concentrations. This leads to the assumption that the local sediment features are the predominant influence for the methane concentration in the pore water.

Importance of deployment time

A primary factor for the correct interpretation of the potential methane concentration in the sediment is the equilibration time. The time depends on the diffusive flux of the relevant gas or ion species. Only if the DPS's are deployed as long as it takes to reach equal concentrations in the membrane bags as in the surrounding pore water, the measured concentrations give back the real situation in the sediment. For this purpose DPS 2 and DPS 7 were deployed at the same position (distance ca. 3–4 m) with a time delay. The time difference between the placements of two DPS was 69 hours (Table 5-14).

The expectation is that the concentrations are at the same range if the shorter deployment time is sufficient for full equilibration. As Figure 5-49 shows, both DPS feature similar concentrations in the corresponding chambers. The shorter deployed DPS 7 even reaches a higher dissolved methane concentration in the lower most chamber than DPS 2. Since DPS 7 is one of the DPS with shortest equilibration time, this suggests that full equilibration was reached in all of the deployed DPS's.

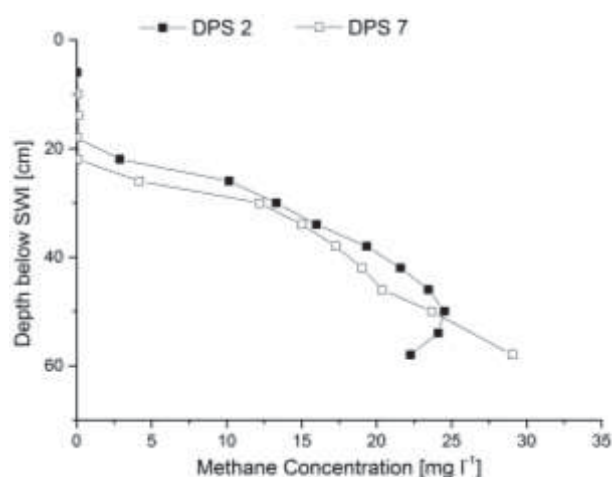


Figure 5-49: Methane concentrations of DPS 2 & DPS 7 depicted against sediment depth.

5.3.2 Ion Concentrations

From the analyzed ions (NO_2^- , NO_3^- , SO_4^- , F^- and Cl^-) in the pore water of the sediment the SO_4^- has the closest relation to the formation of methane, since it is part of the last redox-step before the CH_4 formation (Jorgensen, 2000). Therefore, the rest of the ions will be addressed only briefly while the depth distribution of SO_4^- is discussed in detail.

Generally the presence of NO_2^- and NO_3^- in the water column or the sediment is limited to areas of 250–400 Eh [mV] (Förstner & Grathwohl, 2007, 30–31). In this regard all DPS show similar results. Both species are depleted in the sediment overlaying water phase or latest in the second chamber below the SWI. In this case only low concentrations can be found. All graphs are given in Appendix A.12. Especially fluoride, but also chloride concentrations increase analogous to the dissolved methane concentration. Research did not show any explanation for this behavior since both ions are not connected to relevant metabolisms of the formation of methane.

Sulfate

Apart from the concentrations measured in DPS 1 and DPS 4, the SO_4^- concentrations below the SWI decrease within the first 8 cm under the sediment to values close to zero (Figure 5-50). Therefore, the behavior of SO_4^- corresponds to the anticipated course.

These expectations are founded on the previously analyzed gradients of methane concentration. In accordance to the fact that sulfate needs to be reduced before effective formation of methane can take place, the presented values decrease before or at the same depth as the methane concentrations increase (Martens et al., 1998). Due to the minimal depth resolution of 4 cm (dependent on the chamber size of the DPS) it is not possible to closer investigate the spatial occurrence of both species. However, it is possible to identify that at some locations the hypolimnion features significant reducing conditions. At this locations the reduction of SO_4^- already starts above the SWI (e.g. DPS 0, 2 & 5). Biochemically it is most likely that the reduced sulfur will be bound to the available iron species. As long as oxygen is unavailable in the sediment and especially in the hypolimnetic layer above the SWI the sulfur and iron are permanently bound in the sediment matrix (Holmer & Storkholm, 2001). The formation of FeS or FeS_2 in the sediment becomes even more probable since no carbonates are present (van Cappellen & Wang, 1996). The permanent accumulation of FeS in the sediment is supported by the fact that no signs of bioturbation were observed during core analysis.

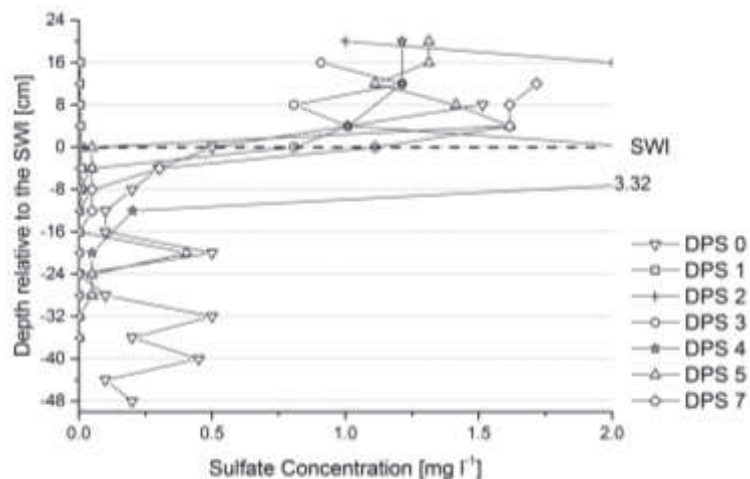


Figure 5-50: Sulfate concentrations in the pore water of the CR; DPS 1 must be discarded due to erroneous placement; DPS 4 reaches a maximum of 3.32 mg l^{-1} but is cut for a better resolution of the other graphs.

5.3.3 Synopsis

Recapitulating the central results of the *dialysis pore water sampling* and the subsequent analysis, the following findings are listed:

- The developed Dialysis Pore water Sampling – Placing System (DPS-PS) was successfully tested in the field. During the two campaigns the handling was significantly improved leading to fast and efficient placement of the samplers.
- As a relevant parameter the equilibration time for the determination of dissolved methane in the sediment was successfully investigated and hence further surveys can be adapted.
- Re-diffusion of oxygen was identified as a biasing factor for DPS onboard oxygen measurements. Presented results were adjusted and expected concentrations could be confirmed. Oxygen is absent in the sediment and at most DPS-sites also above the sediment.
- Basic assumptions regarding the formation conditions of methane were confirmed for the investigated sediment volumes in the Capivari Reservoir.
- The accumulation of iron and sulfur in the sediment was discovered to be a proxy parameter for the potential formation of methane. A temporal factor is suggested, since higher iron contents in the sediment are related to long-term reducing conditions.

5.4 Composed Results

This chapter aims at the synthesis of some of the findings previously described. In regards of the principal questions of this work, the focusing of sediment accumulation in dependence on the lake ground inclination and the carbon stock of the Capivari reservoir is calculated. Moreover, the relation of organic carbon content and methane concentration in the sediment is elucidated. Finally, methane concentrations are related to echo parameters, explaining possible coherences between the two data sets.

5.4.1 Slope Inclination vs. Sediment Thickness

The distribution of accumulated sediment in the reservoir cannot be ascribed to the presence of a single gradient like depth or distance from the inflow. To investigate the focusing of sediment on a small scale, one part of the profundal is magnified (Figure 5-51). In the figure, only the steeper inclination polygons (code 4 = $20^\circ - 11 = 55^\circ$) are visualized, combined with isolines representing the sediment thickness.

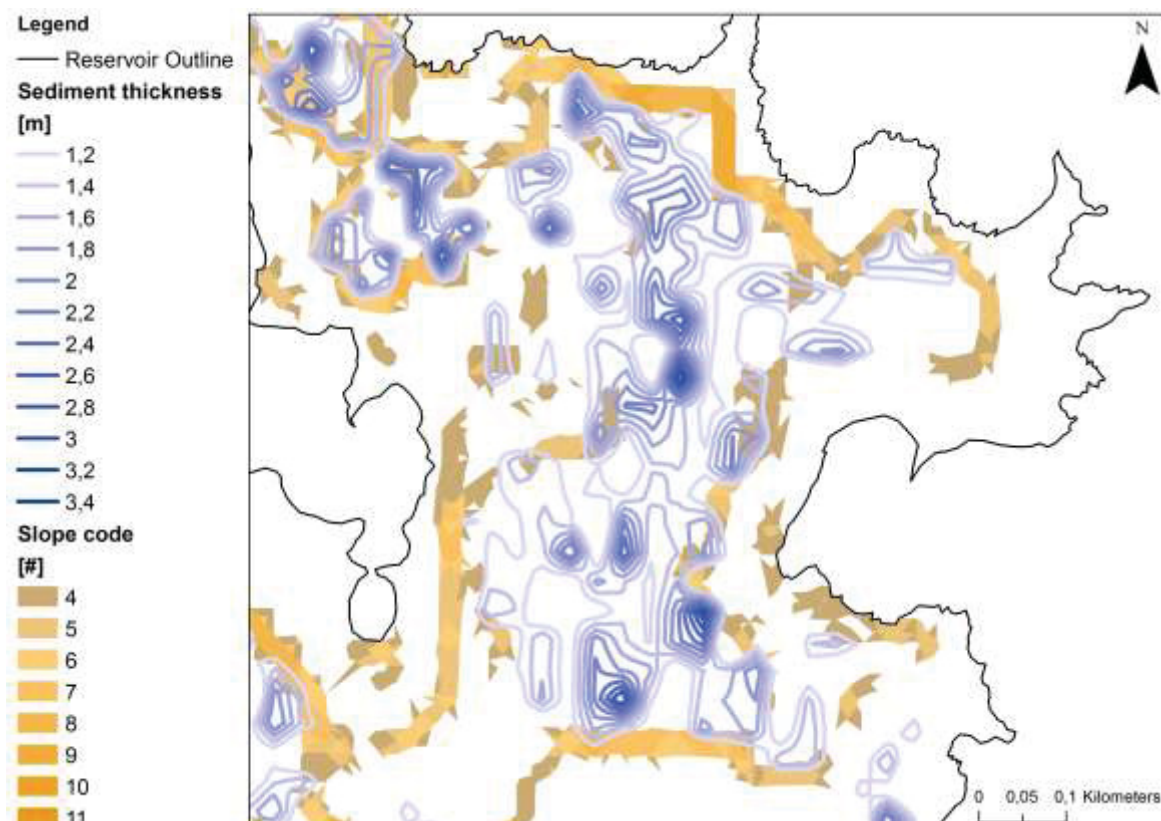


Figure 5-51: Slope inclination of the profundal area of Capivari reservoir is illustrated and combined with sediment thickness isolines.

The sediment accumulation follows the shape of the ridges, which are the old banks of the Capivari River, this stands in accordance to (Likens, 2009). At some locations, the isolines of the sediment thickness overlap with the slope polygons. This can be due to two effects: 1) the dimension of the morphologic features is small in relation to the resolution of the map. Therefore, the outlines of the polygons do not exactly show the real limits. The same may be the case for the interpolated sediment thickness isolines. 2) Volumes of mobilized sediment from shallower parts of the reservoir, were detected above the inclined surface on the way to the bottom.

However, this map does not give a quantitative measure for the influence of the inclination on sedimentation processes, but illustrates the effect of steep slopes within the reservoir. It is suggested that the sediment focusing is particularly effective for fine-grained sediments with high water contents, since these sediments slowly move along the ground of the reservoir. Depressions function as accumulation areas.

Consequently, if the inclination of the lakebed leads small-scale sediment accumulation, it also influences the local methane production. Areas, which collect surrounding sediments, can be seen as potential methane production hot spots.

5.4.2 Carbon Stock Calculation

One important objective of this work is to improve the precision of the carbon stock estimation of a reservoir, as it is closely related to the methane emissions. The developed correlations, coherences and interpolations allow to derive the following scheme for an extensive calculation of the carbon stock in CR (Figure 5-52).

The reservoir was divided into ca. 45.000 single polygons, covering an area of 10.5 km², which is equivalent to 88 % of the entire surface during maximum water level. The proximal, which was too shallow for the echo sounding, and the parts with lacking GPS signal were excluded from the calculation.

The polygons feature the interpolated information about the organic carbon content, the grain size distribution and the sediment thickness. The TOC and the grain size distribution were averaged over the depth of the sediment. Calculating the average carbon content is important, since the first 15 cm of the sediment tend to contain more carbon than the underlying layers (data not shown).

Two correction factors were derived from regression analyses (Appendix A.13) in order to calculate the dry sediment mass. Based on the equations developed, the density and water content were adapted for each single polygon volume.

By merging the OC-contents with the corresponding sediment volumes (polygons), the carbon stock was calculated.

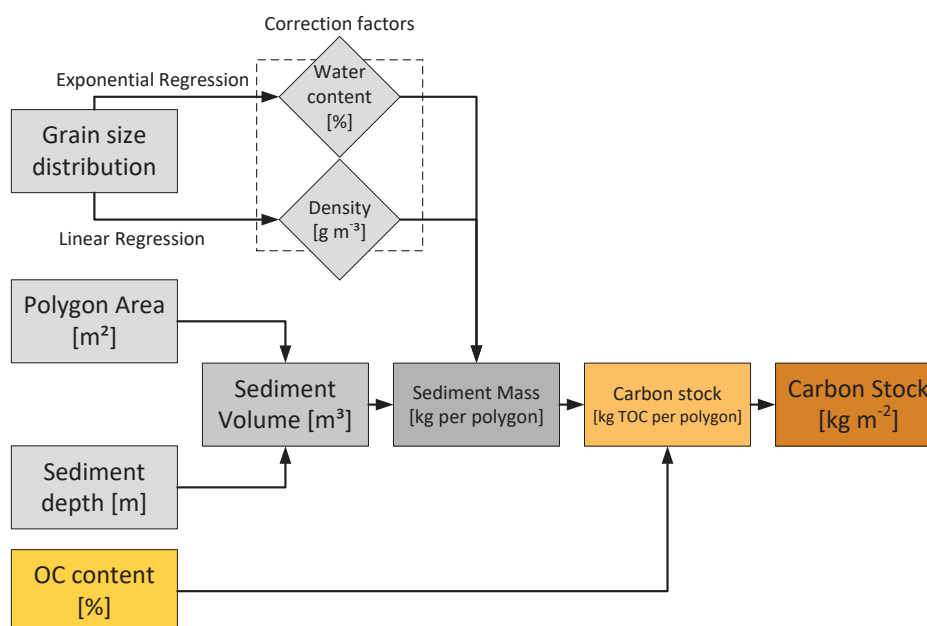


Figure 5-52: Flow chart of the carbon stock calculation.

The calculated mass of organic carbon for the entire reservoir is 205,129 Mg (± 60.8 Mg). This equals an average content of 19.5 kg m^{-2} ($\pm 5.8 \text{ kg m}^{-2}$) of OC. The deviations of around 30% are due to the insecurities enclosed in the correction factor prediction, based on the regression models. Variances originally caused by the measurement techniques are not included in the calculation of the deviation.

Figure 5-53 shows the organic carbon content per square meter. The figure illustrates that the major stocks are located in the area of the former riverbed and in the profundal in front of the dam. In contrast to the distribution of the TC shown in Figure 5-32, chapter 5.2.3.1, the sidearms and the proximal feature relatively low stocks. Since, the average sedimentation rates and accordingly, the sediment thicknesses are low in these parts, the overall stock is also limited.

Having in mind that large shares of the sediment enter the reservoir via the major inflows, the question arises how the carbon stocks in the profundal can develop.

First, it can be assumed that a large proportion of the settling organic material has an autochthonous origin.

This assumption is corroborated by the fact that most of the material found in the profundal is smaller than 63 μm . The particles originating from local primary production are prone to build up very fine-grained sediment layers. Generally, fine sediments settle relatively slow and

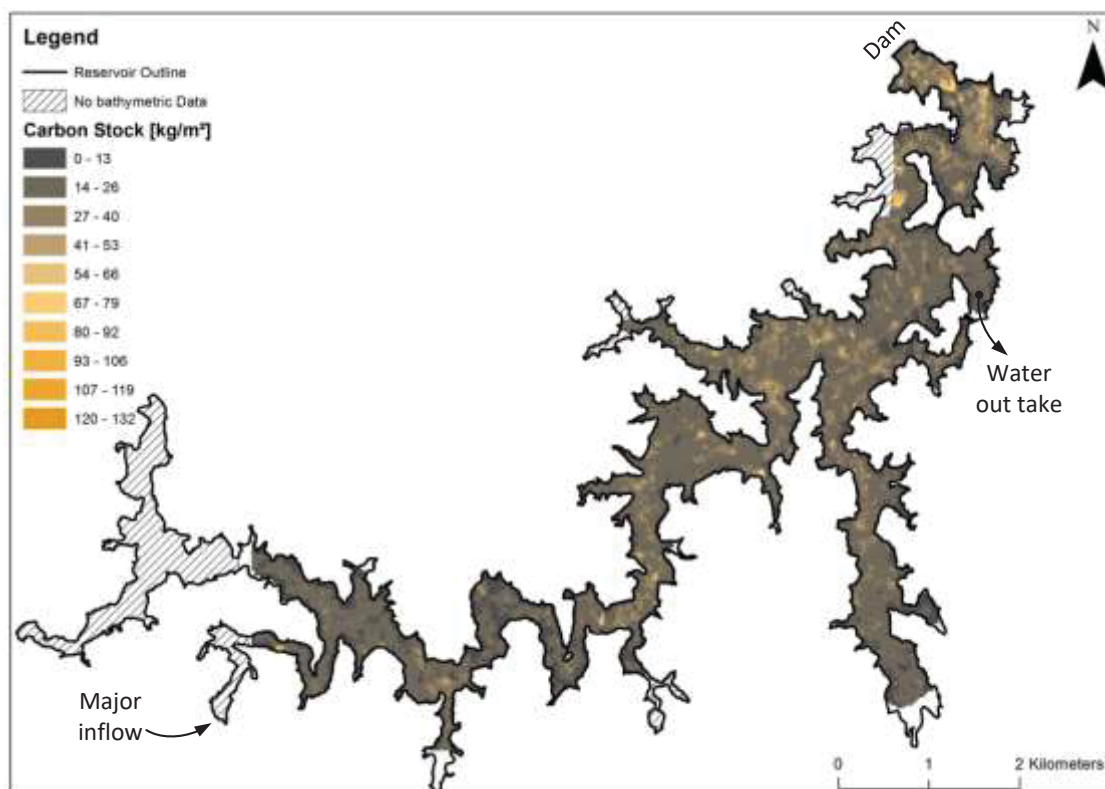


Figure 5-53: Organic carbon stock in the CR [kg m^{-2}]; results of the IDW interpolation process; the maximum interpolation distance of 50 m caused the edges of some shallow areas to stay without value.

hence, are exposed to mineralization processes in the water column for a long time.

To assess the OET of organic matter in the profundal of CR the settling velocity was exemplarily calculated, based on Eq.1. The presented standard values from chapter 2.1.2 (ρ density for water $\approx 1000 \text{ kg m}^{-3}$, $g = 9.81 \text{ m s}^{-2}$, $v \approx 1-1.5 \cdot 10^{-6} \text{ m}^{-2} \text{ s}^{-1}$) were used. The diameter of the particle was set to $D_p = 30 \cdot 10^{-6} \text{ m}$ and the density to 20 kg m^{-3} . These values represent reasonable average values for organic particles in fresh water bodies (Friedl & Wüest, 2002).

The OET is the time, which passes until the particle reaches the oxycline in the water body (Sobek et al., 2009). The shorter the time, the higher will be the carbon burial efficiency.

For this calculation it was assumed, that no wind influence occurs during the settling period.

The resulting settling velocity is 0.845 m d^{-1} , which leads to an OET of around 12 days, if the

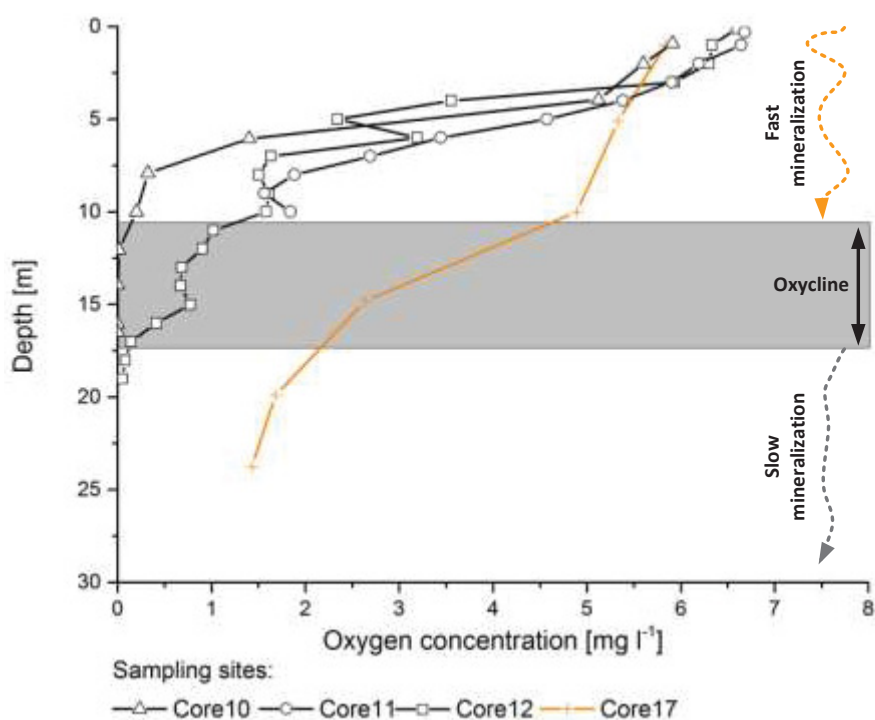


Figure 5-54: Oxygen depth profiles at selected coring sites, the prevalent oxyclyne marks the boundary for fast and slow mineralization of organic matter, core 17 shows the vertical oxygen distribution after a storm event.

oxyclyne lies in a depth of 11 m (Figure 5-54). OETs in a range of some days to three month will lead to a burial efficiency of 30–40% (Bühler L., 2008).

Even if it is unlikely that the particles in the profundal of Capivari reservoir can settle without any external influence (e.g. wind, water level fluctuations), the OET is short compared to other water bodies (Bühler L., 2008).

The orange line from core 17 in Figure 5-54 shows the vertical oxygen distribution after a heavy storm event. It can be suggested that storms cause intense mixing of the water body, but yet the oxygen concentration close to the lakebed is low (1.4 mg l^{-1}). Consequently, it can be assumed that: 1) a fast re-stratification occurs after mixing and 2) the general separation in fast- and slow-mineralizing layers is correct (Figure 5-54).

Taking into account, the prevalent absence of oxygen in the hypolimnion of the profundal, the elevated carbon burial efficiency can be explained. High BE values consequently lead to the formation of increased carbon stocks and therefore to the production of methane.

5.4.3 Methane Concentration and Sediment Parameter

In this section the measured methane concentrations in the pore water are set in relation to further sediment parameters. Three parameters are exemplarily chosen due to their expected direct or indirect connection to methane production in the sediment. As the methane concentration was measured only at the DPS sampling locations a profound relation to other sediment parameters is necessary to spatially transfer the findings.

In the following the TC distribution in the reservoir and also the role of TC in regards of bubble occurrence is discussed. To prove that the hypotheses, that higher OC (here TC) contents lead to elevated methane production rates, the maximum methane concentration at the sampling positions is depicted against the TC content (Figure 5-55). The results from DPS 2 (core 10) were excluded from the correlation. They show significantly lower methane concentrations in relation to the high TC content. This is explained by the local grain size distribution. The results from core 10 indicate higher shares of coarse material (Figure 5-2), compared to the other DPS locations. Based on this data it can be concluded that the permeability for methane in this sediment is higher (Sollberger et al., 2014). Consequently, the diffusion from the sediment to the water phase is elevated and the possible concentrations in the sediment are limited.

Compared to literature (Sobek et al., 2012; Sollberger et al., 2014), results indicate that the CR is no exception. A highly significant positive correlation between the methane concentration and the available TC is found ($r = 0.98$, $N = 5$, $p < 0.01$). It has to be kept in mind that the TC is equivalent to the OC. Hence, this correlation gives a basis for the detection and definition of the most relevant methane producing areas in the CR. Elevated local TC values are suggested to cause higher CH_4 production and consequently emissions.

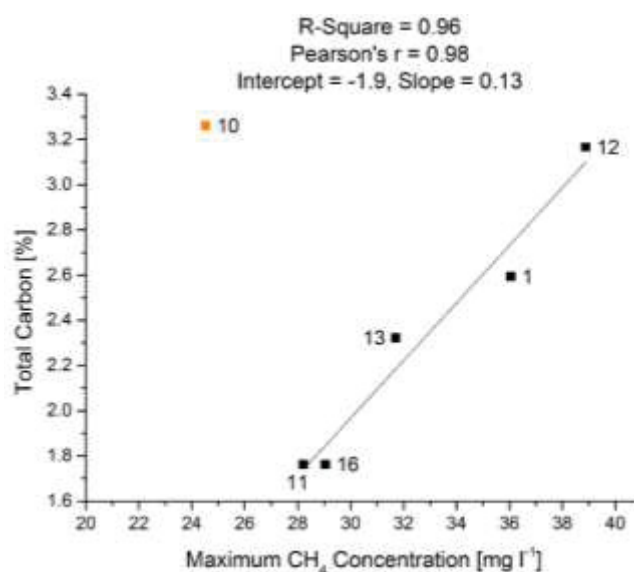


Figure 5-55: TC vs. the maximum concentration of methane in the pore water; location 10 was discarded as an outlier, ($r = 0.98$, $N = 5$, $p < 0.01$).

In addition, an indirect factor, which is able to describe relevant ambient characteristics of methane formation can be derived. The iron content of the sediment also shows a positive correlation with the methane concentration in the pore water ($r = 0.98$, $N = 5$, $p < 0.01$) (Figure 5-56). In this case there is no direct biochemical relation between the two parameters. Iron is not consumed or released during the formation processes of methane. However, the biochemical prerequisites for the methane formation imply the presence of FeS or FeS₂ in the sediment (Passier & deLange, 1998). As described before, this is especially the case if the redox-potential in the upper sediment is constantly low ($Eh < -200$ mV). This again is only possible if the hypolimnion is oxygen-free for the largest part of the year. Therefore, the iron content of the sediment is defined as a proxy parameter, not only for the pore water methane concentration, but additionally for the long term reaction conditions at the corresponding locations. Taking into account the presented depth dependence of the iron contents in the sediment (chapter 5.1.3; equal tendencies for CR and VR) this assumption can be transferred to other reservoirs as well.

Derived from the density-related results, elucidated in chapter 5.1.3 and 5.1.4 a conjunction between the bulk density and the concentration of methane (gas) can be assumed. Consequently, the density is depicted over the CH₄ concentration in the pore

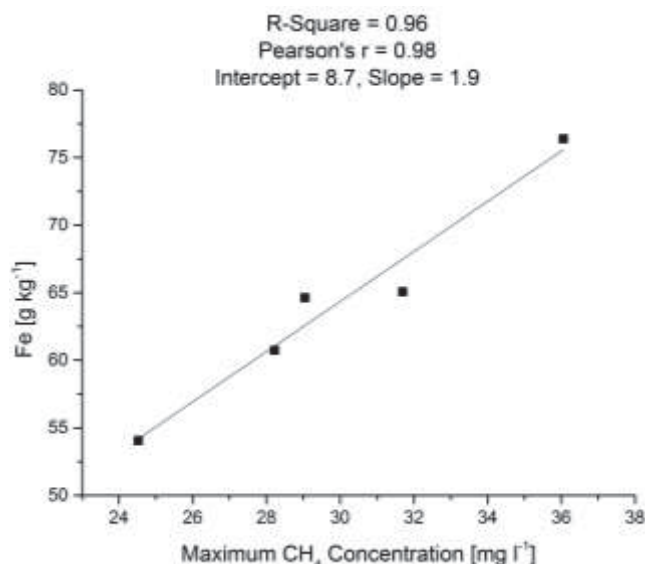


Figure 5-56: TC vs. the maximum concentration of methane in the pore water, $r = 0.98$, $N = 5$, $p < 0.01$.

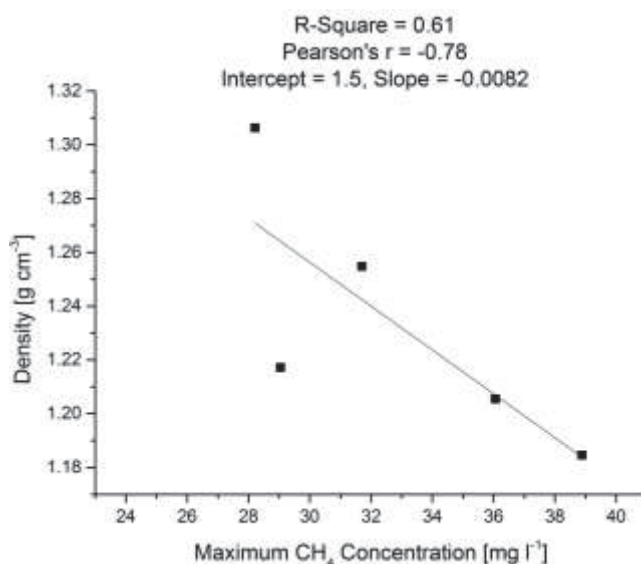


Figure 5-57: Density vs the maximum concentration of methane in the pore water; $r = -0.78$, $N = 5$, $p < 0.1$

water (Figure 5-57). The negative correlation illustrates that higher methane concentrations coincide with lower bulk densities of the sediment volumes. Due to the fact that two DPS's were stolen/lost (core location 5 & 8) valuable information from sediment with coarser material and higher densities was lost. Hence, no ultimate conclusion about the behavior of methane concentration in sediments with elevated densities can be drawn. Still these results imply a certain dependence of methane occurrence and density changes.

5.4.4 Methane Concentration and hydro-acoustic Behavior

To evaluate the relation of methane in the pore water and the hydro-acoustic signature of the sediment, relevant parameters are depicted against each other. Since the 200 kHz frequency was proven to have a significant potential of detecting sediment features, it is chosen over the 38 kHz frequency (Figure 5-58). Figure 5-58 shows the set of hydro-acoustic parameters explaining the reflectivity of the sediment at the DPS-sampling locations. As the various parameters can be assigned to specific parts of the sediment, the reflection patterns can be explained. Even if the presented regressions are statistically reduced in significance due to the limited number of samples; tendencies can be recognized.

The $attSv1$ ($E1'$) value shows a negative correlation to the concentration of methane (Figure 5-58, A). Based on the assumption that the primary feature, which changes the hydro-acoustic behavior in addition to the granulometry, are bubbles in the sediment matrix (chapter 2.3.3 and 2.3.5.2), an interrelation can be confirmed. The core samples at the corresponding locations contained bubbles, however the bubbles occurred mainly in the deeper layers of the cores (lower than 15 cm). If no bubbles are present the main influence for the $E1'$ value is the impedance contrast respectively the direct reflection. More methane (bubbles) can be found in softer sediments (higher share of finest fraction) while the backscatter strength of these sediment surfaces can be assumed to be weaker, due to low impedance contrasts.

Thus, a negative relation of the $E1'$ parameter can be explained by the absence of bubbles close to the SWI and by the previously described correlation between wave signatures and sediment characteristics (see chapter 4.2.4.1). The $E1'$ value is relatively sensitive to changes of the angle of incidence during the measurement as well as the inhomogeneities of the sediment surface. This explains the high standard deviation of the presented mean values.

In contrast, the $decSv1$ ($E1$) value has a positive correlation with the occurrence of higher methane concentrations, as does the $attdecSv1$ value which is mainly influenced by the $E1$

value (Figure 5-58, B & C). Due to the fact, that both values represent the reflectivity of the sediment volume, higher backscatter strengths of the sediment can be explained by the presence of gas bubbles. Larger bubbles and higher numbers per volume occur with more gas in the pore water (Sollberger et al., 2014). This causes the reflection and therefore the volume related hydro-acoustic parameters to increase (Lyons, 1996; Sager et al., 1998).

As an example for a relative acoustic parameter the behavior of the decSv1/attdecSv2 is examined (Figure 5-58, H). Here a clear negative tendency is given. Based on the fact that acoustic turbidity layers (accumulations of bubbles) cause higher reflection intensities, the second bottom echo contains more energy. If the intensity of the E1 value is divided by the intensity of the entire second echo, it is suggested that higher methane concentrations will negatively influence the decSv1/attdecSv2 value. The higher the intensity of the overall reflection, the higher will be the intensity of the second echo, causing the ratio between both values to be smaller.

The interpretation of the methane concentrations and the hydro-acoustic parameters leads to the suggestion that, the presence of gas bubbles and consequently the concentration of methane, can be detected by echo sounder applications. One basic restriction is the local solubility limit of methane. If concentrations are too low, no bubbles can form and hence no acoustic difference can be detected.

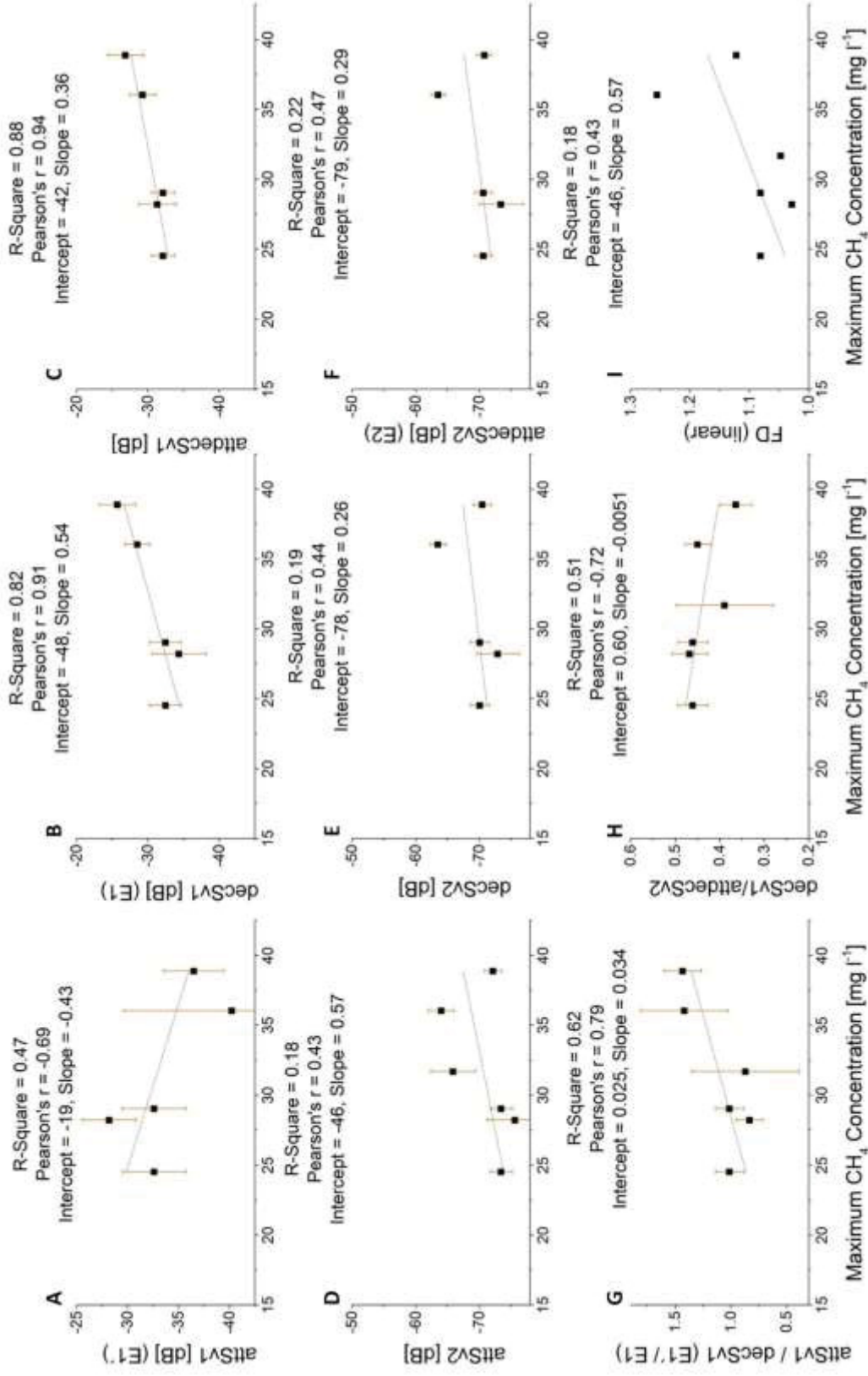


Figure 5-58: Hydro-acoustic parameters of the 200 kHz freq., configuration B, 100 W vs. the maximum methane concentration in the pore water.

5.4.5 Synopsis

Summarizing the principal findings of the *composed results*, the following aspects are named, Figure 5-59 presents a graphical overview of the results.

- Steep inclinations of the lakebed influence the distribution of the sediment. They lead to intense sediment focusing in the depressions, therefore the shape of the accumulation areas follows the morphology of the lakebed. Consequently, the morphology gives a first insight into the accumulation patterns and therefore into the allocation of potential methane emission hot spots. In further surveys, a detailed bathymetric map can already reveal these locations.
- Based on a set of input parameters, which were calculated in this work, the carbon stock in the sediment of Capivari reservoir was calculated. Results show the tendency, that higher stocks are found in the profundal. This is due to elevated contents of carbon, but mainly the thicker sediment layer contributes to the high amounts of carbon stock per m². The reservoir holds an average stock of 19.5 kg m⁻² (± 5.8 kg m⁻²). The oxycline in a depth of around 10–14 m causes a relatively short OET for settling particles in the profundal. This leads to an elevated carbon burial efficiency, and hence creates potential methane production hot spots.
- Iron and TC have been shown to feature a strong positive correlation with the methane concentration, whereas the density is negatively correlated. TC and density are directly related to the methane production or the presence of bubbles. This matches general findings, since carbon is the basic substrate for the methanogenesis and the presence of bubbles strongly influences the bulk density.

Based on the assumption that iron is only accumulated in the sediment if the redox-potentials in and above the sediment are permanently low, it can be suggested that areas with high iron contents and elevated methane concentrations permanently produce methane.

- If bubbles are present in the sediment, it is possible to distinct these sediment volumes from sediments without bubbles. The hydro-acoustic parameters from the 200 kHz frequency show significant correlations with the maximum methane concentration in the pore water. While the E1'parameter is sensitive to the occurrence of bubbles in the upper part of the sediment (0–10 cm), the E1 and

related parameters are able to identify the presence of bubbles in the lower sediment volumes (10–50 cm).

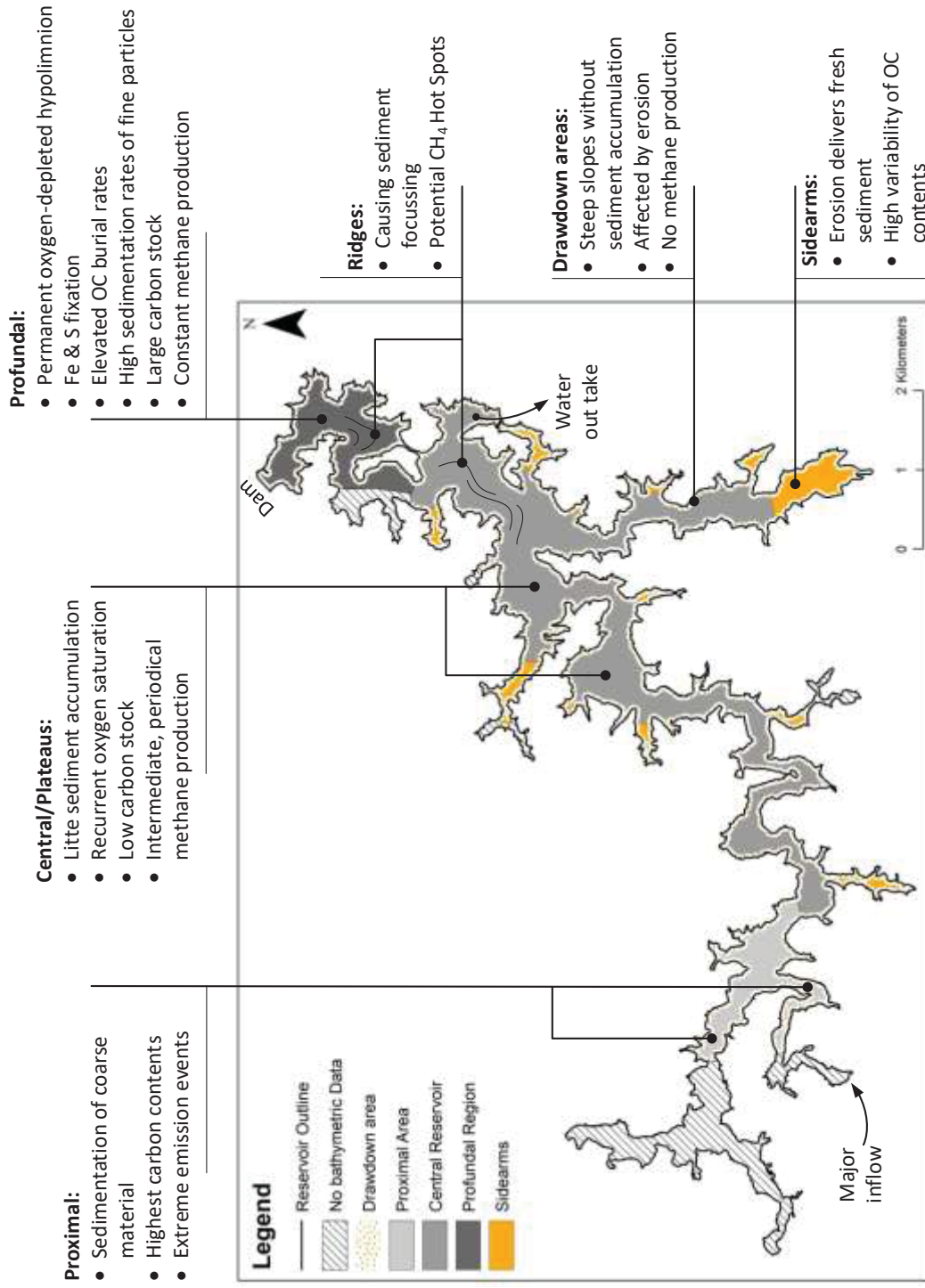


Figure 5-59: Overview of derived characteristics of the determined reservoir zones in Capivari reservoir.

6 Discussion

This study examines the possibility to detect and understand spatial and temporal heterogeneities of methane production, by combining sediment analyses with hydro-acoustic approaches. To what extent is it possible to localize sediment types with intense methane production?

Hydro-acoustic investigations showed that, parameters obtained with various settings of the echo sounder, lead to significant correlations with sediment properties (Anderson & Pacheco, 2011; Anderson et al., 2013). The selected configurations allowed to transfer local sediment features into the area of the entire reservoir, by using echo sounder data from the driven lines (Freitas et al., 2008; Anderson et al., 2013). Created maps of various sediment features are in accordance to general distribution patterns (Gilbert, 2003). However, the detailed investigations indicated that the morphometric influence of the reservoir produces distinctive areas of sediment accumulation (Annandale, 2007), organic carbon burial and hence methane production. These areas were successfully identified.

Consequently, the hydro-acoustic survey can be used as a tool to create a measurement plan for GHG emissions and also to reduce the number of necessary measurements for an adequate emission estimation. Additionally, it can help to interpret the emission measurement results from different areas by putting them in relation to the prevalent sediment types and their methane production potential.

Besides the morphometric influence on sedimentation (Likens, 2010, 478-480), the oxygen exposure time could be determined to have a strong influence on the carbon burial efficiency, this is in accordance with the literature (Heyer & Kalff, 1998; Kirstensen, 2000; Sobek et al., 2009; Sobek et al., 2012). Therefore, the localization of the oxycline and the water depth at corresponding locations were identified to have a major influence on local methane production.

Furthermore, iron and sulfur contents in the sediment were found to be related to the temporal heterogeneity of methane production. Kuivila et al. (1989), Holmer & Storkholm (2001) and Roden & Wetzel (2003) described the connection of iron, sulfur and methane production, but the enrichment of FeS/FeS₂ in a temporal context was not yet assessed. The described fixation of iron and sulfur in dependence on the prevalent redox conditions was

described by Passier & deLange (1998). Consequently, the suggestion, that more iron and sulfur is bound in the sediment if the necessary conditions are met for a long time, seems correct. Passier & deLange (1998) additionally stated, that more iron and sulfur is bound if elevated contents of organic carbon are present. This confirms the increased iron and sulfur values found in the sediments of the profundal, since local carbon values were high as well.

The developed placement system for dialysis pore water samplers (DPS-PS) was successfully tested and produced verified results, while reducing the overall efforts to a minimum compared to previous studies (Teasdale et al., 1995; Adams & Baudo, 2001).

The applied techniques allowed to create a detailed map of the carbon content in the sediment, which in combination with the obtained sediment thickness led to a precise estimation of the carbon stock of the entire reservoir.

In partial contradiction to the literature (Morris & Fan, 1998, 10.3) the findings show that no continuous gradient in the accumulation of sediments from the inflow to the dam was present nor could one presented pattern be identified (chapter 2.1.2). The accumulation pattern found in Capivari reservoir resembles more a mixture between the wedge and delta shape. This can be attributed to the complex shape of the impoundment.

Recently, sediment investigations have shown that especially the depressions like canyons tend to be methane production hotspots (Sollberger et al., 2014). The results of this work support and augment these findings, by showing that the old riverbed is a distinct accumulation region of fine organic-rich sediments and consequently of methane production. Plateau formations were found to accumulate less sediment with lower contents of organic carbon and thus, are areas of low potential methane production. They can be seen as transportation bottoms in accordance to Morris & Fan (1998, 10.3).

Furthermore, the dependence of ebullition events on hydrostatic pressure (Scandella et al., 2011; Maeck et al., 2014) could be substantiated by findings during the conducted surveys. During phases of rising water levels and increasing hydrostatic pressure no bubble events could be observed even though intense ebullition was perceived at the same positions under decreasing pressure.

The overall efficiency of the bubble detection within this study must be critically regarded. Although the data analysis did not show a direct dependency between depth and bubble detections, un-proportional low numbers of bubbles have been detected in the shallow areas.

In spite of the findings from Ostrovsky (2003) which show comparable patterns of bubble distribution since more bubbles could be detected in deeper regions, at least in some sidearms higher bubble-counts were expected. This assumption is based on the visual recognition of bubbles reaching the surface.

A possible explanation is given in the relatively low ping rate during parts of the driven survey. Due to unclear reasons the transducer was not able to maintain the set ping rate of 5 pings s^{-1} during the entire survey. Lower ping rates complicate the detection of bubbles, since less echoes can be received during the ascent of each single bubble. This deteriorates the bubble detection particularly in shallow areas, due to shorter distance from the origin of the bubble (sediment) to the transducer.

An additional point which can be critically discussed, is the detection of the sediment thickness. As described in this study, the detectability of the thickness strongly depends on the sediment properties and the impinging frequency. Anderson et al. (2013) postulate a method for the determination of the sediment depth which is similar to the approach presented in this work. The major difference is the acoustic definition of the lower sediment boundary. Anderson et al. take the back edge of the 38 kHz bottom echo (independent from the dB-value) as the lower boundary. In contrast to this, the last and strongest peak of each single echo was used in their study.

Based on the physical background, defined by the British Standard 6349-5:1991 (1991) and modeled by Williams et al. (2002), the penetration depth of the 38 kHz frequency is limited. Due to the fact that an attenuation of 4–12 dB m^{-1} -sediment can be implied for the 38 kHz frequency (Williams et al., 2002) it seems unlikely to obtain acoustic values from a depth of more than 5–6 m, even if the sediment has a high water saturation and is mostly unconsolidated (Jakubauskas & deNoyelles, 2008). Consequently, the sediment thickness of 15 m calculated by Anderson et al. (2013) appears physically difficult. In this context, the thickness values from this study represent a realistic and scientific correct range. No discrepancies were observed, by comparing the static and dynamic thickness results. Consequently, the results are not biased by the boat movement.

Besides the physical aspects of the sediment thickness determination the calculated magnitudes can be set in relation to literature values. Mulholland & Elwood (1982) published a summary of the accumulation rates of reservoirs around the world. For tropical reservoirs (in this case from Asia) an accumulation rate of 0.8–22 $cm a^{-1}$ is stated. According to the reservoir age of 44 years a sediment layer of 3.5–9.6 m could be expected. Taking into account that the reservoir has been emptied entirely for three times since construction

(COPEL), which causes a loss of sediment, the upper values from 1.5 – 3 m calculated in this study seem reasonable.

Finally, the stated zonation of the reservoir is discussed in terms of methane emissions. Figure 6-1 combines the interpolated carbon stock and the detected bubbles from this work with results from ebullition flux measurements conducted by Kan et al. (2013). For the flux measurements funnels, as described in chapter 2.2.4, were used.

At first, the ebullition flux measurements do not seem to support the bubble detection results, since highest fluxes were measured where small numbers of bubbles were detected and vice versa. Due to the explained limitations of the hydro-acoustic bubble detection in shallow areas, the high fluxes in the sidearms do not oppose the findings of this work. They are rather supported, since the interpolated carbon contents of the sediment in the sidearms was high (Figure 5-32).

Even though some bubbles were present in the central parts of the reservoir, the low fluxes from the funnel measurements agree with the stated theory, that the middle part does not emit significant amounts of methane. This stands in accordance to the low total carbon values measured in the sediment of the central reservoir.

The contradictive results in the profundal close to the dam can only be explained by the temporal heterogeneity of ebullition events. Due to the fact that no flux measurement was conducted directly in the proximal, no suggestion can be made in order to discuss the suggested elevated emissions from this part of the reservoir.

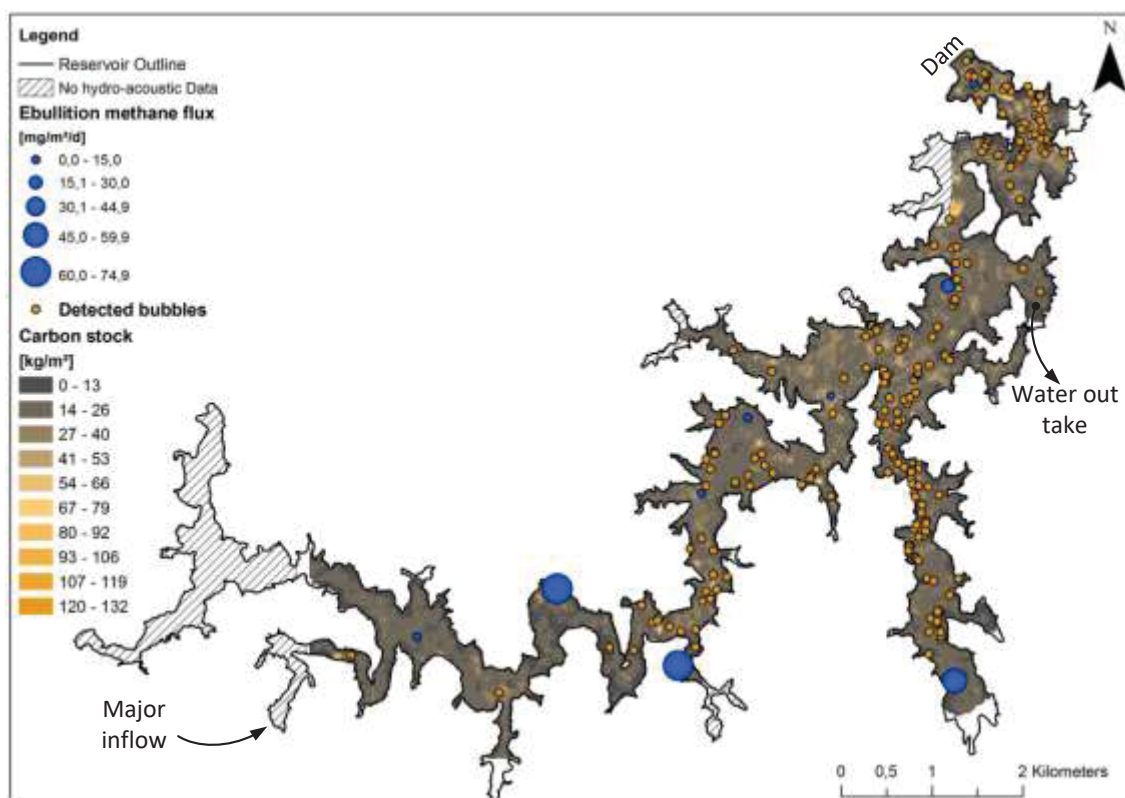


Figure 6-1: Carbon stock distribution in the Capivari reservoir, including detected bubbles in the water column; the blue circles represent averaged results from funnel measurements by Kan et al. (2013).

7 Outlook

After the discussion of the recent findings, this chapter presents opportunities for further research subsequent to this work.

The use of additional echo sounder frequencies could substantially facilitate the interpretation of the hydro-acoustic data. In these regards a lower frequency (15 kHz) would allow an improved detection of the sediment thickness, since it is less attenuated within the sediment volume, and can therefore penetrate the sediment deeper. One promising option is the parametric sonar technology. It would offer the advantages of an exceedingly narrow beam due to the parametric difference frequency, which produces virtually no side lobes, and can be transmitted from a physically small transducer. It combines high resolution imaging with good penetration depth (Wunderlich & Muller, 2003). It is assumed that the high resolution would lead to improved bubble detection in the sediment and more efficient SBC.

As an experimental approach for the bubble detection, the echo sounder could be horizontally arranged at the side of the boat. This arrangement features the advantage, that a large area next to the boat could be scanned for rising bubbles. However, this approach has not been tested yet.

Furthermore, the application of percussion corers with elongated tubes offers the possibility to obtain sediment cores of more than two meters length. This would substantially support the interpretation of long-term sedimentation processes. It would also allow to determine the exact magnitude of the methane-active layer. For a better assessment of the sediment heterogeneity, the utilization of a triple-corer (three cores are taken at the same time with 1 m distance) represents an additional option.

The aim of this work was to investigate the structures and characteristics of the entire reservoir. Consequently, a more detailed sampling campaign could enhance the understanding of the defined zones of the reservoir. Most promising would it be, to measure along designated transects, which cover a range from the drawdown area to the profundal, but are situated within one zone. In this perspective, the deployment of DPS's along this transect could help to understand the methane related processes in relation to the depth and in particular in regards of the position of the oxycline.

References

- Abe, D. S.; Sidagis Galli, C. V.; Tundisi, J. G. & Tundisi, T., M.** (2009a): *Greenhouse gas concentrations and diffusive flux at the sediment-water interface from two reservoirs in Brazil*. Verh. Internat. Verein. Limnol. 30 (6), 830–833.
- Abe, D. S.; Sidagis Galli, C. V.; Tundisi, J. G. & Tundisi, T., M.** (2009b): *The effect of eutrophication on greenhouse gas emissions in three reservoirs of the Middle Tietê River, Southeastern Brazil*. Verh. Internat. Verein. Limnol. 30 (6), 822–825.
- Abe, D. S.; Sidagis Galli, C. V.; Tundisi, J. G. & Tundisi, T., M.** (2012): *Sediment sampling for Gas Measurements*.
- Abegg, F. & Anderson, A. L.** (1997): *The acoustic turbid layer in muddy sediments of Eckernförde Bay, Western Baltic: methane concentration, saturation and bubble characteristics*. Marine Geology. 137 (1–2), 137–147.
- Abraham, J.; Allen, P. M.; Dunbar, J. A. & Dworkin, S. I.** (1999): *Sediment type distribution in reservoirs: sediment source versus morphometry*. Environmental Geology. 38 (2), 101–110.
- Abril, G.; Guérin, F.; Richard, S.; Delmas, R.; Galy-Lacaux, C.; Gosse, P.; Tremblay, A.; Varfalvy, L.; dos Santos, M. A. & Matvienko, B.** (2005): *Carbon dioxide and methane emissions and the carbon budget of a 10-year old tropical reservoir (Petit Saut, French Guiana)*. Global Biogeochemical Cycles. 19 (), 1–16.
- Adams, D. D. & Baudo, R.** (2001): *Gases (CH₄, CO₂ and N₂) and pore water chemistry in the surface sediments of Lake Orta, Italy: Acidification effects on C and N gas cycling*. Journal of Limnology. 2001 (60), 79–90.
- Airmar Technology Corporation** (2012): *Theory of Operation*.
- Aller, R., C.** (2004): *Conceptual models of early diagenetic processes: The muddy seafloor as an unsteady, batch reactor*. Journal of Marine Research. 62 (6), 815–835.
- Amiri-Simkooei, A. R.; Snellen, M. & Simons, D. G.** (2011): *Principal Component Analysis of Single-Beam Echo-Sounder Signal Features for Seafloor Classification*. Oceanic Engineering, IEEE Journal of. 36 (2), 259–272.
- Anderson, A. L.; Abegg, F.; Hawkins, J. A.; Duncan, M. E. & Lyons, A. P.** (1998): *Bubble populations and acoustic interaction with the gassy floor of Eckernförde Bay*. Continental Shelf Research. 18 (14-15), 1807–1838.
- Anderson, M. A.** (2010): *Bathymetric, sedimentological and retrospective water quality analysis to evaluate effectiveness of lake Elsinore recycled water pipeline Project*.
- Anderson, M. A. & Pacheco, P.** (2011): *Characterization of bottom sediments in lakes using hydroacoustic methods and comparison with laboratory measurements*. Water Research. 45 (15), 4399–4408.
- Anderson, Michael A.; Conkle, Jeremy L.; Pacheco, Porfirio & Gan, Jay** (2013): *Use of hydroacoustic measurements to characterize bottom sediments and guide sampling and remediation of organic contaminants in lake sediments*. Science of The Total Environment. 458–460 (0), 117–124.
- ANEEL** (2013): *Relatório ANEEL 2012*. [In: Portugues].
- Annandale, G. W.,** 2007: *Reservoir Sedimentation*. In: Anderson, G. M.; McDonnell, J. J. Encyclopedia of Hydrological Sciences. John Wiley & Sons, 1–86.

- Avnimelech, Yoram; Ritvo, Gad; Meijer, Leon E. & Kochba, Malka** (2001): *Water content, organic carbon and dry bulk density in flooded sediments*. *Aquacultural Engineering*. 25 (1), 25–33.
- Balk, H.; Lindem, T. & Sánchez-Carnero, N.** (2011): *Sonar4 and Sonar5 post processing systems. Operator manual version 6.0.1. Extension for Seabed Classification Tool*.
- Barros, N.; Cole, J. J.; Tranvik, L. J.; Prairie, Y. T.; Bastviken, D.; Huszar, V. L. M.; del Giorgio, P. & Roland, F.** (2011): *Carbon emission from hydroelectric reservoirs linked to reservoir age and latitude*. *Nature Geosci.* advance online publication.
- Bartram, J. & Richard, B.** (1996): *Water Quality Monitoring - A Practical Guide to the Design and Implementation of Freshwater Quality Studies and Monitoring Programmes*. New York.
- Bastviken, D.; Cole, J. J.; Pace, M. L. & Tranvik, L. J.** (2004a): *Methane emissions from lakes: Dependence of lake characteristics, two regional assessments, and a global estimate*. *Global Biogeochemical Cycles*. 18 (), 1–12.
- Bastviken, D.; Cole, J. J.; Pace, M. L. & van de Bogert, M. C.** (2008): *Fates of methane from different lake habitats: Connecting whole-lake budgets and CH₄ emissions*. *Journal of Geophysical Research*. 113 (G2), G02024.
- Bastviken, D.; Persson, L.; Odham, G. & Tranvik, L. J.** (2004b): *Degradation of Dissolved Organic Matter in Oxidic and Anoxic Lake Water*. *Limnology and Oceanography*. 49 (1), 109–116.
- Bastviken, D.; Tranvik, L. J.; Downing, J. A.; Crill, P. M. & Enrich-Prast, A.** (2011): *Freshwater Methane Emissions Offset the Continental Carbon Sink*. *Science*. 331 (6013), 50.
- Baulch, Helen M.; Dillon, Peter J.; Maranger, Roxane & Schiff, Sherry L.** (2011): *Diffusive and ebullitive transport of methane and nitrous oxide from streams: Are bubble-mediated fluxes important?* *Journal of Geophysical Research: Biogeosciences*. 116 (G4), G04028.
- Blais, J. M. & Kalff, J.** (1995): *The influence of lake morphometry on sediment focusing*. *Limnology and Oceanography*. 40 (3), 582–599.
- Borges, P.; Train, S. & Rodrigues, L.** (2008): *Spatial and temporal variation of phytoplankton in two subtropical Brazilian reservoirs*. *Hydrobiologia*. 607, 63–74.
- Boudreau, B., P.; Algar, C.; Johnson, B., D.; Croudace, I.; Reed, A.; Furukawa, Y.; Dorgan, K., M.; Jumars, P., A.; Grader, A., S. & Gardiner, B., S.** (2005): *Bubble growth and rise in soft sediments*. *Geology*. 33 (6), 517–520.
- Brainard, L. & Martinez-Diaz, L.** (2009): *Brazil As an Economic Superpower?* Washington D.C. The Brookings Institution.
- Brandl, H. & Hanselmann, K. W.** (1991): *Evaluation and application of dialysis porewater samplers for microbiological studies at sediment-water interfaces*. *Aquatic Sciences*. 53 (1), 55-73.
- British Standard 6349-5:1991** (1991): *Maritime structures*.
- Brouwer P.** (2008): *Seafloor classification using a single beam echosounder*. Delft.
- Buchanan, L. A.** (2009): *Using a dual frequency echo sounder for the determination of suspended sediment in the water column*.
- Bühler L.** (2008): *Burial of Organic Carbon in Lakes*. Zürich.

- Burczynski, J.** (1999): *Bottom Classification*.
- Caetano de Souza, A. C.** (2008): *Assessment and statistics of Brazilian hydroelectric power plants: Dam areas versus installed and firm power*. *Renewable and Sustainable Energy Reviews*. 12 (7), 1843–1863.
- Carlson, R., E.** (1977): *A trophic state index for lakes*. *Limnology and Oceanography*. 22 (2).
- Casper, P.; Maberly, S. C.; Hall, G. H. & Finlay, B. J.** (2000): *Fluxes of methane and carbon dioxide from a small productive lake to the atmosphere*. *Biogeochemistry*. 49 (1), 1–19.
- Cesare, G. de; Schleiss, A. & Hermann, F.** (2001): *Impact of Turbidity Currents on Reservoir Sedimentation*. *J. Hydraul. Eng.* 127 (1), 6–16.
- Chanudet, V.; Descloux, S.; Harby, A.; Sundt, H.; Hansen, B. H.; Brakstad, O.; Serça, D. & Guerin, F.** (2011): *Gross CO₂ and CH₄ emissions from the Nam Ngum and Nam Leuk sub-tropical reservoirs in Lao PDR*. *Science of The Total Environment*. 409 (24), 5382–5391.
- Chen, H.; Yuan, X.; Chen, Z.; Wu, Y.; Liu, X.; Zhu, D.; Wu, N.; Zhu, Q.; Peng, C. & Li, W.** (2011): *Methane emissions from the surface of the Three Gorges Reservoir*. *Journal of Geophysical Research: Atmospheres*. 116 (D21), D21306.
- Choi, Jeong-Hoon; Seol, Yongkoo; Boswell, Ray & Juanes, Ruben** (2011): *X-ray computed-tomography imaging of gas migration in water-saturated sediments: From capillary invasion to conduit opening*. *Geophysical Research Letters*. 38 (17), L17310.
- Cicerone, R. J.** (1988): *Biochemical aspects of atmospheric methane*. *Global Biogeochemical Cycles*. 2 (4), 299–327.
- Collins, W. T.; Rhynas, K. P.** (1998): *Acoustic Seabed Classification using Echo Sounders: Operational Considerations and Strategies*.
- Conrad, R.**, 1989: *Control of methane production in terrestrial ecosystems*. In: Meinrat, O. A.; Schimel, D. S.; Robertson, G. P. *Exchange of trace gases between terrestrial ecosystems and the atmosphere*. Chichester. John Wiley & Sons, 39–58.
- Conrad, R.** (2009): *The global methane cycle: recent advances in understanding the microbial processes involved*. *Environmental Microbiology Reports*. 1 (5), 285–292.
- Conservation International** (2000): *Megadiversity data tables*. Washington, USA.
- Craft, C. B.; Seneca, E. D. & Broome, S. W.** (1991): *Loss on ignition and kjeldahl digestion for estimating organic carbon and total nitrogen in estuarine marsh soils: Calibration with dry combustion*. *Estuaries*. 14 (2), 175–179.
- Dattagupta, S.; Telesnicki, G.; Luley, K.; Predmore, B.; McGinley, M. & Fisher, C.** (2007): *Submersible operated peepers for collecting pore water from deep-sea sediments*. *Limnology and Oceanography: Methods* (5), 263–268.
- Dean, Walter E. & Gorham, E.** (1998): *Magnitude and significance of carbon burial in lakes, reservoirs, and peatlands*. *Geology*. 26 (6), 535–538.
- Delmas, R.; Richard, S.; Guérin, F.; Abril, G.; Galy-Lacaux, C.; Delon, C. & Grégoire, A.**, 2005: *Long Term Greenhouse Gas Emissions from the Hydroelectric Reservoir of Petit Saut (French Guiana) and Potential*

- Impacts*. In: Tremblay, A.; Varfalvy, L.; Roehm, C.; Garneau, M. Greenhouse Gas Emissions — Fluxes and Processes. Springer Berlin Heidelberg, 293–312.
- DelSontro, T.; Kunz, M. J.; Kempter, T.; Wüest, A.; Wehrli, B. & Senn, D. B.** (2011): *Spatial Heterogeneity of Methane Ebullition in a Large Tropical Reservoir*. Environmental Science & Technology. 45 (23), 9866–9873.
- DelSontro, T.; McGinnis, D. F.; Sobek, S.; Ostrovsky, I. & Wehrli, B.** (2010): *Extreme Methane Emissions from a Swiss Hydropower Reservoir: Contribution from Bubbling Sediments*. Environmental Science & Technology. 44 (7), 2419–2425.
- Demarty, M. & Bastien, J.** (2011): *GHG emissions from hydroelectric reservoirs in tropical and equatorial regions: Review of 20 years of CH₄ emission measurements*. Energy Policy. 39 (7), 4197–4206.
- Deutsches Institut fuer Normung e.V** (2005): *Aggregates test methods. Determination of particle size distribution by wet sieving*. Beuth Verlag GmbH.
- Deutsches Institut fuer Normung e.V** (2007): *Characterization of waste. Determination of loss on ignition in waste, sludge and sediments*. Beuth Verlag GmbH.
- dos Santos, M. A.; Rosa, L. P.; Sikar, B.; Sikar, E. & dos Santos, E. O.** (2006): *Gross greenhouse gas fluxes from hydro-power reservoir compared to thermo-power plants*. Energy Policy. 34 (4), 481–488.
- Duan, Z.; Møller, N.; Greenberg, J. & Weare, J. H.** (1992): *The prediction of methane solubility in natural waters to high ionic strength from 0 to 250°C and from 0 to 1600 bar*. Geochimica et Cosmochimica Acta. 56 (4), 1451–1460.
- Duchemin, E.; Lucotte, M. & Canuel, R.** (1999): *Comparison of Static Chamber and Thin Boundary Layer Equation Methods for Measuring Greenhouse Gas Emissions from Large Water Bodies*. Environmental Science & Technology. 33 (2), 350–357.
- Dunbar, J. A.; Allen, P. M. & Higley, P. D.** (2000): *Color-encoding multifrequency acoustic data for near-bottom studies*. Geophysics. 65 (3), 994–1002.
- Ehhalt, D. H.** (1974): *The atmospheric cycle of methane*. Tellus. 26 (1-2), 58–70.
- Eilers, J.** (2004): *Bathymetry and Lake Management*. LakeLine (), 31–36.
- Eugster, W.; DelSontro, T. & Sobek, S.** (2011): *Eddy covariance flux measurements confirm extreme CH₄ emissions from a Swiss hydropower reservoir and resolve their short-term variability*. Biogeosciences. 8 (9), 2815–2831.
- Evans, R., D.** (1994): *Empirical evidence of the importance of sediment resuspension in lakes*. Hydrobiologia. 284 (1), 5-12.
- Farrow, D. E. & Patterson, J. C.** (1994): *The daytime circulation and temperature structure in a reservoir sidearm*. International Journal of Heat and Mass Transfer. 37 (13), 1957–1968.
- Fearnside, P. M.** (1997): *Greenhouse-gas emissions from Amazonian hydroelectric reservoirs: the example of Brazil's Tucuruí Dam as compared to fossil fuel alternatives*. Environmental Conservation. 24 (01), 64–75.
- Förstner, U. & Grathwohl, P.** (2007): *Ingenieurgeochemie : technische Geochemie*. Berlin. Springer.

- Freitas, R.; Rodrigues, A. M.; Morris, E.; Perez-Llorens, J. L. & Quintino, V.** (2008): *Single-beam acoustic ground discrimination of shallow water habitats: 50 kHz or 200 kHz frequency survey?* Estuarine, Coastal and Shelf Science. 78 (4), 613–622.
- Friedl, G. & Wüest, A.** (2002): *Disrupting biogeochemical cycles - Consequences of damming.* Aquatic Sciences - Research Across Boundaries. 64 (1).
- Garcia, J.-L.; Patel, K., C & Ollivier, B.** (2000): *Taxonomic, Phylogenetic, and Ecological Diversity of Methanogenic Archaea.* Anaerobe. 6 (4), 205–226.
- Gilbert, R.** (2003): *Spatially irregular sedimentation in a small, morphologically complex lake: implications for paleoenvironmental studies.* Journal of Paleolimnology. 29 (2), 209–220.
- Grant, Alastair** (1990): *Multivariate statistical analyses of sediment geochemistry.* Marine Pollution Bulletin. 21 (6), 297–299.
- Gudasz, C.; Bastviken, D.; Steger, K.; Premke, K.; Sobek, S. & Tranvik, L. J.** (2010): *Temperature-controlled organic carbon mineralization in lake sediments.* Nature. 466 (7305), 478–481.
- Gunkel, G.** (2009): *Hydropower - A Green Energy? Tropical Reservoirs and Greenhouse Gas Emissions.* CLEAN - Soil, Air, Water. 37 (9), 726–734.
- Gunkel, G. & Sobral, M.** (2013): *Re-oligotrophication as a challenge for tropical reservoir management with reference to itaparica Reservoir, São Francisco, Brazil.* Water Science & Technology. 67 (4), 708–714.
- Håkanson, L.** (2005): *The Importance of Lake Morphometry for the Structure and Function of Lakes.* International Review of Hydrobiology. 90 (4), 433–461.
- Hamilton, L. J.** (2001): *Acoustic seabed classification systems.*
- Hamilton, L. J.; Mulhearn, P. J. & Poekert, R.** (1999): *Comparison of RoxAnn and QTC-View acoustic bottom classification system performance for the Cairns area, Great Barrier Reef, Australia.* Continental Shelf Research. 19 (12), 1577–1597.
- Heiri, O.; Lotter, A. F. & Lemcke, G.** (2001): *Loss on ignition as a method for estimating organic and carbonate content in sediments: reproducibility and comparability of results.* Journal of Paleolimnology. 25 (1), 101–110.
- Hesslein, R.** (1976): *An in situ sampler for close interval pore water studies.* Limnology and Oceanography (21(6)), 912–914.
- Heyer, C. den & Kalff, J.** (1998): *Organic Matter Mineralization Rates in Sediments: A Within- and Among-Lake Study.* Limnology and Oceanography. 43 (4), 695–705.
- Hilgert, S.; Gauger, F.; Hölzlwimmer, S. & Fuchs, S.** (2014): *Development of a flexible dialysis pore water sampler placement system: Easy handling and related error sources.* Journal of Limnology. Journal of Limnology ().
- Hilton, J.** (1985): *A conceptual framework for predicting the occurrence of sediment focusing and sediment redistribution in small lakes.* Limnology and Oceanography (30), 1131–1143.
- Holland, C. W. & Gerig, A. L.,** 2006: *Acoustic Clutter from buried submarine mud Volcanoes.* In: Caiti, A.; Chapman, N. R.; Hermand, J-P.; Jesus, S. M. Acoustic Sensing Techniques for the Shallow Water Environment. Dordrecht. Springer, 109–124.

- Holmer, Marianne & Storkholm, Peter** (2001): *Sulphate reduction and sulphur cycling in lake sediments: a review*. *Freshwater Biology*. 46 (4), 431–451.
- Hözlwimmer, S.** (2013): *Analysis of the relationship between sediment composition and methane concentration in sediments of subtropical reservoirs using sediment peepers*. Weihenstephan-Triesdorf.
- Horn, H.; Horn, W.; Paul L.; Uhlmann, D. & Röske, I.** (2006): *Drei Jahrzehnte kontinuierliche Untersuchungen an der Talsperre Saldenbach*. Lengefeld.
- IEA Hydropower Agreement** (2012): *Hydropower and the Environment: Managing the Carbon Balance in Freshwater Reservoirs*.
- Intergovernmental Panel on Climate Change (IPCC)** (2014): *IPCC Fifth Assessment Report (AR5) "CLIMATE CHANGE 2014"*. Copenhagen.
- IPCC** (2007): *Climate Change 2007: Synthesis Report*. Valencia, Spain.
- Istvánovics, V.**, 2009: *Eutrophication of Lakes and Reservoirs*. In: Likens, G. E. *Encyclopedia of inland waters*. Academic Press, 221–228.
- Iversen, N. & Jørgensen, B. B.** (1993): *Diffusion coefficients of sulfate and methane in marine sediments: Influence of porosity*. *Geochimica et Cosmochimica Acta*. 57 (3), 571–578.
- Jacobs, P. H.** (2002): *A new rechargeable dialysis pore water sampler for monitoring sub-aqueous in-situ sediment caps*. *Water Research*. 36 (12), 3121–3129.
- Jain, A. & Juanes, R.** (2009): *Preferential Mode of gas invasion in sediments: Grain-scale mechanistic model of coupled multiphase fluid flow and sediment mechanics*. *Journal of Geophysical Research: Solid Earth*. 114 (B8), B08101.
- Jakubauskas, M. & deNoyelles, F.** (2008): *Methods for Assessing Sedimentation in Reservoirs*.
- Jorgensen, B. B.**, 2000: *Bacteria and Marine Biogeochemistry*. In: Schulz, H. D.; Zabel, M. *Marine Geochemistry*. Springer Berlin Heidelberg, 173-207.
- Kan, A.; Lipski, B.; Fernandes, C. ao V. S.; Oliva, E.; Esmanhoto & Pires, E. G.** (2013): *Defining a methodological approach for monitoring and 408 assessing GHGs emmissions in hyropower plants reservoirs*.
- Kansas Water Office** (2008): *Sedimentation in our Reservoir: Causes and Solutions*.
- Karrasch & Eeckert Gesellschaft für Wassertechnologie mbH** (2014): *Umrechnungsfaktoren für Einheiten der Wasserchemie*.
- Katsman, R.; Ostrovsky, I. & Makovsky, Y.** (2013): *Methane bubble growth in fine-grained muddy aquatic sediment: Insight from modeling*. *Earth and Planetary Science Letters*. 377–378 (0), 336–346.
- Kennedy, Robert H.; Gunkel Jr. , Robert C. & Thornton, Kent W.** (1982): *The establishment of water quality gradients in reservoirs*. *Canadian Water Resources Journal / Revue canadienne des ressources hydriques*. 7 (1), 71–87.
- Kennedy, R., H. & Walker, W., W.**, 1990: *Reservoir Nutrient Dynamics*. In: Thornton, K. W. *Reservoir limnology: ecological perspectives*. New York. Wiley, 109–132.

- Kirstensen, E.** (2000): *Organic matter diagenesis at the oxic/anoxic interface in coastal marine sediments, with emphasis on the role of burrowing animals*. *Hydrobiologia* (4), 1–24.
- Kuivila, K. M.; Murray, J. W.; Devol, A. H. & Novelli, P. C.** (1989): *Methane production, sulfate reduction and competition for substrates in the sediments of Lake Washington*. *Geochimica et Cosmochimica Acta*. 53 (2), 409–416.
- Länderarbeitsgemeinschaft Wasser (LAWA)** (2001): *Gewässerbewertung stehende Gewässer*. Schwerin.
- Lehner, B.; Liermann, R. C.; Revenga, C.; Vorosmarty, C.; Fekete, B.; Crouzet, P.; Doll, P.; Endejan, M.; Frenken, K.; Magome, J.; Nilsson, C.; Robertson, J. C.; Rodel, R.; Sindorf, N. & Wisser, D.** (2011): *Global Reservoir and Dam Database, Version 1 (GRanDv1): Dams, Revision 01*. Bonn, Germany. Global Water System Project (GWSP).
- Leifer, I. & Patro, R. K.** (2002): *The bubble mechanism for methane transport from the shallow sea bed to the surface: A review and sensitivity study*. *Gas in Marine Sediments: Contributions from the 5th International Conference organised by the Shallow Gas Group, Bologna, Italy, September 1998*. 22 (16), 2409–2428.
- Lempérière, F.** (2006): *The role of dams in the XXI centuri*. France.
- Leroy, C., C.; Robinson, S., P., R. & Goldsmith, M., J.** (2008): *A new equation for the accurate calculation of sound speed in all oceans*. *Journal of the Acoustical Society of America*. 124 (5), 2774–2782.
- Lewandowski, J.; Rüter, K. & Hupfer, M.** (2002): *Two-Dimensional Small-Scale Variability of Pore Water Phosphate in Freshwater Lakes: Results from a Novel Dialysis Sampler*. *Environmental Science & Technology*. 36 (9), 2039–2047.
- Likens, G. E.** (2009): *Encyclopedia of inland waters*. Academic Press.
- Likens, G. E.** (2010): *Lake Ecosystem Ecology: A Global Perspective*. Millbrook, NY.
- Lima I; Ramos F.; Bambace L. & Rosa R.** (2008): *Methane Emissions from Large Dams as Renewable Energy Resources: A Developing Nation Perspective*. *Mitigation and Adaptation Strategies for Global Change*. 13 (2), 193–206.
- Lurton, X.** (2010): *An introduction to underwater acoustics*. London. Springer.
- Lyons, Anthony P.** (1996): *Predictions of the acoustic scattering response of free-methane bubbles in muddy sediments*. *The Journal of the Acoustical Society of America*. 99 (1), 163.
- Lyons, W.; Gaudette, H. E. & Smith, G. M.** (1979): *Pore water sampling in anoxic carbonate sediments: oxidation artefacts*. *Nature*. 277 (5691), 48–49.
- Maeck, A.; DelSontro, T.; McGinnis, D. F.; Fischer, H.; Flury, S.; Schmidt, M.; Fietzek, P. & Lorke, A.** (2013): *Sediment Trapping by Dams Creates Methane Emission Hot Spots*. *Environ. Sci. Technol.* 47 (15), 8130–8137.
- Maeck, A.; Hofmann, H. & Lorke, A.** (2014): *Pumping methane out of aquatic sediments – ebullition forcing mechanisms in an impounded river*. *Biogeosciences*. 11 (11), 2925–2938.
- Mah, R. A.** (1977): *Biogenesis of methane*. *Annual Review of Microbiology* (31), 309–341.
- Mäkinen, K. & Khan, S.** (2010): *Policy considerations for greenhouse gas emissions from freshwater reservoirs*. *Water Alternatives*. 3 (2), 91–105.

- Martens, C. S.; Albert, D. B. & Alperin, M. J.** (1998): *Biogeochemical processes controlling methane in gassy coastal sediments—Part 1. A model coupling organic matter flux to gas production, oxidation and transport.* Continental Shelf Research. 18 (14–15), 1741–1770.
- Materon B. & Maurer E.** (1979): *Technical Report Capivari/Cachoeira Dam.*
- McCave, I. N.** (1971): *Sand waves in the North Sea off the coast of Holland.* Marine Geology. 10 (3), 199–225.
- McGinnis, D. F.; Greinert, J.; Artemov, Y.; Beaubien, S. E. & Wüest, A.** (2006): *Fate of rising methane bubbles in stratified waters: How much methane reaches the atmosphere?* Journal of Geophysical Research. 111 (C9).
- Medwin, H.** (1975): *Speed of sound in water: A simple equation for realistic parameters.* The Journal of the Acoustical Society of America. 58 (6), 1318–1319.
- Medwin, H.** (1977): *In situ acoustic measurements of microbubbles at sea.* Journal of Geophysical Research. 82 (6), 971–976.
- Mendonça, R.; Barros, N.; Vidal, L. O.; Pacheco, F. S.; Kosten, S. & Roland, F.** (2012): *Greenhouse Gas Emissions from Hydroelectric Reservoirs: What Knowledge Do We Have and What is Lacking? | InTechOpen.*
- Morris, L. G. & Fan, J.** (1998): *Reservoir Sedimentation Handbook.* New York. McGraw-Hill Book Co.
- Mulholland, P. J. & Elwood, J. W.** (1982): *The role of lake and reservoir sediments as sinks in the perturbed global carbon cycle.* Tellus. 34 (5), 490–499.
- Naudts, Lieven; Greinert, Jens; Artemov, Yuriy; Beaubien, Stan E.; Borowski, Christian & Batist, Marc de** (2008): *Anomalous sea-floor backscatter patterns in methane venting areas, Dnepr paleo-delta, NW Black Sea.* Marine Geology. 251 (3-4), 253–267.
- Niederreiter, R.** (2012): *Uwitech Sampling Equipments.*
- Nilsson, C.,** 2009: *Reservoirs.* In: Likens, G. E. Encyclopedia of inland waters. Academic Press, 211–218.
- Nilsson, C.,** 2010: *Reservoirs.* In: Likens, G. E. Lake Ecosystem Ecology: A Global Perspective. Millbrook, NY, 211–219.
- OECD** (1982): *Eutrophication of Waters: Monitoring, assessment and control.* Paris, France.
- Okafor, N.** (2011): *Environmental microbiology of aquatic and waste systems.* Springer.
- Orlowski, A.** (1984): *Application of multiple echoes energy measurements for evaluation of sea bottom type.* Oceanologia. 1984 (19), 61–78.
- Ortt, JR. & Richard, A.** (2000): *Bathymetric survey and sedimentation analysis of Loch Raven and Prettyboy reservoirs.*
- Ostrovsky, I.** (2003): *Methane bubbles in Lake Kinneret: Quantification and temporal and spatial heterogeneity.* Limnology and Oceanography. 48 (3), 1030–1036.
- Ostrovsky, I.** (2009a): *Fish and methane bubbles in aquatic ecosystems: hydroacoustic separation and quantification.* Verhandlungen: Proceedings. Travaux. 30 (6-7), 870–873.
- Ostrovsky, I.** (2009b): *Hydroacoustic assessment of fish abundance in the presence of gas bubbles.* Limnology and Oceanography: Methods. 7, 309–318.

- Ostrovsky, I.; McGinnis, D. F.; Lapidus, L. & Eckert W.** (2008): *Quantifying gas ebullition with echosounder: the role of methane transport by bubbles in a medium-sized lake*. *Limnology and Oceanography: Methods*. 6 (), 105–118.
- Park, Y.-S.; Kwon, Y.-S.; Hwang, S.-J. & Park, S.** (2014): *Characterizing effects of landscape and morphometric factors on water quality of reservoirs using a self-organizing map*. *Environmental Modelling & Software*. 55 (0), 214–221.
- Passier, H. F. & deLange, G. J.** (1998): *Sedimentary Sulfur and Iron Chemistry in Relation to the Formation of Eastern Mediterranean Sapropels*.
- Peel, M. C.; Finlayson, B. L. & McMahon, T. A.** (2007): *Updated world map of the Köppen-Geiger climate classification*. *Hydrology and Earth System Sciences*. 11 (5), 1633–1644.
- Poulain, T.; Argillier, C.; Gevrey, M. & Guillard, J.** (2011): *Identifying lakebed nature: is it feasible with a combination of echosounder and Sonar5-pro?* *Advances in Oceanography and Limnology*. 2 (1), 49–53.
- Rasmussen, R. A. & Khalil, M. A. K.** (1981): *Atmospheric methane (CH₄): Trends and seasonal cycles*. *Journal of Geophysical Research: Oceans*. 86 (C10), 9826–9832.
- Republic of Brazil** (1969): *Power Study of South Brazil: Canambra Engineering Consultants Limited*.
- Roden, E. E. & Wetzel, R. G.** (2003): *Competition between Fe(III)-Reducing and Methanogenic Bacteria for Acetate in Iron-Rich Freshwater Sediments*. *Microbial Ecology*. 45 (3), 252-258.
- Rosa, L. P.; dos Santos, M. A.; Matvienko, B.; Sikar, E.; Lourenço, R., S. M. & Menezes, C., F.** (2003): *Biogenic gas production from major Amazon reservoirs, Brazil*. *Hydrological Processes*. 17 (7), 1443–1450.
- Rowan, J. S.; Goodwill, P. & Greco, M.** (1995): *Temporal variability in catchment sediment yield determined from repeated bathymetric surveys: Abbeystead Reservoir, U.K.* *Sediment, Circulation and Water Quality in Lakes and Reservoirs*. 20 (2), 199–206.
- Rudd, J. W. M.; Harris, R.; Kelly, C. A. & Hecky, R. E.** (1993): *Are Hydroelectric Reservoirs Significant Sources of Greenhouse Gases?* *Ambio*. 22 (4), 246–248.
- Sager, W. W.; Lee, ChangS.; MacDonald, I. R. & Schroeder, W. W.** (1998): *High-frequency near-bottom acoustic reflection signatures of hydrocarbon seeps on the Northern Gulf of Mexico continental slope*. *Geo-Marine Letters*. 18 (4), 267-276.
- Scandella, B. P.; Varadharajan, C.; Hemond, H. F.; Ruppel, C. & Juanes, R.** (2011): *A conduit dilation model of methane venting from lake sediments*. *Geophysical Research Letters*. 38 (6), L06408.
- Schubert, C. J.; Vazquez, F.; Lösekann-Behrens, T.; Knittel, K.; Tonolla, M. & Boetius, A.** (2011): *Evidence for anaerobic oxidation of methane in sediments of a freshwater system (Lago di Cadagno)*. *FEMS Microbiology Ecology*. 76 (1), 26–38.
- Seber, G. A. F. & Wild, C. J.**, 2005: *Growth Models*. In: . *Nonlinear Regression*. John Wiley & Sons, Inc, 325–365.
- Sherman, B.; Ford, P.; Hunt, D. & Drury, C.** (2012): *Reservoir Methane Monitoring and Mitigation - Little Nerang and Hinze Dam Case Study*.
- Sidagis Galli C.; Abe, D. S. & Tundisi, J. G.** (2009): *Greenhouse gas concentrations and diffusive flux at the sediment-water interface from two reservoirs in Brazil*. *Verh. Internat. Verein. Limnol*. 30 (6), 830–833.

- Sobek, S.** (2009): *Begraben im See - so binden Sedimente CO₂*. Zürich.
- Sobek, S.; DelSontro, T.; Wongfun, N. & Wehrli, B.** (2012): *Extreme organic carbon burial fuels intense methane bubbling in a temperate reservoir*. *Geophysical Research Letters*. 39 (1), L01401.
- Sobek, S.; Durisch-Kaiser E.; Zurbru R. & Wongfun N.** (2009): *Organic carbon burial efficiency in lake sediments controlled by oxygen exposure time and sediment source*. *Limnology and Oceanography*. 54 (6), 2243–2254.
- Soille, P. & Rivest, J.-F.** (1996): *On the Validity of Fractal Dimension Measurements in Image Analysis*. *Journal of Visual Communication and Image Representation*. 7 (3), 217–229.
- Sollberger, S.; Corella, J. P.; Girardclos, S.; Randlett, M.-E.; Schubert, C. J.; Senn, D. B.; Wehrli, B. & DelSontro, T.** (2014): *Spatial heterogeneity of benthic methane dynamics in the subaquatic canyons of the Rhone River Delta (Lake Geneva)*. *Aquatic Sciences*. 76 (1), 89-101.
- Soumis, N.; Lucotte, M.; Canuel, R.; Weissenberger, S.; Houel, S.; Larose, C. & Duchemin, E.**, 2005: *Hydroelectric Reservoirs as Anthropogenic Sources of Greenhouse Gases*. In: . *Water Encyclopedia*. John Wiley & Sons, Inc.
- St. Louis, V. L.; Kelly, C. A.; Duchemin, E.; Rudd, J. W. M. & Rosenberg, D. M.** (2000): *Reservoir Surfaces as Sources of Greenhouse Gases to the Atmosphere: A Global Estimate*. *BioScience*. 50 (9), 766–775.
- Teasdale, P. R.; Batley, G. E.; Apte, S. C. & Webster, I. T.** (1995): *Pore water sampling with sediment peepers*. *TrAC Trends in Analytical Chemistry*. 14 (6), 250–256.
- Tęgowski, J.; Klusek Z. & Jakacki J.**, 2006: *Nonlinear acoustical methods in the detection of gassy sediments*. In: Caiti, A.; Chapman, N. R.; Hermand, J.-P.; Jesus, S. M. *Acoustic Sensing Techniques for the Shallow Water Environment*. Dordrecht. Springer, 125–137.
- The World Bank** (2010): *Greenhouse gas emissions related to freshwater reservoirs*.
- Thomas, B. & Arthur M., A.** (2010): *Correcting porewater concentration measurements from peepers: Application of a reverse tracer*. *Limnology and Oceanography: Methods* (8), 403–413.
- Tremblay, A.; Varfalvy, L.; Roehm, C. & Garneau, M.** (2004): *The issue of Greenhouse Gases from hydroelectric reservoirs- from boreal to tropical*.
- Tremblay, A.; Varfalvy, L.; Roehm, C.; Garneau, M.** (2005): *Greenhouse Gas Emissions — Fluxes and Processes*. Springer Berlin Heidelberg.
- Tundisi, T.** (2013): *Determinação das concentrações e das taxas de produção de dióxido de carbono (CO₂), metano (CH₄) e óxido nitroso (N₂O) nos sedimentos e estimativas dos fluxos difusivos desses gases na interface sedimento-água do reservatório de Capivari (UHE Gov. Parigot de Souza)*.
- Uhlmann, D. & Horn, W.** (2001): *Hydrobiologie der Binnengewässer*. Stuttgart. UTB.
- Urban, N. R.; Dinkel, C. & Wehrli, B.** (1997): *Solute transfer across the sediment surface of a eutrophic lake: I. Porewater profiles from dialysis samplers*. *Aquatic Sciences*. 59, 1–25.
- US Environmental Protection Agency (EPA)** (2001): *Measurement and Monitoring Technologies for the 21st Century (21M²). Sampling for Contaminants in Sediments and Sediment Pore Water*.
- Vagle, S. & Farmer, D. M.** (1992): *The Measurement of Bubble-Size Distributions by Acoustical Backscatter*. *J. Atmos. Oceanic Technol.* 9 (5), 630–644.

- Vagle, S.; Hume, J.; McLaughlin, F.; MacIsaac, E. & Shortreed, K.** (2010): *A methane bubble curtain in meromictic Sakinaw Lake, British Columbia*. *Limnology and Oceanography*. 55 (3), 1313–1326.
- van Cappellen, P. & Wang, Y.** (1996): *Cycling of iron and manganese in surface sediments; a general theory for the coupled transport and reaction of carbon, oxygen, nitrogen, sulfur, iron, and manganese*. *American Journal of Science*. 296 (3), 197–243.
- van Walree, P., A.; Tęgowski, J.; Laban, C. & Simons, D. G.** (2005): *Acoustic seafloor discrimination with echo shape parameters: A comparison with the ground truth*. *Continental Shelf Research*. 25 (18), 2273–2293.
- Vörösmarty, C. J.; Meybeck, M.; Fekete, B.; Sharma, K.; Green, P. & Syvitski, J. P. M** (2003): *Anthropogenic sediment retention: major global impact from registered river impoundments*. The supply of flux of sediment along hydrological pathways: Anthropogenic influences at the global scale. 39 (1–2), 169–190.
- Vos, B. de; Vandecasteele, B.; Deckers, J. & Muys, B.** (2005): *Capability of Loss-on-Ignition as a Predictor of Total Organic Carbon in Non-Calcareous Forest Soils*. *Communications in Soil Science and Plant Analysis*. 36 (19-20), 2899–2921.
- Voulgaris, G. & Collins, M.** (1990): *USP RoxAnn ground discrimination system: a preliminary evaluation*.
- WCD** (2000): *Dams and Development: A New Framework for Decision-Making*.
- Wessels, M.; Bussmann, I.; Schloemer, S.; Schülter, M. & Böder, V.** (2010): *Distribution, morphology, and formation of pockmarks in Lake Constance, Germany*. *Limnology and Oceanography*. 55 (6), 2623–2633.
- Wiesenburg D. A. & Guinasso N. L.** (1979): *Equilibrium solubilities of methane, carbon monoxide, and hydrogen in water and sea water*. *Journal of Chemical & Engineering Data*. 24 (4), 356–360.
- Williams, K. L.; Jackson, D. R.; Thorsos, E. I.; Tang, D. & Schock, S. G.** (2002): *Comparison of sound speed and attenuation measured in a sandy sediment to predictions based on the Biot theory of porous media*. *Oceanic Engineering, IEEE Journal of*. 27 (3), 413–428.
- Winfrey, M. R. & Zeikus, J. G.** (1977): *Effect of sulfate on carbon and electron flow during microbial methanogenesis in freshwater sediments*. *Applied and Environmental Microbiology*. 33 (2), 275–281.
- Wunderlich, J. & Muller, S.** (2003): *Non linear echo sounders for high-res sub-bottom profiling*. *Sea Technology*.

Appendix

A.1 Photos of the core samples

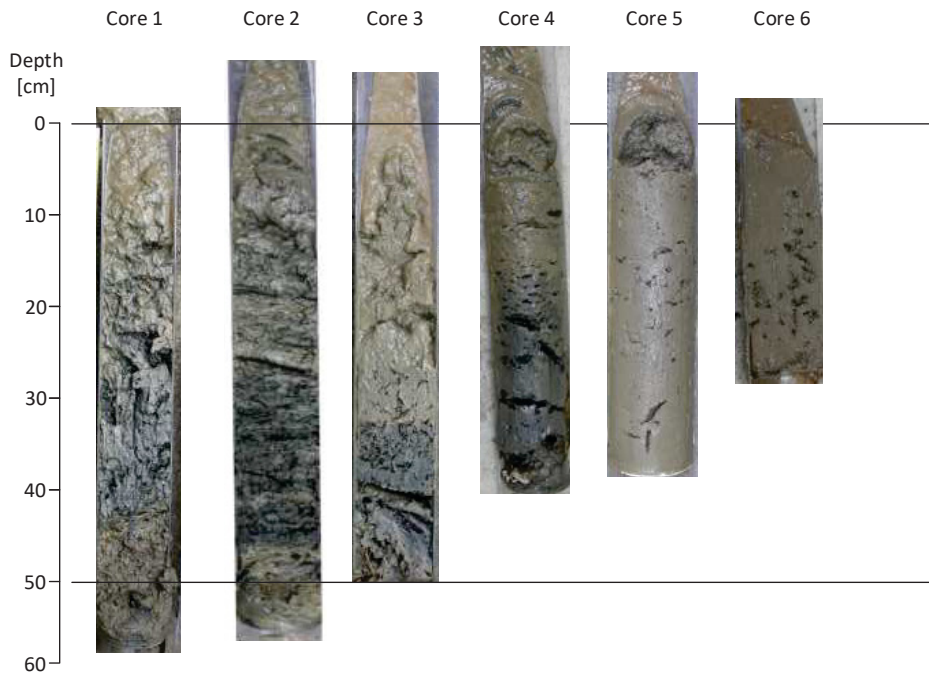


Figure A1- 1: Photos of the core samples from Capivari reservoir plotted over sediment depth, part 1

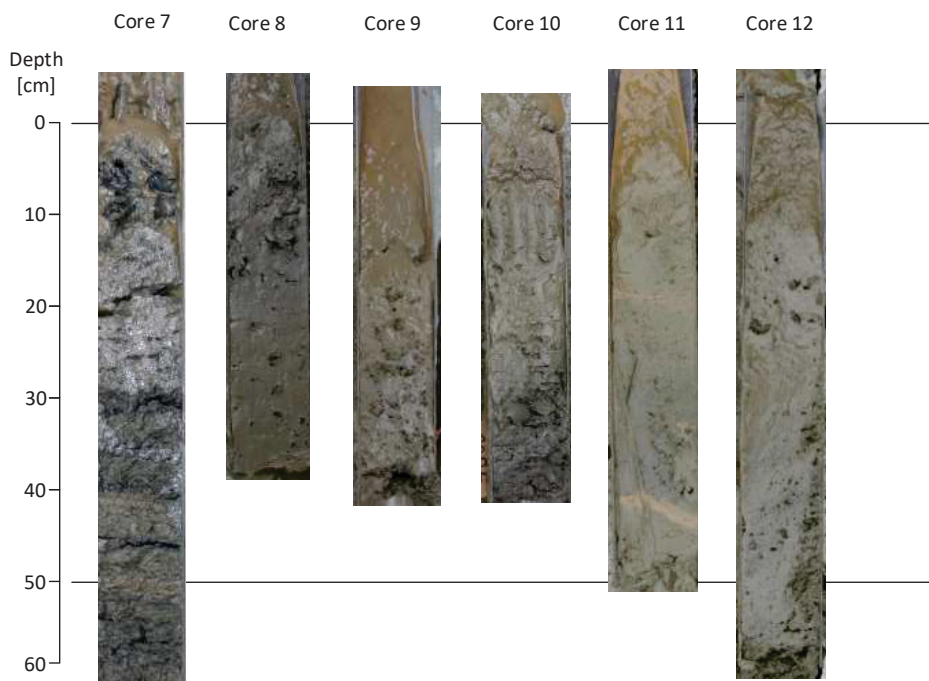


Figure A1- 2: Photos of the core samples from Capivari reservoir plotted over sediment depth, part 2

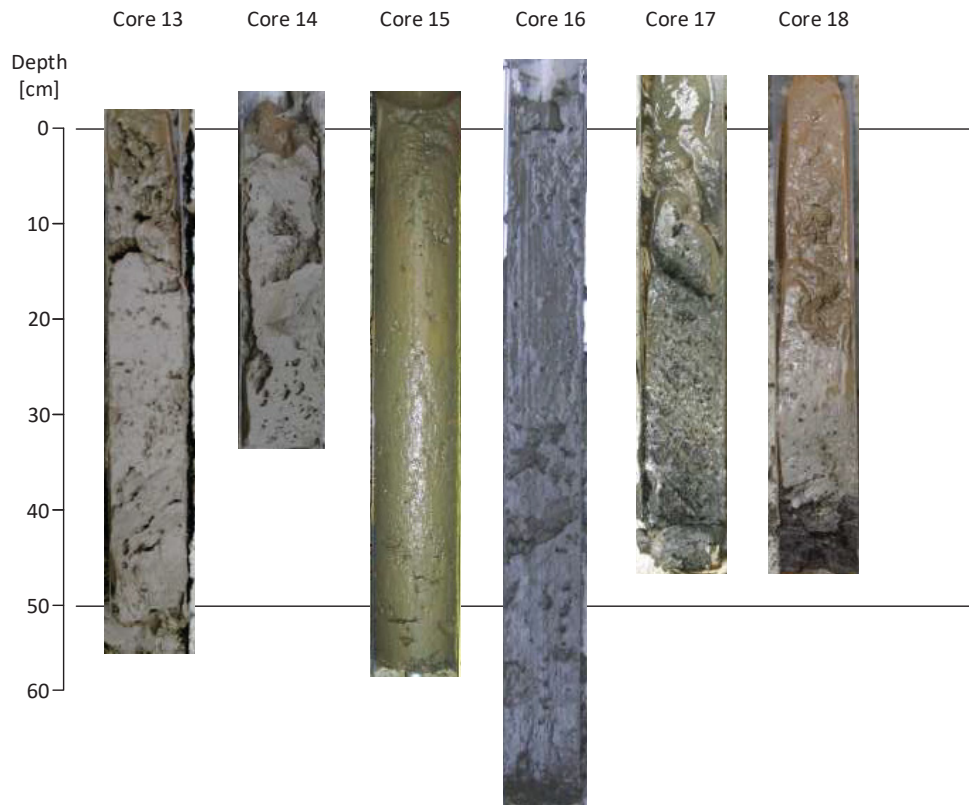


Figure A1- 3: Photos of the core samples from Capivari reservoir plotted over sediment depth, part 3

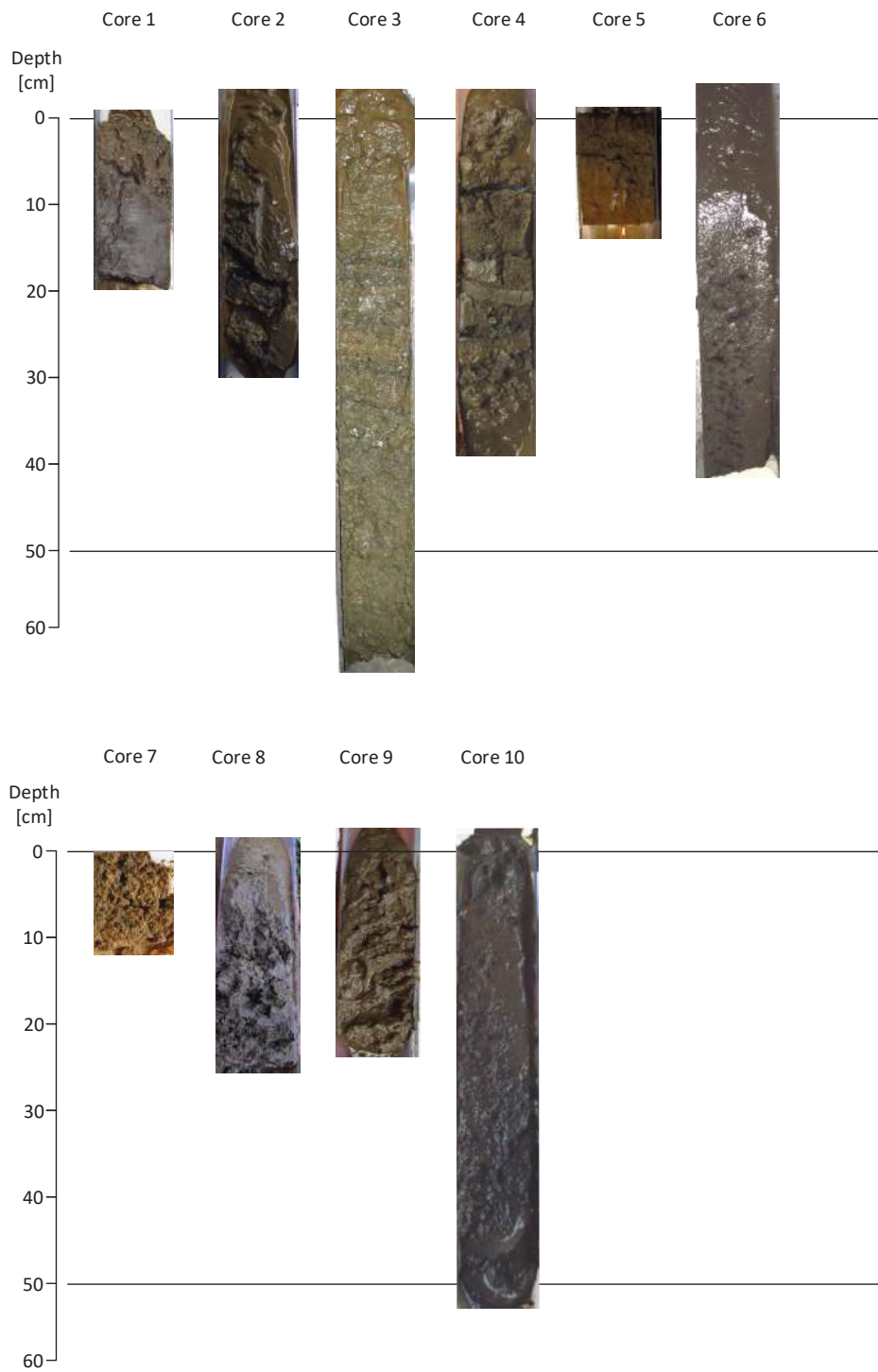


Figure A1- 4: Photos of the core samples from Vossoroca reservoir plotted over sediment depth

A.2 Beam lobes of EA 400 echo sounder

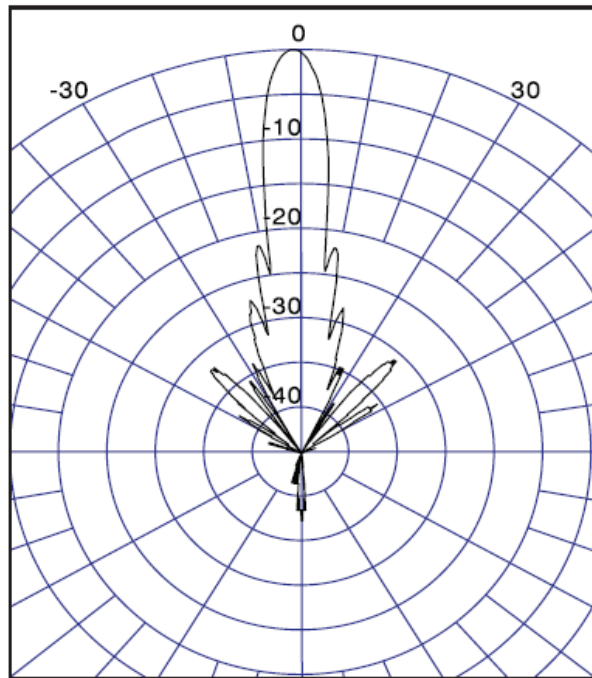


Figure A2 - 1: Beam Pattern 200 kHz (both directions)

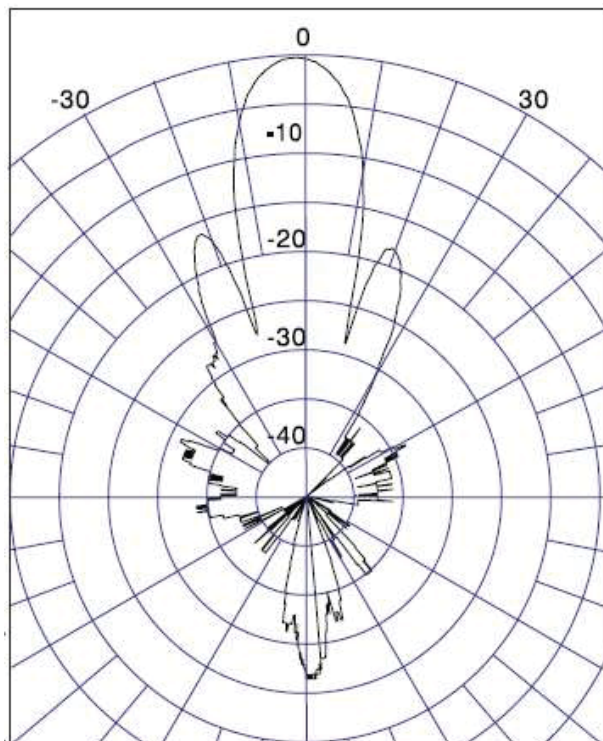


Figure A2 - 2: Beam Pattern 38 kHz longitudinal

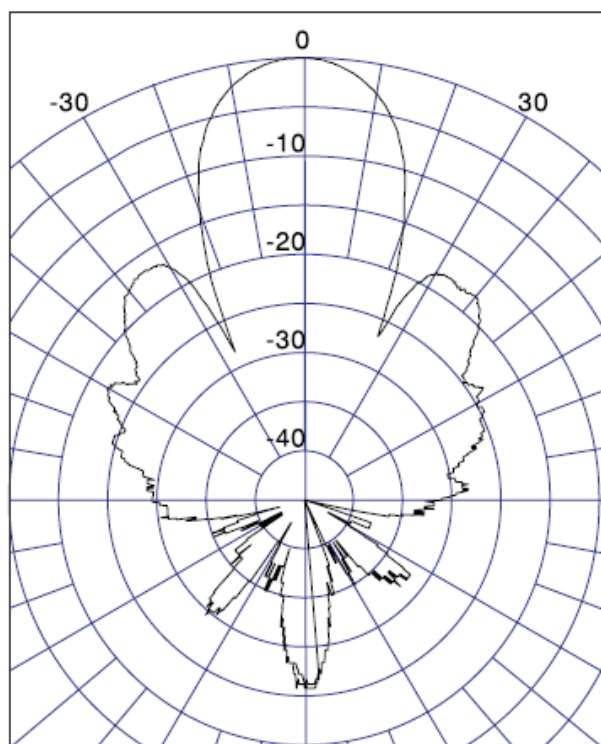


Figure A2 - 3: Beam Pattern 38 kHz transversal

A.3 The standard Sonar5 pro GPS import format

Table A3- 1: Table showing the GPS-data import format for Sonar5 pro

;date	time	Longitude	Latitude
1.12.2012	12:54:13.54	-48.8675498	-25.142525
1.12.2012	12:54:13.91	-48.8675503	-25.1425293
1.12.2012	12:54:14.28	-48.8675508	-25.1425337
1.12.2012	12:54:14.66	-48.8675513	-25.1425379
...

Data is imported as *.txt files

A.4 Temperature and conductivity depth profiles

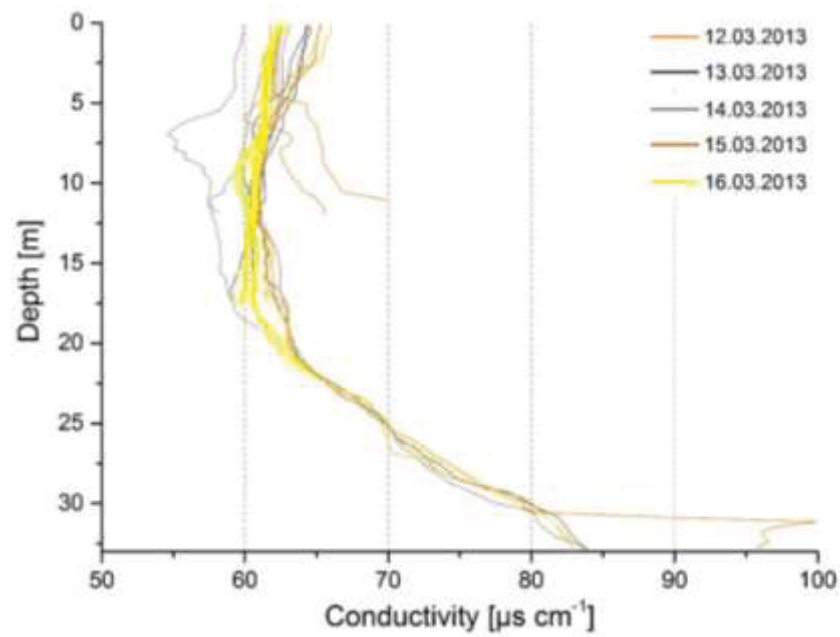


Figure A4- 1: Conductivity depth profiles measured in Capivari reservoir during campaign two in phase two

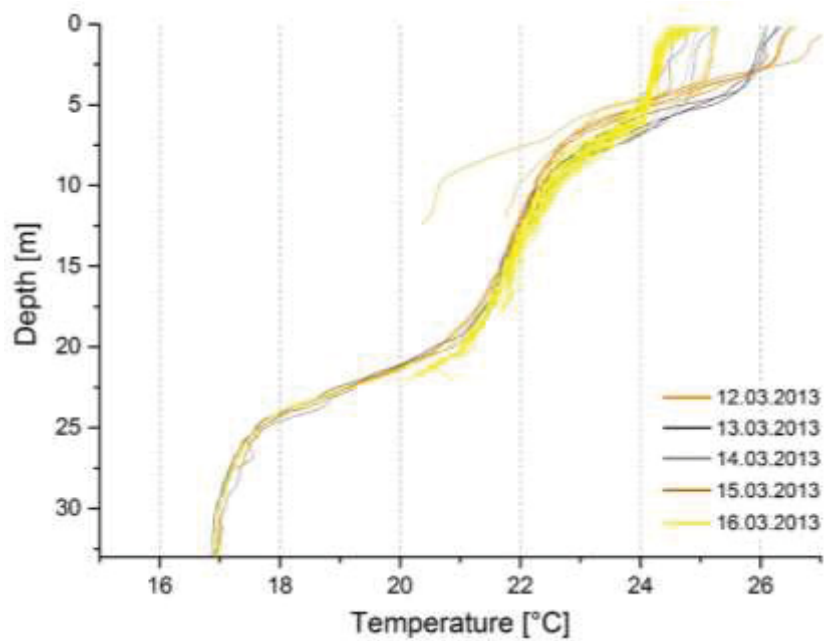


Figure A4- 2: Temperature depth profiles measured in Capivari reservoir during campaign two in phase two

A.5 Calibration standards for the ion and gas chromatography

Table A5- 1: Concentrations of the calibration standards for ion chromatography

Analyte	Fluoride	Chloride	Bromide	Nitrite	Nitrate	Phosphate	Sulfate
Concentration [mg/l]	0,1	0,1	0,1	0,1	0,1		0,1
	0,2	0,25	0,25	0,25	0,2		0,2
	0,58	0,5	0,5	0,5	0,5	0,5	0,5
	1	1	1	1	1	1	1
		2,9	2,9	2,9	2,9		2,9
	2	5	5	5	5	5,8	5
	10	10	10	10	10	10	10

Table A5- 2: Composition and concentrations of the calibration standards for gas chromatography

Analyte	Nitrous oxide	Methane	Carbon dioxide	Oxygen	Nitrogen	Standard Nr.
Concentration	0,294 ppm					1
	0,504 ppm					2
	1,000 ppm					3
	10,660 ppm	48,800 ppm	98,840 ppm			4
	40,800 ppm	103,000 ppm	200,100 ppm			5
	600,100 ppm		818,100 ppm			6
		1210,000 ppm	1590,000 ppm			7
				20%	80%	8
		59,82%	30,15%			9

A.6 Calculation for dissolved gases in water samples using headspace gas chromatography

Collection and order of calculations after Hölzlwimmer (2013):

Calculation of diffusion coefficients D_s [$\text{m}^2 \times \text{s}^{-1}$] in sediments (Iversen & Jørgensen, 1993):

$$D_s = \frac{D_0}{1 + n(1 - \Phi)} \quad \text{Eq. A6- 1}$$

with D_0 [$\text{m}^2 \times \text{s}^{-1}$] as diffusion coefficient in free water, n [-] as a factor describing the type of sediment and Φ [-] representing the porosity of the sediment.

Values of

$n = 3$ for clay-silt sediments

$n = 2$ for sandy sediments

gave reasonable estimates for D_s

If D_0 is given in temperatures different than in-situ conditions it can be recalculated by Stokes-Einstein relation:

$$\frac{D_1 \eta_1}{T_1} = \frac{D_2 \eta_2}{T_2} \quad \text{Eq. A6- 2}$$

with η [N s m^{-2}] the viscosity and T [K] the absolute temperature.

According to Henry`s law, gases in the aqueous phase will equilibrate in the headspace and aqueous phase if headspace is given. Then the total concentration (Conc_{tot}) [g l^{-1}] of gas in the original aqueous phase is the concentration in the headspace that was originally in the liquid phase but was partitioned into the gas phase (C_{GH}) [g l^{-1}], plus the concentration in the aqueous phase (C_{GA}) [g l^{-1}]:

$$\text{Conc}_{\text{tot}} = C_{\text{GH}} + C_{\text{GA}} \quad \text{Eq. A6- 3}$$

The concentration in the aqueous phase (C_{GA}) is calculated as follows:

$$C_{\text{GA}} = \frac{n_W}{V_W} \times \frac{p_g}{H} \times M \quad \text{Eq. A6- 4}$$

with n_w/V_w [mole l⁻¹] as the molar concentration of water being 55.5 mole l⁻¹, p_g [atm] as the partial pressure of the gas, H [atm] as the Henry coefficient and M [g mole⁻¹] as the molar weight.

p_g calculated as:

$$p_g = C_G \times p_T \quad \text{Eq. A6- 5}$$

with C_G [%] as the gas volumetric concentration in the headspace and p_T as the atmospheric pressure assumed to be equal to 1 atmosphere.

The concentration in the gas phase (C_{GH}), which was previously in the liquid phase and then transferred into the gas phase is calculated as follows:

$$C_{GH} = \frac{V_H}{V_L} \times C_G \times \rho \quad \text{Eq. A6- 6}$$

with V_H [l] as the headspace volume, V_L [l] as the liquid volume and C_G as above multiplied with the gas density [g l⁻¹], which is calculated at standard temperature as follows:

$$\rho = \frac{M}{V_{m0}} \times \frac{273.15 \text{ }^\circ\text{K}}{273.15 \text{ }^\circ\text{K} + T} \quad \text{Eq. A6- 7}$$

with M as above, V_{m0} [l/mole] as molar volume of ideal gases and T [°C] as the sample temperature.

Henry's coefficients (k_h) in [M atm⁻¹] converted to sample temperature by van't Hoff equation:

$$k_H = k_{H0} \times \exp \left[C \times \left(\frac{1}{T} - \frac{1}{T_0} \right) \right] \quad \text{Eq. A6- 8}$$

with C as a constant [°K] and T and T_0 as sample temperature respectively standard temperature.

k_h [M atm⁻¹] values were then converted into H [atm] by knowing the product of k_h and H being constantly 55.3.

$$H = \frac{55.3}{k_H} \quad \text{Eq. A6- 9}$$

Correcting concentrations of samples for additional volumes (mixing rule):

Result obtained from the gas chromatography and the results of ion chromatography had finally to be corrected by the volume of preserving agent contained in the vial by following equation:

$$C_{OS} = \frac{C_M \times V_M - C_A \times V_A}{V_{OS}} \quad \text{Eq. A6- 10}$$

with C_{OS} [g/l] as the concentration in the original sample, C_m and C_A as the concentrations in the mixture, respectively in the additional volume and V_m , V_A and V_{OS} [l] as the volume of the mixture, the additional volume and the original sample.

A.7 Calculation of the water quality index

Table A7- 1: Calculation table for the water quality index after OECD criteria

Criteria	Index (Ind.)	Data Capivari	Result Ind.	Weighting factor W_f	Result: Ind.* W_f
Chlorophyll-a (CHL) , [$\mu\text{g l}^{-1}$]	$0.0560 + 0.856 * \ln(\text{Chl}\alpha)$	4.51	1.35	10	13.45
Secchi-depth (SD) [m]	$3.739 - 1.127 * \ln(\text{SD})$	2.064	2.92	8	23.8
Total phosphorus spring (PSP) , [$\mu\text{g l}^{-1}$]	$-0.155 + 0.813 * \ln(\text{P}_{\text{SP}})$	16.00	2.1	5	10.45
Total phosphorus summer (P_s) , [$\mu\text{g l}^{-1}$]	$-0.939 + 1.066 * \ln(\text{P}_s)$	12.50	1.75	7	12.27
Sum Σ			1.99	30	59.60
			Index = (Result)/ΣW_f = 1.99		

A.8 Sediment analysis results

Table A8- 1: Overview table of the sediment analysis parameter from Capivari reservoir

Core#	Depth [m]	Rel. Depth [%]	LOI [%]	Total Carbon [%]	Density [g cm ⁻³]	Proportion of particles [%]			Fe [g kg ⁻¹]	Sulphur [%]	Phosphor [mg kg ⁻¹]	Mn [mg kg ⁻¹]		
						<63µm	<250µm	<2mm					>2mm	
1	32.5	100	16.1	2.7	1.21	99.3	16	1.5	0.2	0.2	82.1	0.07	1777	1095
2	31	95.3	15.7	3	1.14	81	15.2	0.1	0	0.1	85.4	0.09	1610	1545
3	17.5	53.8	15.1	2.2	1.16	99.3	1.2	0.3	0.4	1.3	82.1	0.03	1519	777
4	25.4	78.1	16	2.4	1.23	99.6	0.3	0	0.4	1	86.2	0.08	1730	903
5	2.7	8.3	11.4	3.1	1.43	38.8	34.6	12.9	5.4	1	61.5	0.05	1022	320
6	4.3	13.1	15.2	4.3	1.18	51.5	43.2	2.4	0.9	2.1	57.5	0.04	1623	720
7	24.4	75.1	15	2.3	1.17	98.5	3.6	0.2	0	0	79.8	0.08	1697	798
8	4.3	13.2	13.6	3.6	1.22	78.9	20.5	0.4	0.2	0.1	55.6	0.03	1261	472
9	11.5	35.3	12.2	2.8	1.36	58.9	32.3	5.7	2.1	1	70.4	0.03	1323	544
10	12.3	37.8	13.8	2.3	1.22	78.9	12.5	6.6	6.8	0.5	63.2	0.02	1261	479
11	7	21.5	11.3	1.6	1.31	95.3	1.2	0.6	0	0	68.3	0.02	1396	390
12	14.2	43.7	13.4	2.8	1.18	88.7	8.4	1.6	0.9	0	65.6	0.03	1423	670
13	6.3	19.4	14	2.3	1.25	97.2	2.7	0.1	0	0	65.1	0.03	1057	336
14	7.7	23.7	11.9	2.5	1.32	92.7	6.8	0.3	0.2	0	57.1	0.03	1052	564
15	16.6	51.1	12.4	1.9	1.27	93.9	4.6	0.7	0.7	0	77.1	0.03	1837	875
16	12	36.9	15.3	3.6	1.23	94.4	5.4	0.2	0.1	0	64.7	0.04	1471	650
17	19.4	59.7	13.8	2.3	1.19	99.9	0	0	0	0	75.2	0.06	1878	551
18	14.4	44.3	13.9	2.7	1.4	79.9	25	12.2	5.9	1.2	63.7	0.02	1161	554

Table A8- 2: Overview table of the sediment analysis parameter from core samples from Vossoroca reservoir

Core #	Depth [m]	Rel. Depth [%]	LOI [%]	Total Carbon [%]	Density [g cm ⁻³]	Proportion of particles [%]				Fe [g kg ⁻¹] ¹	Sulphur [%]	Phosphor [mg kg ⁻¹]	Mn [mg kg ⁻¹]		
						<63µm	<250µm >63µm	<500µm >250µm	<2mm >500µm					>2mm	
1	Core	4.7	27.6	10.3	3.5	1.4	35.9	26.7	10.8	8	0.7	29.1	0.01	533	230
2	Core	12.6	74.1	16.7	3.6	1.1	99.6	0.3	0.1	0	0	57.3	0.07	1179	335
3	Core	12.3	72.4	15	3.2	1.1	99.5	0.1	0	0	0	68.3	0.04	1273	341
4	Core	11.4	67.1	13.4	2.9	1.1	95.2	0.1	0	0	0	48.3	0.03	1038	348
5	Core	2	11.8	5.4	1.1	1.6	40.8	9.2	19	26.5	4.6	21.6	0.02	225	316
6	Core	9.9	58.2	14.7	3.6	1.1	98.2	1.9	0.2	0	0	56.1	0.03	1233	413
7	Core	3.4	20	8.2	1.1	1.6	57.2	10.8	16.5	12.2	3.3	48.1	0	713	263
8	Core	9.1	53.5	16	4.2	1.1	63.9	3.9	0.2	0	0	47.8	0.02	1344	488
9	Core	5.3	31.2	18.7	6.5	1.1	71.4	20.7	5.1	1.3	1.6	47.7	0.03	1173	488
10	Core	15.7	92.4	17.3	4.3	1.1	99.7	0.2	0	0	0	49.7	0.13	1050	382

Table A8- 3: Overview table of the sediment analysis parameter from grab samples from Vossoroca reservoir

Core #	Depth [m]	Rel. Depth [%]	LOI [%]	Total Carbon [%]	Density [g cm ⁻³]	Proportion of particles [%]				Fe [g kg ⁻¹]	Sulphur [%]	Phosphor [mg kg ⁻¹]	Mn [mg kg ⁻¹]	
						<63µm	<250µm	<500µm	>2mm					
1	Grab	7.5	44.1	4.2	0.6	42.7	11.3	23	8	15	35.8	0.01	576	411
2	Grab	7.5	44.1	13.5	2.7	95.5	4.3	0.2	0	0	46.4	0.02	941	424
3	Grab	7.2	42.4	14.7	3.6	97.6	2.2	0.2	0	0	37.3	0.02	825	341
4	Grab	15.5	91.2	16.2	3.7	99.2	0.7	0.1	0	0	45.5	0.1	1064	352
5	Grab	10	58.8	9	2.2	41.4	17.7	26.8	13.4	0.7	36	0.02	547	378
6	Grab	4.9	28.8	11.4	4.3	43.2	21.2	24.6	9.5	1.5	21.2	0.02	560	418
7	Grab	14.1	82.9	15.1	3.1	98.9	0.8	0.4	0	0	49.7	0.08	1167	376
8	Grab	12.8	75.3	16.3	3.6	99	0.8	0.2	0	0	66.3	0.08	1309	375
9	Grab	5.9	34.7	2.9	0.4	29.8	6.1	15.6	42.5	6	11.4	0	232	204
10	Grab	12.3	72.1	15.7	3.1	99.6	0.3	0.1	0	0	50.7	0.04	1088	329
11	Grab	8	47.1	8.5	2.8	31.1	11.7	16.2	36	5	30.1	0.02	339	245
12	Grab	6.8	40	11.9	2.4	42.7	11.4	16.7	27.5	1.7	51.7	0.03	713	345
15	Grab	6.5	38.2	3.4	0.7	15.6	12.9	36.8	31.2	3.6	23.4	0.01	332	334
16	Grab	7.5	44.1	6.5	1.3	59.6	24.9	5.9	5.4	4.3	33.3	0.02	352	310
17	Grab			14.6	3	95.5	2.6	2	0	0	40	0.03	906	288
18	Grab	12	70.6	14.9	3.1	99.5	0.4	0	0	0	38.7	0.03	747	273
19	Grab	12.2	71.8	11.9	2.5	83.3	15.5	0.7	0.6	0	46.7	0.03	882	402
20	Grab	11.2	65.9	14.5	3.2	99.4	0.5	0.1	0	0	44.1	0.02	941	363
21	Grab	9.5	55.9	14.7	3.3	99.2	0.8	0	0	0	38.2	0.03	755	289
22	Grab	9	52.9	14.3	2.9	99.3	0.7	0	0	0	46.8	0.02	955	328

A.10 Water level and air pressure data

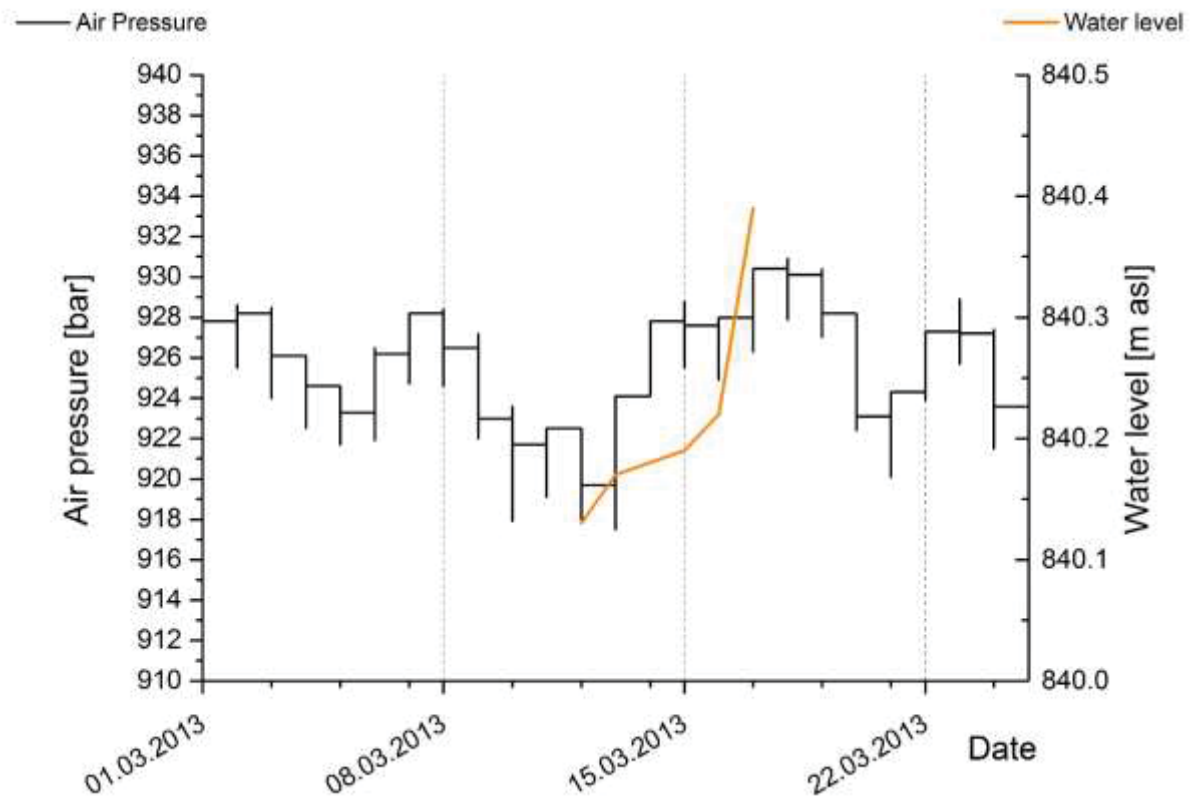


Figure A10- 1: Water level and air pressure changes depicted over the time of measurement campaign two, phase two (12.03.–17.03.2013)

A.11 Technical sheet of the DPS

Table A11- 1: Technical specifics of DPS-generation I; after Gauger (2013)

Total Length	700mm
Total Width	107mm
Total Depth	51mm
Body Length	600mm
Body Width	107mm
Body Depth	40mm
Total Weight	2,68 kg
# Chambers	15
Chamber Height	34mm
Chamber Width	94mm
Chamber Depth	40mm
Single Chamber Volume	127,8 ml
Mesh Type used (ISO 9044)	Woven Wire Cloth, Plain Screen, Type A
Aperture	Square
Wire Dia d	0,16 mm
Aperture Width w	0,25 mm
Open Screening Area A ₀	37 %
Window Size A (both Sides)	6392 mm ²
Sample Interval I	40 mm
Nominal Design Factor F	20 (mm)
Effective Design Factor F _{eff}	54 (mm)

Table A11- 2: Technical specifics of DPS-generation II; after Hölzlwimmer (2013)

Total Length	690mm
Total Width	104mm
Total Depth	45mm
Body Length	605mm
Body Width	104mm
Total Weight	1,63 kg
Body Depth	45mm
# Chambers	15
Chamber Height	34mm
Chamber Width	94mm
Chamber Depth	40mm
Single Chamber Volume	127,8 ml
Perforated plate Type (DIN/ISO 24041)	"Rv 2-3,5"; Staggered round holes
Individual Hole Diameter	2mm
Hole center Distance	3,5mm
Thickness	1 mm
Relative open hole Area	30%
Window Size A (both Sides)	6392 mmE2
Sample Interval I	40 mm
Nominal Design Factor F	20 (mm)
Effective Design Factor Feff	66,6 (mm)

A.12 Depth profiles of various analytes in the DPS

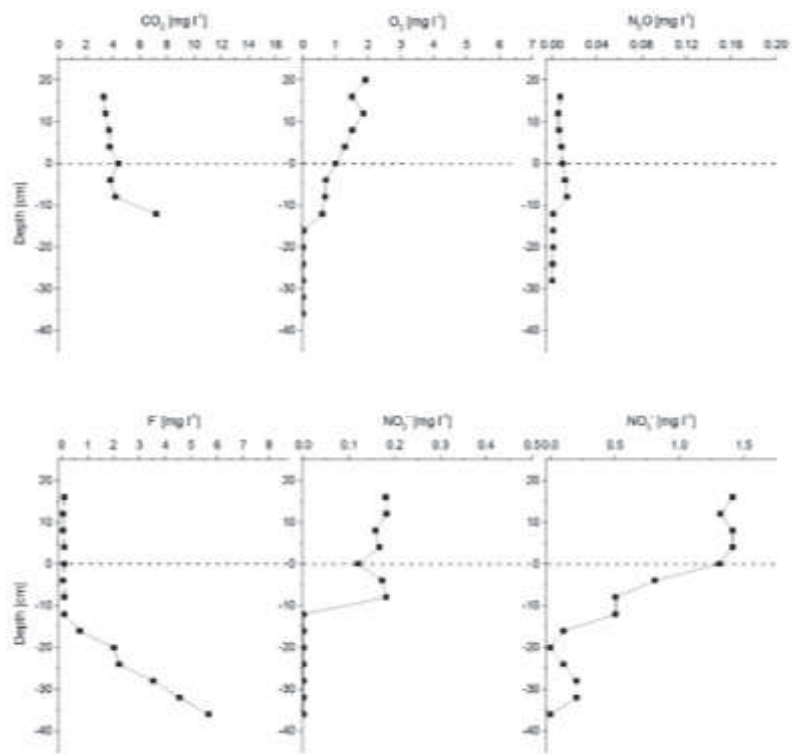


Figure A12- 1: Depth profiles of various analytes in DPS 1

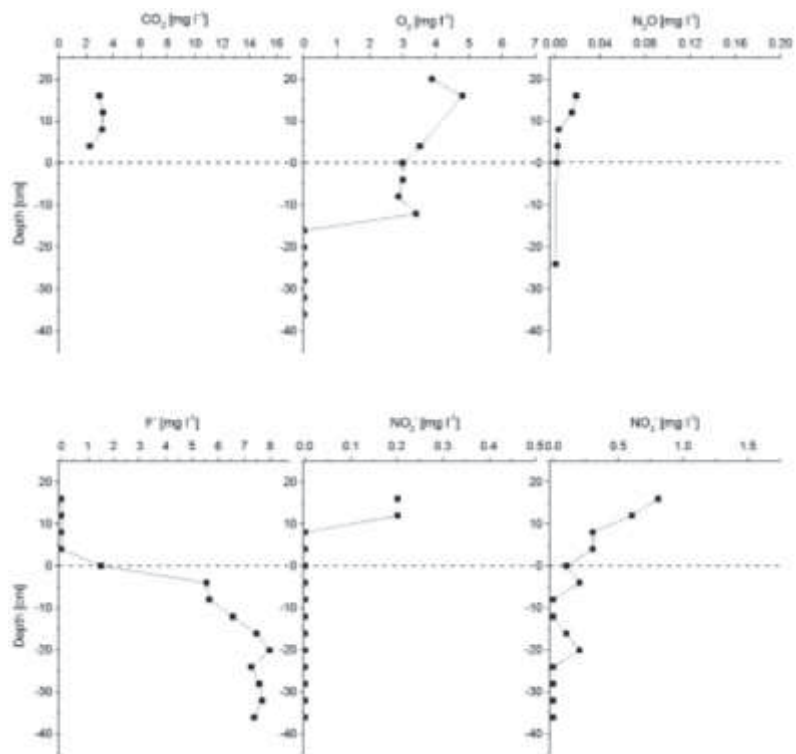


Figure A12- 2: Depth profiles of various analytes in DPS 2

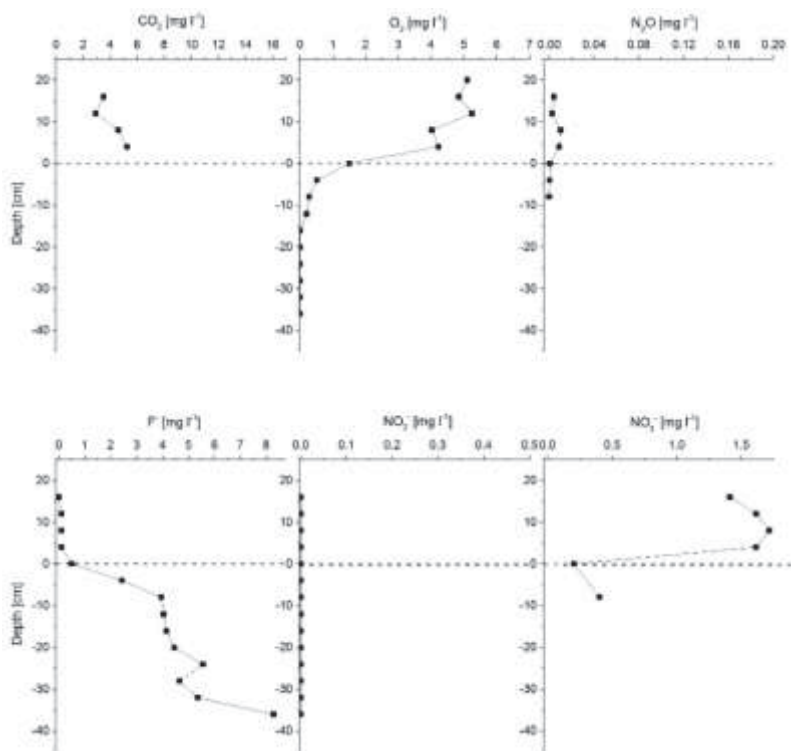


Figure A12- 3: Depth profiles of various analytes in DPS 3

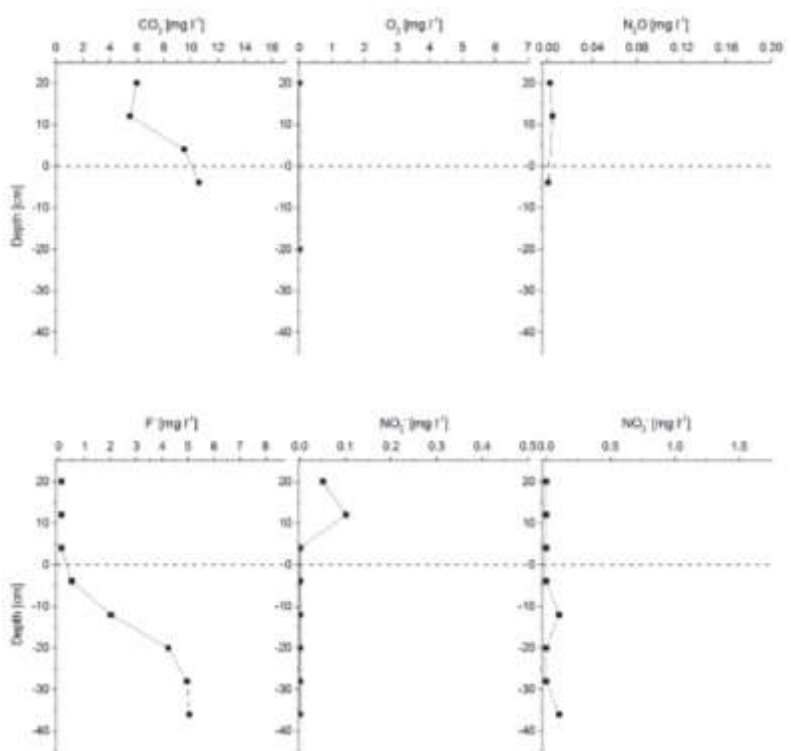


Figure A12- 4: Depth profiles of various analytes in DPS 4

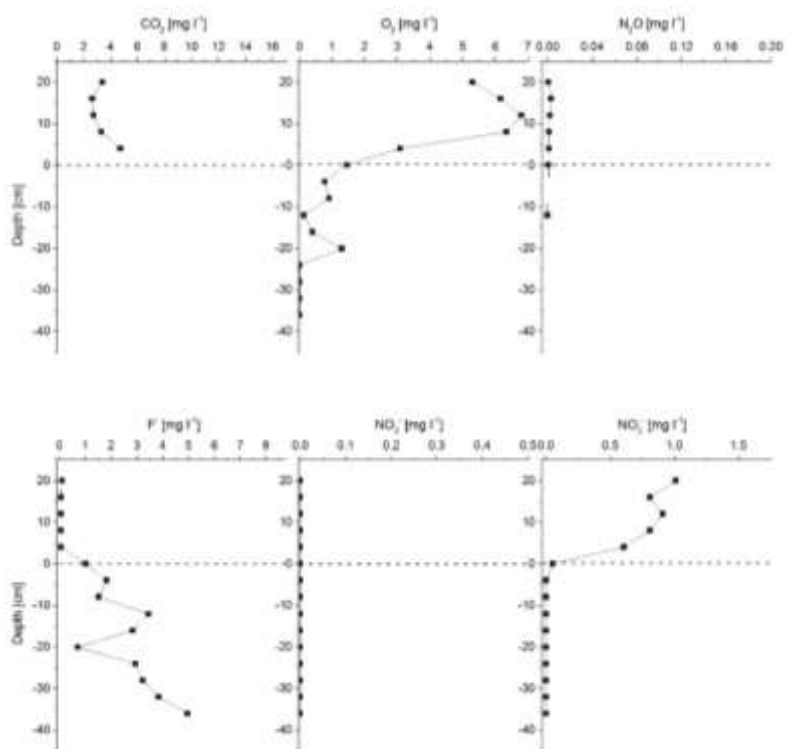


Figure A12- 5: Depth profiles of various analytes in DPS 5

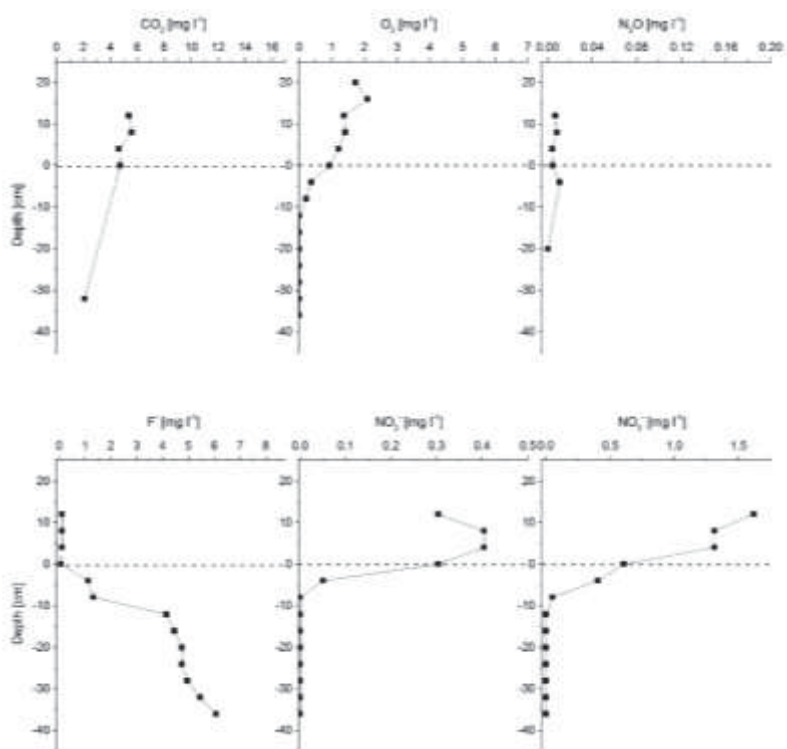


Figure A12- 6: Depth profiles of various analytes in DPS 7

A.13 Regression analysis of the sediment density correction

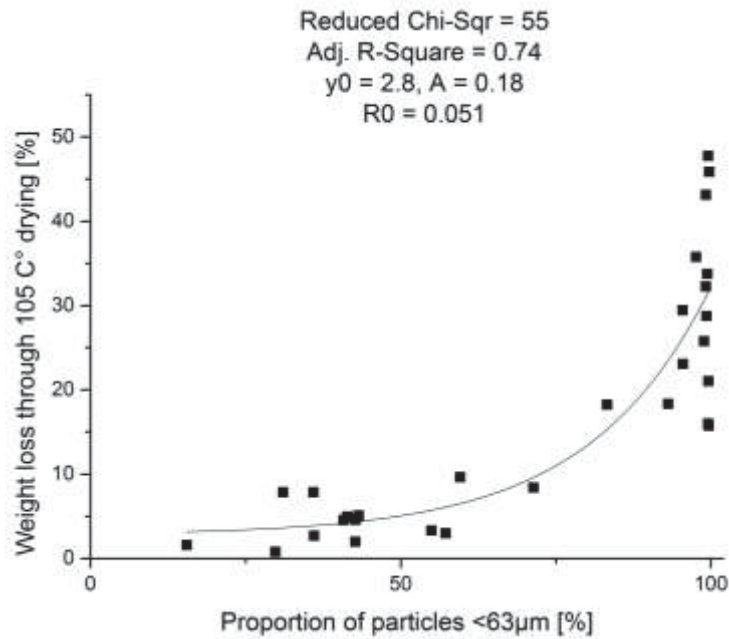


Figure A13- 1: Regression analysis of the weight loss through 105 °C drying plotted over the proportion of particles, N=16; $p < 0.01$

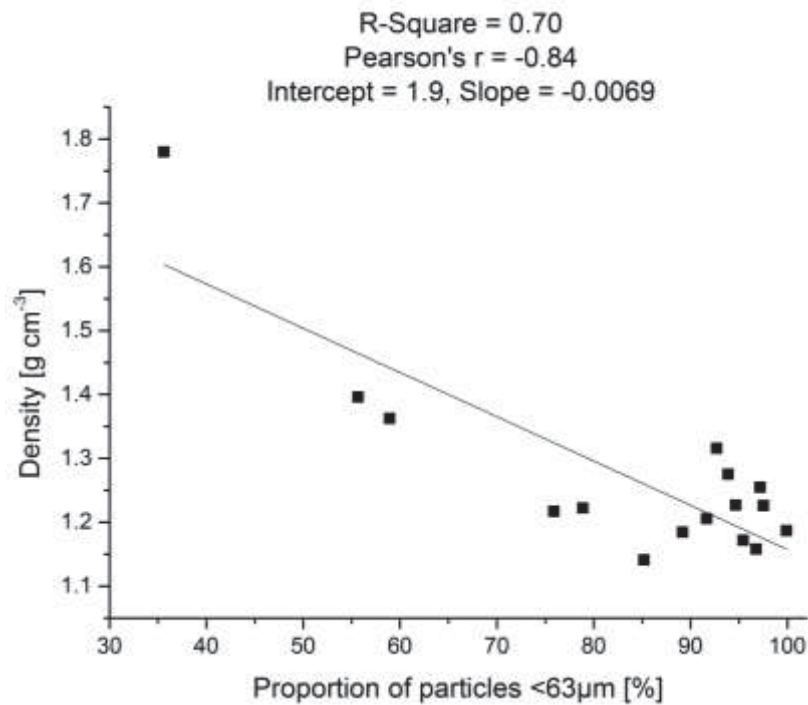


Figure A13- 2: Linear regression analysis for the estimation of the density in relation to the share of fine material; N=16; $p < 0.01$

factors

A.14 Model results for the proportion of particles in the sediment

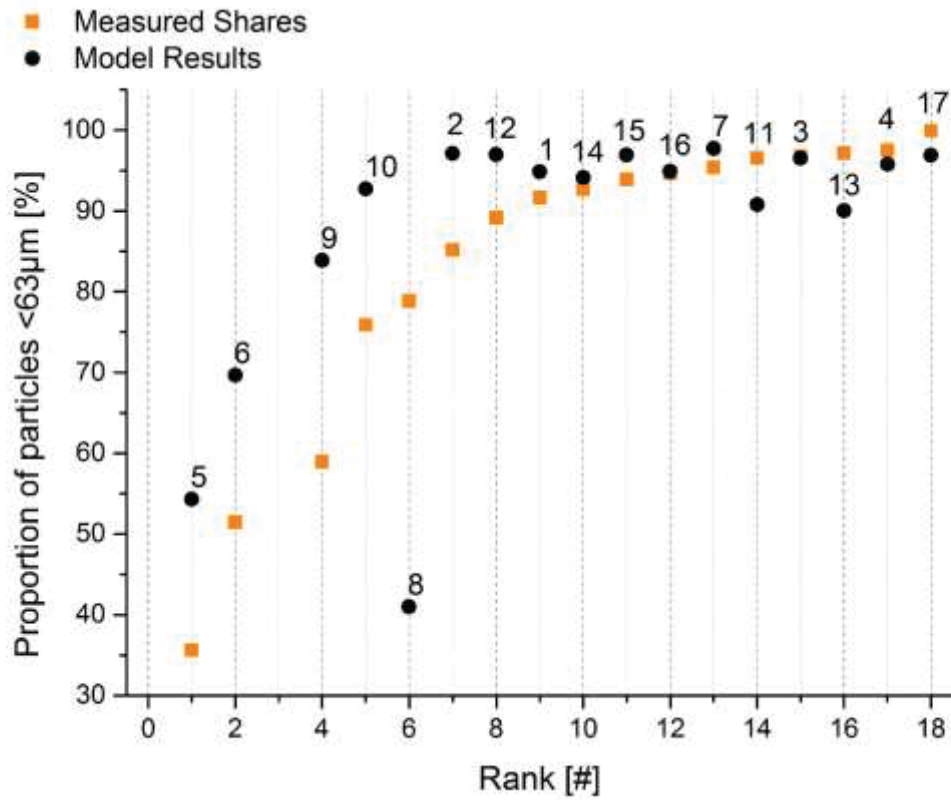


Figure A14- 1: Comparison of the measured and modelled results of the particle proportion at 18 coring sites in Capivari reservoir